Università
Ca'Foscari
Venezia

Corso di Dottorato di ricerca

in Science and Technology of Bio and Nanomaterials

ciclo 35°

Tesi di Ricerca

Novel Chiral Luminescent Nanomaterials: Synthesis, Characterisation and Application in Enantioselective Chemosensing

SSD: CHIM/02

Coordinatore del Dottorato
Prof. Flavio Rizzolio

Supervisore
Prof. Alvise Benedetti

Cosupervisore
Prof. Adolfo Speghini

Dottorando
Lorenzo Branzi
Matricola 956507

List of Contents

This PhD thesis is focused on the investigation of novel chiral luminescent nanomaterials systems. Particular attention is dedicated to the development of new synthetic methods and to the characterisation of the physico-chemical properties of chiral nanoparticles. In addition, the investigation on potential applications in the enantioselective luminescence chemosensing is reported.

In the thesis, three class of systems characterised by luminescent activity are covered independently: i) Carbon Dots, ii) Quantum Dots, focusing on ternary and quaternary I-III-VI silver, copper and indium sulfide systems and iii) copper halides. All these systems present well-known photoluminescent activity and the introduction of chiroptical properties is attracting the interest of the scientific community due to their potential technological impact.

This chapter is dedicated to a brief introduction presenting the definition of chirality and chiroptical properties in inorganic nanosystems focusing on the description of the origin of the chiroptical properties conventionally observed in nanoparticles. A proper introduction on the three specific types of systems is provided in the relative chapters. The scope of the project is also presented at the end of the chapter.

CHAPTER I

INTRODUCTION AND SCOPE OF THE THESIS

1 INTRODUCTION

Chirality is the geometrical property which describes an object not superimposable with its mirror image. More specifically, according to the definition reported in the IUPAC gooldbook, chirality is:[1]

The geometric property of a rigid object (or spatial arrangement of points or atoms) of being non-superposable on its mirror image; such an object has no symmetry element of the second kind (a mirror plane, $\sigma = S_1$, a centre of inversion, $i = S_2$, a rotation-reflexion axis, S_{2n}).

Two objects that are non-superposable mirror images of each other are called enantiomers and are characterised by the same physical properties (melting point, boiling point etc.). In the case of molecules, different behaviour between the enantiomers is usually proved by the interaction with other chiral systems such as circular polarized light and adsorption or chemical reactivity with chiral substrates. Chiral molecules that present the same chemical composition but are not related by the mirror symmetry, are called diastereoisomers or diastereomers.

Chirality is mainly known as a property related to the stereoisomerism of organic molecules and coordination complexes even though it is not restricted to a specific type of object, without any limitation to their composition and size scale.

Typical examples are the stereogenic centre presents in carbon sp^3 atoms substituted by four different groups (**Fig. 1a**) and the axial chirality observed in more complex systems (e.g., helicenes and BINAP) where chirality is originated by their connectivity or steric constrains (**Fig. 1b,c**).[2,3] In inorganic chemistry, it is particularly well-know the stereosimerism of octahedral trischelate complexes (e.g. $Cr(acac)_3$, acac = acetylacetonate) able to produce two distinct stereoisomers Δ and Λ according to the arrangement of the ligands (**Fig. 1d**).[4,5] A particular example of the role of chirality is observed In biological systems, where homochirality or the property of a system containing only a single enantiomer of a chiral molecule, has revealed interesting details on the relevant role of symmetry breaking in life science.[6]

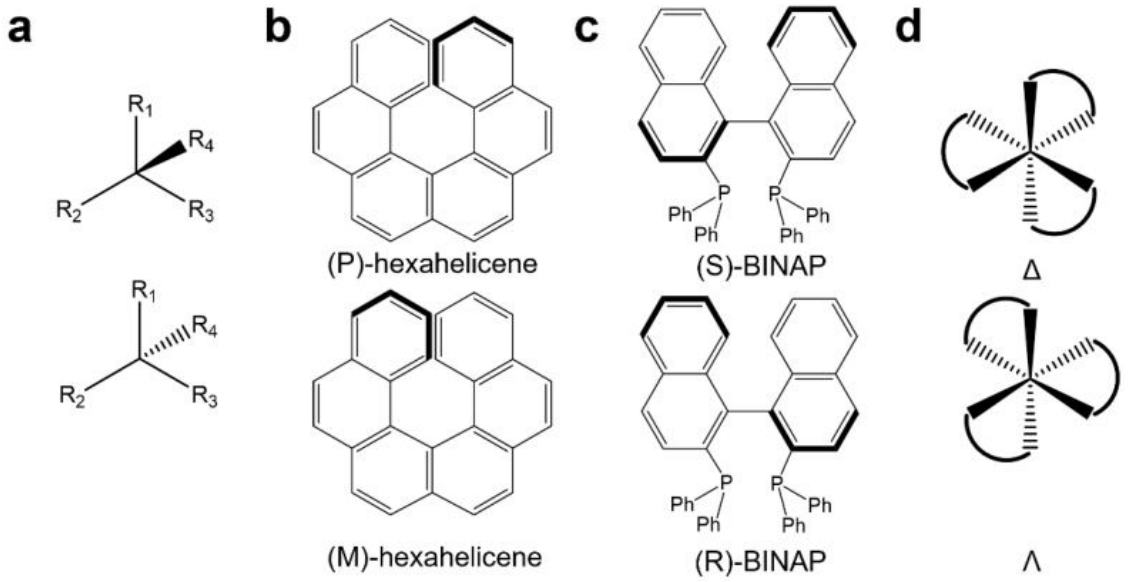

Figure 1: examples of chiral molecules. a) tetrasubstituted sp^3 carbon atoms, b) axial chirality in helicene and c) BINAP enantiomers and d) octahedral trischelate complexes.

Chiral systems show some properties which are strongly linked with their characteristic structural features. Among them, the most exploited one is the interaction with polarized light. When linear polarized light passes through a chiral medium, it is bent of a certain angle α. This effect, due to different refraction indexes (n_L and n_R) affecting the propagation of the polarized light in the chiral medium, (see **Eq. 1)** is the basis of the optical rotatory dispersion spectroscopy. On the other hand, the differential absorption of left- and right-handed circular polarized light is the basis of the circular dichroism spectroscopy. This property is directly related to the Rotatory power (R) of a chromophore given by the imaginary part of the scalar product of the electronic (μ_{if}) and magnetic (m_{if}) transition dipole moments (**Eq. 2**). These techniques are commonly used to assess chirality in different chiral systems, especially when the complete determination of the geometry is particularly challenging. However, the optical properties of chiral systems (named chiroptical properties) are secondary effects, consequences of the object geometry, which defines its chirality, and particular attention is required to relate the chiroptical properties to their origin. For instance, the effects on polarized light produced by one enantiomer are reduced or completely cancelled (in the case of a perfect racemate) by the other one, the optical characterisations are challenging due to the possible presence of both the enantiomers (racemic mixtures). For this reason, relying on enantioselective syntheses, which allow for the preferential formation of one enantiomer over the other, is often fundamental for detecting chirality, especially in the case of chiral nanosystems where the

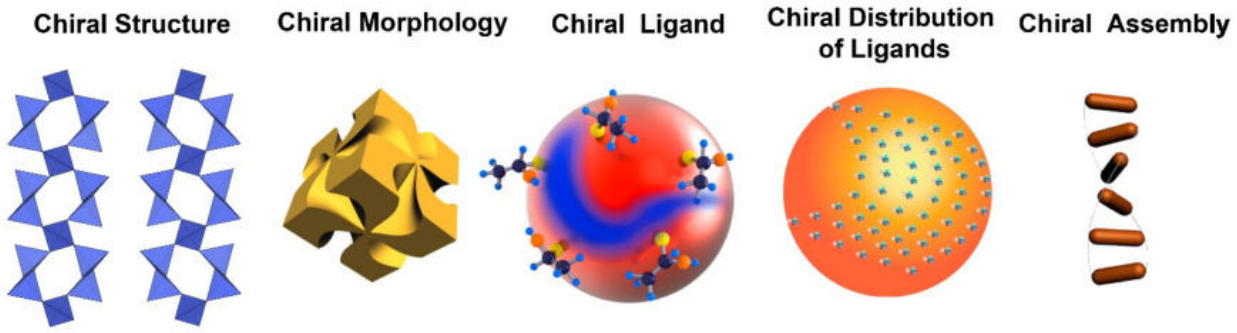

Figure 2: representation of the major types of origin of chirality in inorganic nanomaterials, figures adapted from References: [30,34,35].

investigation of the nanoparticles geometry (especially in the range of few nanometers) is often challenging or inconclusive.

Eq. 1

$$\alpha = \frac{\pi}{\lambda}(n^L - n^R)$$

Eq. 2

$$R = Im(\mu_{if} \bullet m_{if})$$

In inorganic nanostructures, chirality can be related to multiple origins. In **Fig. 2**, some examples of chirality in inorganic nanostructures are reported and classified in categories according to their different origins.

More in detail:

- **Chiral Structure:** atoms of inorganic systems that crystallise in a chiral space group present a specific chiral spatial distribution. Typical examples of chiral crystals are: α-quarts, lanthanide phosphate, gallium phosphate and α-HgS. In most cases, the solid phase crystallises in one of the 22 possible chiral space groups in R3. However, chiral structures can crystallise in other 43 space groups characterised by the presence of only symmetry operation of the first kind (rotations, rototranslations and translations) forming the Sohncke group.[7] These systems are usually associated with strong chiroptical properties. However, due to thermodynamic reasons, non-stereoselective syntheses tend to form racemic mixtures presenting low or none chiroptical activity. In this case, the use of chiral ligands is fundamental to direct the symmetry breaking promot-

ing the preferential formation of one enantiomer over the other. Although a spontaneous symmetry breaking was observed under certain conditions, the use of chiral ligands remain critical to control the stereochemistry of final products and amplify the particles chirality.[8] The paper of Ben-Moshe et al.[9] on α-HgS (cinnabar phase) nanoparticles produced by spontaneous conversion of achiral β-HgS in the presence of penicillamine as chiral inductor, revealed a dissymmetry factor (g-factor) of 0.012, higher by one order of magnitude than the value observed for other semiconductor nanoparticles with chirality originated at the interface. Further control on the enantiopurity on α-HgS nanoparticles was achieved by the optimization of a second growth step, via Oswald ripening, mediated by the chiral ligand.[10] Concerning gold nanocluster, another example of chiral structure, Zeng et al.[11] observed a chiral atomic structure in $Au_{28}(TBBT)_{20}$ nanocluster (TBBT: 4-*tert*-butylbenzenethilate). The resolution of the racemate mixture by chiral-HPLC, allowed for isolating the two enantiomers and thus characterising their chiroptical activity.

- **Chiral Morphology:** nanoparticle syntheses can be properly designed to favour the formation of distorted morphology with chiral shapes. An example is the production of the chiral gold helicoid nanoparticles developed by Nam and coworkers.[12–14] In this case, the deposition of metal atoms on the surface of a gold polyhedral nanoparticle (achiral seed) characterised by high-Miller indexes facets could be modulated exploiting the enantioselective interaction between the chiral ligand and the intrinsic chirality of the particle surfaces. Thanks to a multi steps process, the production of highly distorted gold nanostructures was obtained with high control. Another example of chiral shape is given by the production of chiral mesoporous silica. Che et al.[15,16] reported the preparation of chiral mesoporous silica using a synthetic route based on soft templating with anionic surfactants like N-myristoil-L-alanine evidencing the presence of some degree of enantioselectivity.
- **Chiral Ligand:** nanoparticles are stabilised using chiral ligands. In this condition, chiral plasmonic or chiral excitonic effects are induced by the physi- or chemisorption of a chiral ligand on the particles surface. This approach covers both structural and electronic chirality origin. The structural origin is associated to the formation of chiral defects on the particles surface promoted by the chiral ligand, while the electronic origin

is related to the chiral induction by the electronic coupling between the chiral ligand and the nanoparticles electronic transitions.

This type of chirality is characteristic of metallic and semiconductor nanoparticles when a chiral ligand is present. Usually, chiral metallic nanoparticles show CD active transitions at the frequency of their plasmonic resonance. For instance, Gautier et al.[17] observed CD active transitions associated to the particle core in N-isobutyryl-L/D-cysteine stabilised gold nanoparticles. Based on the vibrational circular dichroism observations, the particle chirality was related to ligand induced chirality by a preferential bidentate interaction trough thiol and carboxylic groups. Park et al.[18] evidenced the fundamental role of the thiol group for the chiral induction on silver nanoparticles stabilised by different amino acids (cysteine, penicillamine, glutamine and lysine) and glutathione. Slocik et al.[19] reported the chiral induction in 10 nm gold nanoparticles by the functionalization with peptides with different secondary structures. The CD activity in the plasmonic transition (520 nm) was simulated with a theoretical model based on coulombic interactions, which considers the electric and magnetic transition moments (dipole and quadrupole) of the chiral ligand and the nanocrystal plasmonic surface.[20]

This type of chirality is also common for semiconductor nanoparticles that usually show some degree of chirality in the exciton region, far from the frequency related to the electronic transitions of the chiral ligand (typically in the UV range). Elliott et al.[21] considered the effect of structural distortions on the outer layer of a CdS clusters at the origin of the chiroptical properties of CdS quantum dots stabilised by penicillamine. Ben-Moshe et al.[22] modelled the circular dichroism spectra of several semiconductor quantum dots considering the electronic coupling between the chiral ligand and the nanocrystal core. Another theoretical approach was developed by Gao et al.[23,24] using a non-degenerative coupled-oscillator model to simulate the induced chirality in CdSe nanorods and nanoplatelets.

- **Chiral Distribution of Ligands:** it is another example of chirality at the particle-ligand interface, but, in this case, chirality can be induced using also achiral ligands and the origin of the symmetry breaking is related to the asymmetric ligand arrangement on the particle surface. The $Au_{38}(SCH_2CH_2Ph)_{24}$ nanocluster is an example of this type of chirality: the nanocluster is composed by a face fused biicosahedral Au_{23} core and a gold thiolate staples layer formed by gold atoms and achiral thiolates.[25,26] Although

both the Au_{23} core and the thiolate ligand are achiral, the asymmetry in the staple layer causes a reduction of the total nanocluster symmetry from D_{3h} to D_3. Dolamic et al.[27] successfully isolated the nanocluster enantiomers and collected the chiroptical spectra of the two enantiomers.

- **Chiral Assembly**: achiral nanoparticles can be appropriately arranged in a chiral assembly to produce systems with dimensions that span over several orders of magnitude. Ma et al[28]. reported the preparation of dimers produced by the side-by-side assembly of achiral gold nanorods. The dimers showed an intrinsic chirality due to their structure. Due to thermodynamic reasons, the dihedral angle $\theta \neq 0$ between the two gold nanoparticles is favoured to reduce electrostatic repulsions. The chiroptical activity of a single dimer proved the origin of the chirality. Smith et al.[29] reported a dimeric system based on achiral gold nanodumbbells assembled inside polymeric nanoparticles. The analysis of the dimers solution did not show any CD active transition, while the circular differential scattering measurements on single dimers revealed the relationship between the chiroptical activity and the dihedral angle. The observation of the chiroptical properties of single dimers further confirmed the relation between the lack of optical chirality of the ensemble and the racemic nature of the sample. Lan et al.[30] reported the formation of helical superstructures composed by achiral gold nanorod opportunely oriented inn a chiral helical geometry using DNA origami technique.

More complex systems with multiple levels of organization of their topological elements and characterised by multiple type of chirality are reported in the literature. A fascinating example was described by Jiang et al.[31] who studied hierarchical organized particles composed by cysteine-gold thiolate chiral nanosheets assembled on larger particles with different degree of chirality and complexity. The authors observed that the morphology of the self-assembled structure can be modulated according to the ratio of the cysteine enantiomers used in the synthesis and the conditions employed to promote the nanosheets self-assembly. The investigation of the origin of chirality in inorganic systems, and its propagation from the nano to the micro scale, does not only allow to disclose the origin of homochirality in biominerals, but also inspires new route to improve the design of novel syntheses for the formation of inorganic crystals with complex morphologies with unprecedent control.[32,33]

In this thesis, the experimental work is focused on the study of the origin of chirality at the particle ligand interface using chiral ligand. In particular, amino acids are chosen as chiral inductors due to the availability of both enantiomers with high optical purity, the abundance of functional group that can provide multiple interaction on the particle surface and their biocompatibility.

2 SCOPE OF THE THESIS

The project is based on the study of novel chiral luminescent nanosystems, covering synthesis, characterisation and application in the enantioselective chemosensing. Attention is dedicated to three distinct classes of luminescent materials: carbon dots, I-III-VI semiconductor quantum dots and copper halides. This decision is related to the relatively well-known luminescent properties of these systems as well as to the extensive scientific interest associated to them. Another fundamental aspect is related to the biocompatibility and toxicity of these materials. Carbon dots and I-III-VI quantum dots are promising less toxic alternatives to Cd-based binary quantum dots and the research activity related to copper halides has recently become popular as possible alternative to lead halide perovskites.

The aim of the research is the synthesis and the characterisation of the particles chirality in order to better understand the origin of chirality and to unravel the fundamental parameters for the optimization of the transfer of chirality. The main sections of the project are summarized in the following list:

- Carbon Dots: in this case, the study of the nanoparticles formation mechanism is carried out considering a novel synthetic method based on the radical assisted decomposition of cysteine catalysed by copper ions. The process allows to finely tune the optical and chiroptical properties of the nanoparticles and to highlight fundamental features on their structural origin. Moreover, the study covers the origin of chirality and the relationship between optical/chiroptical properties and the evolution of the nanoparticles structure during the substrate decomposition step.
- I-III-VI Quantum Dots: the design of a novel synthesis is studied to obtain ternary quantum dots with chiral properties. Due to their superior optical performances, non-stoichiometric silver indium sulfide quantum dots are chosen as a reference compound for the optimization of the synthetic procedure, for the investigation on the chirality at

the nanoparticle-ligand interface and for the optimization of the deposition of a ZnS shell with a post synthetic treatment. The investigation considers also different chemical compositions changing the silver to indium ratio, copper indium sulfides as another example of ternary system and multiple quaternary systems based on silver, copper and indium sulfides. In this context, the analysis of structural, optical and chiroptical properties are combined to explain the change of the particle chirality according to the different compositions in the I-III-VI systems.

- Copper halides: this section covers the development of a novel ligand assisted reprecipitation method for the production of cesium copper bromide in the presence of chiral ligand and the characterisation of its chiroptical properties. Moreover, the study considers the effect of the chiral ligand on the morphology and chiroptical properties of the particles, and the possible application of the synthetic procedure to other lead-free metal halides.

Finally, the most promising systems (silver indium sulfide quantum dots and cysteine based carbon dots) are investigated for a potential application in the luminescence enantiselective chemosensing for different amino acids. The investigation considers both Turn-Off and Turn-On chemosensing modes to explore potential extension of the analyte target and concentration range.

3 REFERENCES

1 A. D. McNaught and A. Wilkinson, '"Chirality"' Compendium of Chemical Terminology, 2nd ed. (the "Gold Book").

2 A. Miyashita, A. Yasuda, H. Takaya, K. Torium, T. Ito, T. Souchi and R. Noyori, *J. Am. Chem. Soc.*, 1980, **102**, 7932–7934.

3 M. S. Newman and D. Lednicer, *J. Am. Chem. Soc.*, 1956, **78**, 4763–4770.

4 C. E. Housecroft and A. G. Sharp, *Inorganic Chemistry*, Person Education Limited, Harlow, fourth edition., 2012.

5 F. A. Cotton, G. Wilkinson, C. A. Murillo and M. Bochman, *Advanced Inorganic Chemistry*, Wiley-Interscience, New York, sixth edition., 1999.

6 W. A. Bonner, *Orig.Life and Evol. Biosph.*, 1995, **25**, 175–190.

7 Hanh. T., *International Tables for Crystallography*, Springer, fifth edition., 2005.

8 U. Hananel, A. Ben-Moshe, H. Diamant and G. Markovich, *Proc. Natl. Acad. Sci. U.S.A.*, 2019, **166**, 11159–11164.

9 A. Ben-Moshe, A. O. Govorov and G. Markovich, *Angew. Chem. Int. Ed.*, 2013, **52**, 1275–1279.

10 J. Kuno, K. Miyake, S. Katao, T. Kawai and T. Nakashima, *Chem. Mat.*, 2020, **32**, 8412–8419.

11 C. Zeng, T. Li, A. Das, N. L. Rosi and R. Jin, *J. Am. Chem. Soc.*, 2013, **135**, 10011–10013.

12 Y. Y. Lee, N. H. Cho, S. W. Im, H. E. Lee, H. Y. Ahn and K. T. Nam, *ChemNanoMat*, 2020, **6**, 362–367.

13 H. E. Lee, R. M. Kim, H. Y. Ahn, Y. Y. Lee, G. H. Byun, S. W. Im, J. Mun, J. Rho and K. T. Nam, *Nat. Commun.*, 2020, **11**, 263.

14 H. E. Lee, H. Y. Ahn, J. Mun, Y. Y. Lee, M. Kim, N. H. Cho, K. Chang, W. S. Kim, J. Rho and K. T. Nam, *Nature*, 2018, **556**, 360–364.

15 S. Che, A. E. Garcia-Bennett, T. Yokoi, K. Sakamoto, H. Kunieda, O. Terasaki and T. Tatsumi, *Nat. Mater.*, 2003, **2**, 801–805.

16 S. Che, Z. Liu, T. Ohsuna, K. Sakamoto, O. Terasaki and T. Tatsumi, *Nature*, 2004, **429**, 281–284.

17 C. Gautier and T. Bürgi, *J. Am. Chem. Soc.*, 2006, **128**, 11079–11087.

18 T. Li, H. G. Park, H. S. Lee and S. H. Choi, *Nanotechnology*, 2004, **15**, S660-663.

19 J. M. Slocik, A. O. Govorov and R. R. Naik, *Nano Lett.*, 2011, **11**, 701–705.

20 A. O. Govorov, Z. Fan, P. Hernandez, J. M. Slocik and R. R. Naik, *Nano Lett.*, 2010, **10**, 1374–1382.

21 S. D. Elliott, M. P. Moloney and Y. K. Gun'ko, *Nano Lett.*, 2008, **8**, 2452–2457.

22 A. Ben-Moshe, A. Teitelboim, D. Oron and G. Markovich, *Nano Lett.*, 2016, **16**, 7467–7473.

23 X. Gao, X. Zhang, K. Deng, B. Han, L. Zhao, M. Wu, L. Shi, J. Lv and Z. Tang, *J. Am. Chem. Soc.*, 2017, **139**, 8734–8739.

24 X. Gao, X. Zhang, L. Zhao, P. Huang, B. Han, J. Lv, X. Qiu, S. H. Wei and Z. Tang, *Nano Lett.*, 2018, **18**, 6665–6671.

25 O. Lopez-Acevedo, H. Tsunoyama, T. Tsukuda, H. Häkkinen and C. M. Aikens, *J. Am. Chem. Soc.*, 2010, **132**, 8210–8218.

26 H. Qian, W. T. Eckenhoff, Y. Zhu, T. Pintauer and R. Jin, *J. Am. Chem. Soc.*, 2010, **132**, 8280–8281.

27 I. Dolamic, S. Knoppe, A. Dass and T. Bürgi, *Nat. Commun.*, 2012, **3**, 798.

28 W. Ma, H. Kuang, L. Wang, L. Xu, W. S. Chang, H. Zhang, M. Sun, Y. Zhu, Y. Zhao, L. Liu, C. Xu, S. Link and N. A. Kotov, *Sci. Rep.*, 2013, **3**, 1934

29 K. W. Smith, H. Zhao, H. Zhang, A. Sánchez-Iglesias, M. Grzelczak, Y. Wang, W. S. Chang, P. Nordlander, L. M. Liz-Marzán and S. Link, *ACS Nano*, 2016, **10**, 6180–6188.

30 X. Lan, X. Lu, C. Shen, Y. Ke, W. Ni and Q. Wang, *J. Am. Chem. Soc.*, 2015, **137**, 457–462.

31 W. Jiang, Z. B. Qu, P. Kumar, D. Vecchio, Y. Wang, Y. Ma, J. H. Bahng, K. Bernardino, W. R. Gomes, F. M. Colombari, A. Lozada-Blanco, M. Veksler, E. Marino, A. Simon, C. Murray, S. R. Muniz, A. F. de Moura and N. A. Kotov, *Science (1979)*, 2020, **368**, 642–648.

32 W. Jiang, M. S. Pacella, Di. Athanasiadou, V. Nelea, H. Vali, R. M. Hazen, J. J. Gray and M. D. McKee, *Nat. Commun.*, 2017, **8**, 15066.

33 E. A. Kulp and J. A. Switzer, *J. Am. Chem. Soc.*, 2007, **129**, 15120–15121.

34 W. Ma, L. Xu, A. F. de Moura, X. Wu, H. Kuang, C. Xu and N. A. Kotov, *Chem. Rev.*, 2017, **117**, 8041–8093.

35 S. W. Im, H. Y. Ahn, R. M. Kim, N. H. Cho, H. Kim, Y. C. Lim, H. E. Lee and K. T. Nam, *Adv. Mater.*, 2020, **32**, 1905758.

CHAPTER II

CYSTEINE-BASED CHIRAL CARBON DOTS

This chapter is dedicated to the synthesis of chiral cysteine-derived Carbon Dots by a new approach at room temperature, to the investigation on their formation mechanism and to the evolution of the chiroptical properties during the nanoparticles formation process.

After the first evidence on luminescent carbonaceous nanoparticles in the early 2000s, Carbon Dots have attracted large interest due to their outstanding properties: high biocompatibility, chemical stability, photoluminescence activity and easy production. In particular, Carbon Dots are considered as a more biocompatible alternative to other luminescent nanomaterials, especially compared to Cd-based quantum dots, offering a convenient alternative for the application in nanomedicine.

The synthesis of chiral Carbon Dots has been investigated by several authors, exploiting both top down and bottom-up approaches. This latter synthetic method, that relies on the decomposition of optically pure chiral substrates has become extremely popular. However, the most employed synthetic methods rely on thermal decomposition via pyrolysis or under hydrothermal conditions. Due to the harsh reaction conditions, these approaches lead to an extensive loss of the stereochemistry of the organic substrates inducing the racemisation of the product.

In this chapter a novel synthetic approach based on the radical assisted decomposition of optically pure cysteine solution catalysed by copper is presented. The reaction takes place at room temperature in aqueous environment. The method is particularly suitable to follow in detail the process of Carbon Dots formation with multiple spectroscopic techniques and to investigate the variation of the Carbon Dots chiroptical activity during the Carbon Dots formation.

ACRONYMS

VB: valence band

MWNTs: Multi walled nanotubes

SWNTs: single walled nanotubes

CDs: carbon dots

GQDs: graphene quantum dots

PL: photoluminescence

PLQY: photoluminescence quantum yield

PEG: polyethylene glycol

PAHs: polycyclic aromatic hydrocarbons

PMMA: polymethyl methacrylate

List of Contents

1 INTRODUCTION

Carbon is one of the most abundant elements in the Earth's crust (1000 ppm), it occurs naturally in its elemental form in different structures: diamond, graphite and amorphous carbon. The carbon chemistry, as other group 14 elements, is characterised by an extensive chemistry of catenated compounds. This property arises from the high orbital overlap which increases the bond energy related to homoatomic bonds with respect to heteroatomic bonds. This is particularly evident for carbon (bond energy: 356, 598 and 813 kJ/mol for single, double and triple bond respectively), the small atomic radius guarantees good overlapping of the orbital perpendicular to the bond axis, essential characteristic for the formation of stable homoatomic multiple bonds.[1,2]

Dimond is the densest carbon allotrope (3.51 g/cm^3 respect 2.22 and 1.72 g/cm^3 for graphite and C_{60} respectively), its structure is formed by a covalent network of tetrahedral carbon atoms, in accord with the Valence Bond (VB) theory the atomic orbitals are consider as sp^3, forming $\sigma^{C\text{-}C}$ bonds with a bond order of 1, bond length 1.54 Å and a bond angle of 109.5 °. The cubic *Fd*-3*m* is the most common crystal structure observed for diamond, the unit cell is formed by a face centred cubic lattice of carbon atoms where half of the tetrahedral sites are occupied by carbon atoms (**Fig. 1**). The whole structure can be represented as stacked layers of hexane-like units in chair conformation with ABCABC packing. A rare hexagonal structure called lonsdaleite is also known, it is found in certain meteorites (and also available synthetically) and presents the less stable ABABABA packing.

Graphite in its α form presents a hexagonal layer structure with inter layer distance of 3.35 Å. The large inter layers distance, close to the sum of the van der Waals radii (r_{VdW} = 1.7 Å) evidences the low noncovalent interactions between the layers. The intra-layer structure is completely covalent and is formed by a 2D network of trigonal planar carbon connected in condensed hexagons. In accord with the VB theory the atomic orbitals present sp^2 hybridization, forming a network of molecular orbitals with σ and π symmetry. Graphite-α has a hexagonal structure (space group *P*6$_3$*mc*), the 3D crystal is formed by multiple layers stacked in the ABABAB motive. There is also a rhombohedral form called graphite-β, that is characterised by a ABCABC stacking of the bidimensional layers. The rhombohedral form is less stable and can be converted in the hexagonal one through thermal treatment. Graphite can be chemically modified by the action of strong acids in oxidizing condition with the formation of graphite

oxide, a layered structure rich of oxygen containing functional groups which increase its hydrophilicity. Moreover, graphite can be fluorinated by the action of hydrofluoric acid with the formation of CF_n sp^3 structures with different degree of fluorination, both the treatments strongly affect the intra-layer electrical conductivity.

A brief comparison between the macroscopical properties of diamond and graphite evidences some fundamental features about their structures. Firs of all, a large anisotropic electrical resistance is observed in graphite. Graphite is a strong electrical insulator (≈ 1 Ωm at 293 K) along the direction perpendicular to the layers. Instead, high conductibility is observed for the direction parallel to the layers (1.3×10^{-5} Ωm at 293 K). These properties are related to the presence of molecular orbital delocalized across the whole layer and the presence of a HOMO-LUMO gap close to zero that guarantees low energy barrier for the promotion of electrons from the valence to the conduction band (optical gap close to zero, 0.04 eV). On the other hand, diamond is characterised by high electrical resistance (1×10^{11} Ωm at 293 K) ascribed to the high degree of localization of the electron density along the carbon-carbon bond axis. Moreover, the vibrational modes of the σ bond network of the diamond structure guarantee high thermal conductivity (25 W/cm°C at 25 °C).

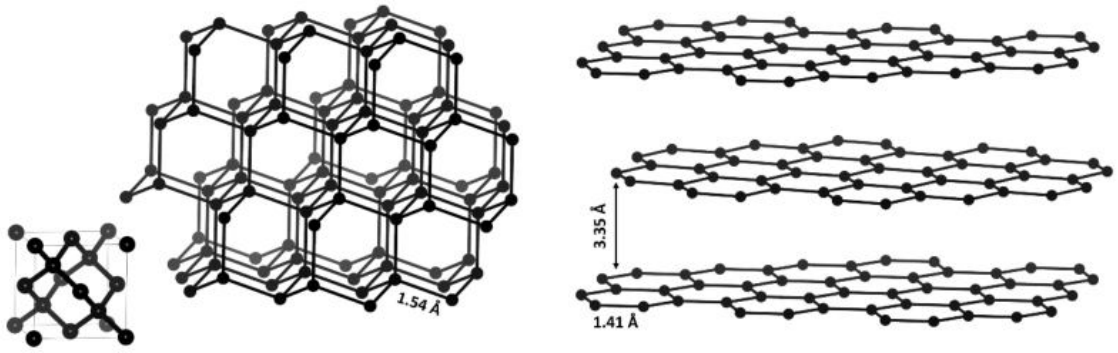

Figure 1: diamond unit cell and representation of a portion of the cubic dimond lattice (left). Representation of few layers of alpha graphite section.

Conversely to previous cases, amorphous carbon is a broad definition that includes a wide range of structures mainly composed of elemental carbon and a lack of long-range order. [3–5] Several artificial categories of amorphous carbon are known, some examples are: carbon fiber and glassy carbon that are formed by controlled thermal decomposition of organic polymers and are rich of disordered graphitic domines. Microcrystalline carbon (μC) is produced by the irradiation of graphite, the amorphous carbon (a-C) is produced by the evaporation under an

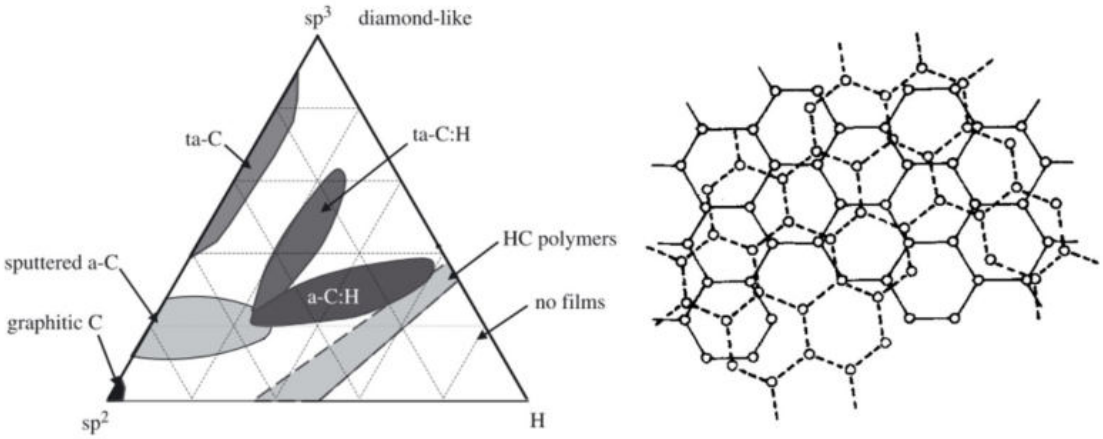

Figure 2: Ternary phase diagram of amorphous carbon. The three corners correspond to graphite, diamond and hydrocarbons respectively (left); image from ref.[5] and representation of two graphitic layers in the turbostratic model (right); image from ref.[100]

electron beam or by sputtering; and hydrogenated amorphous carbon (a-C : H) is produced by plasma deposition or ion-beam deposition from gaseous hydrocarbons. Fundamental features that characterise the different amorphous carbon forms are (**Fig. 2**): sp^2/sp^3 ratio, the hydrogen content and the degree of short or medium range order. The structure of amorphous carbon is rationalized as a heterogeneous system formed by small graphitic domines embedded in an aliphatic sp^3 matrix, and the presence of turbostratic disorder in the graphitic regions (**Fig. 2**) is used to explain the absence of diffractions that can be related to the three-dimensional order. [6]

1.1 CARBON BASED NANOSTRUCTURES

Several other allotropic forms of carbon were discovered in the last decades: graphene, fullerenes and carbon nanotubes are all example of carbon allotropes presenting a well-defined nanostructure.

Graphene is virtually an isolated, one atom thick, graphite layer (**Fig. 3a**). Graphene can be produced by different exfoliation processes starting from bulk graphite crystals, these approaches take advantage of the high chemical stability of the σ and π network and the low non-covalent inter layer interactions. The presence of intercalating molecules can facilitate the exfoliation process. Sample composed of few layers as well as the single monolayer were prepared by Novoselov et al. [7,8] by piling a block of high ordered pyrolytic graphite with adhesive tape. Then, the films were deposited onto oxidized silicon substrate and connected with Au/Cr electrodes prepared by electron beam lithography in hall-bar-type configuration for the measurement of magnetoresistance and Hall resistance. With this sort of device Zhang et al. [9] were able to observe the quantum hall effect and the formation of the Berry's phase in single

layer samples. The outstanding properties of graphene (such as a current density up to 10^8 A/cm^2) simulated the interest of researchers worldwide, and in 2010, Andre K. Geim and Kostantin S. Novoselov were awarded of the Nobel prize in physics ''for ground breaking experiments regarding the two-dimensional material graphene''. The chemistry of graphene is mainly focused on its functionalization in order to tune the band gap and dispersibility in solvents. In this context, graphene can be hydrogenated by fluxing H_2 over a Ni/Al_2O_3 catalyst at 1000 K to produce hydrogen radical that can react with graphene forming saturate graphene (CH)x. Thermal annealing of this product at 720 K in argon atmosphere can regenerates the unsaturated structure. Another common treatment is the acidic oxidation reaction, using strong oxidating agents like $KClO_3$ and HNO_3 or $KMnO_4$ in H_2SO_4 to introduce oxygen-containing functional groups producing the so-called graphene oxide.[10]

The Buckminsterfullerene is the first member of the fullerenes family that have been discovered. The first identification was reported by Kroto, Smalley and coworkers in 1985,[11] they were investigating the formation mechanism of chain hydrocarbons in interstellar space by studying the decomposition of a graphite disc under irradiation with Nd:YAG (30 mJ) laser pulses, when they observed an unusual signal in the time of flight mass spectra for the molecular ion C_{60}. They speculated that the observed signal was produced by a particularly stable carbon cluster composed by 60 carbon atoms, and the truncated icosahedron (**Fig. 3b**) was recognized as the hypothetical most stable structure (this structure was previously consider theoretically by Ōsawa, E.).[11,12] The unusual name of the C_{60} cluster was a reference to the American architect Richard Buckminster Fuller who is universally recognized for the design of the geodesic domes, structures that reminds the truncated icosahedron polyhedron proposed by Kroto et al. for the C_{60} molecular cluster.[13] In the following years, several carbon molecular cluster with a closed cage (polyhydric structures) were discovered and they are summarized in the formula C_{2n} with n in the range of 30 – 48 (the more stable examples are 2n = 60, 70, 76, 78, 82 and 84 with their respective isomers), these structure are defined as fullerenes. A synthetic approach to produce large quantity of C_{60} was developed by Krätschmer and Huffman. [14] During their investigation of the formation of carbon nanoparticles produced by a conventional ball-jar carbon evaporator under helium atmosphere, they observed the production of small soot particles that contained C_{60} with a yield of 10 % and more. The crystallographic analysis of C_{60} revealed that while the carbon atoms are all equivalent by symmetry, single and double bond can be distinguished with C-C distance of 1.453 and 1.383 Å respectively.[1,2]

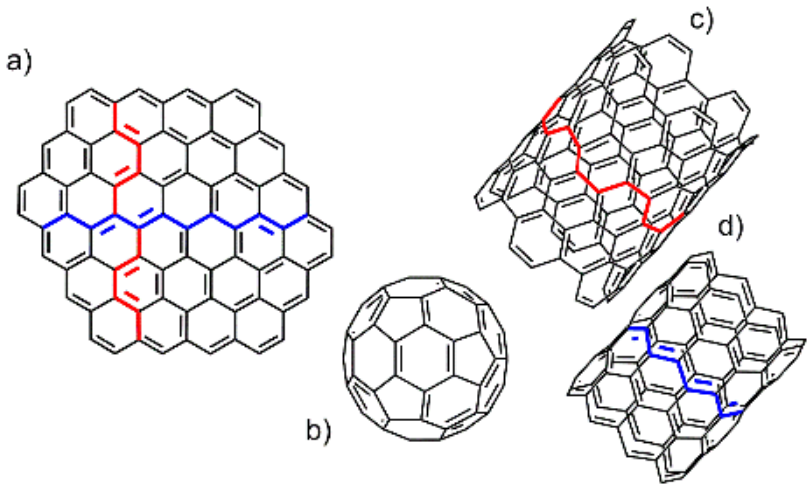

Figure 3: Representation of the discussed carbon nanostructures a) Section of a graphene layer, the red and blue bonds highlight the chair-saddle and zig-sag direction respectively; b) a C_{60} buckminsterfullerene; c) Section of a 6,6 armchair SWNT and d) section of a 9,0 zigzag SWNT.

Carbon nanotubes may be considered as elongated fullerenes with high aspect ratio, they are formed by the typical 2D graphitic structure wrapped around a cylinder (**Fig. 3c, d**), and eventually capping units close the extremity of the nanotubes (if the cylindrical section is composed only by hexagon, due to its curvature, the capping unit requires hexagon and pentagon as observed for fullerenes). Carbon nanotubes are produced in large scale by several physical methods such as: electrical arc discharge between graphite rods, laser vaporization of graphite or chemical vapor deposition. Although, the work by Iljima S.[15] in Nature 1991, which was certainly the more influent paper at that time, is frequently reported as the first observation of carbon nanotubes, several papers on the observation of carbon nanotubes were already available in the literature.[16] Carbon nanotubes are differentiate by the structure of their cylindrical section, considering: conformations (some limit structures that present the zig-zag and arm-chair conformation observed in graphite are reported in **Fig. 2c,d**) diameter of the tube and by the number of concentric elements. All the synthetic methods mentioned above give the formation of Multi Walled Nanotubes (MWNTs) as the major product, these structures are formed by concentric nanotubes with increasing diameter. Instead, the observation of relatively large-scale production of Single Walled Nanotubes (SWNTs) was reported only in 1993 by Iljima et al. and Bethune et al. independently.[17,18] In both the articles, the scientists were working with transition metals (iron and cobalt) in the attempt to fill the tubes cavity with metal ions, while they observed an unexpected catalytic activity of transition metals for the production of SWCNTs. Several chemical modifications for carbon nanotubes have been investigated, the most common is the oxidizing treatment with HNO_3 and H_2SO_4 that gives the formation of carboxylic functional groups that allow to increase the nanotubes solubility and

split the micrometrical bundles observed by scanning electron microscopy in single nanotubes.[10]

1.2 CARBON DOTS

Carbon Dots (CDs) are carbon nanoparticles with almost spherical shape and characterised by photoluminescent activity. The definition covers a broad range of materials, regardless of their structures, crystallinity, and elemental composition. Carbon nanodots, carbon quantum dots and other names are diffuse in literature, and at the time, there is still a lack of a proper nomenclature. A widely accepted distinction is applied between Carbon Dots (CDs) and Graphitic Quantum Dots (GQDs) based on the spherical shape that is typical for CDs and the plate-like shape of the nanometric GQDs.[19–21]

1.2.1 Carbon Dots Synthesis

Xu et al. reported in 2004 the first observation of CDs during a gel electrophoresis separation of a reaction mixture produced *via* arc discharge process employed for the synthesis of SWCNTs.[22] As usual, the crude product of the arc discharge synthesis was partially oxidized by treatment with HNO_3 to increase the solubility in aqueous solution. The electrophoretic purification revealed the presence of three main fractions: i) huge fibers with no migration properties, ii) the desired product composed by SWNTs and iii) small particle with lateral size and height around 18 and 1.4 nm respectively. The energy dispersive X-ray analysis showed carbon, oxygen and hydrogen as principal components of these nanoparticles. Furthermore, the material was characterised by a strong photoluminescence. The authors investigated the effect of the oxidizing treatment on the generation of the side products, and they confirmed that under the harsh oxidizing condition, SWNTs (fraction ii) are decomposed giving the formation of the other two fractions. After the observation of Xu and coworkers, the international interest for this unusual product has risen, mainly due to its optical properties. Indeed, CDs are differentiated by the other carbon nanostructure presented above by their photoluminescence activity. Another typical feature of CDs is the high content of heteroatoms (hydrogen, oxygen, and nitrogen are the most commons) that is related to the surface functional groups and structural defects.

Thanks to the large number of efforts that have been spent in the investigation on CDs synthesis, several synthetic approaches are now available. Among them, we can distinguish be-

tween: top-down processes where macroscopic carbon structures are decomposed by physical treatment (such as: arc discharge, laser ablation etc.), and the bottom-up processes where molecular organic substrates (citric acid, glucose, etc.) are decomposed in specific condition (hydrothermal, pyrolytic etc.).[20]

Top-down approaches: in these methods CDs are formed by first decomposition and subsequent reassembly of an extended carbon network already present in the starting materials. The products obtained by these processes usually do not present any photoluminescence activity, and the photoluminescence is observed after an appropriate oxidative post-synthetic treatment.[22]

Arc-discharge: two electrodes are placed in a closed chamber filled with gas (usually: He, H_2 or Ar). The anode is formed by the precursor (graphite or graphite with metallic catalyst), and the product is collected on the cathode surface. The application of an electric potential generates an electron flux between the electrodes, which gives the formation of a plasma with temperature in the 4000 – 6000 K range. Due to the high temperature, the carbonaceous precursor is vaporised and ionised, the ion flux impacts on the anode and condenses on the surface with the formation of several carbon structures in relation with the specific experimental conditions.[23]

Laser ablation: a high energy laser pulse is irradiated on the surface of the starting material inducing the vaporisation into plasma state, the vapours crystallise during the condensation step with the formation of nanoparticles. [24,25] Usually, the process is conducted in solvents, Hu et al.[26] have produced luminescent carbon dots with diamond lattice through a one step process by irradiation of a graphite particle dispersion in polyethylene glycol with 1064 nm Nd-YAG laser; they established the dramatic role of the solvent in the control of the surface defects formation. In fact, working with water instead of polyethylene glycol, the CDs with similar particle size and shape are formed but no luminescent was observed. The photoluminescence in the sample produced in water can be achieved by a post-synthetic oxidative treatment in $HClO_4$.[26] Sun et al. [27–29] observed that the luminescence in CDs prepared by plasma-assisted pulse laser deposition of graphite carbon target in silicon matrix can be observed after oxidation in HNO_3 2.6 M under reflux for 12 h and followed by surface passivation with polyethylene glycol.

Electrochemical synthesis: Zhou et al.[30] reported on the formation of CDs through the electrochemical decomposition of MWCNTs supported on the working electrode. The exposure to 1000 cyclic voltammograms cycles in the voltage range - 2.0 to + 2.0 V working with a scan rate of 0.5 V/s in 0.1 M tetrabutylammonium perchlorate in acetonitrile as electrolyte solution, gives the formation of 2.8 ± 0.5 nm graphitic carbon dots that presents a strong absorption band localized a 270 nm. The production of CDs by electrochemical treatment of graphite (graphite column electrode) was achieved by Zhao et al. [31] working with a constant potential 3.0 V using 0.1 M H_2PO_3 in water as electrolyte solution.

Acidic oxidation: as already discussed, the acidic oxidation treatment has been widely employed for graphite exfoliation, as well as to introduce oxygen-rich functional groups (mainly carboxylic groups) on the surface of carbon nanostructures. Zang et al. [32] observed the formation of CDs after refluxing a fullerene carbon soot in HNO_3 and H_2SO_4 mixture. Yang et al. [33] reported the large-scale synthesis of sulfur and selenium doped CDs from Chinese Ink trough a first step of oxidative cutting in HNO_3, H_2SO_4 and $NaClO_3$. An alternative process was reported by Shin and coworkers, [34] they investigated the CDs production by top-down acid-free wet method. According to their findings, several different carbonaceous precursors (e.g.: graphite, MWCNTs, carbon fibers and charcoal) can be converted in CDs in solvothermal conditions in the presence of potassium monopersulfate through a radical mediated process.

These general top-down approaches have also given inspiration to several bottom-up syntheses where the macroscopic carbonaceous precursor, characterised by a well-formed extended C-C network is replaced by molecular precursors. The GQDs synthesis through toluene decomposition by laser irradiation is reported by Yu et al.[35] and the electrolysis of sodium citrate and urea solutions (1 h, 5 V at DC voltage) reported by Hou et al. [36] are just a couple of examples of this approach.

Bottom-up approaches: in these synthetic methods, the C-C bonds network is formed by the thermal decomposition of molecular precursors in specific conditions, such as: pyrolysis, hydrothermal or solvothermal. Despite the large number of reports on these methods, the processes that are involved in the decomposition step are still not clear. Citric acid is probably the most investigated starting material for the preparation of CDs through the bottom-up route,

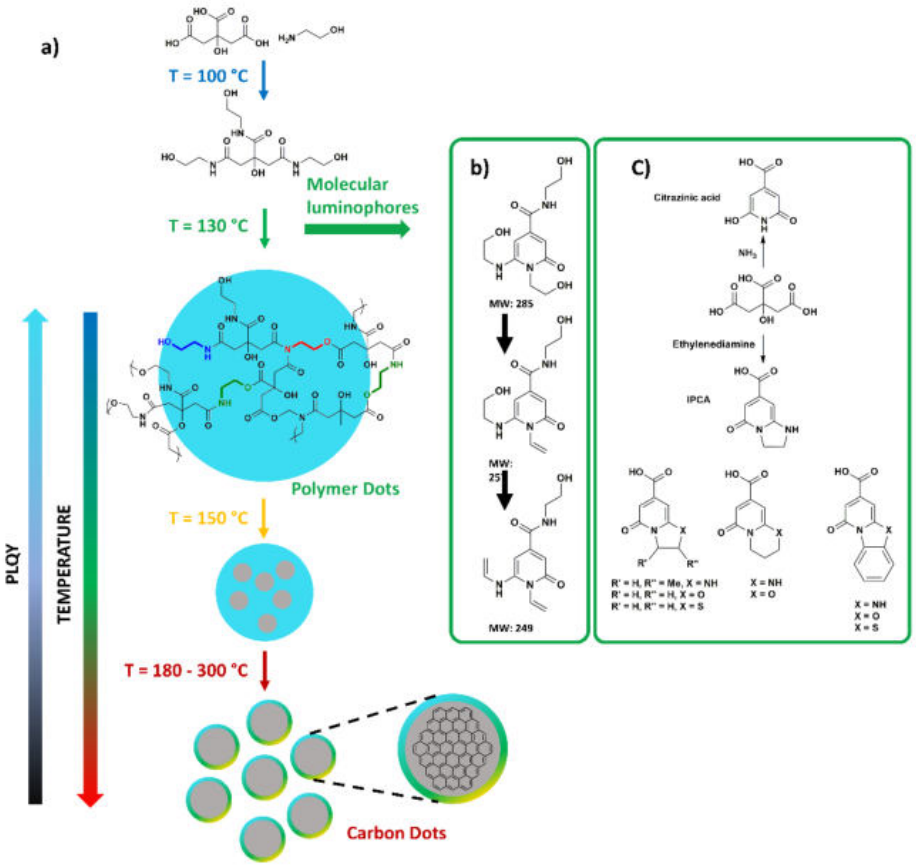

Figure 4: schematic representation of the CDs formation mechanism. Molecular luminophores derived by the condensation of citric acid and ethanolamine b) and in the presence of ammonia or ethylenediamine c).

as well as citric acid mixtures with amines (ethanolamine, ethylenediamine etc.). Several observations collected working with pyrolysis and hydrothermal decomposition of these substrates allowed to build up a model of the decomposition process.[37] The schematic process reported in **Fig. 4a** is related to the pyrolytic decomposition of citric acid and ethanolamine mixture according to by Krysmann and coworkers.[38] However, the evidences reported by Song et al.[39] (hydrothermal decomposition of citric acid and ethylenediamine decomposition), revealed that the main steps of the process reported in **Fig. 4** are observed in other cases, despite the different amine or type of thermal treatment. The principal differences are related to the chemical structure of the molecular fluorophores that are formed as intermediates (with ethanolamine **Fig 4b**, with diamine **Fig 4c**). The main steps of the decomposition process can be summarized in:

i) Polymerization: at lower temperatures (usually below 150 °C), the formation of polymer dots is observed. This product, also defined as amorphous CDs, is formed by condensation reactions such as esterification and amidation. Since citric acid contains both carboxylic and

hydroxyl functional groups, it can be involved in esterification reaction, and ethanolamine can connect the citric acid units in different way (**Fig. 4a** terminal, intrachain and interchain cross links are indicated in blue, green and red respectively). In the temperature range (T < 150 °C), a fraction of the organic substrate/s is consumed by the formation of molecular fluorophores. **Fig 4b** shows some of the products, typically, citrazinic acid derivates produced by intramolecular condensation and water elimination reactions.[38] Other molecular fluorophores obtained in similar reaction conditions were confirmed in several works. A brief summary of the most representative structures is reported in **Fig. 4c**. IPCA, formed by the reaction with citric acid and ethylenediamine, is of particular importance. These molecular fluorophores can be grafted on the Polymer Dots surface and are responsible for a blue strong PL which λ_{em} is insensitive to variation of λ_{ex} (excitation independent emission).

ii) Carbonization: at higher temperatures (150 – 300 °C), the dehydration of the Polymeric Dots network is observed.[38] This process gives the formation of new C-C single and multiple bonds. Elimination reactions are responsible for the formation of multiple C-C bonds in the polymeric aliphatic structure, as well as, intra and intermolecular cyclizations and electrocyclic reactions are considered as main reactions involved in the formation of aromatic and heteroaromatic groups, and associated with the growth of the CDs crystalline core.[40] As can be shown by the high magnification TEM images, the crystalline core is evidenced by the interference fringe, and d-spacing 0.32 and 0.22 nm is commonly observed and related to the graphite structure (some variations can be ascribed to the presence of heteroelements). Krysmann et al.[38] observed the reduction of the photoluminescence quantum yield with the extension of the carbonization step. They related this finding to the decomposition of the molecular fluorophores which are the main emissive centres. This hypothesis was further confirmed by the UV/Vis absorption spectroscopy; a strong reduction of the bands related to the well localized transition and to the formation of a broad absorption band was observed during the carbonization step. The same behaviour was also observed for PL properties which showed a significant increasing in the λ_{em} dependency from the λ_{ex} (excitation dependent emission).

As mentioned above, the generalization of the decomposition mechanism is mainly related to the CDs prepared by citric acid and mixture citric acid with amines. Significant differences are observed for the CDs formation mechanism starting from conjugated molecules. [40,41] These

methods reported in the work of Jiang et al.[40] are promising for the preparation of red and near-IR emitting photoluminescent CDs.

In contrast to the large number of publications covering citric acidbased CDs, there is a lack of investigations on the formation mechanism of CDs using other organic non conjugated substrates such as carbohydrates and amino acids. A particular example came from the study by Li et al. [42] on cysteine-based CDs produced by hydrothermal treatment. The authors observed the presence of graphitic structure extended over several hundreds of nanometers as decomposition intermediate of cysteine-based CDs. This finding supports the presence of other phases in the decomposition process where the starting particle system is cut in smaller particles under the reaction conditions.

Pyrolysis: Dong et al.[43] observed that the decomposition of neat citric acid at 200 °C (above its melting point T = 153 °C), after 30 min the formation of an orange solution containing GQDs was detected, and for extended reaction time the product was converted in graphene oxide (GO). The authors recognized the carbonization step and considered GQDs as an intermediate in the formation of GO. Krysmann et al.[38] investigated the decomposition of mixture of citric acid and ethanolamine at different temperatures. They observed the formation of amides at low temperature (180 °C). At 230 °C, the polyamide structure starts to decompose forming CDs with high content of amidic bonds. At higher temperature (300 and 400 °C), an extensive reduction of the amidic bonds and the formation of aggregates with size around 100 nm was observed.

Hydrothermal and Microwave: the decomposition of aqueous solutions of citric acid and ethylenediamine under hydrothermal condition was investigated by Zhu et al. [44] at different reaction temperatures (150, 200, 250 and 300 °C). The formation of polymeric amorphous CDs through amidic condensation was observed at 150 °C. These structures are characterised by: i) absence of electron interference fringes in the TEM images, ii) highly localized absorption band related to the presence of molecular like luminophore and iii) almost excitation independent photoluminescent emission. Increasing the hydrothermal temperature increased the graphitic content, significantly affecting the optical properties with a reduction of the absorption of the localized band and increasing of photoluminescence excitation dependence.

1.2.2 PL Origins in Carbon Dots

Photoluminescence (PL) is the most considered and characteristic proprerty of CDs. Typically, strong emission in the blue and green range are observed for CDs dispersed in water. In some case, the incorporation of heteroatoms (nitrogen, sulfur, boron, selenium and phosphorous),[45–47] called elemental doping in analogy with semiconductor doping, has been considered as a beneficial strategy to improve the PhotoLuminescence Quantum Yield (PLQY). Tuning the optical properties to achieve CDs with red or near-IR emissions was investigated exploiting several approaches as phosphorus doping or decomposition of conjugated starting material (p-phenylenediamine).[40,47] The most common features of the CDs PL is the large stokes-shift (70 - 100 nm) and the strong λ_{ex} dependency that allows to tune the emitted wavelength (λ_{em}) over a large rage of frequencies changing the excitation wavelength (λ_{ex}). This last property is ascribed to the broad heterogeneity of the emitting sites. The heterogeneity could be related to the different type of CDs produced in the same batch (fraction with independent PL can be isolated with the proper purification step like silica chromatography, gel electrophoresis or gradient centrifugation),[48,49] or to the copresence of different emitting groups in the same particle.

The first attempt to explain the PL properties of CDs was based on the quantum confinement effect that can strongly affect the electronic band gap with the formation of distinct energy levels. This parallelism with PL properties of the semiconductor nanoparticles can be considered only when the particle presents a well crystallised structure and a diameter below 5 nm. In fact, this size dependent red-shift was observed by Li et al. [50] on CDs prepared by top-down electrochemical decomposition of graphite rods in NaOH/EtOH solution. The crude product was separated in four CDs fractions with narrow size distribution (average diameters 1.2, 1.5, 3 and 3.8 nm) and the increase of the PL emission maxima from 400 to 600 nm along with the increasing of the particles size was observed. Yang et al.[51] obtained similar results on the CDs produced by bottom-up hydrothermal decomposition of glucose in the presence of different amount of KH_2PO_4. According to their findings, glucose/ KH_2PO_4 molar ratio = 1/36 gives the formation of blue emitting CDs with average diameter of 1.83 nm and glucose/ KH_2PO_4 molar ratio = 1/26 produces green emitting CDs with average diameter of 3.83 nm. Ding et al.[48] isolated four CDs fractions with different emission maxima (383, 410, 488 and 528 nm) after purification, by silica chromatography, of a CDs mixture prepared by a bottom-up hydrothermal decomposition of urea and p-phenylenediamine. However, they did not observe any size-

emission dependency (all the fractions presented an average diameter around 3 nm). Similar observations were reported by Vinci et al. [49] about the CDs fraction produced by HPLC purification of a CDs mixture prepared *via* top-down acidic oxidation of carbon nanofibers. Zhao and coworkers, [31] reported on size-dependence of CDs on PL suggesting that the red-shift might be related to the system degree of conjugation and showing that the optical effect could be more related to the crystallinity rather than the physical size. Structural disorder in the CDs core can reduce the extension of the conjugated system affecting the luminescence.

Starting from the considerations about the electronic band structure in the macroscopic crystals, J. Robertson [3] reported a model for graphite and diamond. As mentioned above, carbon with diamond structure is an electric insulator characterised by a wide optical band gap of 5.5 eV (**Fig. 5a**), instead, carbon with graphite structure presents high electrical conductivity along the sp^2 layers direction. This property is reflected in the band structure **Fig. 5a** by the intersection between valence and conductive band. Since the optical band gap of extended graphite structure is close to zero, the PL property of CDs (especially the GQDs) are modelled through the size confinement of this structure in systems with dimensions of few nanometers. Kozawa et al.[52] reported a computational study on the investigation of the election transition in graphene dots (**Fig. 5b**) with diameters between 0.74 – 2.7 nm (related band gap 2.5 - 1.5 eV). Accordingly, GQDs with diameter between 1.4 – 2.2 nm were predicted to have a band gap in

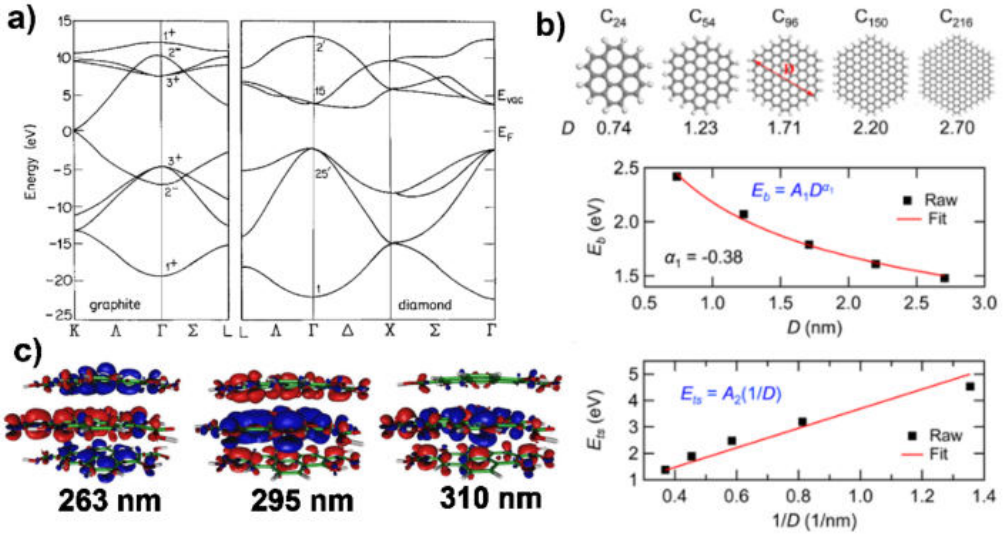

Figure 5:**a**) electronic band structure for carbon allotropes graphite and diamond (figure from ref.[3]). **b**) graphene dots model, from top to bottom: investigated systems (number of carbon atoms, structure and diameter in nm), size-dependency of the E_b parameter (difference between Energy of one electron band gap GW model and the energy of the first optical allowed transition energy E_{ts}, corresponding to the absorption energy), size-dependency of the E_{ts} parameter (figure from ref.[52]). **c**) electron density difference between ground and exited stated in the main transition (absorption λ reported below) in the three layers model, charge depletion and charge accumulation areas are indicated in blue and red respectively (figure from ref.[53]).

the visible range and to show size-dependent luminescence, in agreement with the observation reported for GQDs with crystal size below 3 nm.[50] Models formed by three graphene layers, with oxygen functional groups were investigated in order to simulate the absorption properties of graphitic CDs with 1.2 nm diameter (**Fig 5c**).[53]

Based on these considerations, Fu et al. [54] investigated a model system based on three specific (PAHs) Polycyclic Aromatic Hydrocarbons (anthracene, pyrene and perylene) embedded in an amorphous matrix of polymethyl methacrylate (PMMA), such a system should emulate the distribution of the emission centres in CDs. The authors observed that using small PAHs with three to five condensed aromatic rings it is possible to emulate the CDs absorption and emission properties (photoluminescence range 350 – 550 nm). Moreover, when the concentration of the aromatic fluorophores was increased, intramolecular processes like self-trapping (excimer emission) caused a large red-shift (pyrene emission is centred at 370 nm instead the pyrene excimer emission is centre at 450 nm) and strongly affected the fine structure: only a large band was observed, and the Frank Condon vibronic fine structure was no longer detectable. Although, a proper selection of the fluorophore and its concentration in PMMA can simulate absorption and emission property of CDs, only a mixture of different PHAs can reproduce the λ_{ex} dependency typical of CDs. This evidence supports the hypothesis that the luminescence of the carbon dots is not related to the whole carbon matrix, and the emission is generated by a mixture of small aromatic conjugated systems present in the core or on the particle

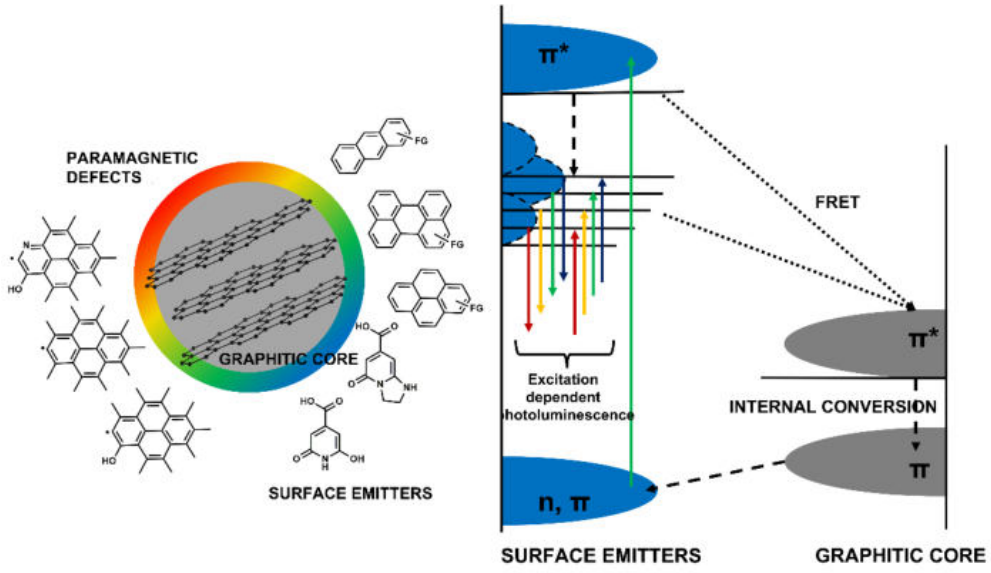

Figure 6: General Core-shell representation of a multicolor emitting CDs, the structure is divided in graphitic core and surface that present a distribution of polycyclic aromatic surface emitters (left). Representation of the PL mechanism, the bands formed by the delocalized orbitals are divided between surface emitters (blue) and graphitic core (grey). The excitation and relaxation transitions are represented by upward and downward direction of the arrows, dashed lives are related to Förster resonance energy transfer and non-radiative internal conversion.

surface. It must be mentioned that similar hypothesis was used to explain the λ_{ex} dependence of the PL in a-C films ten years before the first CDs related publication appear.[55–57]

Since is frequently observed that the luminescence of CDs solutions is strongly affected by the pH, the luminophores must be in certain way exposed to the solvent or conjugated to pH-sensitive functional groups located on the particles surface. Dhenadhaylan et al. [58] investigated steady state and time resolved luminescence of different CDs, prepared by bottom-up microwave decomposition of citric acid, and concluded that the observed luminescence is entirely generated from surface exposed luminophores.

According to these observations, a general model that describe the PL of CDs produced by bottom-up methods was proposed (**Fig. 6**). [37,59] In this model, the CDs is described as a spherical core-shell structure, composed by a crystalline graphitic core and an outer amorphous shell. The amorphous CDs surface is composed by small aromatic conjugated systems covalently bonded to the CDs core. These groups are the main emissive centres, and their composition and structure are dramatically affected by the starting material and synthetic conditions. As mentioned above, the decomposition of CA with ethanolamine or ethylenediamine gives the formation of citrazinic acid and IPCA derivates respectively. Instead, the graphitic core is considered as non-luminescent and can act as a quencher since it can promote non-radiative relaxations of the excited state *via* internal conversion. This is mainly due to its size which is above the quantum confinement regime.

The HOMO-LUMO transition in the molecular-like emissive centre is related to the $\pi \rightarrow \pi^*$ or $n \rightarrow \pi^*$ transitions that produced localized absorption bands. The PLQY of these contributes is usually high and it is dominant in the blue region of the PL spectra (citrazinic acid and IPCA derivates present symmetrical emissions centred at 430 and 420 nm respectively), these molecular-like emissive centre are also related to an excitation independent PL. Moreover, the presence of structural defects has been observed, Fang et al. [60] recorded the EPR singlet signal with g = 2.003 for several CDs prepared by bottom-up hydrothermal decomposition of citric acid with nitrogen containing molecules (L-cysteine, ethanolamine, ethylenediamine and glycine). The observed signal was interpreted as an unpaired electron on a carbon atom, probably associated to dangling bonds. The authors ascribed the luminescence produced by excitation at lower frequency to a distribution of these defects with different energy. The formation of stable carbon-centred radicals in graphitic structure is well documented by several ERP data

that show the presence of the paramagnetic nature of CDs. Li et al. [61,62] investigated the formation of carbon-centre radicals in graphene and graphite oxides. Carbon-centred radical are a wide group of high reactive species, the stability of the radical can be evaluated by its chemical inertia. For this purpose, the reactivity of the radical centre is tested considering several chemical reactions such as: hydrogen abstraction, oxidation and radical coupling.[63] By comparison of the reactivities of several different structures, the stability of carbon-centred radicals was related to three main factors: i) presence of bulky functional groups that reduce the accessibility to the active site through steric hindering (kinetic stabilisation), ii) spin delocalization over extended conjugated structure (thermodynamic stabilisation), iii) presence of electron donating and electron withdrawing groups that can influence the electronic density and stabilise the carbon centre by a captodative effect (thermodynamic stabilisation).

1.2.3 Chirality in Carbon Dots

Nakagawa et al.[64] reported the first observation of chirality in CDs. They used a top-down approach to produce achiral CDs, successively passivated by (S) or (R) 2-penyl-1-propanol. According to this method, the achiral carbon nanoparticles were produced by acidic-oxidation of graphite and a second functionalization step with thionyl chloride was used to activate the carboxylic functions for the carbonylic addition-elimination reaction with optical pure (S) or (R) 2-penyl-1-propanol. The chirality of the nanoparticles was not investigated directly with circular dichroism spectroscopy. However, the authors reported the chirality induction in N-methyl pyrrolidone added to the colloidal solution that formed a supramolecular chiral system containing the nanoparticles. The main advantage of this post functionalization approach is the possibility to avoid the exposition of the chiral inductor to the harsh conditions that are employed for the nanoparticles formation. In this way, it is possible to reduce the detrimental effect of reactions that can alter its stereochemistry.

After this fist investigation via a top-down approach, several bottom-up alternatives were developed. In 2016, Zhang et al.[65] reported the synthesis of chiral CDs through the hydrothermal decomposition of mixture of citric acid and optical pure cysteine. The isolated product shows similar features of the systems reported by Gao et al.[66] and Fang et al.[60] who investigated the production of CDs using binary mixtures based on citric acid (among then citric acid – cysteine). A typical absorption band, localized at 340 nm and related to the presence of grafted thio-IPCA derivates was observed.[67] Zhang and coworkers[65] proved the enantioselectivity of

the synthetic method by the isolation of both the enantiomers starting from L and D cysteine, respectively. The enantioselective interaction between (R) and (S) CDs, with (R) and (S) tartaric acid, was proved by electrochemical impedance spectroscopy and linear sweep voltammetry. Other authors reported bottom-up synthesis employing different chiral organic substrates, such as: (L) glutathione and ethylenediamine,[68] (D) glucose and melanine,[69] (L) cysteine and para benzoquinone,[70] guanosine-5'-monophosphate,[71] (L and D) methionine,[72] (L and D) glutamic acid,[73] (L and D) penicilamine,[74] (L and D) tryptophan,[75] (L) arginine with (R, R and S, S) cyclohexamethyldiamine,[76] (L and D) cysteine.[42,77,78] As evidenced by these examples, amino acids are a well-investigated pool of substrates for the preparation of chiral CDs. This is mainly justified by some typical features of these molecules, such as: high availability, high optical purity, presence of functional groups that guarantees high hydrophilicity and presence of heteroatoms (N, O and S). However, despite the large scientific interest in the topic, few examples can be found in literature about the investigation on the formation mechanism of chiral CDs and the origin of their chiroptical activity. In their seminal work Đorđević et al. [76] analysed the formation of chiral CDs from microwave assisted decomposition of optical pure L-arginine. They observed that despite the chiral nature of the starting material, the particle did not show any circular dichroism signal. Instead, chiroptical properties could be introduced by the addition of optical pure (R, R and S, S) cyclohexane-1,2-diamine. The authors related this observation to the low thermal stability of arginine under the reaction conditions, which decomposes forming the CDs core and, at the same time, the stereochemical configuration in the α carbon is lost. Thus, the observed optical chirality was related to the surface functionalization with the optical pure cyclohexane-1,2-diamine which has higher thermal stability. This hypothesis was further proved by the microwave treatment of citric acid solutions and functionalization with optical pure amine.

In contrast to these observations, several articles report on the presence of chiroptical signal of amino acids derived chiral CDs after direct decomposition of the optical pure amino acids. Among these works, Wei et al. [75] reported the investigation on the origin of the chiroptical signal of tryptophan derived CDs. In their study, the authors compared the products of the hydrothermal decomposition of (L and D) tryptophan, (L and D) alanine, indole and a mixture (L and D) of alanine and indole. So doing, it was possible to isolate the chiroptical signal of the amino acid-derivates grafted to the particle surface.

These experimental observations suggest that chiral CDs are composed by a graphitic achiral carbon core and an outer chiral amorphous shell, probably due to the presence of partially undecomposed substrates molecules (or derivates formed during the decomposition reactions) grafted on the particles surface (as concluded by the observation of the characteristic circular dichroism signal related to the n → π* absorption).[75] When the carbonization step is prolongated enough to completely decompose these grafted groups, the stereochemistry in the α carbons is gradually lost, causing the reduction of the chiroptical activity.

2 RESULTS AND DISCUSSION

Cysteine based chiral CDs are prepared by the copper catalysed radical assisted decomposition. As schematized in **Fig. 7**, at pH 10.5, the addition of a 4%$_{mol}$ of Cu(II) acetate, in an optical pure cysteine solution, forms L or D CDs after 2 h. Due to its simplicity, the process is suitable for a scale up to larger scale. Salts and other by-products can be eliminated during the purification step and carbon dots in gram scale can be isolated. The characterisations are focused on **L-CDs** prepared by the decomposition of L-cysteine. The production of **D-CDs** confirms the enantioselectivity of the synthesis.

TEM micrographs of the **L-CDs**, in **Fig. 8** and **Fig. A1,** show the presence of CDs with average size of 6 ± 2 nm. The phase contrast images (**Fig. 8c,d**) show the diffraction fringes of the graphitic core. From the analysis of the fringes, the d spacings of 0.19, 0.22 and 0.31 nm are measured and related to (101), (100) and (002) facets of the graphitic CDs core. Further details are gained by the Fourier filtered image (**Fig. 8e**), showing the expected hexagonal pattern. The selected area electron diffraction (SAED) analysis of an assembly of CDs reveals the Debye-Scherrer rings typical of a polycrystalline

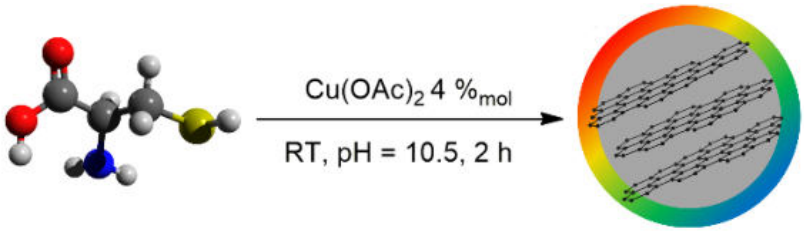

Figure 7. Scheme of the synthesis conditions for the preparation of **L-CDS** from L-cysteine.

sample (**Fig. 8f**). The Powder X-Ray Diffraction (PXRD) pattern, shown in **Fig. A2**, shows a very broad halo ascribed to a structure rich of defects. A band centred at about 28° in 2θ, corresponding to a d = 0.32 nm, can be ascribed to the d-spacing of the (002) plane of the graphite lattice. This feature is commonly observed in CDs samples.[77]

The surface functional groups of **L-CDs**, investigated by Fourier transform infrared spectroscopy (FTIR), are compared with zwitterionic L-cysteine (**Fig. 9a,b**). The identification of the absorption bands of zwitterionic L-cysteine is based on the detailed experimental and computational analyses reported by Pawlukojć and coworkers.[79] The absorption of **L-CDs** shows many common features with the L-cysteine even if all the bands are broader and some signals are significantly modified. The wide region related to the absorption of the amine groups is blue shifted to the 3800 – 3300 cm^{-1} range. This result

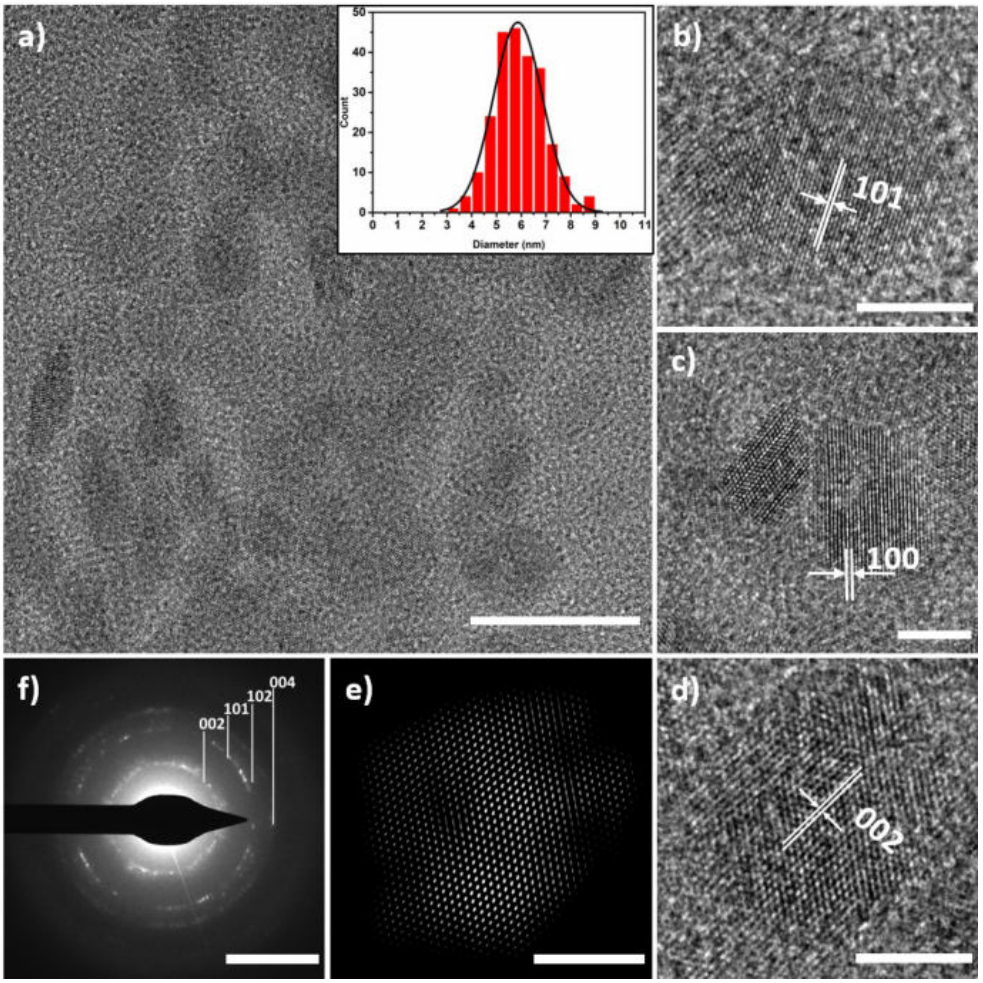

Figure 8. TEM analysis of **L-CDs**: a) low magnification image, particle size distribution 6 ± 1 nm, scale bar: 10 nm. b-d) phase contrast images, scale bar: 5 nm. e) image d after the application of a Fourier filter, scale bar: 5 nm. f) SAED analysis, scale bar: 5 nm^{-1}.

explained in terms of the formation of amidic bonds, is further supported by the observation of the ν_{CO}^{amide} at 1700 cm^{-1} (amide I band), by the strong absorption related to the amide II band at 1590 cm^{-1}, as well by the absence of absorption bands related to $-NH_3^+$ (although the product is isolated in acidic condition, see materials and methods section).[80,81] The FTIR spectrum of the final product shows:

1) a band at 1465 cm^{-1} associated to C=C stretching in the aromatic structures produced during the decomposition.

2) the bands in the 1400 – 1370 cm^{-1} range related to C-N stretching modes.

The band related to the δ_{SH} mode located at 943 cm^{-1} in the L-Cys spectrum are not present, suggesting the inclusion of sulfur as C-S-C or the oxidation to sulfoxide derivates (such as cysteic acid and taurine) related to the absorption at 1020 cm^{-1} of SO_3^- and further confirmed by the XPS analysis (see below).[80]

The UV/Vis spectrum, reported in **Fig. 9c,** shows a wide and diffuse absorption with no well-defined absorption band and with a shoulder at about 280 nm. The absorption below 250 nm can be associate to n→π* transitions in amidic and carboxylic bond and to transitions in the graphitic core. The shoulder at 280 nm and the absorption at higher wavelength, is ascribed to π→π* transitions in the surface aromatic and heteroaromatic groups. The photoluminescence excitation (PLE) analysis reveals that the luminescence derives mostly by a heterogeneous population of photoluminescent species absorbing in the 300 - 450 nm range. The maximum is strongly red shifted as function of the collected wavelengths in the 400 – 450 nm range. This feature is further confirmed by the strong effect of the exciting radiation energy on the emission properties, as observed in **Fig. 9d** and in **Fig. 9e** by normalised PL spectra. The **L-CDs** emission has a maximum intensity between 400 - 500 nm, that corresponds to the excitation wavelengths in the range 360 - 400 nm. The three main components of the emission profiles,

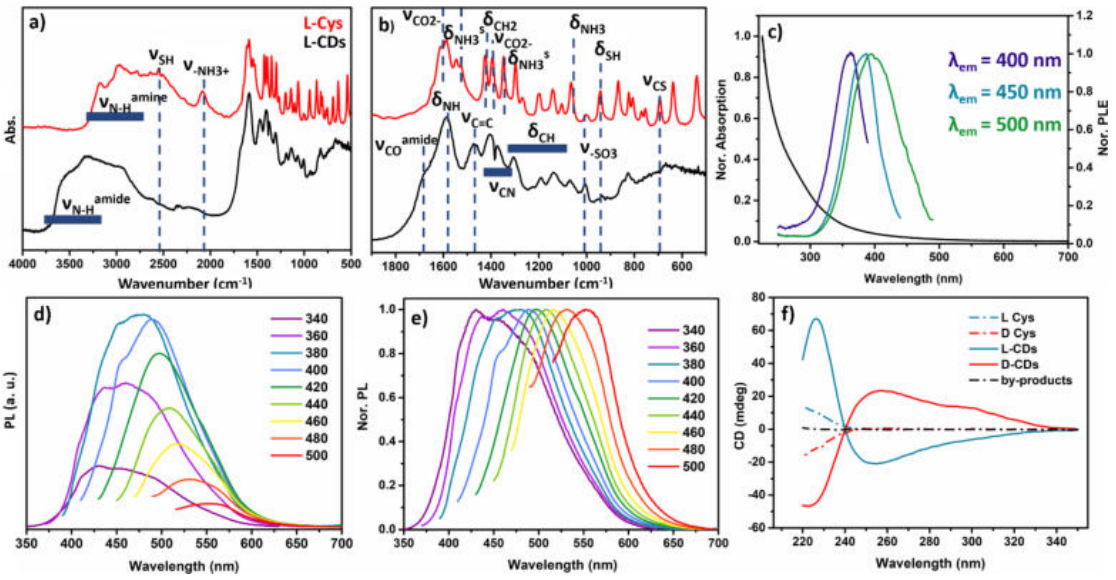

Figure 9. Characterisation of **L-CDs**: a ,b) FTIR analysis and detail of the analysis in the 1900 – 500 cm^{-1} range. c) UV/Vis and PLE collected at 400, 450 and 500 nm emission wavelengths. d,e) PL and normalised PL spectra collected at different excitation wavelengths. f) electronic circular dichroism of L,D-Cysteine, **L,D-CDs** and the by-product.

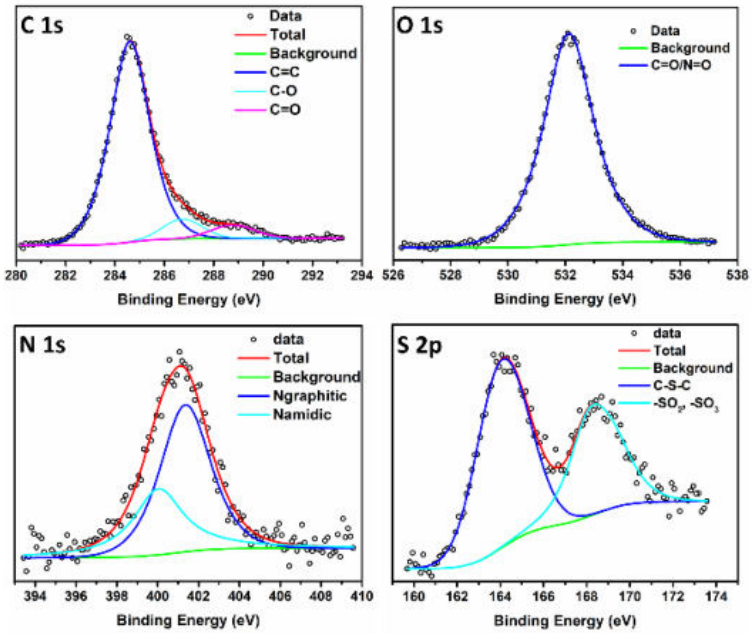

Figure 10. XPS spectra of: C 1s, O 1s, N 1s and S 2p peaks of **L-CDs**.

centred at 415, 455 and 500 nm, are assigned to broad families of luminophores with different degree of conjugation[54] or heteroatom doping.[82] The quantum yield efficiency of the emission with excitation at 350 nm is 0.8 % in deionized water and 1.5 % in H_2SO_4 0.1 M solution. All the values agree with the observation on similar systems.[83]

The chirality of **L-CDs** is also confirmed by the circular dichroism analysis (**Fig. 9f**). **L-CDs** shows a strong positive circular dichroism at 222 nm and a negative signal at 250 nm that can be associated to the $n \rightarrow \pi^*$ transition in amidic bonds and to the $\pi \rightarrow \pi^*$ transition that derives from aromatic surface groups. During the reaction, the formation of new optical active chromophores is evidenced by the absorption in the range 240–340 nm, where none signal from L-cysteine can be detected. In particular, the positive maximum at 206 nm is absent. In our experimental conditions, **Fig. 9f**, only the tail of the signal can be observed.[84] Probably, on the surface of the **L-CDs** are still present some cysteine molecules (or cysteine derivates), grafted trough amidic bound, that preserve the chiral information in the C_α and are responsible for the absorption at 222 nm. The absorption at 250 nm could be ascribed to aromatic systems that are in local proximity of the stereocenter so the electronic transitions of these groups are influenced by the effect of the asymmetric groups.

D-CDs sample is prepared by radical decomposition of D-Cysteine solution. The circular dichroism signal, shown in **Fig. 9f**, confirms the synthesis of the second enantiomer and the enantioselectivity of the synthetic protocol.

The relative elemental analysis of **L-CDs**, performed by XPS, starts considering the peak area of the single signals (**Fig. 10**) corrected by the elemental sensitivity factors. The composition, related to the typical XPS sampling depth of 5-10 nm, is C 68.7 %, O 23.5 %, N 4.1 % and S 3.7 %. The deconvolution of the C 1s signal shows three different components: the most intense, centred at 284.6 eV, can be assigned to carbon-carbon bonds related to the graphitic core of the nanoparticles and possibly in aromatic structures; the other two low intensity components, centred at 286.6 eV and at 288.5 eV, can be related to the oxidation of carbon existing in C–O/C-N and C=O/C=O–N bonds.[35] The O 1s band can be well-fitted by using only one component, centred at 532.1 eV. This BE position can be attributed to C=O/N=O bonds,[77] and probably also to sulfur-oxygen bonds. Furthermore, the presence of some weak components due to C-O bonds in the O 1s band, cannot be excluded. The deconvolution of the N 1s peak suggests a signal composed by two components centred at 399.8 and 401.3 eV ascribed to nitrogen involved in the amidic bonds and to nitrogen included in the graphitic structures.[82] The S 2p signal shows two well distinct components centred at 163.8 eV and at 168.1 eV. The first component is related to sulfur atoms in low oxidation state (as for instance C-S-C groups), while the second one is related to sulfur in high oxidation states such as sulfenic and sulfonic acids and derivates $-SO_2$, $-SO_3$.[77,85]

During the purification process it is possible to isolate a carbonaceous by-product (see experimental section) that corresponds to around 10 % of the product mass. It is composed by larger carbonaceous residuals (up to few micrometers **Fig. A3**) and it does not present any chiroptical activity (**Fig. 9f**). The optimization of the reaction condition does not allow to further reduce this fraction that is removed during the purification step. However, in order to have a complete view of the process that forms **L-CDs** by copper catalysed oxidation of cysteine, the by-product is purified and analysed (see appendix, **Fig. A3-6**).

Inspired also by previous work[37] **Fig. 11** shows a schematic structure of the CDs produced by this method. The main reaction product consists of CDs with an achiral graphitic core of about 6 nm as reported in **Fig. 8** by the TEM analysis. The core is surrounded by an amorphous shell which contains the luminophores, probably a heterogeneous family of conjugated structures rich of heteroatoms confined by sp^3 regions. The structure of the shell gives rise to the broad absorption and to the emission dependent PL as suggested by Fu et al.[54] in their study on the origin of the excitation dependent PL of CDs. Finally, the chirality is probably originated from undecomposed cysteine or for cysteine derivates grafted by amide bond that form a ''chiral shell''. This conclusion is suggested by our experimental evidence (circular dichroism and FTIR analysis, **Fig. 9**), and by Wei et al.[75] study on the formation of chiral CDs from tryptophan.

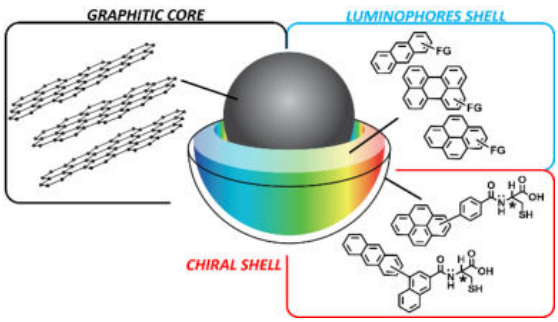

Figure 11. General scheme of the Cys-based CDs.

2.1 INVESTIGATION ON THE CDs FORMATION MECHANISM

State of the art

Since the first observation at the beginning of the XXth century,[86] the process of Cu(II) catalysed self-oxidation of cysteine have been considered of remarkably significance in the research on the oxidative decomposition of biologically active thiols involving many researchers in the investigation of the mechanism and kinetics. The self-oxidation of thiols is mainly described by **equation 1** and **2** in **Scheme 1**. The formation of the disulfide results in the production of water or hydrogen peroxide. The formation of other reactive sulfur species such as sulfenic, sulfinic and sulfonic acids was also considered, and the amount of the different products is mainly related to the pH.[87]

Scheme 1. Overall reactions of thiol RSH self-oxidation into its disufide dimer RSSR

1. $2\ RSH + O_2 \rightleftharpoons RSSR + H_2O_2$
2. $4\ RSH + O_2 \rightleftharpoons 2\ RSSR + 2\ H_2O$

Due to the wide scientific interest in biomolecule decomposition under oxidative stress conditions, copper catalysed self-oxidation of cysteine was deeply investigated by several authors. The reaction at pH = 7.4 by Pecci et al.[88] evidenced the active role of a Cu (I) bis thiol complex in the catalytic cycle. Rigo et al.[89] studied the formation of Cu(I) complexes by ^{1}H-NMR following the titration of cysteine solution with Cu(I) and Cu(II) solutions. Several details on the reaction mechanism were reported by Buzuk et al.[90] by monitoring the Cu(II) concentration with a Cu ion selective electrode during the oxidation process. Bagiyan and coworkers evidenced the coordination role of the thiol molecules.[91] They compared the kinetic characteristics of a wide pool of thiols compounds and related their activity to different chelating capability. In particular, they divided the investigated pool in three groups: non-chelating, weakly chelating and chelating (cysteine, glutathione and cysteamine are some examples of this third class). The analysis of the oxygen and hydroxyl radical concentrations in solution during the oxidation process, reported by Kachur et al.,[92] revealed the presence of two distinct phases active separately in the self-oxidation process: phase 1: free cysteine is still present in solution and it can take part in the metal binding; and phase 2: when there is no longer free cysteine in solution. In the first phase, the oxygen consumption can be related to the cysteine oxidation into cystine and the concentration of hydroxyl radicals is still

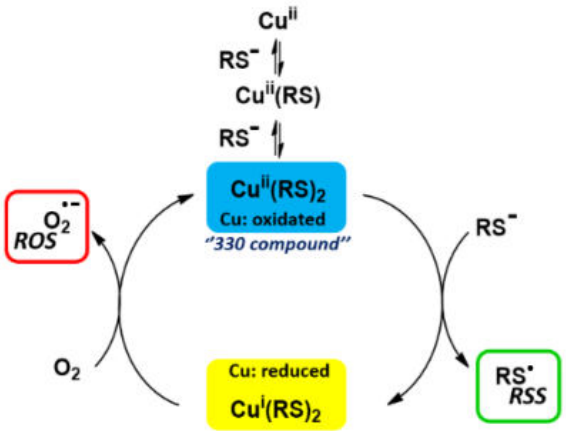

Scheme 2. Representation of the copper role during the catalytic self-oxidation cycle of thiols

low, while in the second phase the oxygen consumption increase due to the activity of reactions that convert cysteine in the sulfinic and sulfonic acids with an increasing of the hydroxyl radical concentration. Moreover, the authors recognized the different behaviours between cysteine and cysteine derivates (N-acetylcysteine, cysteamine and cysteine ethyl ester) and correlated the different capabilities of the thiol compounds to bind the metal centre in relation to the thiol/Cu ratio observed at the beginning of the second phase.

Cavallini et al.[93] investigated the catalytic cycle in alkaline pH. They observed the catalytic oxidation and recognized a fundamental intermediate that takes part in the catalytic self-oxidation cycle. The intermediate, named *''330 compound''*, is characterised by the intense absorption band at 330 and a shoulder at 390 nm. The compound is stable in presence of oxygen and its concentration in solution remains constant until all the free cysteine is consumed. The EPR analysis of frozen solutions evidenced the paramagnetic nature of the *''330 compound''*. By spectrophotometric titration, a 1:2 ratio Cu (II): thiol was evaluated, and a Cu(II) coordination complex with two molecules of cysteine has been proposed. The author suggested that the transfer of one electron from the thiol to the molecular oxygen should occur according to a two steps process: *i*) from cysteine to Cu(II), giving the formation of thiyl radical and the metal in the reduced form, and *ii*) from Cu(I) to oxygen with formation of superoxide radical ion and the oxidation of the metal centre. Since in alkaline solutions, the second step is faster, the copper is mainly observed in the oxidized Cu(II) state. In **Scheme 2** a simplified picture of the role of the metal centre in the catalytic process is reported.

Experimental observations

Table 1 reports the different experimental conditions used to study the processes of the CDs formation investigated also by ^{1}H-NMR and UV/Vis spectroscopy.

The ^{1}H-NMR analysis of the reaction at pH = 7.0 (**Fig. 12a**) shows a complex signal between 4.00 and 3.97 ppm ascribed to the H_{α} proton and a signal between 3.15 and 2.99 ppm ascribed to the methylene protons in the lateral chain (H_{β}). Both the signals are produced from cysteine.

Table 1: reaction conditions considered for the investigation of the mechanism.

Entry n°	Organic substrate	mol (mmol)	pH
1	Glycine (Gly)	1.24	10.5
2	Thioglycolic Acid (TGA)	1.24	10.5
3	Gly + TGA	1.24, 1.24	10.5
4	Methionine	1.24	10.5
5	Penicillamine	1.24	10.5
6	Cysteamine	1.24	10.5
7	Cysteine	1.24	7.0
8	Cysteine	1.24	10.5
9	Cysteine	1.24	12.0

The signals from the cystine, indicated in figure with an asterisk, observed also before the copper addition (**Fig. A7**) is due to the cystine impurity present in commercial cysteine.[89]

After the addition of Cu(II), the increasing of the cystine signals can be related to the catalytic role of the metal ion in the aerobic ''self-oxidation'' of cysteine. The activities of the metal centre are mainly ascribed to its roles as mediator in the electron transfer between thiol and oxygen and in the dismutation of hydrogen peroxide in Fenton-like reactions[92] Recently, kinetics analyses conducted by Begiyan et al.[87] evidenced that Cu(II) is more active that other variable-valent metals such as Mn, Fe, Ni and Co in the catalytic oxidation of thiols.

At pH 10.5, in contrast with the observation at pH = 7.0, the formation of cystine is not observed (**Fig. 12b**). The cysteine signals become broad and after 60 – 90 min all the

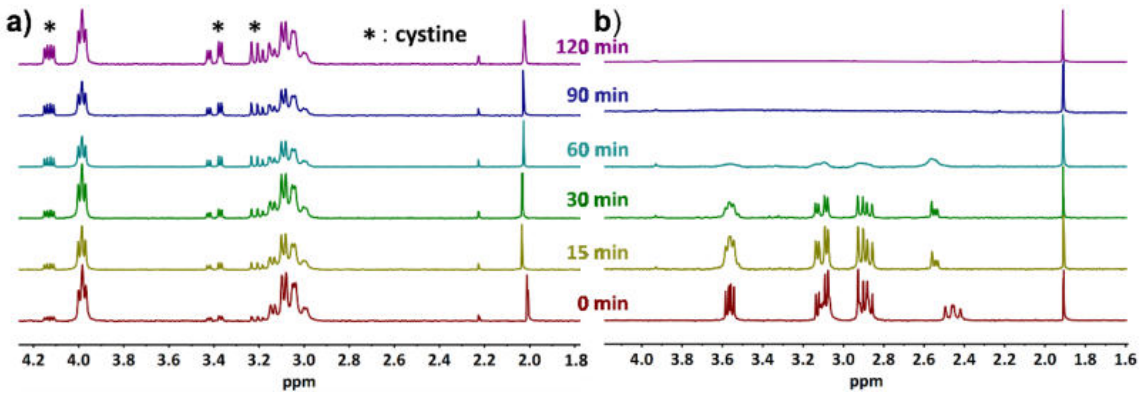

Figure 12. ^{1}H-NMR analysis of the reaction with L-cysteine at pH 7.0 a) and 10.5 b)

signals associated to the organic substrate disappear. This behaviour disagrees with the observations reported by Cavallini et al. about the interaction between Cu(II) and cysteine in alkaline pH.[93] However, the formation of the *''330 compound''* can be evidenced by UV/Vis spectroscopy (**Fig. 13**). After the addition of Cu(II) acetate the solution turns yellow and strong absorptions at 330 and 390 nm can be observed. In agreement with Cavallini and coworkers, the absorption of these bands remain constant until all the free cysteine is consumed (around 30 min). Then, in agreement with the second phase, the Cu(II) mono-cysteine complex is reduced intramolecularly to Cu(I) and cysteine thiyl radical.[92] At longer reaction times, the absorption at 280 nm related to $\pi \rightarrow \pi^*$ transition, as well as to the broad absorption in the visible increase, evidence that is related to the formation of CDs.

The observation of the *''330 compound''* proves the presence of the active species involved in the Cu(II) cysteine self-oxidation cycle, and suggests the formation of several radical reactive species such as RSS (thiyl radicals, disulfides radical anion) and ROS ($O_2^{\bullet-}$, $HO^{\bullet}$, $HOO^{\bullet}$, H_2O_2). However, other processes, different from the cystine formation, can lead to the decomposition of the organic substrate, probably due to the specific reaction conditions (pH and concentrations). FTIR, TEM and XPS analyses reported above, show the formation of sulfoxides and conjugated structures that can be related to the action of several radical species that are generally produced during the catalytic cycle, such as ROS and RSS that can take part in the formation process of CDs.

In agreement with the chemistry of thiyl radicals, the sulfur radical is in equilibrium with carbon-centred radicals trough 1,2 and 1,3 radical hydrogen transfer reactions

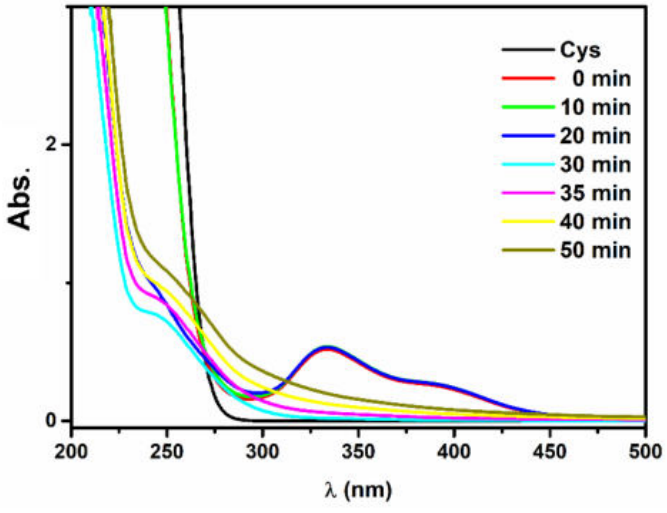

Figure 13: UV/Vis Absorption spectra of the reaction mixture collected at different reaction times.

(**Scheme 3**). Zhao et al.[94] measured the kinetics of radical proton transfer in several substrates such as cysteine, glutathione and homocysteine by pulse radiolysis. They suggested an intramolecular mechanism that pass through a cyclic transition state. These finding has been confirmed, at acidic pH, by Nauser et al.[85] on cysteine, cysteamine and penicillamine with the determination of equilibrium and kinetics constants.

Scheme 3. Equilibrium of thiyl radical with carbon centre radicals on C_α and C_β in the anionic form of cysteine.

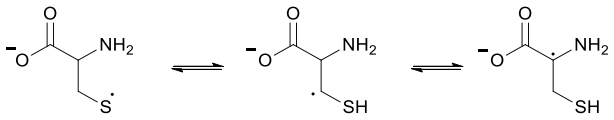

The hypothesis that the equilibrium between thiyl and carbon-centred radicals could play a fundamental role in CDs formation is supported by the pH dependence. At pH = 10.5 the amine group is mainly present in its neutral form and the electron density of the lone pair in the nitrogen atom could increase the stability of the vicinal C_α captodative radical. The formation of the C_α radical is thermodynamically favourite under this condition, meanwhile this process is suppressed at lower pH.[85] In oxygenated solution, carbon centre radicals are readily converted in peroxyl radicals that form α-imino acids and superoxide radicals according to Abramivitch and Rabani.[95]

To further validate this hypothesis, the behaviour of different substrates with similar proton dissociation constants and structural elements (functional groups and protons involved in the radical hydrogen transfer reactions H_α and H_β) is investigated. Cysteine,

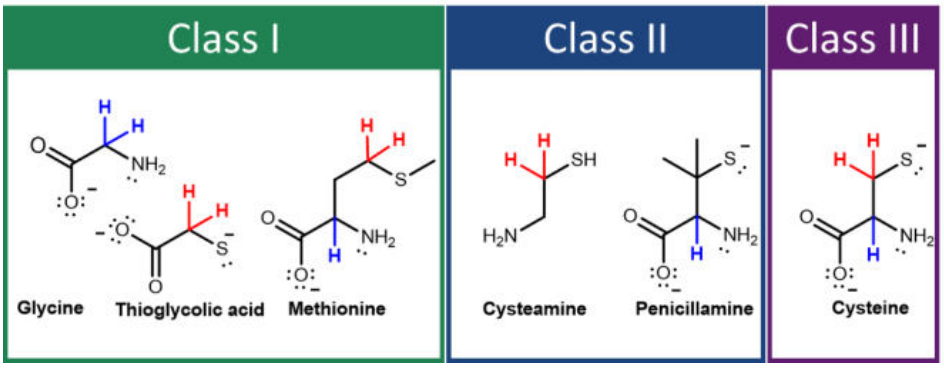

Figure 14: Structure of the different organic substrate considered in this investigation, H_α and H_β are represented in blue and red respectively.

penicillamine, cysteamine, methionine, thioglycolic acid and glycine (**Fig. 14**) are investigated in the same reaction conditions (**Table 1**). Based on our observations, the organic substrates can be divided in three categories.

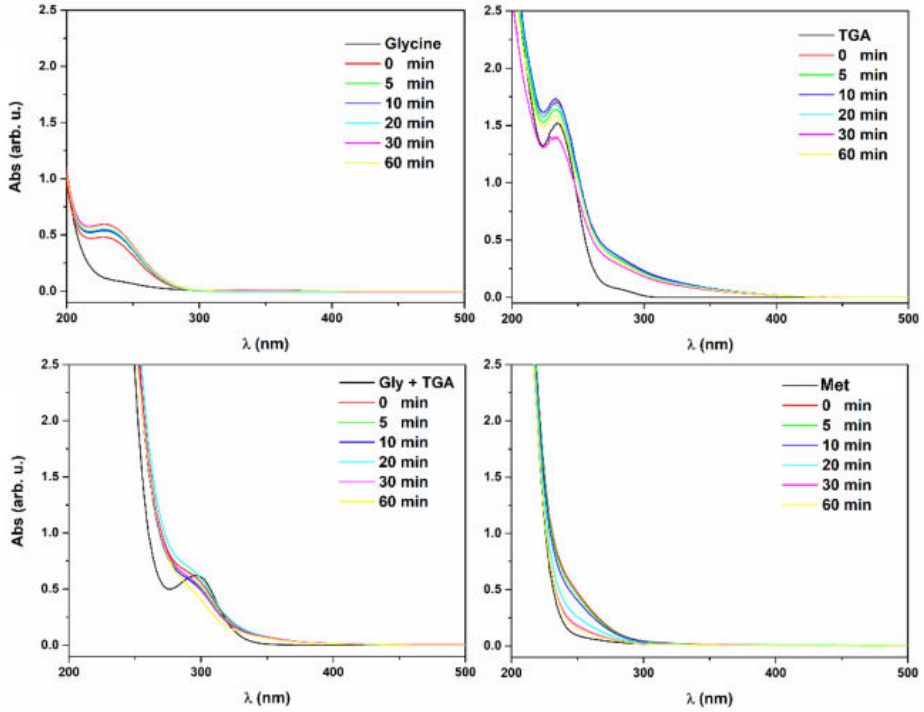

Figure 15. UV/Vis spectroscopy investigation on the reaction between Cu(II) and different organic substrates: Glycine, Thioglycolic acid, mixture of Glycine and Thioglycolic acid and Methionine.

Class I: glycine, thioglycolic acid and methionine. The formation of the *''330 compound''* is not observed since this class of organic substrates is not able to stabilise the Cu(II) (**Fig. 15**). The reaction with a mixture of glycine and TGA 1:1 contains both the protons in the glycine C_α position (H_α) and the protons in the thiol vicinal position C_β (H_β) (entry 1-3), the process follows a completely different pathway and the formation of the *''330 compound''* is not observed after the addition of the Cu(II) acetate (**Fig. 15**). The same behaviour is observed by the reaction with methionine (entry 4) whose thioether group precludes the interaction with the metal centre as anionic binding site (**Fig. 15**). This finding suggests that the multidentate (κ-S, κ-N) binding mode as well as the di anionic electronic state of cysteine, which is the most common ionisation form in alkaline pH, are both necessary for the stabilisation of the Cu(II) and to ensure the catalytic oxidation of cysteine. Thus, the scission of thiol and amine functions or the protection of thiol group in methionine affect the capability of the organic species that are present in solution to stabilise the Cu(II) oxidation state. Probably, in entry 2 and 3 the metal is rapidly reduced to Cu(I) by thioglycolic acid. This hypothesis is supported

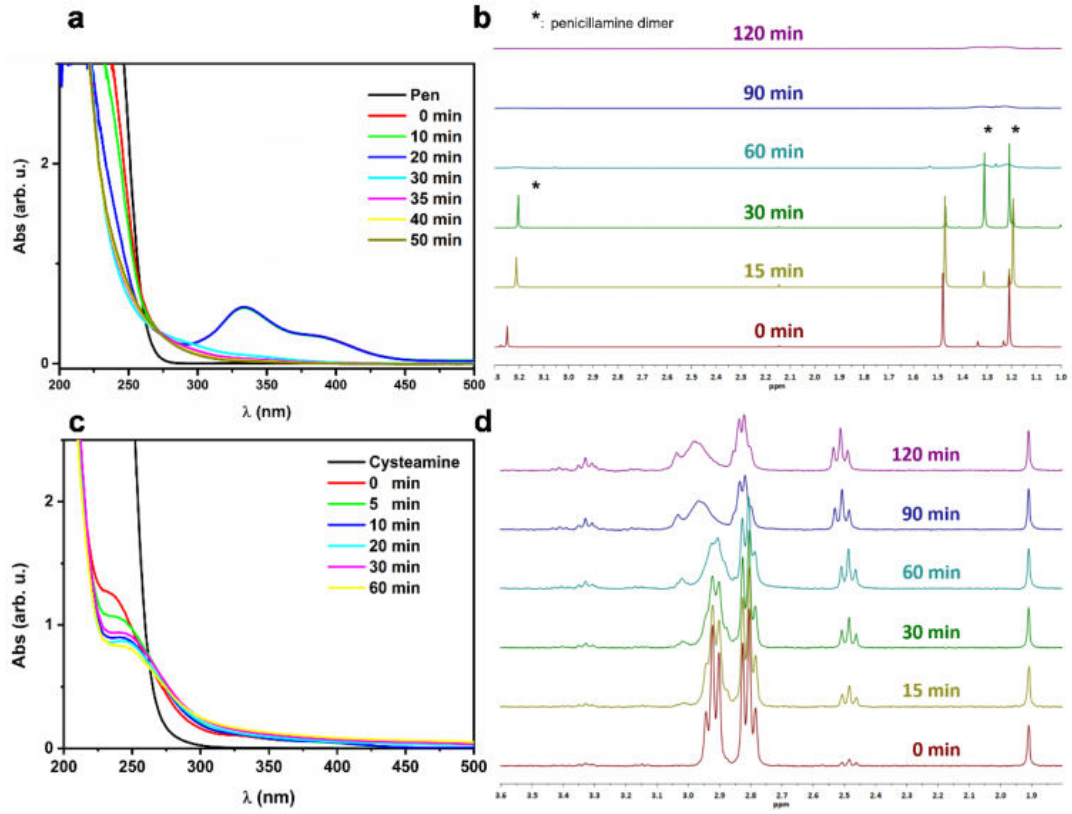

Figure 16: spectroscopic analysis of the decomposition process of Penicillamine and Cysteamine. a) UV/Vis and b) 1H-NMR spectra of the reaction mixture in the presence of L-Penicillamine. c) UV/Vis and d) 1H-NMR spectra of the reaction mixture in the presence of Cysteamine

by the formation of a transient violet colour during the copper addition, feature that was ascribed to the formation of mixed valence compound. EPR and stopped flow UV/Vis analyses on this process were reported by Hanaky Akira.[96]

Class II: penicillamine and cysteamine. These molecules show the formation of the *''330 compound''* after the Cu(II) addition. However, the CDs formation is heavily influenced by the presence of only one group of acidic protons on the organic substrate: H_α penicillamine and H_β cysteamine. As expected, penicillamine (entry 5) is able to bind the metal centre and stabilise the copper oxidation state. The formation of the *''330 compound''* can be recognized by the characteristic absorption bands at 330 and 390 nm in the **Fig. 16a**. As observed for the reaction with cysteine, after 20-30 min almost all the free penicillamine is consumed and the bands at 330 and 390 nm disappear. However, in contrast with the reaction with cysteine, the increase in the absorption at 280 nm related to $\pi \rightarrow \pi^*$ transitions, the absorption in the visible range, due to the formation of aromatic and heteroaromatic surface groups, as well as any luminescence

properties are not observed. The ^{1}H-NMR analysis **Fig. 16b** shows that, even if chromophore groups are not produced during the reaction, the organic substrate is completely decomposed by the process. As observed for cysteine, the signals of the organic substrate became broad and lose intensity. Based on the UV/Vis spectroscopy analysis, it is plausible that the reaction forms heterogeneous intermedium with non-regular polymeric structure rather that CDs. Moreover, the ^{1}H-NMR analysis shows that the amount of oxidised disulfide dimer increases in the first 60 min of reaction. Probably, this effect is due to the higher chemical stability of penicillamine disulfide than cystine. Cavallini et al.[93] investigated the reaction between Cu(II) and cysteamine in alkaline solutions and they observed the formation of the ''*330 compound*'' characterised by a faster decomposition than for cysteine. This behaviour is also confirmed by our results (entry 6). **Fig. 16c** shows a small signal (detail in **Fig. A8**) that can be related to the formation of the *''330 compound''* with cysteamine, but the intensity is not comparable with cysteine or penicillamine findings. The signals remain constant for around 10 min after the decomposition of the ''330 compound'', then the absorbance, at longer wavelength, starts to increase in contrast with the other substrates suggesting the formation of chromophores. The ^{1}H-NMR analysis of the reaction with cysteamine (**Fig. 16d**) shows that the process proceeds slower than the reactions with cysteine and penicillamine. The signals observed at 2.92 ppm and 2.80 ppm, at the moment of the copper addition, are ascribed to the methylene protons attached to nitrogen and sulfur respectively. After 30 min, the signals from both the methylene protons lose their hyperfine structure, the signal at 2.92 ppm becomes broad and it is upshifted to 3.0 ppm after 90 min.

Due to the similar structure of cysteine and penicillamine, it is possible to assume that the reactivities that interest the carboxylic and amine functional groups and the formation of captodative radicals on the C_{α} are comparable for both the substrates. Therefore, the different behaviour of penicillamine could be ascribed to the presence of the two methyl groups in the C_{β} position. The substitution of these hydrogens has the consequence to prevent the 1,2 radical hydrogen transfer reaction, as observed by precedent studies.[85] The evidence on the formation of chromophores when the reaction involves cysteamine further validate this hypothesis. However, the decomposition of cys-

teamine solution is slower than cysteine and penicillamine and only a pale luminescence can be observed when the solution is irradiated by 365 nm lamp; suggesting the low efficiency of the processes involved in the CDs formation. This feature can be related to the different stabilisation capability of the oxidated metal form. Kachur et al.[92] observed that the second phase of the self-oxidation cycle of cysteine derivates started first than what observed with cysteine, behaviour that they related to the different binding mode analysing several thiol compounds.

Class III: cysteine. As already discussed, cysteine (entry 7-9) forms the ''*330 compound*'' after the copper addition (**Fig. 13**), and the organic substrate is readily converted in CDs after few hours (**Fig. 12b**). Therefore, it can be concluded that several structural features, characteristic of cysteine molecule, are in some way fundamental for the participation of the organic substrate in the radical assisted formation process. In particular, it is possible to recognise the synergic roles played by: 1) free thiol groups that can interact with the metal centre and take part in the redox reactions with the formation of radical species. 2) Amine and carboxylic functional groups that complete the biding mode with the metal and control the electron density on the metal centre as well as the stability of the oxidised state. 3) Hydrogen atoms that can take part in radical hydrogen transfer reactions (H_α and H_β) and give the formation of carbon centred radicals. Especially, the observations with penicillamine highlight the dramatic role of H_β in the formation of the luminophores.

2.2 CHIRALITY EVOLUTION DURING THE CDs FORMATION

The evolution of the chiroptical signal during the cysteine decomposition is investigated collecting the circular dichroism spectra of 1 ml of the reaction mixture at different reaction times. The reaction is quenched before the analysis with the addition of 20 µl of HCl 2 M solution and the by-product is removed by centrifugation (5000 rpm for 5 min). The circular dichroism analysis in **Fig. 17a** shows a rapid increasing of the CDs signal characterised by a maximum at 219 nm and a minimum at 250 nm, with a maximum intensity around 1.5 h remaining almost constant until 2 h. For longer reaction time, see **Fig. 17b**, the intensity of the circular dichroism signal decrease progressively. In order to correlate these observations with the evolution of the nanoparticle structure, the absorption in the UV/Vis region and the photoluminescent properties of the

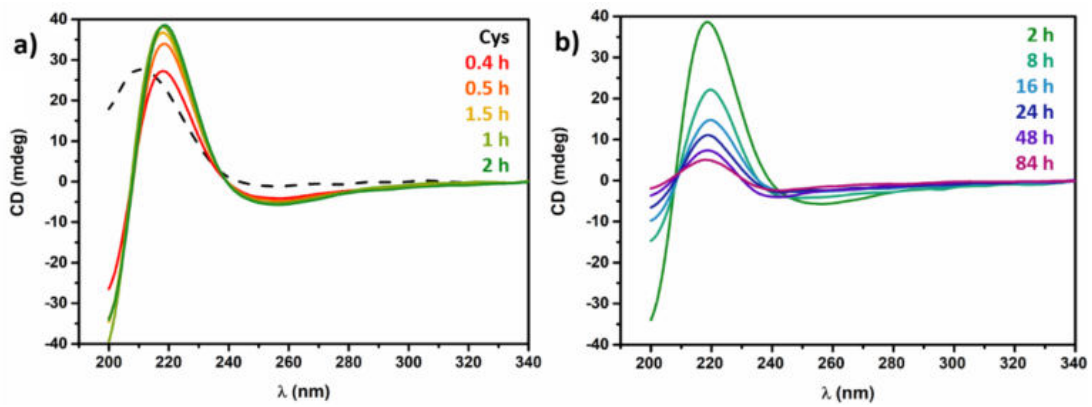

Figure 17: Evolution of the chiroptical signal during the reaction coarse a) 0 – 2 h, b) and 2 – 84 h.

samples are analysed. The UV/Vis spectroscopy analysis reported in **Fig. 18a** shows the progressive evolution of the chromophores on the CDs surface. Furthermore, the samples collected within 2 h of reaction show a considerable absorption at 250 nm. The intensity of this band increases until 1.5 h and becomes almost constant at 2 h. Based on the time dependence and position of this absorption band, the absorption band at 250 nm can be ascribed to the chiroptical active chromophores present in the CDs. At longer reaction times, the formation of other achiral chromophores is favoured: strong absorption at 270, 325 and 390 nm appear after 8 h and their intensity increase with the reaction time. The PL investigation (**Fig. A9-11**) covers both different pH and excitation wavelength for a complete optical characterisation on the CDs formation process. It must be remarked that, all the samples that are collected at reaction times shorter than 0.5 h do not show any significant luminescence; in this phase the cysteine decomposition is not completed and the formation of luminophores is not active yet. Instead, a constant increase in the PL intensity is observed for the sample collected at longer reaction time. Since the sample collected at 2 h and 84 h show similar values of PLQY around 1.5 %. For this reason, the variation of the PL intensity can be related to the increasing concentration of luminophores on the nanoparticles. For the sample collected in the 0.5 – 2 h range, a strong pH dependence is observed. In particular, samples collected after 0.5 and 1 h show the more intense emission related to luminophores excited at 350 nm at pH 2 and pH 7, meanwhile at alkaline pH the components that absorb at 375 nm are more active. This behaviour is gradually lost at longer reaction time and it is ascribed to the evolution of luminophores species that present a lower pH dependence, probably due to the consumption of vicinal functional groups that are

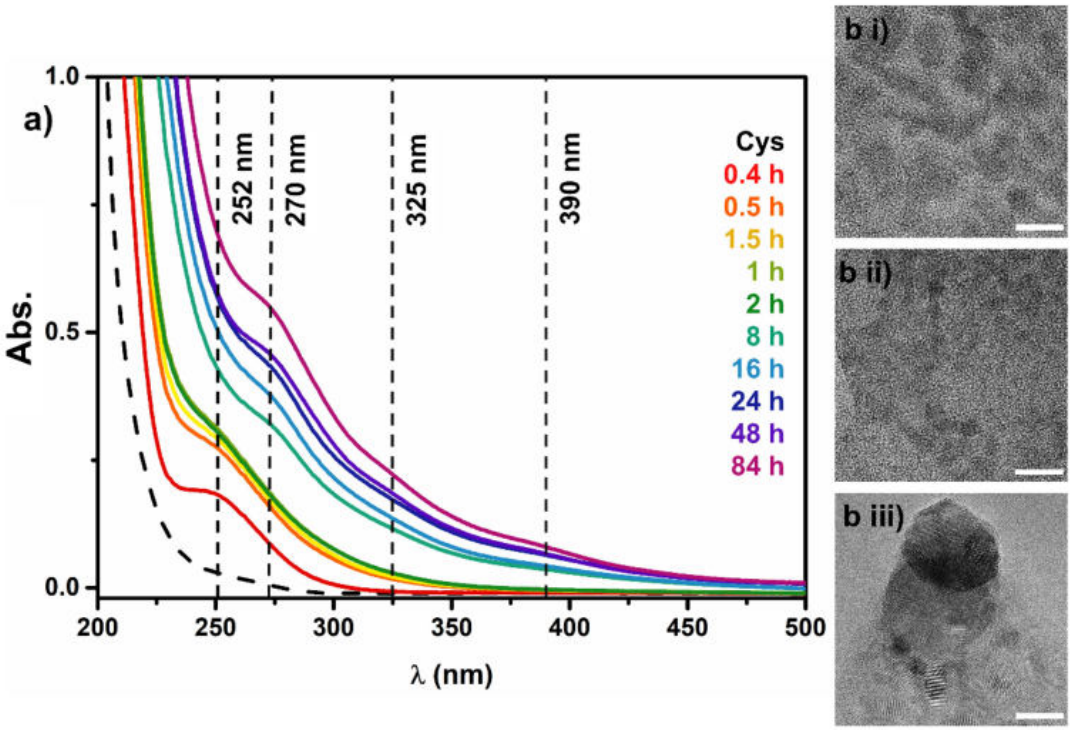

Figure 18: a) UV/Vis spectra of the fractions collected at different reaction time. b) TEM micrograph of the **L-CDs** after purification isolated at i) 2 h ii) 48 h and iii) 84 h; the scale bars i-iii correspond to 10 nm.

affected by protonation equilibria and can act as quenchers for the luminophores. Intermedia molecular-like luminophore can be observed in the sample collected in the 0.5 – 1.5 h range, by the high symmetrical and the excitation independent emission at 550 nm active at pH 2 and 7 when excited around 500 nm. This specie is further consumed for longer reaction time.

The morphologies of the samples collected at 2 h, 48 h and 84 h are characterised by TEM analysis (**Fig. 18b i-iii** and **Fig. A12-14**). The samples collected at 2 h and 48 h show the presence of well separated nanoparticles, the average diameter around 6 nm for 2 h and slightly smaller, around 5 nm, for 48 h (however, further consideration about this feature are complicated by the low contrast in the micrographs) and the crystalline structure of the particle core can be observed by the phase contrast images (**Fig. A14iii,iv**) In contrast, the materials collected at longer reaction time 84 h shows the presence of structures of hundreds of nanometers, as observed in the low magnification images (**Fig. A14i**). The high magnification images (**Fig. A14ii-iv**) allow to highlight the presence of the CDs graphitic cores with an average diameter around 6 nm that compose, with random orientation, the large polycrystalline aggregates.

The FTIR analysis (**Fig. 19**) of samples collected at different reaction times shows a significant increase in the absorption bands related to carboxylic acids functions, in particular the υ_{O-H} 3500- 2500 cm^{-1}, the υ_{CO} at 1720 cm^{-1} for the samples collected at 48 h and 84 h. This feature is followed by the reduction of the amidic bands (amide I and amide II at 1700 and 1590 cm^{-1}). Moreover, the sulfonic acids related absorption at 1030 cm^{-1} and the absence of signals of δ_{SH} at 941 cm^{-1} and υ_{CS} at 692 cm^{-1} shows that the materials isolated at different reaction times contain sulfur in high oxidation state, as expected by the oxidative reaction environment.[31]

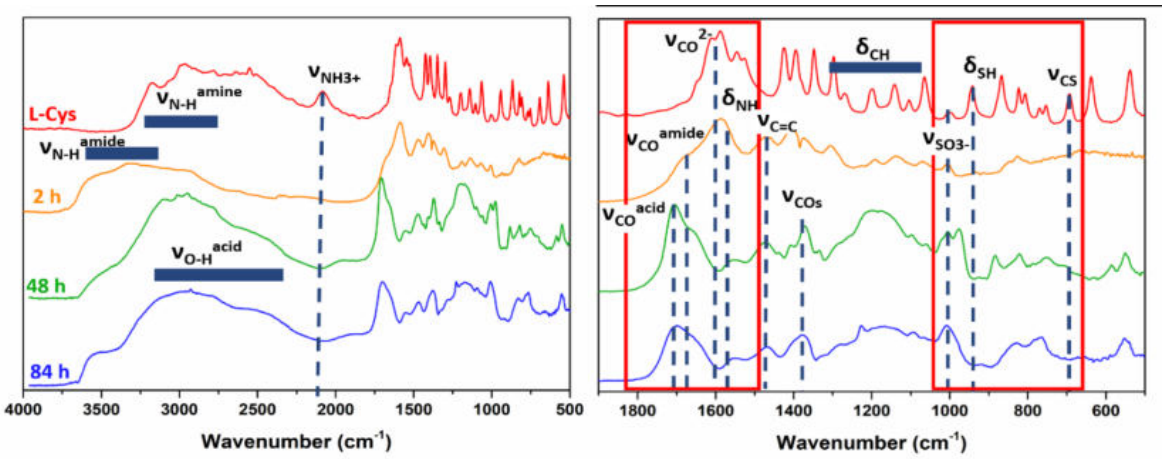

Figure 19. FTIR analysis of L-Cysteine and L-CDs isolated at different reaction times (2, 48 and 84 h).

We concluded that the chiroptical activity of cysteine based chiral CDs produced by radical assisted decomposition is originated by cysteine molecules or cysteine derivates (amides, disulfide or sulfonic acid) grafted on the outer shell of the nanoparticles through amidic bonds. As shown in **Fig 17a, b,** the circular dichroism signal at 220 nm reaches a maximum between 1.5 – 2 h, that is associated to the formation of the maximum population of the chiral chromophores in the CDs chiral shell. For reaction times longer than 2 h the chiral information is progressively lost, feature that can be related to the activity of decomposition processes that affect the grafted molecules that compose the ''chiral shell'' and give the formation of the inner structure such as achiral chromophores, luminophores and the graphitic core. Although the amount of luminophores increase at longer reaction time, their structure seems to be preserved as suggested by the similar PLQY values estimated for the samples isolated at different reaction times. This process can be related to the generation of the carbon centre radicals in the C_α position by the above-mentioned radical hydrogen transfer mechanisms that

gives to the planarization of the stereocenter with the consequence loss of the chiral information. This hypothesis is supported by the UV/Vis and PL measurements, and our conclusions are in agreement with the observation on the chirality evolution for cysteine based CDs reported by others.[77,97] Finally, significant modifications in the CDs morphology are observed only for the sample collected at longer reaction time (84 h) probably due to aggregation process that take place when the functional groups present in the outer amorphous shells are sufficiently decomposed. Since optical chirality and luminescence seems to follow an opposite trend in this system. It is necessary to consider which property suits best the interest for a specific application in order to design the proper synthesis. Short reaction times preserve the chiral structures and gives a higher chiroptical activity, on the other hand, long reaction times promote the formation of luminophores rich structures at the expenses of the chiroptical active groups.

3 CONCLUSIONS AND FUTURE PERSPECTIVES

In this investigation, a novel room temperature method for the synthesis of cysteine based chiral CDs is developed. The produced nanoparticles have an average size around 6 nm with a crystalline graphitic core. The characterisation of the optical properties reveals a strong excitation dependent emission, with a PL maximum at around 460 nm and a PLQY of 1.5 %. Despite the low PLQY, the particles show strong CD signals in the UV region that can be related to cysteine derivates group grafted on the nanoparticles surface. The observations on the mechanism involved in the nanoparticle formation suggest a catalytic role of the multivalent transition metal (copper) in the production of radical species (ROS and RSS) active in the decomposition of the organic substrate. In this context a reaction intermedia *''330 compound''* is identified and exploited to investigate the substrate decomposition process.

Thanks to the analysis of the reactivity of similar substrates, it is possible to define the role of different structural features that involve the organic substrate in the CDs formation process. For example: i) the presence of a free thiol and amino groups that bind the metal centre in its oxidised form, ii) the oxidation of thiol group to thiyl radical, iii) the presence of acidic protons involved in radical hydrogen abstraction reactions and iv) the stabilisation effect for the formation of captodative radicals on the C_α position thanks to the synergistic effect of amine and carboxylate groups.

The investigation by circular dichroism and supported by UV/Vis absorption, TEM and FTIR on the chirality evolution during the reaction reveals fundamental details on the origin of the nanoparticles chirality and the relationship with the CDs structure. In particular, the detrimental effect for the particles chirality related to the radical reactions involved in the particle formation is evidenced. This finding can be related to the formation of carbon radical on the C_α position that affects its stereochemistry causing racemisation. This process is especially impactful for long reaction time giving an extensive reduction of the particle chirality. For this reason, is fundamental to understand the mechanisms that are involved in the particle formation to properly design the synthesis according to the desired optical and chiroptical properties.

4 MATERIALS AND METHODS

4.1 CHEMICALS

L-Cysteine (98 %) and D-Cysteine (98 %) are purchased by Alfa Aesar. L-penicillamine (99 %), Cysteamine (95 %), $Cu(OAc)_2$ (99 %), deuterium oxide (99.9 %), thioglycolic acid (98 %), Glycine (99 %) and sodium hydroxide, hydrochloric acid (37 %) are purchased by Sigma Aldrich. All the chemicals are employed without further purification.

4.2 SYNTHESIS

Cysteine derived CDs Synthesis: 1.24 mmol of L or D Cysteine is solubilised in 100 ml of deionized water. The pH of the solution is adjusted to 10.5 with the addition of some drops of NaOH 2 M solution. Then, 0.200 ml of $Cu(OAc)_2$ 0.25 M solution (50 µmol) is added under vigorous stirring. The reaction mixture is left stirring at room temperature for 2.0 h. Then, the reaction in quenched by adjusting the pH below 7 with the addition of few drops of HCl 2 M solution. At acidic pH the by-product precipitates and it is removed by centrifugation (5000 rpm, 5 min). The supernatant is collected and purified by dialysis (3500 kDa, 24 h). The solvent is removed by vacuum distillation at room temperature to obtain a brown power. CDs dispersion with concentration 1 mg/ml in MilliQ water were prepared for the spectrophotometric analyses. The by-product fraction is dried in vacuum at room temperature to obtain a black powder. By-product dispersion 1 mg/ml in MilliQ water is prepared adding NaOH to adjust the pH around 7.

4.3 CHARACTERISATIONS

Structural characterisation: the powder diffraction measurement is recorded with a Panalytical Advanced Powder Diffractometer.

Morphological characterisation: ThermoFisher Talos FEI TEM is employed for the TEM analysis working with 300 kV electrons beam. Zeiss Sigma VP Field Emission Scanning Electron Microscope (FE-SEM) is employed for the SEM analyses and Bruker Quantax 200 analyser is employed for the EDS analysis.

Absorption spectra: The UV/Vis analysis is carried out with a Cary 60 (Agilent) UV/Vis spectrophotometer.

Photoluminescence Quantum Yield determination: the quantum yield is estimated by comparison with a known fluorescence standard according to **Eqs. A1** and **A2**. Quinine

sulfate is chosen as standard considering a quantum yield 0.54 in sulfuric acid 0.1 M solution.[98]

Steady state luminescence spectra: The PL and PLE measurements are collected with a Jasco FP-8200 spectrofluorometer. The quantum yield measurements are collected with a Nanolog/Fluorolog-3-2iHR320, (Horiba-Jobin Yvon) spectrometer.

FTIR spectra: FTIR spectra is recorded using a NEXUS-FTIR instrument implementing a Nicolet Diffuse Reflectance accessory (DRIFT).

CD measurements: the CD spectra is collected with a Jasco J1500 polarimeter using colloidal dispersion in water and adjusting the particles concentration to keep the absorbance at 350 nm around 0.5. For the spectra acquisition, the scan speed is set to 50 nm/min with 5 acquisitions for each spectrum.

NMR: ^{1}H-NMR data are acquired with a Bruker 300 MHz NMR in D_2O.

XPS: XPS measurements are performed using a Perkin Elmer Φ 5600ci spectrometer, working in the 10^{-7} Pa pressure range at room temperature with nonmonochromatic Al K_α radiation (1486.6 eV). The BE values are referred to the Fermi level.

Effect of the organic substrate: 1.24 mmol the organic substrate is added in 100 ml of deionized water. The pH of the solution is adjusted to 10.5 (or 7.0 and 12.0 as reported in entry 7 and 9 in table 1 respectively) with the addition of some drops of NaOH 2 M solution. Then, 0.200 ml of $Cu(OAc)_2$ 0.25 M solution (50 µmol) is added under vigorous stirring. The reaction mixture is left stirring at room temperature for 2.0 h. Specimens are collected at different reaction time for the spectrophotometric analysis. The reaction that are investigated by ^{1}H-NMR are prepared using D_2O instead of deionized water.

Study of the evolution of chirality: 1.24 mmol of L-Cysteine is solubilised in 100 ml of deionized water. The pH of the solution is adjusted to 10.5 with the addition of some drops of NaOH 2 M solution. Then, 0.200 ml of $Cu(OAc)_2$ 0.25 M solution (50 µmol) is added under vigorous stirring. The reaction mixture is left stirring at room temperature. Specimens of 1 ml of the reaction mixture are collected at different reaction times for the circular dichroism and UV/Vis analyses. The reaction is quenched before the analysis with the addition of 20 µl of HCl 2 M solution and the by-product is removed by centrifugation (5000 rpm for 5 min). The TEM and FTIR analysis are performed on sample prepared after purification at acidic pH the by-product

to remove the by-product by centrifugation (5000 rpm, 5 min). Then, the supernatant is collected and purified by dialysis (3500 kDa, 24 h). The solvent is removed by vacuum distillation at room temperature to obtain a brown powder. The powder is used for the FTIR analysis and a portion of it is redispersed in ethanol and used for the preparation of the TEM grids.

5 REFERENCES

1 F. A. ; W. G. ; M. C. A. ; B. M. Cotton, *Advanced Inorganic Chemistry*, Wiley-Interscience, New York, sixth edition., 1999.
2 C. E. ; S. A. G. Housecroft, *Inorganic Chemistry 1*, Person Education Limited, Harlow, fourth edition., 2012.
3 J. Robertson, *Adv. Phys.*, 1986, **35**, 317–374.
4 W. I. Milne and J. Robertson, *Encyclopedia of materials : science and technology*, 2001, 1–3.
5 A. C. Ferrari and J. Robertson, *Phylos. Trans. Royal Soc. A*, 2004, **362**, 2477–2512.
6 B. E. Warren, *Phys. Rev.*, 1941, **59**, 693–698.
7 K. S. Novoselov, A. K. Geim, S. v Morozov, D. Jiang, Y. Zhang, S. v Dubonos, I. v Grigorieva and A. A. Firsov, *Phys. Rev. Lett.*, 2000, **404**, 3824.
8 A. K. Geim and K. S. Novoselov, *Nat. Mater.*, 2007, **6**, 183–191.
9 Y. Zhang, Y. W. Tan, H. L. Stormer and P. Kim, *Nature*, 2005, **438**, 201–204.
10 C. E. Housecroft and A. G. Sharp, *Inorganic Chemistry 2*, Person Education Limited, New York, fourth edition., 2012.
11 H. W. Kroto, J. R. Heath, S. C. O'Brien, R. F. Curl and R. E. Smalley, *Nature*, 1985, **14**, 162–163.
12 E. Osawa, *Phil. Trans. R. Soc. A*, 1993, **343**, 1–8.
13 H. W. Kroto, *Angew. Chem. In. Ed.*, 1992, **31**, 111–246.
14 W. Krätsehmer, *Synth. Met.*, 1995, **70**, 1309–1312.
15 S. IIjima, *Nature*, 1991, **354**, 56–58.
16 M. Monthioux and V. L. Kuznetsov, *Carbon N Y*, 2006, **44**, 1621–1623.
17 S. Iijima and T. Ichihashi, *Nature*, 1993, **363**, 603–605.
18 D. S. Bethune, C. H. Kiang, M. S. de Vries, G. Gorman, R. Savoy, J. Vazquez and R. Beyer, *Nature*, 1993, **363**, 605–607.
19 O. Kozák, M. Sudolská, G. Pramanik, P. Cígler, M. Otyepka and R. Zbořil, *Chemistry of Materials*, 2016, 28, 4085–4128.
20 S. N. Baker and G. A. Baker, *Angew. Chem. Int. Ed.*, 2010, 49, 6726–6744.
21 S. Y. Lim, W. Shen and Z. Gao, *Chem. Soc. Rev.*, 2015, **44**, 362–381.
22 X. Xu, R. Ray, Y. Gu, H. J. Ploehn, L. Gearheart, K. Raker and W. A. Scrivens, *J. Am. Chem. Soc.*, 2004, **126**, 12736–12737.
23 N. Arora and N. N. Sharma, *Diam. Rel. Mater.*, 2014, **50**, 135–150.
24 V. Thongpool, P. Asanithi and P. Limsuwan, *Procedia Eng.*, 2012, **32**, 1054–1060.
25 X. Li, H. Wang, Y. Shimizu, A. Pyatenko, K. Kawaguchi and N. Koshizaki, *Chem. Commun.*, 2011, **47**, 932–934.
26 S. L. Hu, K. Y. Niu, J. Sun, J. Yang, N. Q. Zhao and X. W. Du, *J. Mater. Chem.*, 2009, **19**, 484–488.
27 Y. Suda, T. Ono, M. Akazawa, Y. Sakai, J. Tsujino and N. Homma, *Thin Solid Films*, 2002, **415**, 15–20.
28 Y. P. Sun, B. Zhou, Y. Lin, W. Wang, K. A. S. Fernando, P. Pathak, M. J. Meziani, B. A. Harruff, X. Wang, H. Wang, P. G. Luo, H. Yang, M. E. Kose, B. Chen, L. M. Veca and S. Y. Xie, *J. Am. Chem. Soc.*, 2006, **128**, 7756–7757.
29 L. Cao, X. Wang, M. J. Meziani, F. Lu, H. Wang, P. G. Luo, Y. Lin, B. A. Harruff, L. M. Veca, D. Murray, S. Y. Xie and Y. P. Sun, *J. Am. Chem. Soc.*, 2007, **129**, 11318–11319.
30 J. Zhou, C. Booker, R. Li, X. Zhou, T. K. Sham, X. Sun and Z. Ding, *J. Am. Chem. Soc.*, 2007, **129**, 744–745.
31 Q. L. Zhao, Z. L. Zhang, B. H. Huang, J. Peng, M. Zhang and D. W. Pang, *Chem Commun.*, 2008, 5116–5118.
32 Q. Zhang, X. Sun, H. Ruan, K. Yin and H. Li, *Sci. China Mater.*, 2017, **60**, 141–150.
33 S. Yang, J. Sun, X. Li, W. Zhou, Z. Wang, P. He, G. Ding, X. Xie, Z. Kang and M. Jiang, *J. Mater. Chem. A*, 2014, **2**, 8660–8667.
34 Y. Shin, J. Park, D. Hyun, J. Yang, J. H. Lee, J. H. Kim and H. Lee, *Nanoscale*, 2015, **7**, 5633–5637.
35 J. Yu, C. Xu, Z. Tian, Y. Lin and Z. Shi, *New J. Chem.*, 2016, **40**, 2083–2088.
36 Y. Hou, Q. Lu, J. Deng, H. Li and Y. Zhang, *Anal. Chim. Acta*, 2015, **866**, 69–74.
37 D. Qu and Z. Sun, *Mater. Chem. Front.*, 2020, **4**, 400–420.
38 M. J. Krysmann, A. Kelarakis, P. Dallas and E. P. Giannelis, *J. Am. Chem. Soc.*, 2012, **134**, 747–750.
39 Y. Song, S. Zhu, S. Zhang, Y. Fu, L. Wang, X. Zhao and B. Yang, *J. Mater. Chem. C*, 2015, **3**, 5976–5984.
40 K. Jiang, S. Sun, L. Zhang, Y. Lu, A. Wu, C. Cai and H. Lin, *Angew. Chem. Int. Ed.*, 2015, **54**, 5360–5363.
41 H. Wang, T. Zhang, J. Zhu, Y. Zhai, H. Wang, X. Bai, B. Dong and H. Song, *Nanoscale*, 2017, **9**, 13042–13051.
42 F. Li, Y. Li, X. Yang, X. Han, Y. Jiao, T. Wei, D. Yang, H. Xu and G. Nie, *Angew. Chem. Int. Ed.*, 2018, **130**, 2401–2406.

43 Y. Dong, J. Shao, C. Chen, H. Li, R. Wang, Y. Chi, X. Lin and G. Chen, *Carbon N Y*, 2012, **50**, 4738–4743.
44 S. Zhu, Q. Meng, L. Wang, J. Zhang, Y. Song, H. Jin, K. Zhang, H. Sun, H. Wang and B. Yang, *Angew. Chem. Int. Ed.*, 2013, **52**, 3953–3957.
45 M. K. Barman, B. Jana, S. Bhattacharyya and A. Patra, *J. Phys. Chem. C*, 2014, **118**, 20034–20041.
46 S. K. Bhunia, A. Saha, A. R. Maity, S. C. Ray and N. R. Jana, *Sci. Rep.*, 2013, **3**, 1473.
47 P. Yu, X. Wen, Y. R. Toh and J. Tang, *J. Phys. Chem. C*, 2012, **116**, 25552–25557.
48 H. Ding, S. B. Yu, J. S. Wei and H. M. Xiong, *ACS Nano*, 2016, **10**, 484–491.
49 J. C. Vinci, I. M. Ferrer, S. J. Seedhouse, A. K. Bourdon, J. M. Reynard, B. A. Foster, F. v. Bright and L. A. Colón, *J. Phys. Chem. Lett.*, 2013, **4**, 239–243.
50 H. Li, X. He, Z. Kang, H. Huang, Y. Liu, J. Liu, S. Lian, C. H. A. Tsang, X. Yang and S. T. Lee, *Angew. Chem. Int. Ed.*, 2010, **49**, 4430–4434.
51 Z. C. Yang, M. Wang, A. M. Yong, S. Y. Wong, X. H. Zhang, H. Tan, A. Y. Chang, X. Li and J. Wang, *Chem. Commun.*, 2011, 11615–11617.
52 D. Kozawa, X. Zhu, Y. Miyauchi, S. Mouri, M. Ichida, H. Su and K. Matsuda, *J. Am. Chem. Soc*, 2014, **5**, 1754–1759.
53 M. Sudolská, M. Dubecký, S. Sarkar, C. J. Reckmeier, R. Zboril, A. L. Rogach and M. Otyepka, *J. Phys. Chem. C*, 2015, **119**, 13369–13373.
54 M. Fu, F. Ehrat, Y. Wang, K. Z. Milowska, C. Reckmeier, A. L. Rogach, J. K. Stolarczyk, A. S. Urban and J. Feldmann, *Nano Lett.*, 2015, **15**, 6030–6035.
55 F. Demichelis, S. Schreiter and A. Tagliaferro, *Phys. Rev. B*, 1995, **51**, 15–1995.
56 Rusli, J. Robertson and G. A. J. Amaratung, *J. Appl. Phys.*, 1996, **80**, 2998–3003.
57 J. Robertson, *Phys. Rev. B.*, 1996, **53**, 16302–16305.
58 N. Dhenadhayalan, K. C. Lin, R. Suresh and P. Ramamurthy, *J. Phys. Chem. C*, 2016, **120**, 1252–1261.
59 F. Yan, Z. Sun, H. Zhang, X. Sun, Y. Jiang and Z. Bai, *Microchim. Acta*, 2019, 186.
60 Q. Fang, Y. Dong, Y. Chen, C. H. Lu, Y. Chi, H. H. Yang and T. Yu, *Carbon N Y*, 2017, **118**, 319–326.
61 Z. Komeily-Nia, J. Y. Chen, B. Nasri-Nasrabadi, B. Yuan, J. Zhang, A. Gupta, L. T. Qu and A. Gupta, *Phys. Chem. Chem. Phys.*, 2020, **22**, 3112–3121.
62 Z. K. Nia, J. Y. Chen, B. Tang, B. Yuan, X. G. Wang and J. L. Li, *Carbon N Y*, 2017, **116**, 703–712.
63 K. Kato and A. Osuka, *Angew. Chem. In. Ed.*, 2019, **58**, 8978–8986.
64 M. Vázquez-Nakagawa, L. Rodríguez-Pérez, M. A. Herranz and N. Martín, *Chem. Commun.*, 2016, **52**, 665–668.
65 Y. Zhang, L. Hu, Y. Sun, C. Zhu, R. Li, N. Liu, H. Huang, Y. Liu, C. Huang and Z. Kang, *RSC Adv.*, 2016, **6**, 59956–59960.
66 F. Gao, S. Ma, J. Li, K. Dai, X. Xiao, D. Zhao and W. Gong, *Carbon N Y*, 2017, **112**, 131–141.
67 F. Copur, N. Bekar, E. Zor, S. Alpaydin and H. Bingol, *Sens. Actuators B*, 2019, **279**, 305–312.
68 X. Zeng, L. Zhang, J. Yang, Y. Guo, Y. Huang, H. Yuan and Y. Xie, *New J. Chem.*, 2017, **41**, 15216–15228.
69 E. Lizundia, T. D. Nguyen, J. L. Vilas, W. Y. Hamad and M. J. Maclachlan, *Mater. Chem. Front.*, 2017, **1**, 979–987.
70 F. Arshad and M. P. Sk, *New J. Chem.*, 2019, **43**, 13240–13248.
71 A. Ghosh, B. Parasar, T. Bhattacharyya and J. Dash, *Chem Commun.*, 2016, **52**, 11159–11162.
72 M. J. Deka and D. Chowdhury, *RSC Adv.*, 2017, **7**, 53057–53063.
73 L. Zhou, D. Zheng, B. Wu, Y. Zhu and L. Zhu, *ACS Appl. Nano Mater.*, 2020, **3**, 946–952.
74 X. Rao, M. Yuan, H. Jiang, L. Li and Z. Liu, *New J. Chem.*, 2019, **43**, 13735–13740.
75 Y. Wei, L. Chen, J. Wang, X. Liu, Y. Yang and S. Yu, *RSC Adv.*, 2019, **9**, 3208–3214.
76 L. Đorđević, F. Arcudi, A. D'Urso, M. Cacioppo, N. Micali, T. Bürgi, R. Purrello and M. Prato, *Nat. Commun.*, 2018, **9**, 3442.
77 L. Hu, H. Li, C. Liu, Y. Song, M. Zhang, H. Huang, Y. Liu and Z. Kang, *Nanoscale*, 2018, **10**, 2333–2340.
78 L. Hu, Y. Sun, Y. Zhou, L. Bai, Y. Zhang, M. Han, H. Huang, Y. Liu and Z. Kang, *Inorg. Chem. Front.*, 2017, **4**, 946–953.
79 A. Pawlukojć, J. Leciejewicz, A. J. Ramirez-Cuesta and J. Nowicka-Scheibe, *Specrochim. Acta. A*, 2005, **61**, 2474–2481.
80 G. Socrates, *Infrared and Raman Characteristic Group Frequencies*, 2001.
81 L. Li, L. Liao, Y. Ding and H. Zeng, *RSC Adv.*, 2017, **7**, 10361–10368.
82 S. Do, W. Kwon, Y. H. Kim, S. R. Kang, T. Lee, T. W. Lee and S. W. Rhee, *Adv Opt Mater*, 2016, **4**, 276–284.
83 T. Yoshinaga, Y. Iso and T. Isobe, *J. Lumin.*, 2019, **213**, 6–14.
84 N. Amdursky and M. M. Stevens, *ChemPhysChem*, 2015, **16**, 2768–2774.
85 T. Nauser, W. H. Koppenol and C. Schoöneich, *J. Phys. Chem. B*, 2012, **116**, 5329–5341.
86 A. P. Mathews and S. Walker, *J. Biol. Chem*, 1909, **6**, 299–312.

87 G. A. Bagiyan, I. K. Koroleva, N. v Soroka, A. v Ufimtsev and B. P. Konstantinov, *Russ. Chem. Bull.*, 2003, **52**, 1075–1081.
88 L. Pecci, G. Montefoschi, G. Musci and D. Cavallini, *Amino Acids*, 1997, **13**, 355–367.
89 A. Rigo, A. Corazza, M. Luisa Di Paolo, M. Rossetto, R. Ugolini and M. Scarpa, *J. Inorgan. Biochem.*, 2004, **98**, 1495–1501.
90 M. Buzuk, S. Brinić, N. Vladislavić, M. Bralić, M. Buljac and I. Š. Rončević, *Monatsh. fur Chem.*, 2016, **147**, 359–367.
91 G. A. Bagiyan, I. K. Koroleva, N. v. Soroka and A. v. Ufimtsev, *Kinet. Catal.*, 2004, **45**, 372–380.
92 A. v Kachur, C. J. Koch and J. E. Biaglow, *Free Pad. Res*, 1999, **31**, 23–34.
93 D. Cavallini, C. de Marco, S. Duprb and G. Rotilio, *Arch. Biochem.*, 1969, **130**, 354361.
94 R. Zhao, J. Lind, G. Merbnyi and T. E. Eriksen, *J. Am. Chem. Soc.*, 1994, **116**, 12010–12015.
95 S. Abramovitch, J. Rabani, K. D. Asmus, A. Henglein, M. Ebert, J. P. Keene, B. Bunsangas Phys, M. Mockel and J. Phys Cham, *J. Phys. Chem.*, 1973, **77**, 53.
96 A. Hanaki, *Chem. Pharm. Bull.*, 1974, **22**, 2491–2492.
97 F. Victoria, J. Manioudakis, L. Zaroubi, B. Findlay and R. Naccache, *RSC Adv.*, 2020, **10**, 32202–32210.
98 A. M. Brouwer, *Pure Appl. Chem.*, 2011, 83, 2213–2228.
99 U. Resch-Genger and K. Rurack, *Pure Appl. Chem.*, 2013, **85**, 2005–2026.
100 A. Oya and H. Marsh, *J. Mater. Sci.*, 1982, **17**, 309–322.

6 APPENDIX

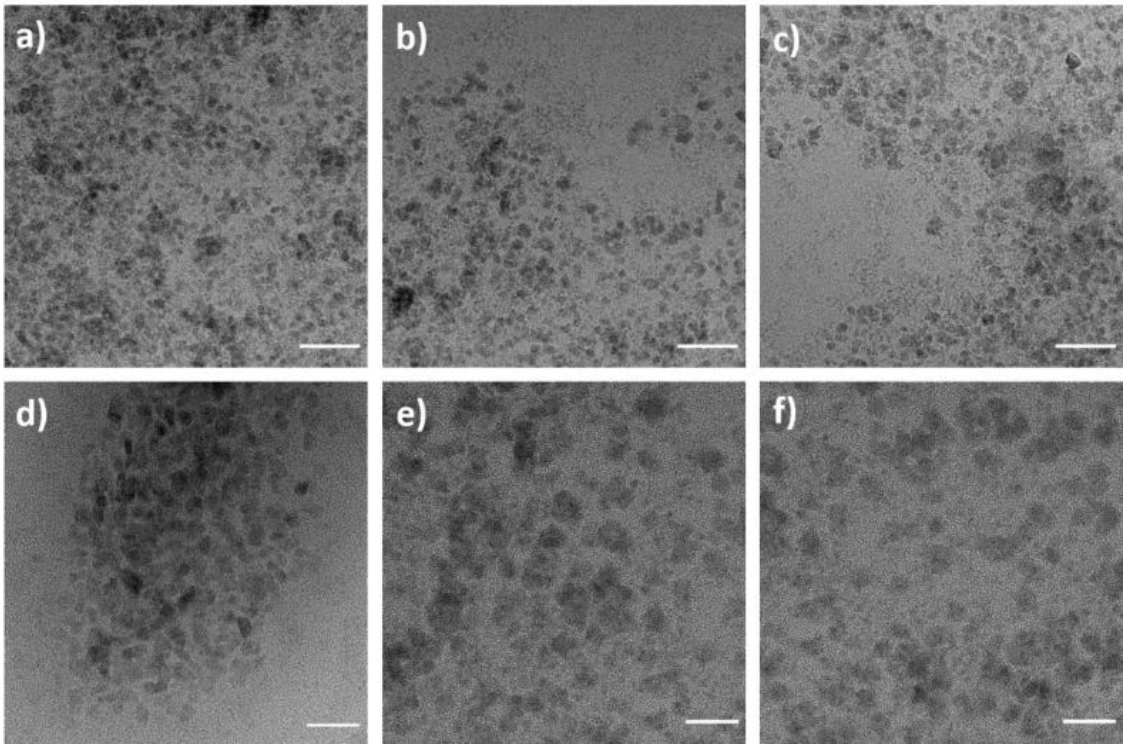

Figure A1: TEM images of L-CDs. a)-c): scale bar 50 nm; d)-f): scale bar 20 nm.

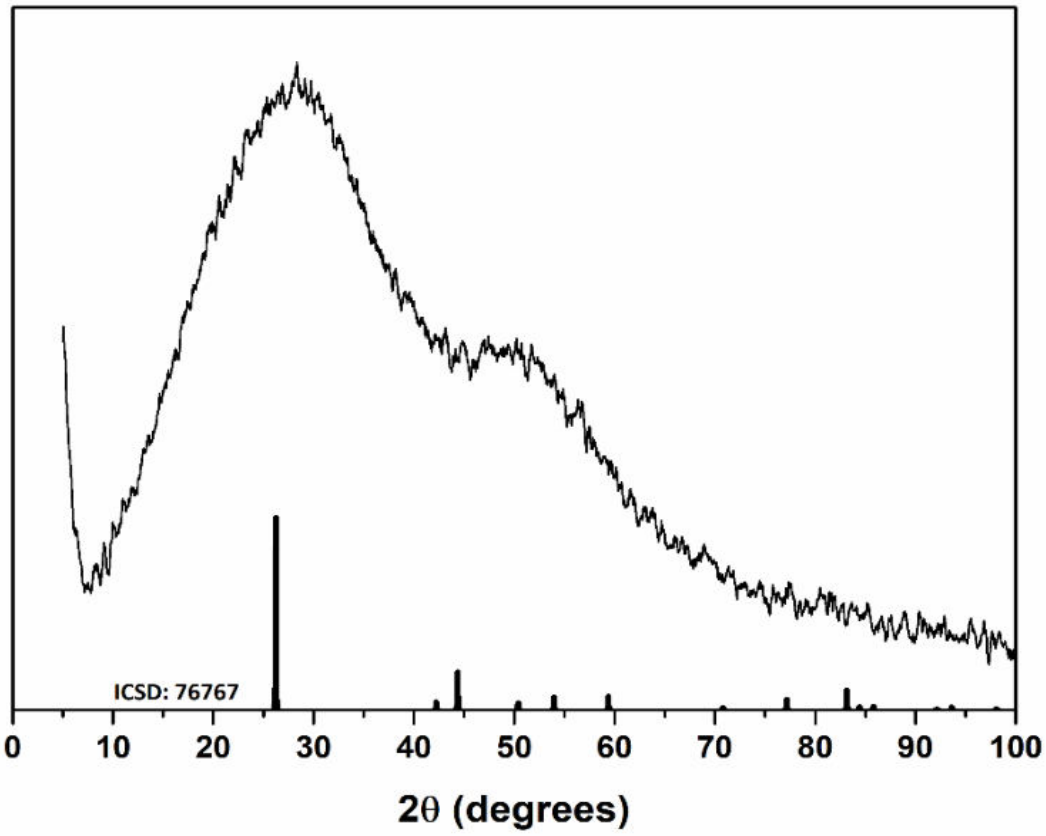

Figure A2: X-Ray Powder Diffraction pattern for L-CDs and reference pattern for graphite (ICSD: 76767).

Photoluminescence Quantum Yield Determination:

Equation A1[98,99]

$$\Phi_{QDs} = \Phi_{st} \frac{I_{QDs} f_{st} n_{QDs}^2}{I_{st} f_{QDs} n_{st}^2}$$

The subscripts *QDs* and *st* refer to the quantum dots or the fluorescence standard respectively. The PLQY is represented by *Φ*, *I* represent the integrated intensity corrected by the fluorimeter sensitivity and the source intensity, *n* represents the diffraction index of the solvent and *f* the absorption factor

Equation A2[98,99]

$$f_{QDs,st} = 1 - 10\text{^}(-A_{QDs,st})$$

Where *f* and *A* represent the absorption factor and the absorbance for quantum dots (*QDs*) and fluorescence standard (*st)*.

By-Products: isolation and characterisation: This fraction, that correspond to about 10 % of the mass of the product, is composed by micrometrical carbon structures with broad distribution of sizes and shapes (see SEM micrographs of **Fig A3**). As described in the main text, this fraction can be isolated by precipitation at acidic pH and it is easily removed by centrifugation and collected as a powder after vacuum distillation at room temperature. Sample suitable for the UV/Vis, PL and CD characterisation can be prepared by dispersion of the powder in deionized water after the addition of NaOH 0.2 M solution to neutralize the pH (see experimental section). The PL behaviour of the by-product (**Fig. A4**) resembles the **L-CDs** one, the most intense emission is observed in the 375 – 500 nm range and the emission wavelength is strongly affected by the excitation wavelength. As shown in **Fig. 12f**, this fraction does not present any circular dichroism activity, feature that can be related to a high degree of decomposition (see main text).

Considering all these findings, we can conclude that the by-product fraction is produced by an extended carbonization of the organic substrate that strongly reduce its optical chirality. The EDS analysis (**Fig. A5**) of the by-product reveals the average composition ($\%_{at}$): C 24.48, N 7.94, O 5.33, Na 0.59, S 25.80, Cl 2.44, Cu 33.42. In contrast with **L-CDs**, this fraction is rich of copper and sulfur and poor in carbon and oxygen. Considering the copper concentration added in the reaction mixture, and the amount of the by-product collected, the copper mass present

in the by-product could be estimated close to the total amount of copper added during the synthesis. Evidence that confirms the absence of copper in the carbon dots as observed by energy dispersive X-ray spectrometry EDS (**Fig. A5**) and XPS. The FTIR analysis **Fig A6** allows to investigate the functional group that are present in this fraction: the wide band in the range 3500 -2500 cm^{-1} is ascribed to υ_{O-H} of carboxylic acids, the strong band between 1700 and 1550 cm^{-1} is ascribed to υ_{CO} of carboxylic acid and amides that overlaps the amide II band at 1590 cm^{-1}. The band at 1470 cm^{-1} is related to $\upsilon_{C=C}$ in the graphitic structures and the sharp peak at 1375 cm^{-1} is related to $\upsilon_{CN.}$ Finally, intense bands at 1180 and 1030 cm^{-1} are ascribed to υ_{-SO3-} suggesting the presence of sulfonic acids.

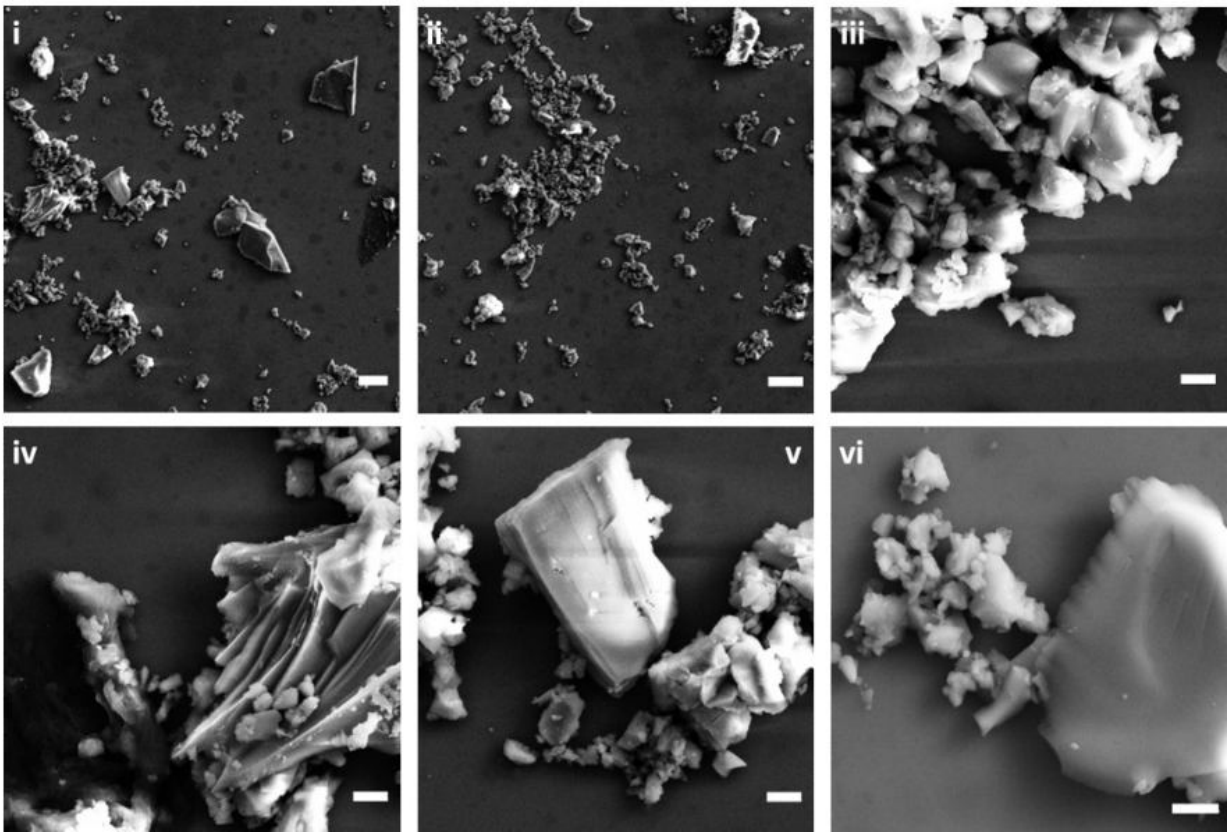

Figure A3: SEM images showing the by-product morphology. The scale bars in the figure corresponds to: i, ii: 10 µm; iii-vi: 2 µm.

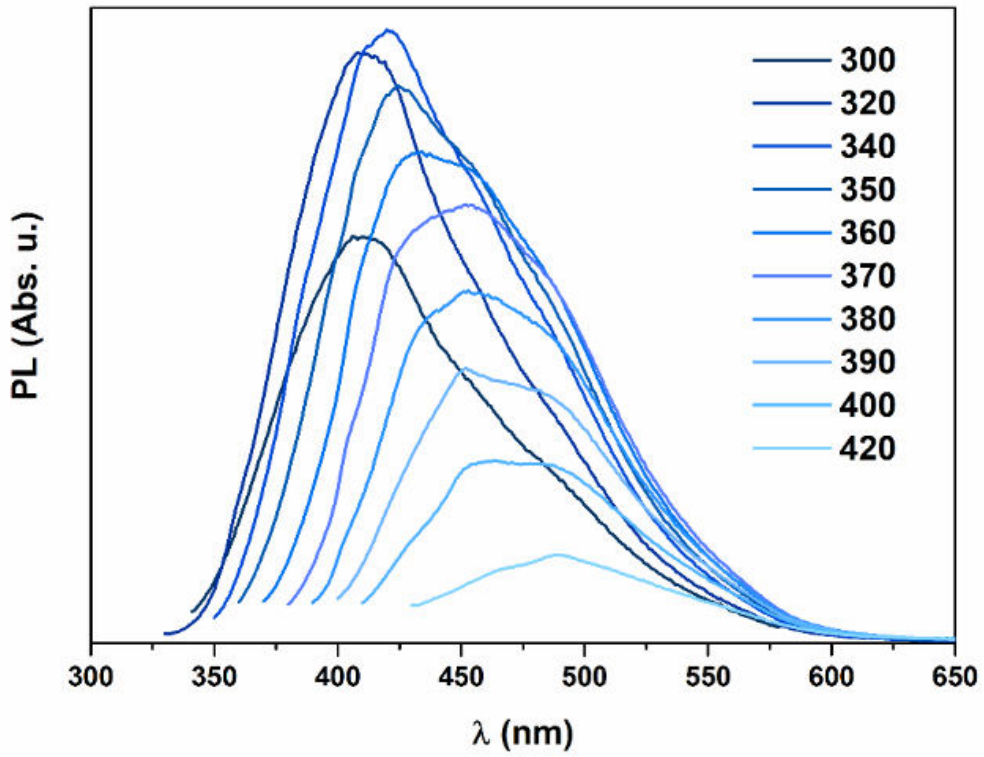

Figure A4: PL spectra of the by-product excited with radiations at different excitation wavelengths (in nm)

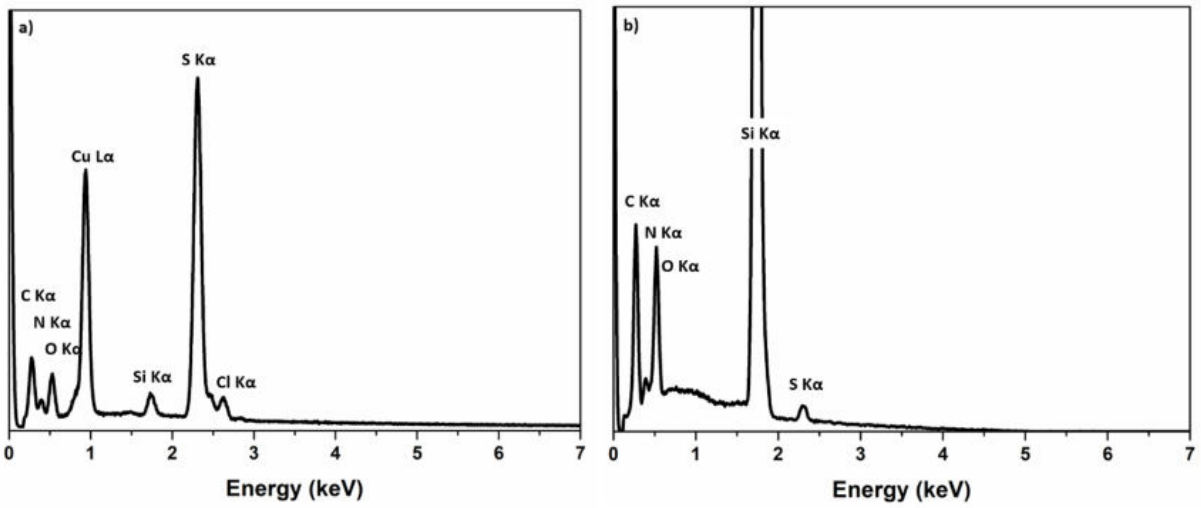

Figure A5: EDS analysis of the by-product (left) and **L-CDs** (right).

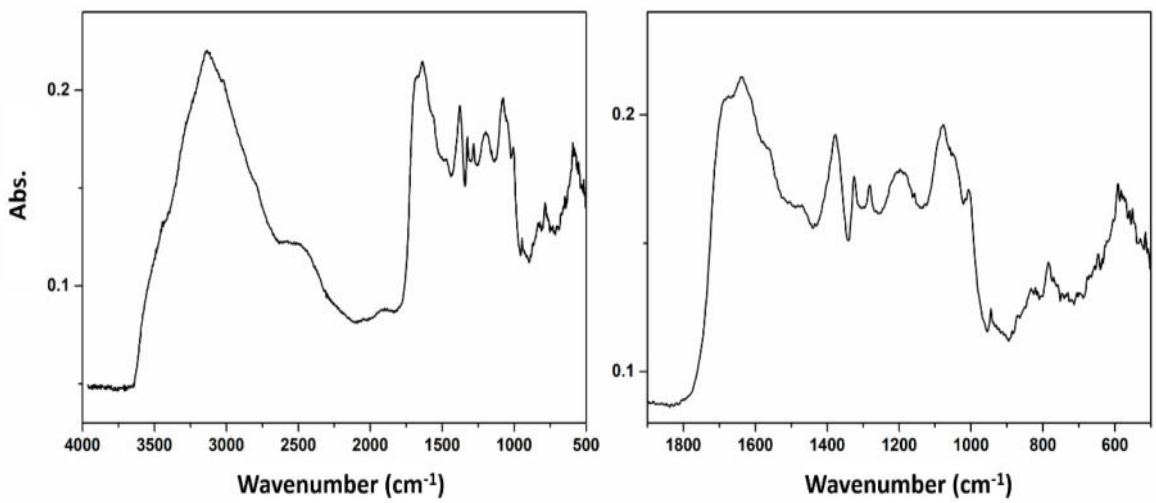

Figure A6: FTIR analysis of the by-product, in the 4000 – 500 cm^{-1} range (left) and detail of the 1800 – 500 cm^{-1} range (right).

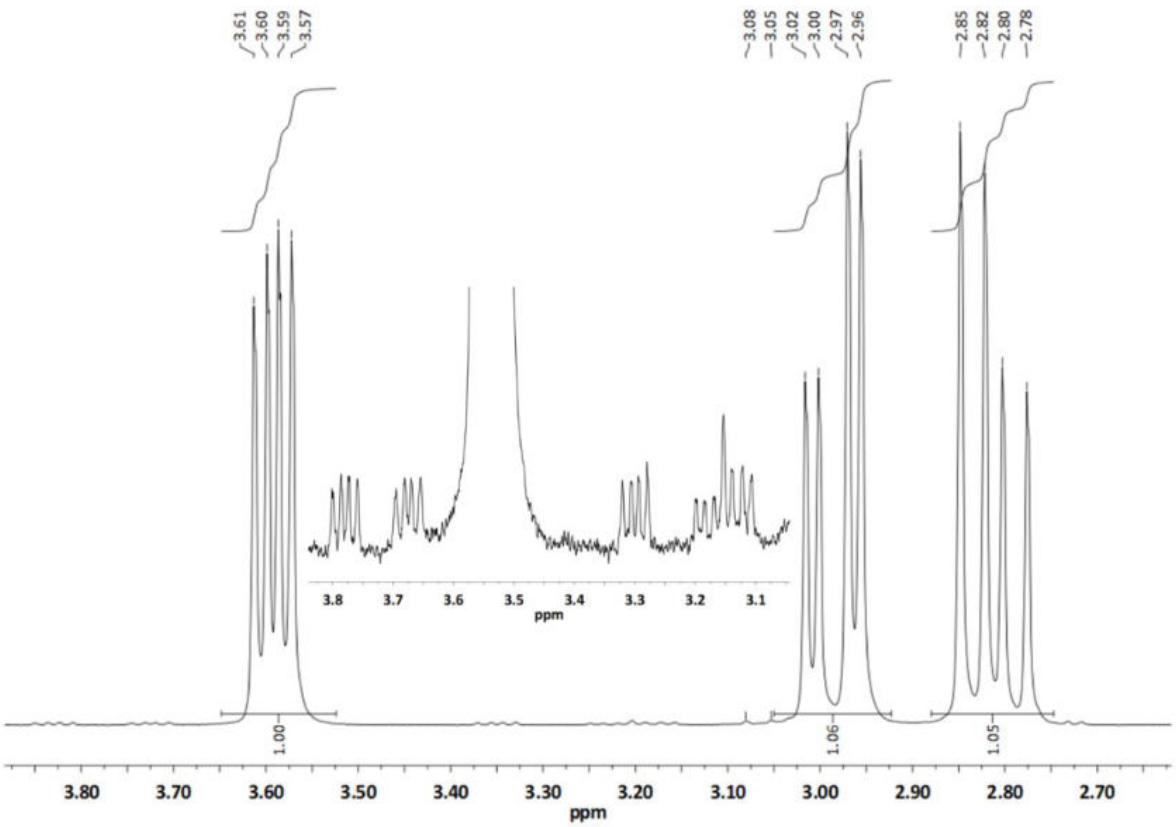

Figure A7. ^{1}H-NMR analysis of L-Cysteine in D_2O pH = 10.5. The signals from cystine protons are evidenced in the inset.

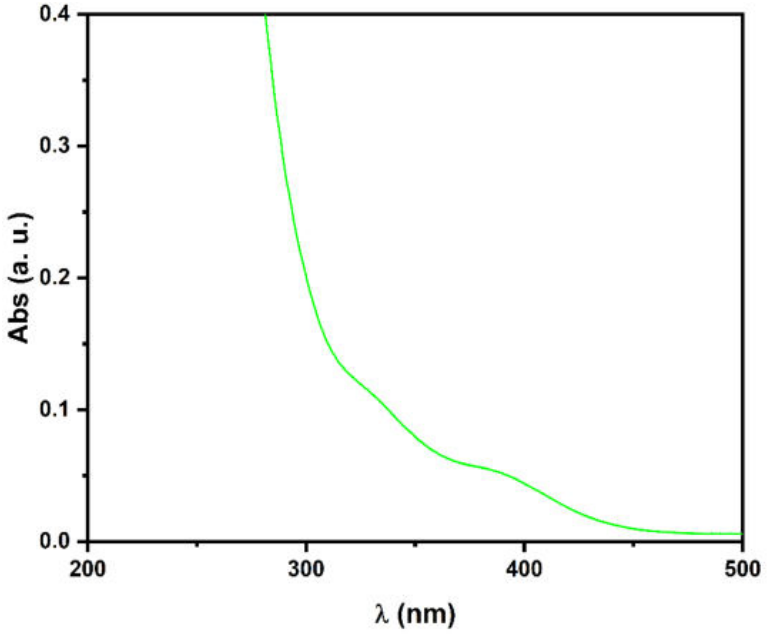

Figure A8: detail of the UV/Vis spectrum of the reaction mixture in the presence of cysteamine after a reaction time of 10 min

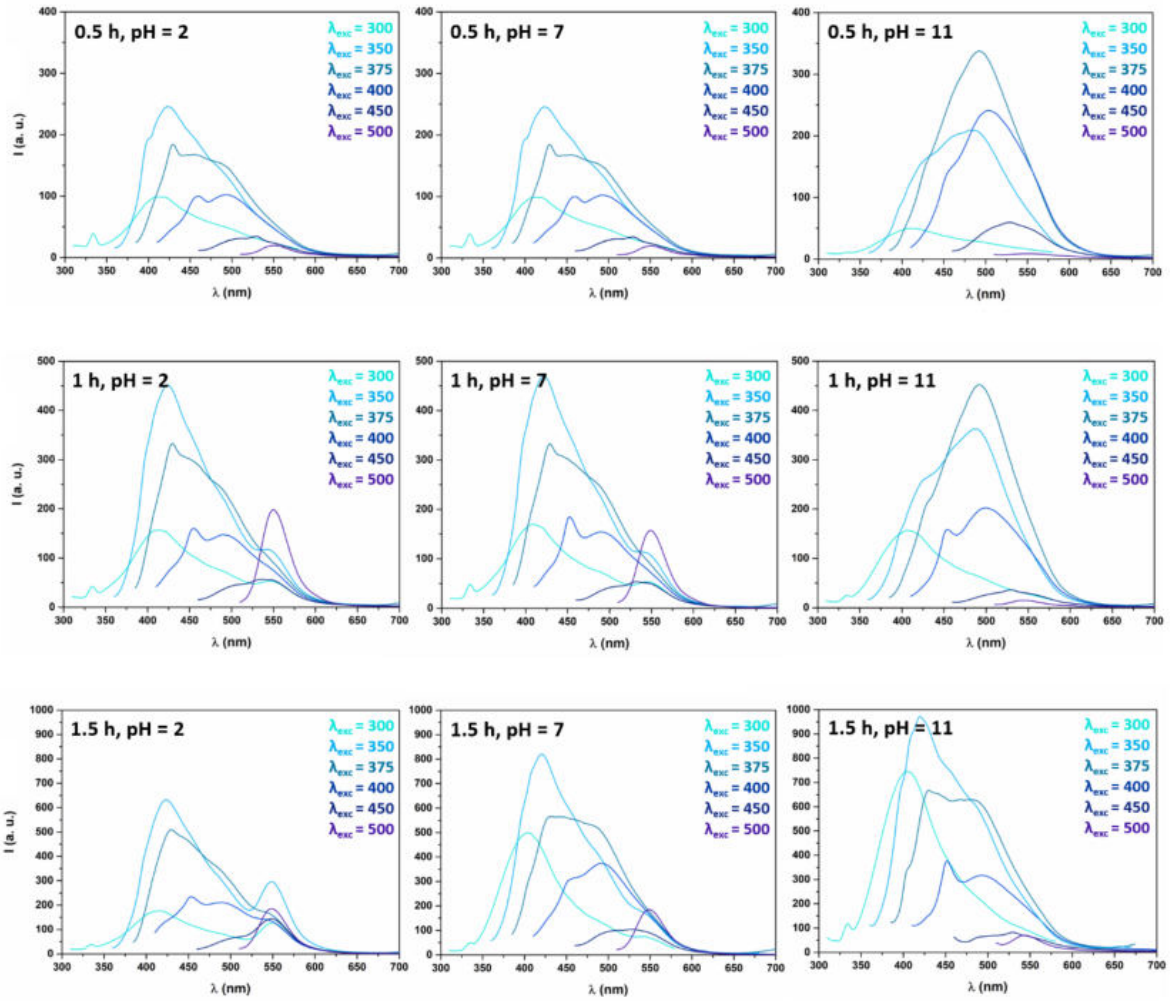

Figure A9: PL analyses of the sample collected at 30 min, 1 h and 1.5 h. The different pH valued and excitation wavelength λ_{exc} during the measurement are reported in the graphs

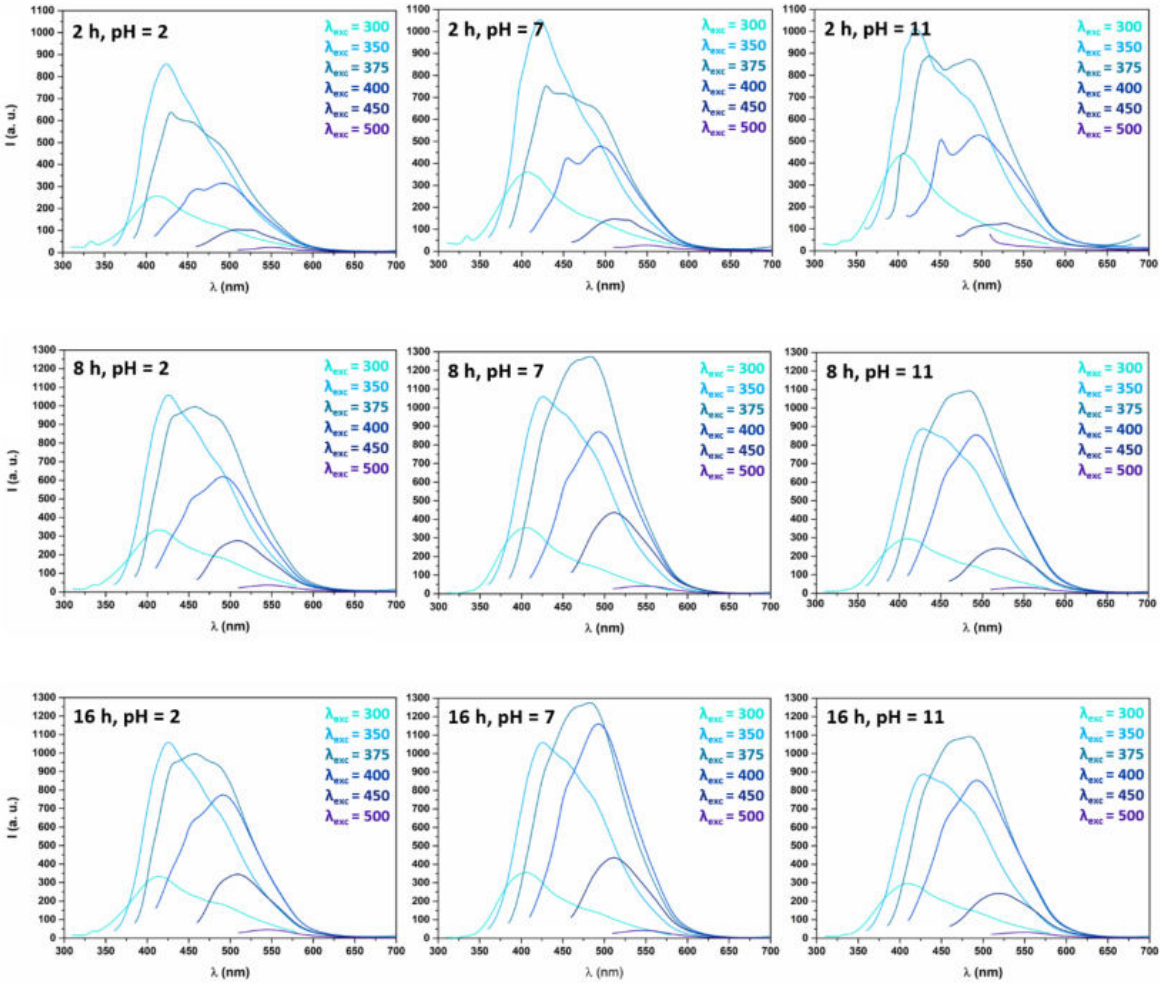

Figure A10: PL analyses of the sample collected at 2h, 8 h and 16 h. The different pH valued and excitation wavelength λ_{exc} during the measurement are reported in the graphs

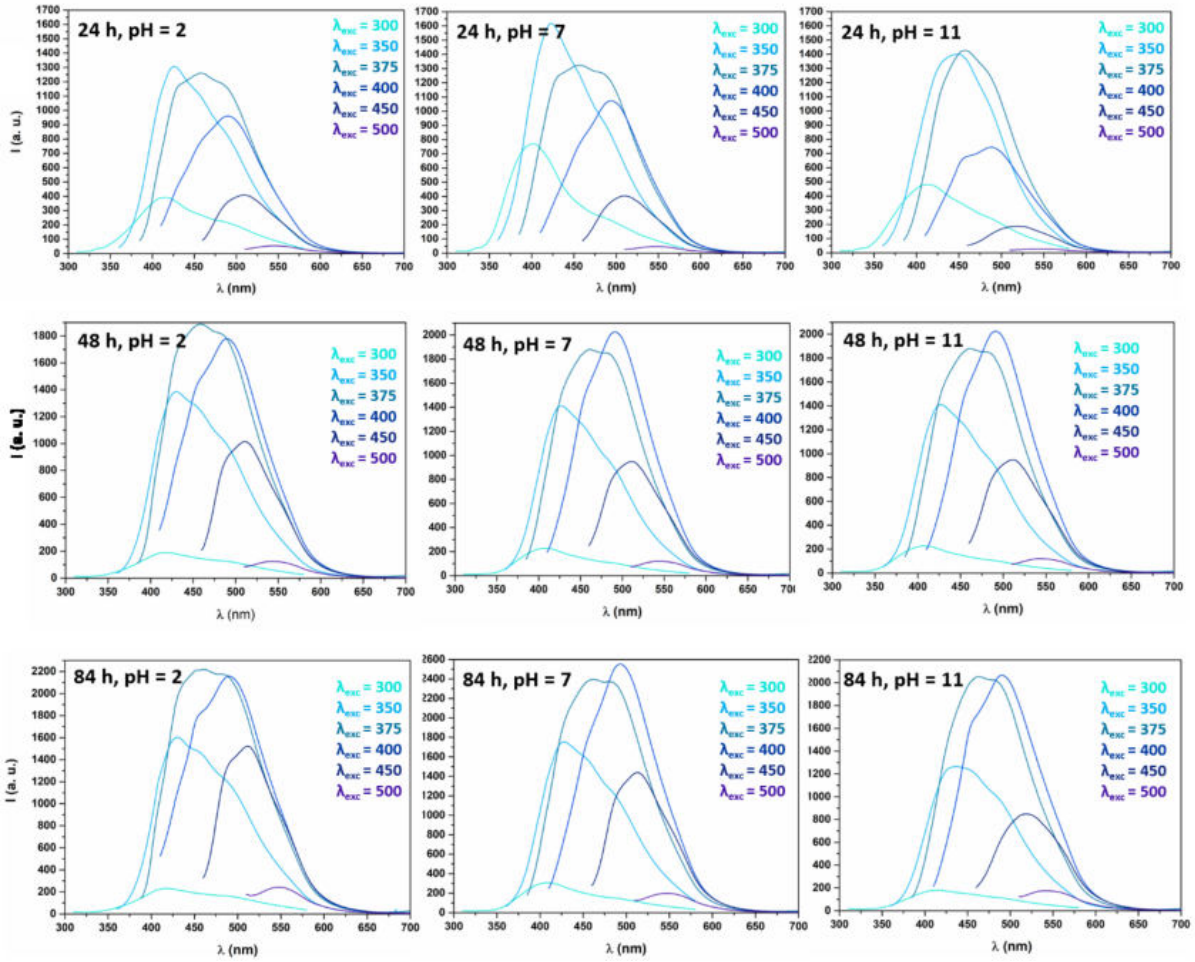

Figure A11: PL analyses of the sample collected at 24 h, 48 h and 84 h. The different pH valued and excitation wavelength λ_{exc} during the measurement are reported in the graphs

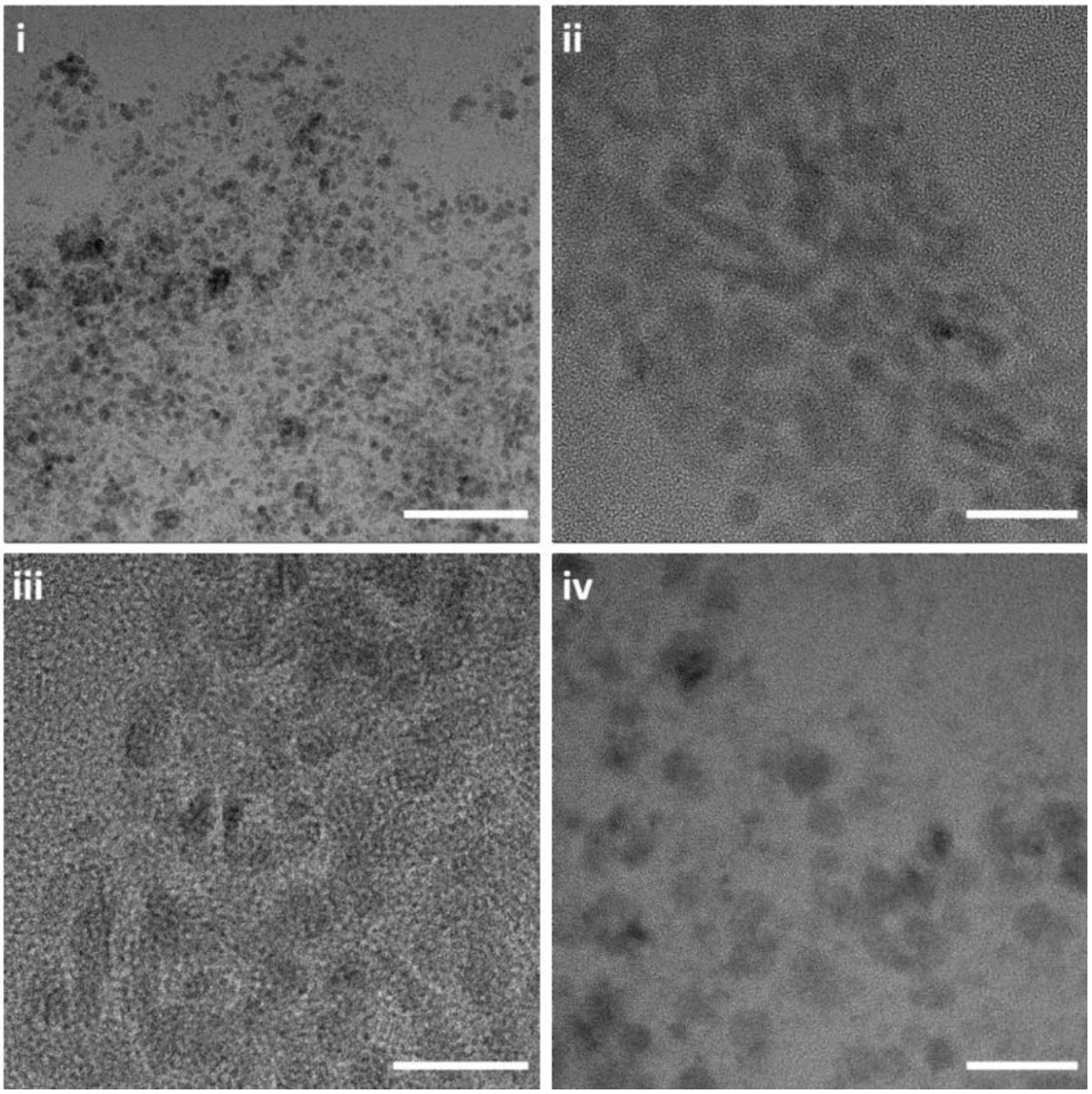

Figure A12. TEM images of the **L-CDs** sample isolated after a reaction time of 2 h. The scale bars in the figures correspond to: (i) 100 nm; (ii)-(iv) 20 nm.

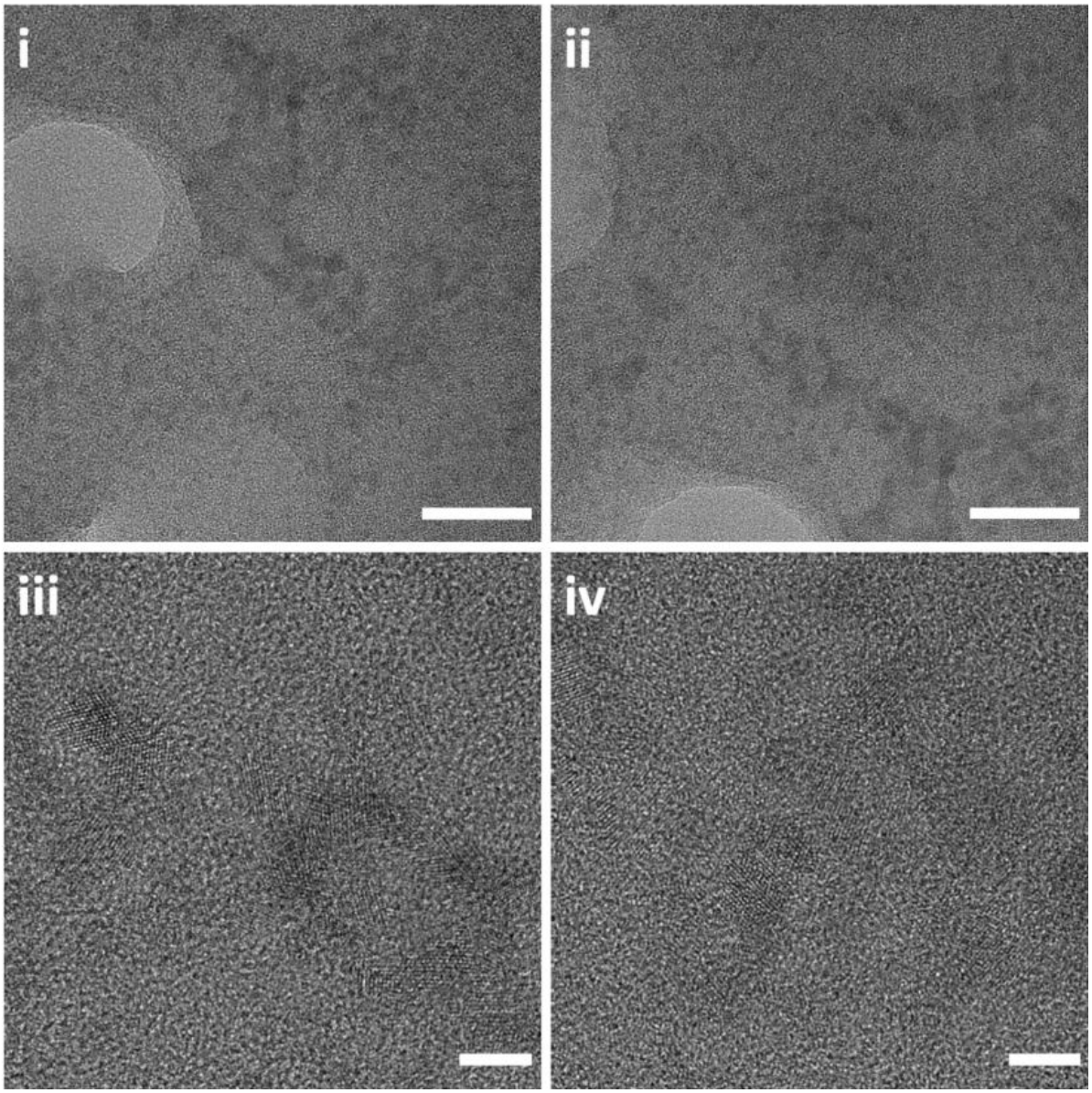

Figure A13. TEM images of the **L-CDs** sample isolated after a reaction time of 48 h. The scale bars in the figures correspond to (i),(ii) 20 nm, (iii) and (iv) 5 nm.

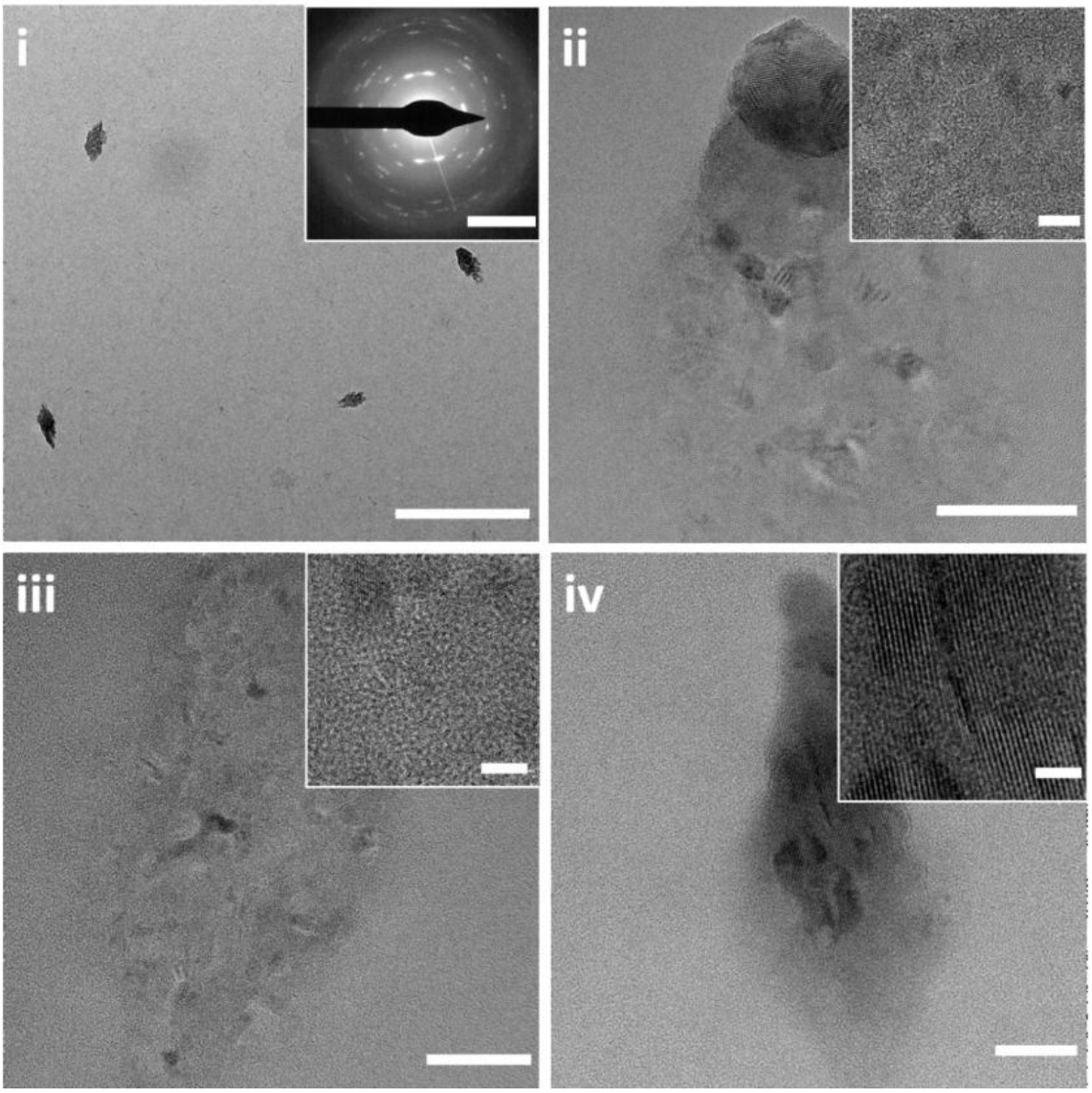

Figure A14. TEM images of the **L-CDs** sample isolated after a reaction time of 84 h. The scale bars in the figures correspond to: (i) 500 nm, (i, inset) 5 nm^{-1}; (ii)-(iv) 20 nm, (ii, inset)-(iv, inset) 5 nm.

CHAPTER III

CHIRAL TERNARY AND QUATERNARY QUANTUM DOTS

This chapter is devoted to the investigation of the production of novel chiral I-III-VI quantum dots (QDs): silver and copper indium sulfides QDs. Due to their optical properties and their biocompatibility these systems are a promising alternative to Cd-based binary systems. Despite the large number of papers that describe the chiroptical activity of binary QDs, the chirality in I-III-VI QDs is still unexplored.

The chapter starts with a brief introduction related to the general concept of quantum confinement in semiconductor nanocrystals discussing the model proposed by Luis Brus (1984) to describe the effect of the size on the electronic properties of semiconductors. Then, some considerations related to the synthesis of semiconductor quantum dots colloidal solutions are presented. Particular attention is paid to the characteristic properties of I-III-VI QDs considering some relevant examples related to the interpretation of the optical properties of semiconductors of the silver copper and indium sulfide family. Finally, the chirality in quantum dots is discussed considering both the synthesis and the origin of the chirality.

The research reported in the Result and Discussion section can be summarized in 5 items: i) synthesis and characterisation of AIS14 QDs, a system investigated in detail and used for the optimization of the synthesis and further post treatments, ii) investigation on the origin of chirality by the analysis of the chemistry at the particle-ligand interface, iii) post synthesis treatments for the deposition of a ZnS shell to improve the optical properties, iv) a compositional study considering the effect of the variation of Ag/In, Cu/In and Ag/Cu ratios on the structure, on the optical and on the chiroptical properties of the QDs, v) some preliminary analysis on the QDs formation mechanism, and on the role of nanoclusters in the process.

ACRONYMS

QDs: quantum dots

PL: photoluminescence

PLQY: photoluminescence quantum yield

FWHM: full width at half maximum

AIS: silver indium sulfide

CIS: copper indium sulfide

CIGS: copper indium gallium sulfide

CZTS: copper indium tin sulfide

CIZS: copper indium zinc sulfide

AIZS: silver indium zinc sulfide

CD: circular dichroism

BE: binding energy

RM: reaction mixture

NCs: nanoclusters

CONTENTS

1 INTRODUCTION

Semiconductor nanocrystal characterised by an effect of the crystal size on the electronic properties are known as Quantum Dots (QDs). Since the first investigations, the effect of the crystal size on the energy required for the generation of the exciton, on the electron affinity and on the ionisation potential was clearly evidenced.[1,2] This behaviour is characteristic of semiconductor nanocrystals whose dimensions are comparable with the Bohr radius of their exciton, a condition usually satisfied in the size range between one and ten nanometers.

The first theories on the effect of the size on the electronic structure of semiconductors can be found in the extensive works by Alexei Ekimov and Alexander Efros, who studied the optical properties of nanocrystals embedded in glass matrix, and by Luis Brus who focused his attention on colloidal nanocrystals.

With their work, Ekimov and Efros, clarified the origin of various colours in semiconductor-activated glasses.[3] To prove the relationship between the optical properties of the glasses and the morphology of the embedded nanocrystals, they investigated several glasses activated by a single compound (CuCl, CuBr, CdSe and CdS).[4] By controlling the conditions of the thermal treatments, the authors were able to modulate the ions diffusion in the glass matrix and to control the final size and size distribution of the nanocrystals. Concerning the optical properties, the study on the absorption of CuCl activated glasses showed a characteristic blue shift of the two excitonic transition for nanocrystal size reduced from 31 to 2 nm (**Fig. 1a**).

The investigation from Brus and his group started by the accidental observation of the variation of the absorption of a CdS colloid.[3] The freshly prepared nanocrystals dispersion showed a blue-shifted absorption with respect to the typical absorption, expected for the bulk semiconductor, shown by the aged solution. The nanocrystals size was increased from 4.5 nm to 12.5 nm by moving from the fresh solution to the aged one. This observation stimulated Brus to formulate his theory based on effective masses and dielectric polarization to describe the nanocrystal size effect on the electronic properties of semiconductors.[1,2] Further observations on other semiconductors (ZnS, ZnSe, PbS, CdSe and silver halides) nanocrystals with different

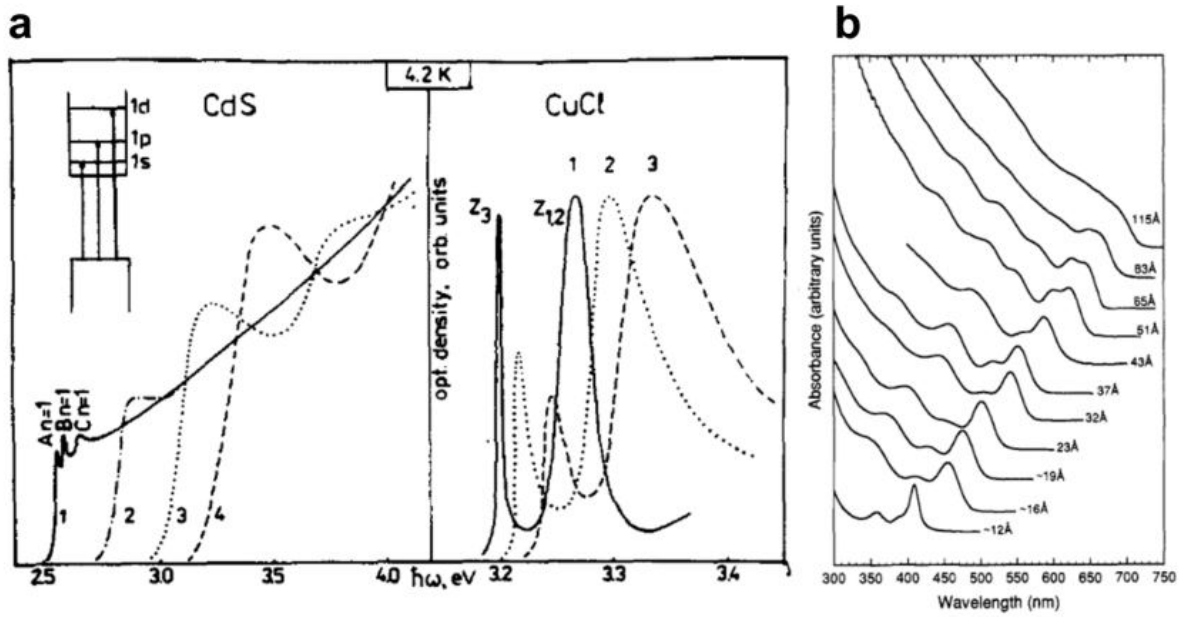

Figure 1: effect of the size in a) CdS and CuCl nanocrystals embedded in glass matrix from Ekimov et al.4 b) CdSe colloidal solutions form Murray and coworkers.11

sizes confirmed the initial findings.[5–7] Beyond theoretical investigations, several efforts were invested to design novel synthetic methods to promote the formation of high-quality nanocrystals with narrow size distributions. All these nanosystems allowed the experimental observation of the relative optical trends.

The synthesis by an inverse micelle solution allowed to control the nanocrystal growth thanks to the structural confinements of the soft template. With this method it was possible to prepare CdSe nanocrystals (but also HgTe and CdTe) with different sizes related to the water/surfactant ratio and to the amount of the inorganic precursors.[8] After that, Henglein et al. [9] synthetised core shell systems such as CdSe/ZnS and ZnS/CdSe analysing the effect of the inorganic passivation of the nanocrystal surface on the Photoluminescence Quantum Yield (PLQY). Successive observations were reported on the increase of the degree of crystallinity of CdSe nanocrystals after refluxing in organic solvents, such as: pyridine, 4-ethylpyridene and tributylphosphine.[10] The synthesis of nanocrystals with higher quality was achieved by using a partially oxidized tributylphosphine instead of a fresh batch, suggesting a particular role of the tributylphosphine oxide in the nanocrystal stabilisation. In 1993 Murray et al.[11] reported one of the first example of hot-injection method for the synthesis of highly monodisperse Cd chalcogenide nanocrystals. The method was based on rapid injection of the inorganic precursors in the reaction mixture at high temperature and in the presence of

trioctylphosphine/trioctylphosphine oxide mixture (**Fig. 1b**). A further reduction of the size distribution was obtained by a size selective precipitation.[12]

The successful separation of fractions of nanocrystals with narrow size distributions, both embedded in glass matrix and in colloidal solutions, highlighted the effect of the particles dimension on the optical properties in detail, providing experimental evidence on the quantum confinement effect.

1.1 QUANTUM CONFINEMENT IN SEMICONDUCTOR NANOCRYSTALS

The variation of the electronical properties of semiconductor nanocrystals with the size, in a range between molecular clusters and bulk-like particles, is particularly interesting, both for basic science and for technological applications. It is important to consider the boundaries of this size regime. The lower limit is restricted by the relevant structural rearrangement observed in molecular clusters composed by 10 -100 atoms. In this size range the cluster structure differs significantly from the bulk structure. On the upper limit, the effect on the electronical properties is lost when the size of the particles is much larger than the Bohr radius of the corresponding exciton; this condition is characteristic of bulk-like particles. The effect of the nanocrystal size on the energy required to generate an exciton in a semiconductor nanocrystal was analysed by Louis Brus[2] using an effective masses and dielectric polarisation theory. This approach describes the variation of the electronical properties of small size semiconductor nanocrystals starting from the well-known properties of their respective bulk forms. Introducing the appropriate approximations: i) the potential outside the particles is infinite, ii) the particle is treated as a uniform medium and iii) electron and hole are described according to hyperbolic potentials functions, the system can be approximated to the problem of the particle in a box.[13] In the case of a spherical particle with radius *R*, the Hamiltonian that describe the interaction with the electromagnetic radiation to generate the exciton is reported in **Eq. 1**:

Eq. 1

$$H(\boldsymbol{S_e}, \boldsymbol{S_h}) = -\frac{h^2}{8\pi^2 m_e}\nabla_e^2 - \frac{h^2}{8\pi^2 m_h}\nabla_h^2 + \frac{e^2}{4\pi\varepsilon_i\varepsilon_0 \mid \boldsymbol{S_e} - \boldsymbol{S_h} \mid} + Vpol$$

Where $\boldsymbol{S_e}$ and $\boldsymbol{S_h}$ are vectors that describe the position of electron and hole inside the particle. *h* is the Planck constant, m_e and m_h represent the effective mass for electron and hole and ε_i and ε_0 are the dielectric permittivity of the semiconductor and vacuum. **Eq. 1** is composed by two kinetic terms, the first related to the electron and the second to the hole, a coulombic potential term and a polarisation term (V_{pol}). The last term, related to the polarisation of the semiconductor nanocrystal and of the surrounding dielectric medium, can be written as reported in **Eq. 2** and **Eq. 3**:

Eq. 2

$$V_{pol} = \frac{e^2}{2}\sum_{k=1}^{\infty}\alpha_k \frac{\boldsymbol{S_e^{2k}} + \boldsymbol{S_h^{2k}}}{R^{2k+1}}$$

Eq. 3

$$\alpha_k = \frac{(\varepsilon-1)(k+1)}{4\pi\varepsilon_i(\varepsilon k + k + 1)}\ ;\ \varepsilon = \frac{\varepsilon_i}{\varepsilon_0}$$

The wavefunction of the exciton quasiparticle can be described as the product of individual wavefunctions (**Eq. 4** and **Eq. 5**) that describe electron and hole.

Eq. 4

$$\psi_i(S_i) = \frac{1}{\boldsymbol{S_i}\sqrt{2\pi R}}\sin\left(\frac{n\pi \boldsymbol{S_i}}{R}\right)$$

Eq. 5

$$\phi_{ex} = \psi_e(S_e)\psi_h(S_h)$$

Using these approximations, it is possible to solve the time independent Schrödinger equation and to find the energy required to generate the exciton E_{ex} in the confined system (**Eq .6)**. The energy of the observed optical transition can be evaluated by **Eq. 7** considering the shift with respect to the band-gap value of the bulk semiconductor E_g.

Eq. 6

$$E_{ex} = \frac{h^2}{8R^2}\left(\frac{1}{m_e} + \frac{1}{m_h}\right) - \frac{1.8e^2}{4\epsilon R} + pol.cont.$$

Eq. 7

$$E_{tr} = E_g + E_{ex}$$

Considering the kinetic term, which is the main contribution for several semiconductor nanocrystals, this solution shows a size dependence of E_{tr} with R^{-2}. Other minor contributions from the coulombic and polarisation terms depend on R^{-1} and are especially important in the case of large band gap semiconductors. In **Fig. 2** are reported the predicted energy of the lowest exited state by L. Brus[2]. ZnO and CdS are the systems which show larger band-gap values and a higher contribution due to the coulombic term than GaAs and InSb (**Fig. 2 right**). Due to multiple reasons at small *R* the model fails to describe the experimental findings and the effective mass approximation is no longer valid for substantial kinetic energies (this region is reported with dashed line).

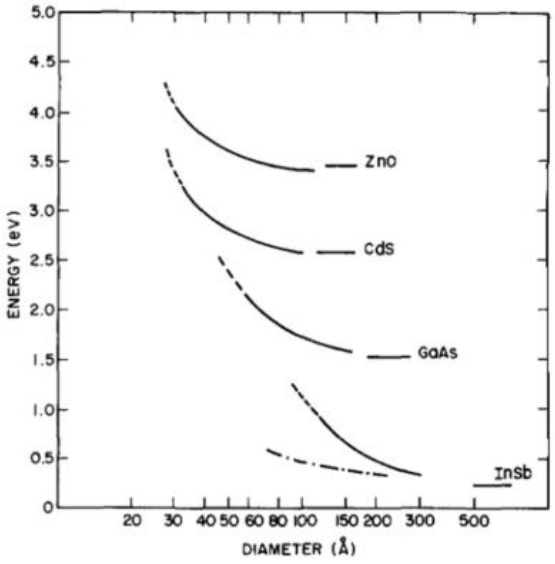

	E_g(0 K) (eV)	m_e^*	m_h^*	ϵ
InSb	0.24	0.015	0.39	15.6
GaAs	1.52	0.07	0.68	10.9
CdS	2.58	0.19	0.8	5.7
ZnO	3.44	0.24	0.45	3.7

	ZnO	CdS	GaAs	InSb
Kinetic	0.27	0.27	≃ 0.65	> 1
Coulomb	− 0.24	− 0.15	− 0.08	− 0.06
Polarization	0.06	0.05	0.03	0.02
Total Shift	0.09	0.17	≃ 0.60	> 1

Figure 2: (left) predicted variation of the energy gap according to the nanocrystals size for different semiconductors (right) value used for the calculation of the nanocrystals properties and the different contribution to the total shift. Data and figure reproduced from L. Brus.[2]

1.2 COLLOIDAL QUANTUM DOTS SYNTHESIS

The synthesis used for the preparation of semiconductor QDs colloidal solutions can be divided in two different routes, the organic and aqueous ones. The first is usually performed in high-boiling point solvents where inorganic and organometallic precursors react at high tem-

peratures to form highly crystalline nanoparticles. The second one exploits the aqueous chemistry of small organic ligands and their interaction with the metals modulated by the pH, to control the precipitation of the inorganic phase at lower temperatures.

1.2.1 Organic synthesis

Organic synthesis is usually performed in high-boiling point solvent where inorganic and organometallic precursors react at high temperatures to gives highly crystalline nanoparticles. Long chain ligands are used to control the crystal growth and the colloidal stability of the QDs. Among the organic synthesis we can distinguish between Hot-injection and heat-up methods:

- Hot-Injection: in the seminal work by Murrey et al.[11] that inspired this method, a precursor solution containing dimethyl cadmium and try-n-octylphosphine selenide in try-n-octylphosphine was prepared in a syringe. The solution was then rapidly injected in try-n-octylphosphine oxide at 300 °C, and before the injection the heating source is removed from the reaction vessel. This condition guaranteed a rapid bust of the heterogeneous nucleation, and further nucleation events were prevented due to a rapid temperature drop (after the injection the temperature of the reaction decreased to ≈ 180 °C) caused by the injection of the solution at room temperature. After the nucleation step, the temperature was gradually raised to 230 – 260 °C to favourite the particle growth. During this phase, the size and size distribution of the QDs was monitored by UV/Vis absorption spectroscopy considering the position and Full Width at Half Maximum (FWHM) of the excitonic transition. Subsequently, the heating was adjusted according to the observed variations. Since along with the increasing of the QDs size, the temperature required to maintain a constant growth increases, the temperature was raised to promote the QDs growth and was reduced when a spreading of the absorption band was observed. By this method, it was possible to collect several fractions at different growth stages, characterised by different sizes and with a size distribution around 10 %. Finally, the size distribution was further reduced down to 5 % by a post synthesis size selective precipitation step. The authors also isolated the chalcogenide series CdS and CdTe using as chalcogenide sources bis(trimethylsilyl)sulfide and bis(tert-butyldimethylsilyl)telluride.

Peng et al.[14,15] investigated other synthetic routes based on the hot-injection approach exploring less toxic cadmium sources to replace dimethyl cadmium. They observed that high quality CdSe QDs could be prepared using CdO, $CdCO_3$ or $Cd(OAc)_2$ in mixture with fatty acids (e. g.: stearic acid) or phosphonic acid (e.g. hexylphosphonic acid) in mixture with try-n-octylphosphine oxide as cosolvent.

- Heat-up: also called non-injection method is a popular approach since it prevents some detrimental issues that affect the hot-injection method (e.g.: the inhomogeneous mixing during the injection step), the compatibility with scale-up and the higher reproducibility are other promising features of this method. Using this approach, the precursors are dispersed in a mixture with the solvent and cosolvent at room temperature. Then, the temperature is raised up using specific thermal ramps. During this step, several chemical reactions convert the precursors, or the complexes formed in the reaction mixture, forming the monomers involved in the nanocrystals nucleation. Due to the difficulty to separate the nucleation by the growth steps, these methods were initially considered unadapt for the production of monodisperse colloids. However, as shown by many examples, a fine selection of the reaction conditions (especially considering the reactivity of the precursors) allows to isolate high-quality QDs with size distribution comparable with the hot-injection method.[16] Chen et al used this method to prepare high-quality CdSe QDs.[17]. The authors used cadmium myristate and selenium oxide in 1-octadecene by a thermal treatment up to 240 °C using a ramp of 25 °C/min. This approach is also quite common for the preparation of ternary QDs. Several examples are available in the literature for the synthesis of $CuInS_2$ QDs by the decomposition of 1-dodecanthiole in 1-octadecene at temperature around 240 °C.[18–21]

1.2.2 Aqueous synthesis

In the aqueous processes, the QDs are formed at lower temperatures, and they are stabilised by small organic ligands or inorganic species by electrostatic repulsions, instead of steric interactions characteristic of QDs prepared in organic media. The role of pH is particularly critical since it affects the coordination chemistry of the organic ligands, as well as the availability of the inorganic precursors such as: protonation equilibria of chalcogenides and precipitation of metal hydroxide with low solubility. In contrast to the reaction performed in organic media, the aqueous syntheses are characterised by a faster reduction of the monomer concentration. The concentration drop lowers the monomer concentration down to the solubility product,

preventing further growth step via diffusion process (characteristic feature of the hot-injection methods). The particles growth is dominated by Oswald ripening process that is often related to an increasing of the size distribution.[22]

Henglein's et al.[23] developed the first example of aqueous synthesis to prepare colloidal QDs solutions. In a typical synthesis of CdS QDs, $Cd(ClO_4)_2$ is solubilised in deoxygenated water in the presence of sodium hexametaphosphate that binds the metal, prevents the hydroxide formation (reaction pH 9.6 – 7.5) and stabilises the nanoparticles. The QDs formation is triggered by the injection of H_2S gas as sulfide source at room temperature and a second treatment at 80°C was employed to complete the nanocrystals growth. Other semiconductor nanoparticles such as ZnS,[24] Cd_3As_2,[25] CdTe[26] and ZnTe[26] were prepared with similar approaches.

Rajh et al. [27] reported the first use of thiols for the stabilisation of colloidal QDs. They investigated the formation of CdTe QDs in the presence of a sodium hexametaphosphate and 3-mercapto-1,2-propandiol. In the paper, they investigated the role of cadmium thiolate as intermediate species in the QDs formation. Moreover, they evidenced the role of the thiol ligand for the passivation of the QDs with an increasing of their PLQY with respect to the polyphosphate stabilised QDs. After this paper, the use of other thiols has been investigated.[28,29]

Gao and coworkers [28,30] obtained a further improvement on the optical properties of chalcogenide colloidal solutions using thioglycolic acid as stabilisers to produce CdTe QDs. Their works are the firsts examples of the very popular mercapto acid route. This method relies on the use of bidentate ligands, characterised by the presence of a thiol and carboxylic acid groups (e.g.: thioglycolic acid, mercaptopropionic acid and glutathione), to stabilise chalcogenide QDs in aqueous solutions. The copresence of the thiol and carboxylic groups guarantees a strong binding on the particle surface mediated by the thiolate group, and the electrostatic stabilisation in alkaline pH due to the deprotonation of the carboxylic group.[31]

The mercapto acid route was extended to the preparation of a wide range of semiconductors nanocrystals such as: PbS,[32] PbSe,[33] HgTe,[34] Ag_2S[35], $CuInS_2$[36–38] and $AgInS_2$.[39–41]

Even though the aqueous methods are usually related to a lower quality of the QDs in terms of crystallinity, size distributions and optical properties, many improvements of the synthesis and of the post synthetic treatment have allowed to produce QDs with comparable properties with the respective organic counterparts. Moreover, the aqueous synthesis guarantees higher biocompatibility, easier modification of the particle surface with bioactive molecules and,

thanks to the small size of the organic ligand used in the electrostatic stabilisation of colloids, even a better compatibility for the formation of heterojunctions.[22]

1.3 TERNARY AND QUATERNARY I-III-VI QUANTUM DOTS: silver and copper indium sulfides

Silver and copper indium sulfides are promising systems that are part of the group of I-III-VI semiconductors.[42] Recently, this family of semiconductor has been largely studied to produce ternary silver indium sulfide (AIS) and copper indium sulfides (CIS) QDs, as well as quaternary QDs such as: silver copper indium sulfide (ACIS), copper indium gallium sulfide (CIGS), copper zinc tin sulfide (CZTS) and copper or silver indium zinc sulfides (CIZS or AIZS).[43] These chalcogenides, of particular interest for their optical properties and low toxicity, represent a promising alternative to cadmium, lead or mercury based QDs for biological applications.[42,44,45]

The major differences with respect to the most investigated binary families (e.g.: II-VI, III-V and IV-VI) concern: i) different emission mechanism that caused characteristic structural features like the large Stoke's shift and broad photoluminescence. ii) the strong relationship between optical properties and chemical composition.

- **EMISSION MECHANISM:** the large Stoke's shift and broad emissions are characteristic of I-III-VI semiconductors QDs. Although some of these features can be partially related to the heterogeneity of the samples (in both size and compositions), single particle measurements showed an intrinsic broad photoluminescence with FWHM in the 240 – 360 meV range observed for AIS/ZnS[46] and 190 – 270 meV for CIS/CdS.[47] Several hypotheses were considered to explain the origin of the photoluminescence activity in these semiconductor QDs. In particular, strong electron-phonon coupling and donor-acceptor recombination mechanism are usually considered.

  Hamanaka et al.[48] investigated the origin of the photoluminescence in chalcopyrite $AgInS_2$ QDs using a donor-acceptor mechanism. According to this mechanism, the radiative recombination does not involve a direct transition between conduction and valence band (**Fig. 3a**). Instead, the levels involved in the radiative recombination are associated to defect states with energies that lie in the band gap region (**Fig. 3b**). These defect states can be distinguished between donor states, involved in the stabilisation

of the photoexcited electrons and with energy close to the conduction band, and acceptor states, involved in the stabilisation of holes and with energy close to the valence band. The observed emission energy can be expressed by **Eq. 8**.

Eq. 8

$$E_{em} = E_g - (E_d + E_a) + \frac{e^2}{\varepsilon r}$$

Where E_{em} is the energy of the emitted photon, E_g is the band gap energy, E_d and E_a are the donor and the acceptor binding energies. The last term in **Eq. 8** is the coulomb interaction between electron and hole.

The studies on time-resolved PL analysis and the effect of the excitation energy on the emission band position made by Hamanaka et al.[48] supported this mechanism for the interpretation of the large Stoke's shift (hundreds of meV) observed in $AgInS_2$. The line broadening was analysed considering the contribution of the electron-phonon coupling. In the single phonon approximation, considering a phonon mode with frequency ω, the PL spectrum can be considered as the sum of the contribute of *n* phonons with energies (E_n) and Intensity (I_n) described by **Eq. 9** and **Eq. 10.**

Eq. 9

$$E_n = E_{ZPL} + n\frac{h}{2\pi}\omega$$

Eq. 10

$$I_n \propto \frac{S^n e^{-S}}{n!}$$

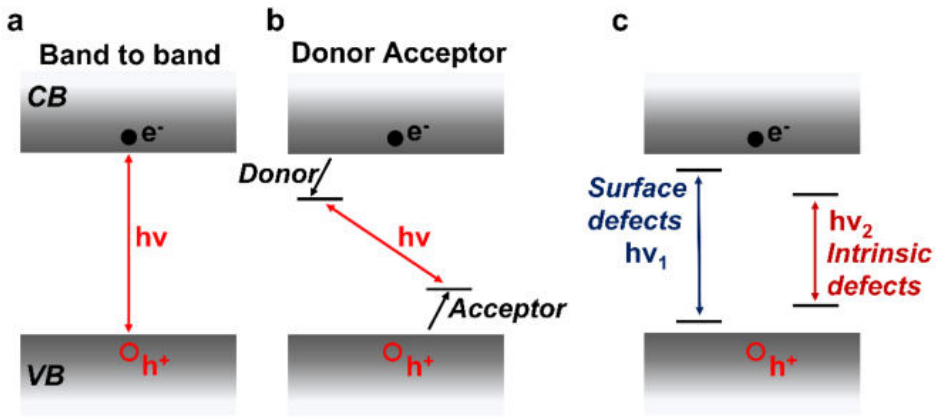

Figure 3: schematic representation of different radiative recombination mechanisms employed to describe the optical properties of ternary QDs, *VB* and *CB* represent valence and conduction band respectively. a) band to band recombination, b) donor acceptor recombination and c) donor acceptor recombination with multiple type of defect states involved.

Where E_{ZPL} is the energy of the zero-phonon line, and S is the Huang-Rhys factor that represents the average number of phonons involved and the strength of the coupling. In their analysis the observed spectrum was well reproduced considering a phonon energy of 33 meV, E_{ZPL} = 2.23 eV and a Huang-Rhys factor of 23 which are reasonable values considering the energy range of the longitudinal phonon observed in bulk silver indium sulfide.[49] Similar approach was employed by Han et al.,[50] in their analysis of the photophysics of spinel $AgIn_5S_8$ phase QDs. They recognized two main contributions to the emission, which were associated to different energies and lifetimes. They were ascribed to two different types of defects involved in the radiative recombination, the most energetic contribution related to surface defects (E_{ZPL} = 2.54 eV, $\hbar\omega$ = 32 meV and S = 14) and the less energetic to intrinsic defects (E_{ZPL} = 2.46 eV, $\hbar\omega$ = 32 meV and S = 15) **Fig 3c**.

Although the donor acceptor emission dominates the photoluminescence properties of I-III-VI QDs, the observation of band-to-band emission has been reported in few specific papers. Hirase et al.[51] reported the observation of a relatively narrow (FWHM 220 meV) emission band in the proximity of the absorption edge in $AgInS_2$ QDs after a post synthesis treatment to replace 1-dodecanthiol with n-trioctylphosphine. This finding was related to the effect of the surface passivation in the promotion of band-to-band emission, while, the original thiol stabilised QDs presented a red-shifted broader emission band that was ascribed to donor acceptor emission. Similar observations were reported by Uematsu et al.[52] on the optical properties of $AgInS_2$ QDs after the deposition of a Ga_2S_3 shell. Both these studies support the hypothesis that I-III-VI QDs

can show band to band emission by proper passivation of surface defects using organic ligands or inorganic shells.

- **COMPOSITION**: the chemical composition can strongly influence the optical properties of I-III-VI semiconductors. This feature can be used to further modulate the optical properties (absorption, PL and PLQY) in addition to the effect of the particle size.[53,54] Several authors investigated the effect of the chemical composition for various I/III cations ratio of Copper Indium Sulfide (*CIS*) and Silver Indium Sulfide (*AIS*) systems. The wide range of prepared compositions is related to the possibility of the chalcogenide phases to stabilise several non-stoichiometric systems either in the chalcopyrite phases (e.g.: $AgInS_2$ and $CuInS_2$) or spinel phases (e.g.: $AgIn_5S_8$ and $CuIn_5S_8$).

  The effect of the I/III cations ratio on the electronic properties of AIS QDs was investigated by Dai et al.[55] The authors studied different QDs with similar size (4.3 nm) and different compositions. They observed a blue shift of the energy gap from 1.7 to 2.1 eV increasing the indium content from a N_{Ag}/N_{metals} (molar ratio of silver ions N_{Ag} to the total metal ions N_{metal}) 0.7 to 0.1 (**Fig. 4a**). They associated this finding to the variation of the composition of the band structure. The valence band maximum of $AgInS_2$ is mainly composed by hybridisation of S 3p and Ag 3d orbitals, instead the conduction band minimum is composed by In 5s5d hybridised with S 3p orbitals.[56] Thus, the observed widening of the band gap with the reduction of the silver content was mainly related to the lowering of the valence band maximum level, as a consequence of the decreasing of the contribution of the Ag 3d orbitals. This feature was also reflected in the photoluminescence that showed a large blue shift of the maximum from 830 to 650 nm (**Fig. 4b**). The PLQY showed a complex trend with a maximum around 0.70 observed for the stoichiometry N_{Ag}/N_{metals} of 0.37. The increase or decrease in Ag content caused a reduction in the PLQY. Several other studies reported similar observations on AIS QDs produced by different methods showing the highest PLQY for silver to indium ratio around 1 to 4 ($N_{Ag}/N_{metals} \approx 0.20$).[40,57–59] The effect on the PLQY was interpretated considering the variation of the populations of defects in the nanoparticles. The most common defects observed in bulk AIS are: silver vacancies (V_{Ag}) and sulfur interstitial (S_i) that can act as acceptor levels and sulfur vacancies (V_s) and silver interstitial (Ag_i) that can ad as donor levels.[60,61] Thus, the optimal condition for the observed PLQY was associated with the appropriate population of silver vacancies (V_{Ag})

as radiative recombination site in donor-acceptor emission mechanism.[55] Similar observation was also reported by Uehara et al.[62] on CIS system (**Fig. 4 d,e**). The authors observed the maximum PLQY for the composition Cu/In of 0.44 and they explained the superior performance of the copper-deficient QDs to the promotion of defects such as copper vacancy and indium interstitial.

Hughes et al.[63] investigated the variation of the electronic properties of a series of quaternary $Ag_{1-x}Cu_xInS_2$ QDs controlling the copper content by ion exchange in $AgInS_2$ QDs. They related the variation of the optical properties with the Cu(I) content to the introduction of localized mid gap Cu 3d orbitals above the valence band of the quaternary phase. The variation of the optical properties is particularly evident in ''diluted'' condition with x below 0.20.

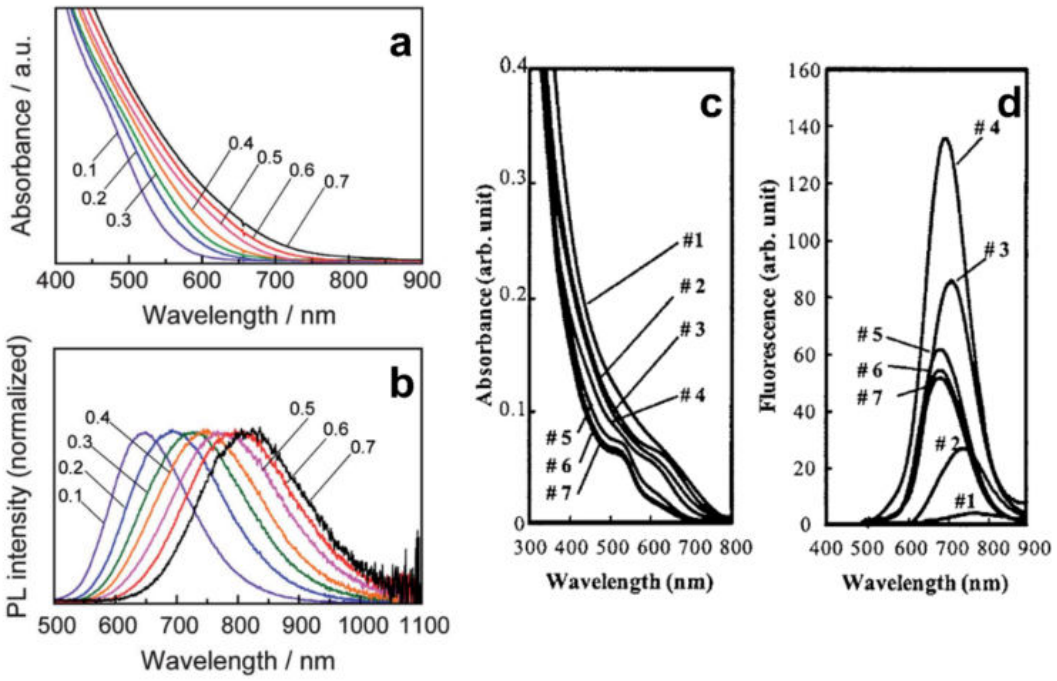

Figure 4: effect of the chemical composition of AIS QDs on the (a) UV/Vis absorption and (b) PL spectra as reported by Dai et al.53 the different composition is reported according to the N_{Ag}/N_{metals}. effect of the chemical composition on CIS QDs on the (c) UV/Vis absorption and (d) PL spectra as reported by Uehara et al.,60 the different samples present the following chemical compositions (Cu/In): 1 = 0.99, 2 = 0.59, 3 = 0.52, 4 = 0.44, 5 = 0.37, 6 = 0.35 and 7 = 0.34.

1.4 CHIRALITY IN QUANTUM DOTS

Chiral semiconductor QDs are among the most investigated chiral nanosystems due to their particular optical properties characterised by a distinctive dichroic absorption or circular dichroism (CD) and circular polarized luminescence (CPL). They have been subjected to an extensive investigation during the past decade after the first observation

of chiroptical activity of CdS quantum dots, prepared via microwave assisted synthesis in presence of L or D-Penicillamine, by Moloney et al.[64] in 2007.

The wide potential applications of this new chiral systems promoted several investigations on other cadmium based binary QDs in order to modulate the chiroptical properties and to study how structural parameters could affect the QDs chirality. The investigation on CdSe[65–68] and CdTe[69–71] QDs revealed the dependence of the chiroptical properties upon the size of the QDs and the ligand type. The influence of 3D nanostructure such as the CdS tetrapods[72] as well as the shell systems with type I and type II band alignments CdSe/CdS[73–75] and CdS/CdSe[73] were investigated to define the effect of structural features such as QDs shape and thickness of the shell layers. Studies on the shape anisotropy of CdSe and CdSe/CdS nanoplates revealed fundamental details on the chiral transfer in anisotropic nanostructures.[76] Moreover, several theoretical models for the description of the chiroptical properties origin in different Cd-based QDs have been developed,[71,73,77,78] and some of the most important results are collected in specific reviews.[76,79,80]

However, despite the wide number of impressive results regarding the chemistry of chiral quantum dots, all these studies were focused only on the Cd-based chalcogenides. To our knowledge there is no literature on other systems.

1.4.1 Chiral Quantum Dots Synthesis

Two synthetic strategies are used to produce chiral QDs: i) one step direct synthesis of chiral QDs assisted by chiral ligand and ii) two-step methods via synthesis of achiral QDs followed by phase transfer ligand exchange assisted by a chiral ligand to introduce particle chirality. Besides the different synthetic pathway that characterises these two approaches, another significant distinction is related to the type of method used to produce the QDs. Since the principal chiral ligand employed to produce chiral QDs (cysteine, penicillamine, glutathione) are hydrophilic thiols, the one-step direct synthesis is only compatible with aqueous QDs synthesis. Instead, the two steps approach is suitable for organic synthesis (typically hot-injection is used for the QDs production) and the chirality is introduced in a phase transfer ligand exchange from organic solvent to the water solutions.

- Direct synthesis: in this method, the QDs are usually formed by a coprecipitation reaction in water, assisted by the chiral ligand that plays multiple roles such as: modulation of the availability of the precursors, QDs stability, surface passivation and transfer of

chirality. Moloney et al.[64] reported the formation of chiral CdS QDs with average size around 2 nm by the precipitation $Cd(ClO_4)_2$, and thioacetamide as sulfur source, via microwave heating in the presence of penicillamine as chiral ligand. Nakasjima et al.[70] used a similar approach to produce Cysteine methylester stabilised CdSe and CdTe nanoparticles. However, despite the presence of CD activity of the nanoparticle, these QDs did not show a CD active transition in the exciton region, suggesting that the observed chirality is not related to the chiral induction on the first excitonic transition of the semiconductor nanocrystals. Instead, the observed CD transition were associated to the effect of the coordination of chiral thiol on the electronic transition of Cd ions on the particle surface. The investigation on cysteine stabilised CdTe QDs from Zhou et al.[71] allowed to observe some degree of chiral induction on the excitonic transition since a weak diffuse CD band was observed above between 250 and 350 nm. However, the authors related the major contribution to the nanoparticles chirality to Cd-Cysteine bond on the particle surface as can be appreciated by the comparison with the CD spectra of the complexes (two bands of apposite sing located at 225 and 250 nm).

In addition to these examples on the use of chiral thiols, other chiral transfer approaches were investigated in the context of the direct synthesis. An interesting approach was proposed by Naito et al.[81] who exploited the protein apoferritin as a chiral nanoreactor to produce chiral CdS QDs. The interaction between the protein nanocage and the CdS surface was promoted by the presence of 72 glutathione residues on the interior surface of apoferritin. Interestingly, this method allowed to observe Circular Polarized Emission with g_{lum} in the order of 10^{-3}. Another example was proposed by Zhou et at.[82] The authors observed the chiral transfer in CdS QDs using as chiral inductor a self-assembled system composed by thioglycolic acid that binds the particle surface with the thiol group and interact, by hydrogen bonds, with the guanidinium group on the arginine lateral chain. The main advantage of this approach is that the chiral ligand arginine can be easily removed by ion exchange thanks to the weak interaction with the ligand shell, an elegant way to decouple the contribution of the chiral transfer due to the presence of chiral ligand from structural distortion of the QDs.

- Phase transfer ligand exchange: this approach allows to prepare high quality lipophilic QDs via organic synthesis and to introduce chirality in a second step via phase transfer to water solution assisted by chiral ligands. The major advantage with respect to the

direct synthesis is related to the high control on the nanocrystal structure that can be accessible using organic synthesis like hot-injection. By this approach, QDs with narrow band to band emission and fine control on size and morphology can be isolated.[66,74,75,77] Instead, broad defects mediated emission dominates the optical activity of QDs produced by aqueous synthesis.[64,67]

This approach was implemented for the first time by Tohgha et al.[83] for tri-n-octylphosphine oxide/oleic acid stabilised CdSe QDs, using a phase transfer ligand exchange between toluene and water at pH 12 (using tetramethylammonium hydroxide to adjust the pH) and cysteine (concentration around 0.08 M). The biphasic mixture was stirred for 24 h in the absence of light to achieve the phase transfer. As confirmed by TEM and UV/Vis absorption spectroscopy, the phase transfer process did not affect size and optical properties of the QDs, and, in contrast to the CdSe isolated by the aqueous methods, a narrow emission (FWHM = 31 nm) close to the first excitonic transition was observed. The chirality on the QDs after the phase transfer was verified by the observation of CD active transition in the exciton region and, when the particles size increases, the expected red shift was confirmed.

This method was used by Ben-Moshe et al.[73] to study the origin of CD signals in chiral QDs. In their analysis, several core-shell systems were produced covering different types of sizes (both for the core ranging between 2.6 to 5.3 nm and the shells from 1 to 5 monolayers thickness) and band alignments (CdSe/CdS and CdS/CdSe). The ligand exchange was performed using a QDs solution in toluene (optical density of 2.5 at the first exciton peak) and a solution of cysteine (0.062 M) in water at pH of 10.5. The mixture was vigorously stirred for 6 h in the absence of light and left for 30 min to rest before removing the aqueous phase.

Although this method allows to produce high quality QDs and the morphology and absorption transition are unaffected by the ligand exchange process, a large loss of PLQY was reported. Purcell-Millton et al.[84] investigated the effect of the shell thickness in CdSe/CdS QDs on both the chiroptical and optical properties. They observed that the increase of the shell size causes a significant reduction on the transfer of chirality (**Fig. 5a,b**). However, this trend is opposite to the PLQY trend (**Fig. 5c**) and a considerable loss is still observed even for the sample produced with the thickest shell (a reduction of the PLQY from 19.2 to 3.9 % was observed during the phase transfer).

The use of non-thiol ligands such as carboxylic acid was investigated using this approach by Varga and coworkers.[68]

1.4.2 Origin of chirality in Quantum Dots

After the first observation of chiroptical properties in semiconductor nanocrystals, several models have been developed to explain the origin of this phenomenon. The chiral QD is described as an organic-inorganic hybrid structure composed by an achiral inorganic core and a chiral ligand shell. The chiroptical properties of the nanocrystal arise at the particle-ligand interface and are affected by the chemistry at the interface such as affinity and binding modes of the chiral ligand.[65,75] The organic shell affects the electronic transitions of the inorganic core by two main mechanisms: i) electronic coupling, ii) structural distortions.

- Structural distortion: the interaction with the chiral ligand can promote the formation of distortions on the particles surface such as chiral defects. Elliott et al.[78] simulated by DFT the distortion caused by dianionic penicillamine on CdS clusters with distorted wurtzite structures. The authors observed that penicillamine binds a Cd cation via N and S coordination and induced structural constrains by the interaction of the carboxylate with a second Cd cation. Moreover, the chiral ligand binding induced distortion in the outer layers, while the core unit of the cluster was almost unaffected (**Fig. 5 d,e**). The observation of chiroptical activity after the removal of the chiral ligand was reported for CdS and CdTe QDs.[70,82] This feature was related to the chiral memory effect and was associated to the stabilisation of surface defects that preserve their chiral structure even after a ligand exchange with achiral ligands.
- Electronic coupling: the hybridization of HOMOs from the chiral ligand with the highest levels of the valence band was investigated by Ben-Moshe et al.[73] to explain the structure of the CD signal of chiral CdSe QDs. This interaction causes the splitting of the hole levels in two sub-levels which absorb right and left circular polarized light differently giving the formation of the characteristic bisignated peaks. Gao et al.[77,85] modelled the chiroptical properties of CdSe nanorods and nanoplates, stabilised by cysteine, with a nondegenerate coupled oscillator model. They divided the nanostructure in different

chromophores (C=O, Cd-S, Cd-O and CdSe) and investigated the effects of distances and orientation of the chromophores.

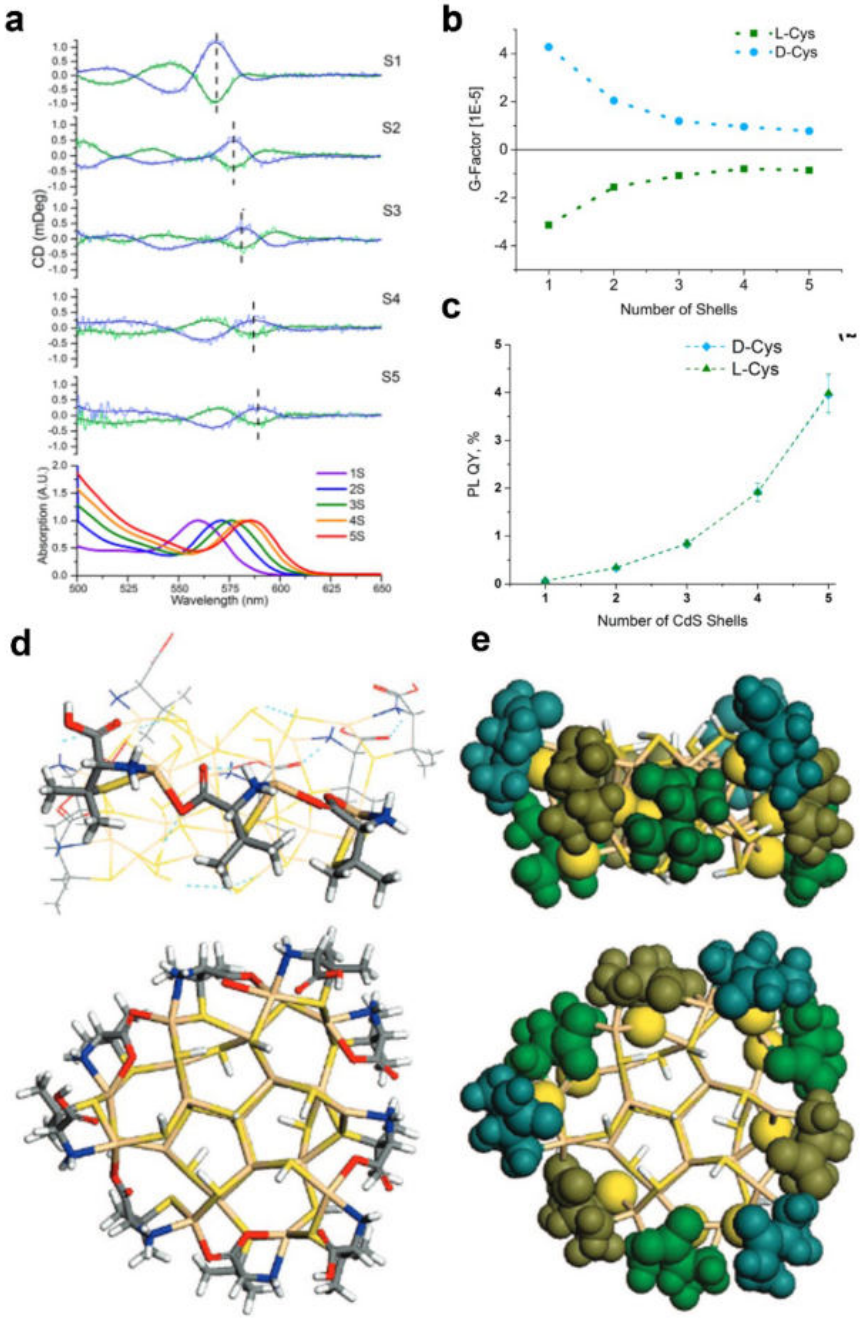

Figure 5: effect of the thickness of the CdS shell layer on CD activity (a,b) and PLQY (c) of chiral CdSe/CdS QDs produced by on the CD activity phase transfer ligand exchange.82 Side and top view of the penicillamine stabilised CdS cluster modelled by Elliott et al.,76 the ligand are represented in stick (C) and space filling (d) representations.

2 RESULTS AND DISCUSSION

2.1 AIS14 SYNTHESIS AND CHARACTERISATIONS

In order to optimise the optical properties of the QDs, in particular the luminescence efficiency, a Ag:In atomic ratio of 1:4 is chosen on the basis of the results reported by other authors in the literature (**AIS14**).[86–89] Cysteine stabilised non-stoichiometric AIS QDs are directly produced by a facile two- steps process at room temperature in water solution depicted in **Fig. 6**. In the 1st step, a L or D-cysteine (Cys) solution is added (see materials and methods section) to the metals precursor solution with pH adjusted to 8.5. Then, the QDs formation is triggered by addition of a solution of Na_2S which acts as the sulfide source. Consequently, the colour of the rection mixture turns rapidly from colourless to bright yellow, presumably due to the start of the nucleation process. In fact, for longer reaction times, the solution turns to an orange colour, that remains stable. The UV/Vis spectra presented in **Fig. 7** shows the rise of an absorption band located around 350 nm, due to the nanocrystals formation. A constant absorbance of the solution is reached after 40 min from the Na_2S addition, indicating the completeness of the reaction.

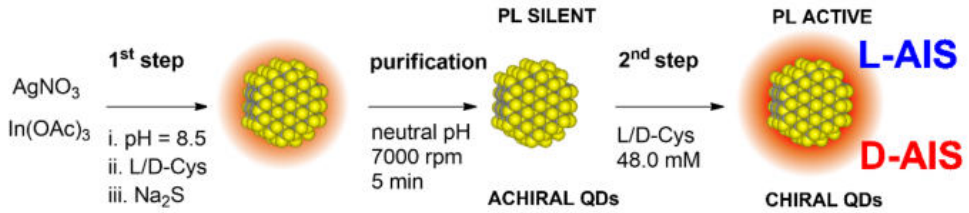

Fig. 6 Schematic representation of the investigated synthesis used to produce AIS QDs

After the purification step, the AIS QDs are easily redispersed in water with addition of a proper concentration of L or D-Cys (see Fig. 1a). During the 2nd step of the synthesis, the nanocrystals are aged for 24 h at room temperature in a solution of the chiral ligand, L or D-Cys, at a specific concentration. Then, the colloidal solution is diluted to a final concentration of 1.0 mg/ml with double distilled water and stored for further characterisations. Here we refer to the QD sample prepared using enantiomerically pure L- or D-Cys in both 1st and 2nd steps of the synthesis as **L-AIS14** or **D-AIS14,** respectively. The TEM images of the QDs after the 2nd step, show the presence of nanocrystals with an average size of 2.1 nm ± 0.9 (**Fig. 8**) and the phase contrast images reveal details on

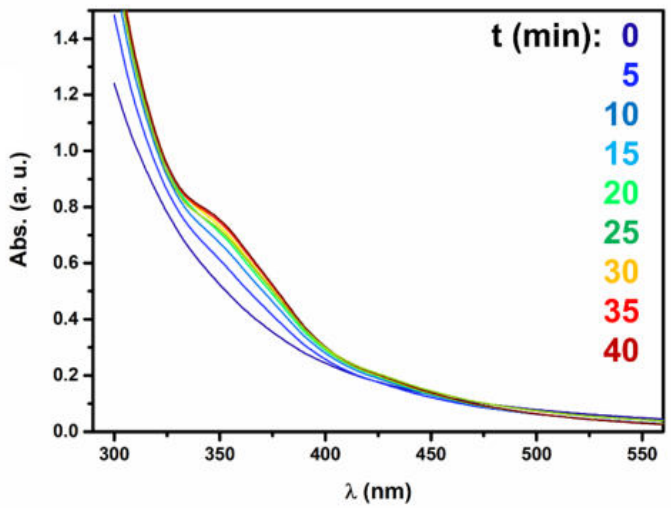

Figure 7: UV/Vis absorption spectra of the rection mixture collected at different time interval after the sodium sulfide injection.

the crystallographic structure of the nanocrystals. Indeed, d-spacings of 0.30 and 0.27 nm are estimated by the analysis of the fringes produced by electron diffraction (**Fig 8d** and **Fig A1**), related to the 311 and 400 facets of the cubic AIS phase. TEM analysis of aqueous quantum dots was particularly challenging due the nanocrystal aggregation process ascribed to the strong capillary forces in the drying drop of aqueous solution.[53]

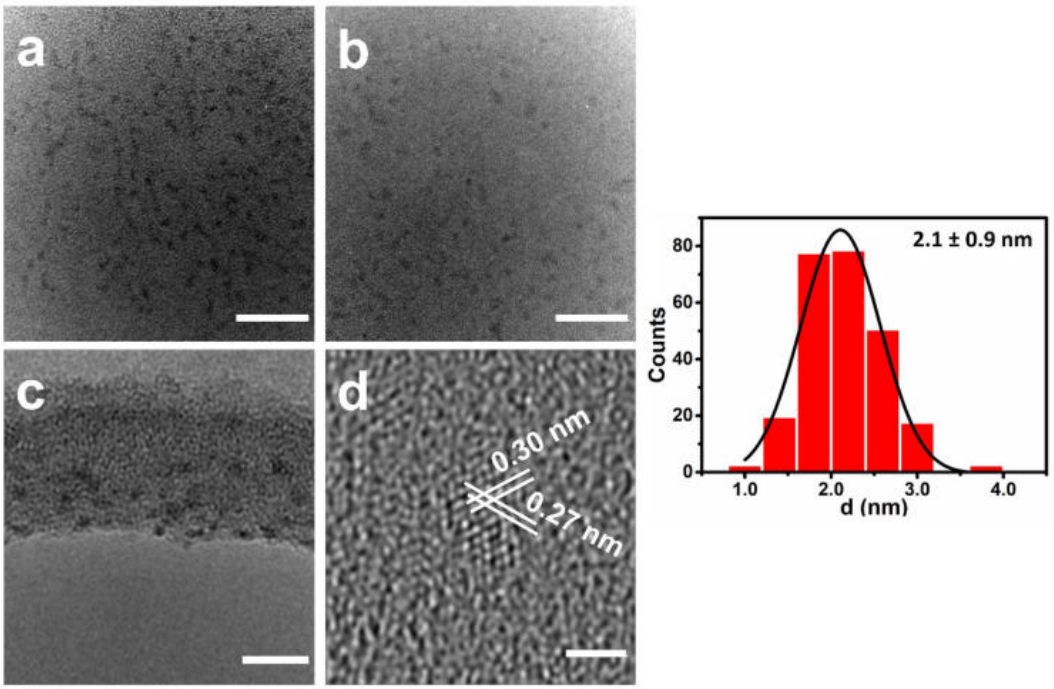

Figure 8: TEM micrographs of non-stochiometric **AIS14** QDs with scale bars: c,d = 20.0 nm, e = 10.0 nm and f = 2.0 nm and size distribution.

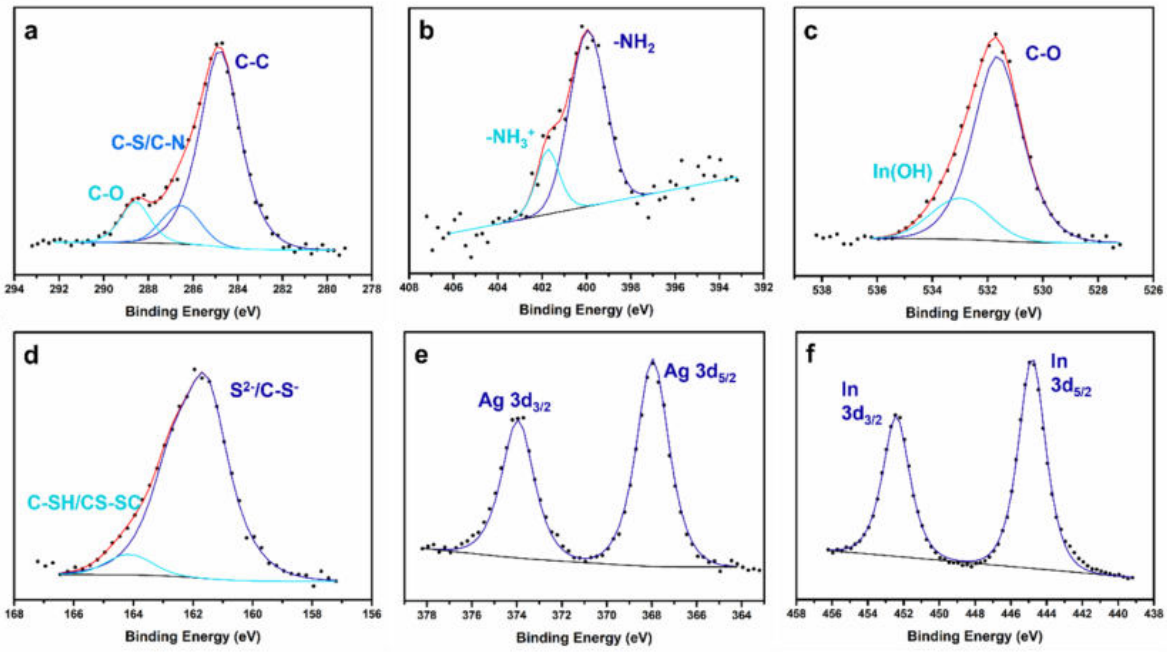

Figure 9: XPS spectra related to a) C 1s, b) N 1s, c) O 1s, d) S 2p, e) Ag 3d and f) In 3d. The baseline is indicated in black and the sum of different components (if any) employed in the fitting process is reported in red.

The XPS elemental quantitative analysis is evaluated by the peak area of the single signals (**Fig. 9**) corrected by the elemental sensitivity factor. The relative atomic composition is estimated as follows: C 42.3%, O 18.4 %, Ag 3.7 %, N 4.6 %, In 14.0 %, S 17.0 %. The relative Ag/In metal ratio is 1/3.8, corresponding to a N_{Ag}/N_{metal} ratio of 0.21 (value similar to the results collected by EDS and ICP analysis discussed below), thus confirming the QD expected stoichiometry according to the molar ratio of the starting reaction mixture. A large part of the detected carbon is due to contamination from the atmosphere, originating a band at very low Binding Energy (BE) related to hydrocarbons and usually used for evaluating the surface charging in non-conductive samples. We assumed this signal to be centred around 248.8 eV, even if the use of carbon contamination as standard for BE correction is currently under strong debate:[90] Our actual choose gives however a consistent picture of the physical-chemical state of the sample surface, starting from the BE positions consequently determined.

Deconvolution of the C 1s (**Fig. 9a**) band shows the compresence of three contributes, related to the presence of hydrocarbon contamination and of chiral ligand: the main one is fixed at 284.8 eV and is related to C-C and/or C-H bonds (as reported above), the second one is centred at 286.5 eV and is related to C-S and/or C-N bonds, and the last one is centred at 288.6 eV and is attributed to C-O bonds.[91] N1s signal (**Fig. 9b**) shows the presence of two contributes centred around 399.9 eV and 401.7 eV, related to the compresence of $-NH_2$ and $-NH_3^+$ respectively,[92] according to the protonation state of the cysteine molecules after the purification.

The O1s (**Fig 9c**) signal is the overlap of two contribution: the first, at 530.6 eV, is mainly related to the ligand C-O bonds,[91] the second, centred around 533.0 eV, can be related to the presence of hydroxides (possibly In-OH groups) and water contaminant.[93,94] The S2p signal (**Fig. 9d**) can be deconvoluted considering the presence of two contributions: the most intense signal at 161.5 eV can be related to sulfide anions S^{2-} and thiolate groups C-S^-, the second signal centred at 164.1 eV can be related to protonated cysteine thiol groups C-SH or to the disulfide dimer cystine CS-SC.[86,91,92]

Silver presence originates the characteristic 3d band (**Fig. 9e**), showing the $3d_{5/2}$ component centred at 367.9 eV (for a spin-orbit splitting, SOS, of 6.1 eV). The $Ag3d_{5/2}$ binding energy is not very sensitive to the change of the chemical environment of silver atoms; however, the detected BE value is closer to literature data for Ag^+ than Ag^0.[95] In3d (**Fig. 9f**) band is the main signal of indium, whose main component $3d_{5/2}$ is centred at 444.8 eV (7.6 eV of SOS). The detected binding energy suggests the presence of In^{3+}, related to indium sulfide and possibly to small amount of oxide. Also considering the experimental uncertainties, all the reported attributions are consistent with the quantitative analysis for the different elements.

Powder XRD confirms the formation of the cubic $AgIn_5S_8$ phase. This cubic spinel phase is commonly observed in non-stoichiometric indium-rich silver indium sulfide nanocrystals,[87,96] the crystallographic unit cell of the stoichiometric phase is represented in **Fig.10a**. This structure adopts the space group *Fd*-3*m*, In^{3+} occupies the octahedral site and half of the tetrahedral site, and Ag^+ occupies the other half of the tetrahedral sites. The XRD patterns **Fig. 10b**. show diffraction reflections centred at 27.8° 44.0°, 47.5° and 53.5, in 2θ, which can be related to the (311), (330), (440) and (620) crystallographic planes, confirming the formation of the cubic $AgIn_5S_8$ phase. Previous investigations reported on the stabilisation of this phase in a wide range of In/Ag stoichiometries.[87,97–99] The interpretation of the XRD data is still limited by the large FWHM of the XRD reflections which is related to the small nanocrystals size.

The PL properties in the UV/Visible optical range of colloidal **AIS14** QD dispersions stabilised with 16.0 mM concentration of L- or D-Cys ligand are investigated. The emission spectrum upon excitation at 450 nm (**Fig. 10c**) shows a broad emission peak centred at around 635 nm with a large FWHM (around 160 nm, 0.5 eV). According to the model

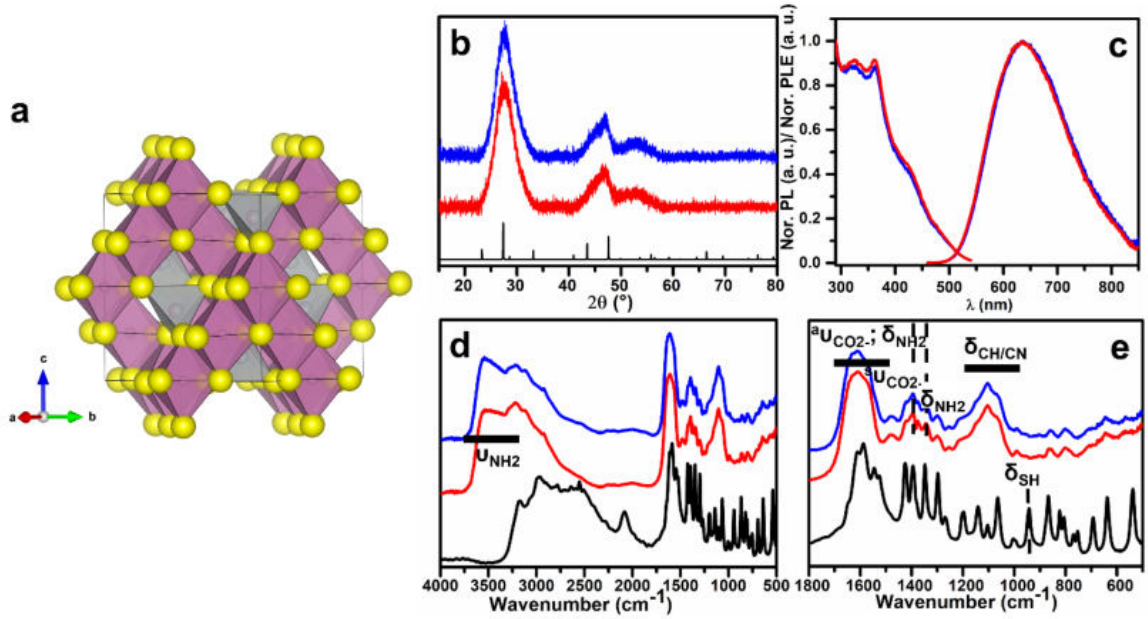

Figure 10: a) representation of the crystallographic unit cell of $AgIn_5S_8$ spinel phase, b-e) Chemical-physical characterisations of **L-AIS14** (blue) and **D-AIS14** (red) QDs: b) XRD patterns; reference pattern: cubic $AgIn_5S_8$, ICSD 51619. c) PLE and PL spectra of the QDs solutions. d) and e) FTIR spectra of the QDs powders and reference spectra for zwitterionic L-Cys (black).

proposed by Han et al.[50] we analyse the electron-phonon coupling dividing the contributions in intrinsic and surface defects. By fitting with a bigaussian function (**Fig. A2a**), we extrapolate the emission profile of the two contributions. The surface defect band has a maximum located at 2.00 eV, while the band related to the intrinsic defects is located at 1.78 eV. The simulation of the contribution of the electron-phonon coupling, considering the contribution of a single phonon ($\hbar\omega$ = 32 meV[48,49]) well represent the observed emission profiles (**Fig. A2b, c**). The intrinsic defect band is modelled considering E_{ZPL} of 2.31 eV and S = 16, values very similar to the ones reported in literature.[50] The surface defect band is modelled with E_{ZPL} of 2.86 eV and S = 26. In this case, the E_{ZPL} is considerably blue-shifted with respect to the value reported by others authors[50] (2.54 eV). Our choice is partially related to the different size of our QDs and to a large contribution associated to the high number of surface defect that characterise nanocrystals produced at room temperature and causes a large broadening.

A PLQY of 0.24 is obtained for this colloidal dispersion (**Eq. A1,2**). The PL excitation spectrum shows the presence of a shoulder around 420 nm and features at 360 nm and around 322 nm. The PL decay curve of a **L-AIS14** QD dispersion upon pulsed excitation at 453 nm, is shown in **Fig. A3**. From a fit of this decay curve with a triple exponential function (**Eq. A3**), an average lifetime of 518 ns is evaluated (see **Eq. A4** and **table A1**),

similar to that reported by other authors for non-stoichiometric AIS QDs.[87,88,100] This value arises from different decay components that are a combination of size-dependent and defects-related de-excitation mechanisms.[101]

The presence of coordinated cysteine on the final AIS QDs has been investigated by FTIR technique (**Fig. 10d,e**). The broad absorption band around 3400 cm^{-1} can be attributed to the ν_{NH} N-H stretching vibration. The broad and intense band centred at 1616 cm^{-1} is ascribed to the overlap of the $^{a}n_{CO2-}$ carboxylate asymmetric stretching and the $^{a}\delta_{NH2}$ asymmetric -NH_2 bending indicated by a shoulder around 1580 cm^{-1}.[102] The sharp bands at 1400 and 1340 cm^{-1} are related to the $^{s}\nu_{CO2-}$ carboxylate symmetric stretching and $^{s}\delta_{NH2}$ -NH_2 bending respectively.[102,103] The absorption bands between 1230 and 1020 cm^{-1} could be related to bending δ_{CN} and δ_{CH} modes.[104] The absence of the sharp peak around 940 cm^{-1} related to the δ_{SH} mode indicates that the -SH thiol group is deprotonated and that sulphur is involved in surface metal coordination mainly as anionic X-type ligand.[105,106]

The chiroptical properties of the QDs colloidal solutions are analysed by UV-visible CD spectroscopy. The UV/Vis spectra in **Fig. 11a** shows the presence of two transitions, the first one located at 220 nm and related to the thiol bond with the metal cation on the particle surface, and the second one at 400 nm that corresponds to the excitonic transition of the QDs. The analysis of the chiroptical properties in the UV region (200 – 300

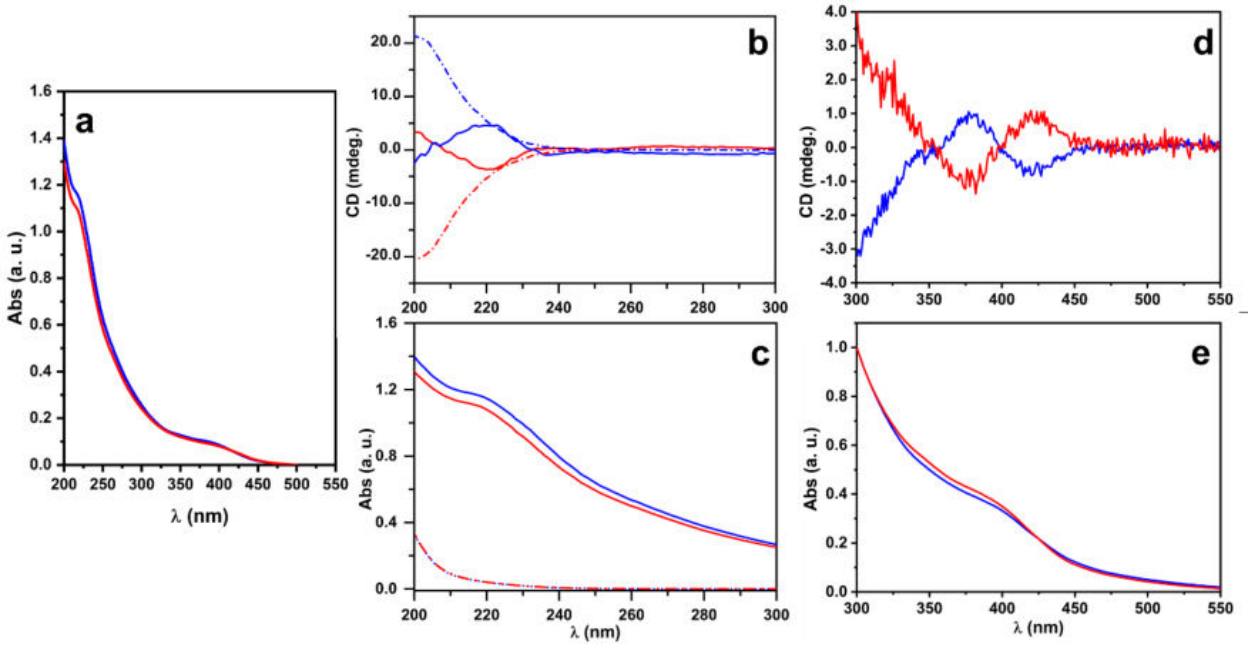

Figure 11: optical characterisations of **L-AIS14** (blue) and **D-AIS14** (red) colloidal solutions: a) UV/Vis absorption spectra, b,c) CD and UV/Vis absorption spectra in the 300 -200 nm range, d,e) CD and UV/Vis absorption spectra in the 300 -550 nm range

nm) reveals a chiroptical active band located at 222 nm (**Fig. 11b,c**) that shows a positive sign for **L-AIS14** and a negative one for **D-AIS14** These transitions are clearly different from the $n_O \rightarrow \pi^*_{C=O}$ observed for free cysteine at 206 nm as can be appreciated by the comparison with the spectra of the free ligand.[77,85] In the visible region, the CD spectrum of **L-AIS14** QDs (reported in **Fig.11d,e**) shows a negative band at 420 nm and a positive one at 375 nm with an inversion point at 400 nm. The observation of the chiroptical activity in the exciton region strongly confirms the transfer of chirality to the AIS nanocrystals. The opposite CD signal is observed for the **D-AIS14** confirming the isolation of the two enantiomers and the enantioselectivity of the synthesis. The analysis of the origin of the characteristic bisignated peak located in the exciton region presenting the typical shape of the Cotton effect was reported by Ben-Moshe et al.[107] on chiral CdSe QDs. The authors related this typical spectroscopic feature to the splitting mechanism induced by the interaction of the chiral ligand on a QDs fundamental transition, giving the formation of two bands that are preferentially excited by alternating circular polarizations. The anisotropic g-factors of -0.92 10^{-4} and 0.63 10^{-4} can be calculated from the bands observed at 420 and 375 nm respectively, for **L-AIS14**. Similar, for **D-AIS14**, values of +0.93 10^{-4} and -0.58 10^{-4} can be calculated for the bands located at 430 and 375 nm, respectively (**Fig. A4**). These chiroptical properties are in accordance with the observation reported by other authors for similar systems in which the chiroptical properties of isotropic QDs are originated by the induction of a chiral ligand (ligand induced chirality).[108–110]

It must be remarked that the 2nd synthetic step significantly affects the spectroscopic properties of the nanocrystals. The PL kinetic measurements (**Fig. A5**) of **L-AIS14** show a high enhancement of the emission after 300 min from the dispersion of the nanocrystals, depending also on the L-Cys concentration (4.0, 8.0 and 16.0 mM). The emission intensity increases up to a plateau value after 24 hours, depending on the ligand concentration. During this period, the maximum of the emission around 600 nm observed for the nanocrystals isolated after the first step is red shifted to 635 nm. Analogously, a raise in the PLE intensity around 430 nm is observed (**Fig. A6**).

In order to clarify the structural differences of the AIS QDs after the 1st and 2nd steps, an XRD analysis of the two samples is carried out. **Fig. 12** shows a comparison of the degree of crystallinity of nanocrystals isolated after the 1st and after the 2nd reaction

steps, and a clear narrowing of the diffraction reflections is observed for both the QDs enantiomers. This behaviour can be reasonably related to the increase of the crystallites size during the ageing process. Further details on this process and the study of the kinetics according to different ligand concentrations are reported in the *Investigation*

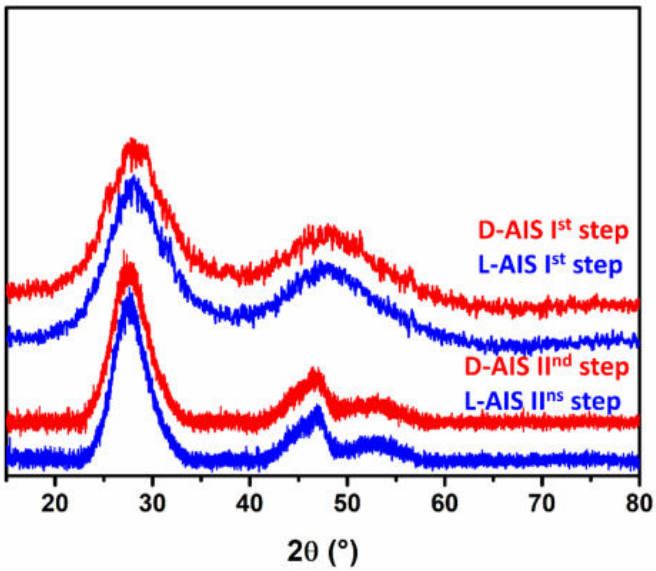

Figure 12: XRD data of **AIS14** QDs isolated at the different step of the synthesis, the pattern for the nanocrystals produced in the presence of L or D-Cys are indicated in blue and red respectively

on the formation mechanism section (2.5).

2.2 ORIGIN OF CHIRALITY

In order to investigate the origin of chirality and to optimise the chiroptical activity of the nanocrystals, the chemisorption equilibrium of the chiral ligand on the nanocrystals surface has been investigated combining CD spectroscopy and NMR titration results. The analysis covers a range of ligand concentrations (2.0-16.0 mM) in which the highest variation of the chiroptical activity at the exciton position was observed.

The ^{1}H-NMR spectrum for the QDs dispersion stabilised in a 2.0 mM solution of L-Cys (**Fig. 13**) shows broad signals without any well resolved fine structure for both H_{α} and H_{β} located at 3.94 and 2.94 ppm respectively. The observed spectral broadening is typically associated to the ligand bonded to the particle surface. The origin of the broadening can be related to several factors: i) distribution of chemical shift due to the ligand absorption on different sites on the QDs surface,[111,112] ii) distribution of the spin-spin relaxation T_2 due to different tumbling dynamics in the absorbed ligands[113] and iii) different packing that can affect the ligand-ligand dynamics.[111,114] On increasing the ligand

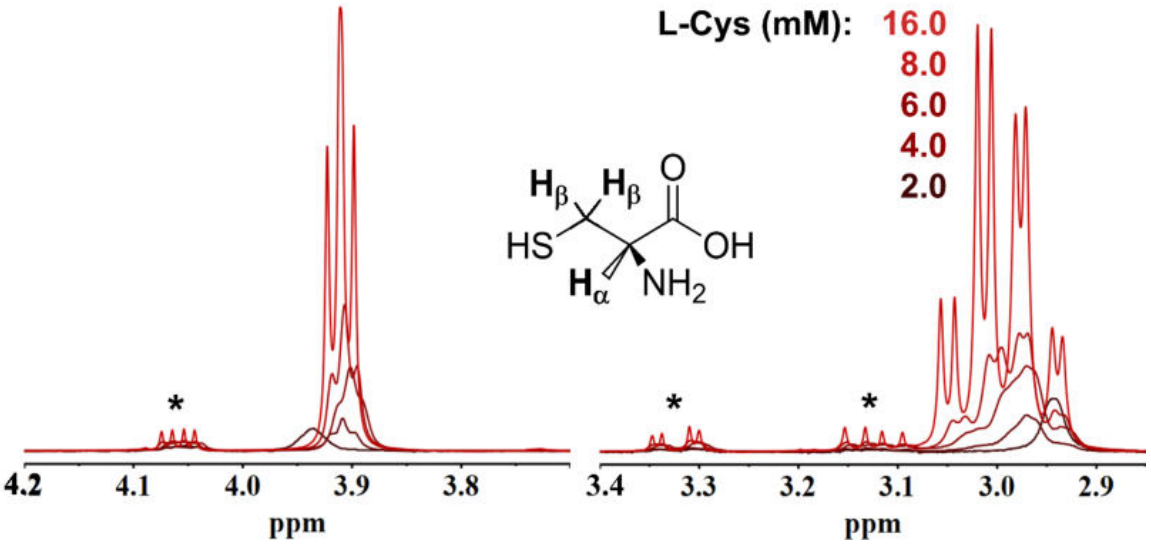

Figure 13: ^{1}H-NMR titration of a solution 1 mg/ml of **L-AIS14** QDs with different L-Cys concentrations, the signals that are ascribed to L-cystine are marked with an asterisk.

concentration, a significant variation of the resonance frequency can be observed; the position of the peaks shifts from 2.94 to 3.00 ppm and from 3.94 to 3.92 ppm for the H_β and H_α, respectively.

At higher L-Cys concentration (16.0 mM) it is possible to observe a significant spectral narrowing and the expected fine structure of free zwitterionic cystine can be observed as well (see **Fig. A7**). This behaviour suggests that the ligand chemisorption dynamic is in the fast chemical exchange regime $k_{ex} >> 1/\tau_{NMR}$.[115] In this case, the chemical exchange between the two (free and bonded) ligand forms exceeds the NMR characteristic time scale and therefore, the exchanging protons cannot be resolved in two distinct set of frequencies. Instead, for each set of protons, the analysis records a single signal whose observable chemical shift reflects the populations of the free and bonded forms.

The same consideration is also valid for the other NMR quantities such as relaxation times T_1 or T_2 and diffusion coefficients.[116,117] Even if, in the presence of a fast chemical exchange, the bands ascribed to the bonded and free forms of the ligand cannot be resolved, further evidence of the ligand-particles interaction can be collected by NOESY analysis (**Fig. 14**).[118] The spectrum shows the presence of characteristic strong negative cross peaks for H_α/H_β protons of L-Cys. This evidence can be related to ligand-nanopar-

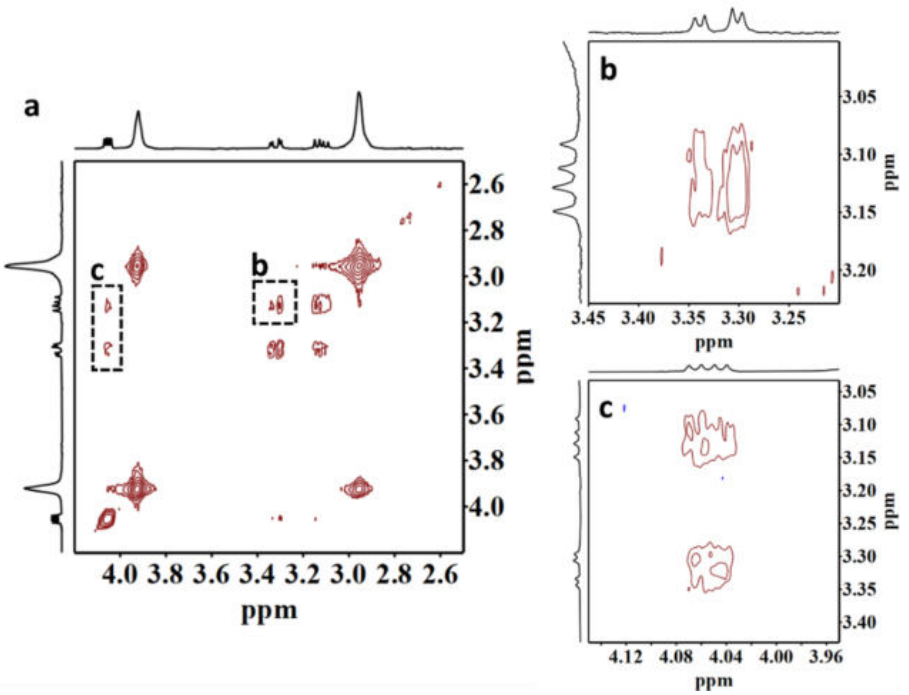

Figure 14: NOESY analysis of a **L-AIS14** QDs solution in the presence of 4.0 mM L-Cys. B and c) expanded areas of the L-cystine negative cross peaks.

ticle interactions that affect the ligand mobility in solution, causing the ligand coordinated on the particle surface to be characterised by a slow tumbling, responsible of the formation of intense negative crosspeaks.[116,118] Under these conditions, we can assume that the resolution of the ligand protons frequencies in different signals according to different binding modes is not feasible and the different contributions are averaged in the single contribution that can be related to the bonded ligand population. However,

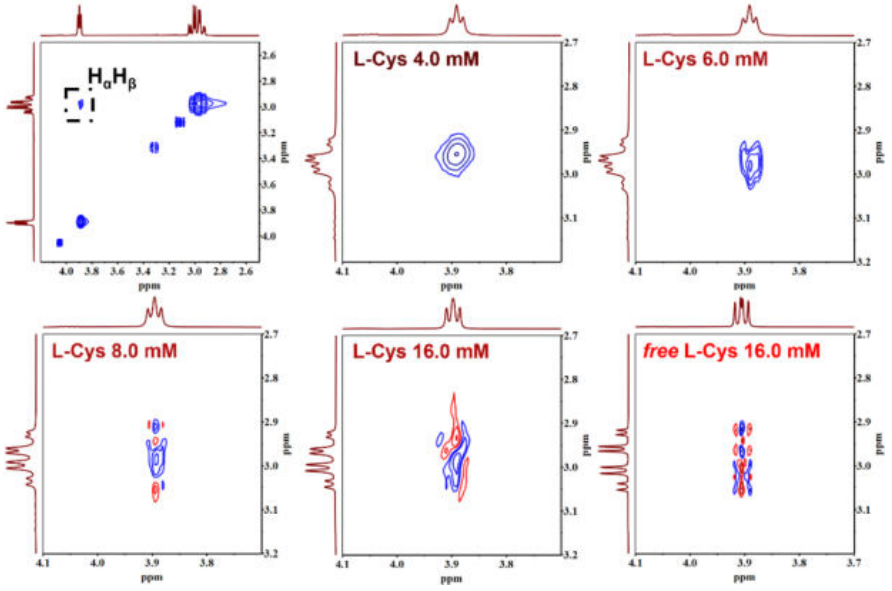

Figure 15: effect of the L-Cys concentration on the HαHβ cross peak in 2D-NOESY spectra of **L-AIS14** QDs colloidal solution.

the effect of the variation of the population of the free and bonded ligand forms according to the ligand added in solution, strongly affects the magnetic properties of the sample. As can be observed in **Fig. 15** the NOESY cross-peak change dramatically with the ligand concentration. As already discussed, a negative phase cross-peak is observed in low ligand concentration, characteristic of the dynamic of a bonded form. Increasing the ligand concentration causes the appearing of the typical feature of the zero-quantum coherence artifacts commonly observed for scalar coupled spins in small molecules such as free cysteine.[119]

A Diffusion Ordered Spectroscopy (DOSY) analysis of the colloidal solutions in the presence of an increasing ligand concentration, shown in **Fig. 16a,** evidences the raise of the diffusion coefficient from 5.25 to $10.23 \cdot 10^{-10} m^2/s$ for the H_β. The variation of diffusion coefficient on the H_α is even more evident, and the following diffusion coefficients can be estimated for the colloidal solutions with different L-Cys concentrations: 4.36 (2.0mM), 6.92 (4.0 mM), 7.41 (6.0 mM), 8.32 (8.0 mM) and 9.12 (16.0 mM) 10^{-10} m^2/s. It must be remarked that the signal for the free L-Cys reference shows a much higher diffusion coefficient, which is estimated around $12.0 \cdot 10^{-10}$ m^2/s for both H_β and H_α. As expected, the presence of a fast exchange between the ligand coordinated on the particle surface and the free ligand in solution prevents the measurement of distinct diffusion coefficients for the two species (D_b and D_f for the bonded and free ligand). However, since the observed diffusion coefficient is the average of the two populations, it is possible to observe the effect of the increasing content of the free ligand population that shifts the observed value for the diffusion coefficient toward D_f. It is worth to note

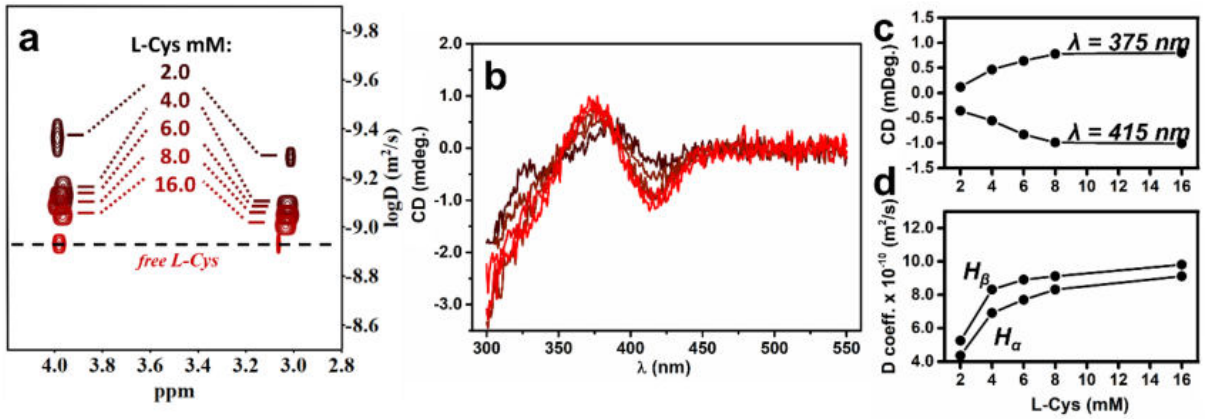

Fig. 16 a) DOSY and b) CD spectra of **L-AIS14** QDs solutions in the presence of different L-Cys concentrations. c and d) plots of the intensity of the CD bands and the measured diffusion coefficients respectively.

that the variations for the observed diffusion coefficient can be related to the intensity variations of the CD bands located at 375 and 420 nm (**Fig. 16b)**. In fact, the intensity of the CD signals increases on increasing the ligand concentration until a certain saturation value around 8.0 mM is reached and no further increase is observed for higher L-Cys ligand concentrations. The UV/Vis absorption spectra of the sample at different L-Cys concentrations are shown in **Fig. A8**. Since no variation are observed in the exciton region, we exclude that the variation of the ligand concentration in the investigated range affects the structure or composition of the **L-AIS14** nanocrystals. The variations of the CD intensity and diffusion coefficients, shown in **Fig. 16 c,d** confirm this trend. It must be remarked that this comparison is possible thanks to the enhancement of the resolution in the diffusion dimension respect to the small variations which are observed in the chemical shift.

An estimation of the bonded (x_b) and free (x_f) ligand populations in the different colloidal solutions can be calculated according to **Eqs. 11** and **12** assuming the diffusion coefficient for the sample with lowest total ligand concentration (2.0 mM) as a reference for the bonded ligand (D_b).

Eq. 11

$$D_i = x_b D_b + (1 - x_b) D_f$$

Eq. 12

$$x_b + x_f = 1$$

Even though this approximation gives an excess in the estimation of the bonded population, it was successfully employed by Copenhaver et al. for the estimation of the ligand coverage of QDs.[111] By means of this rough estimation we observe a large increase in the bonded population for concentrations below 8.0 mM (**Fig. 17a**). Instead, for higher L-Cys concentrations, the free form is favoured, minimizing the effects on the composition of the chiral ligand shell and thus on the transfer of chirality, due to possible saturation of the ligand sites on the particle surface. A similar trend is observed considering the variation of the intensity of the CD band at 222 nm related to the binding of cysteine. In this case the analysis is based on the fitting of the line profile of the spectra collected at different ligand concentrations (**Fig. A9-11**). The line profiles that describe the signals related to the free and bonded ligand forms are chosen appropriately (See Appendix section: Investigation on the particle-ligand interaction via CD). The

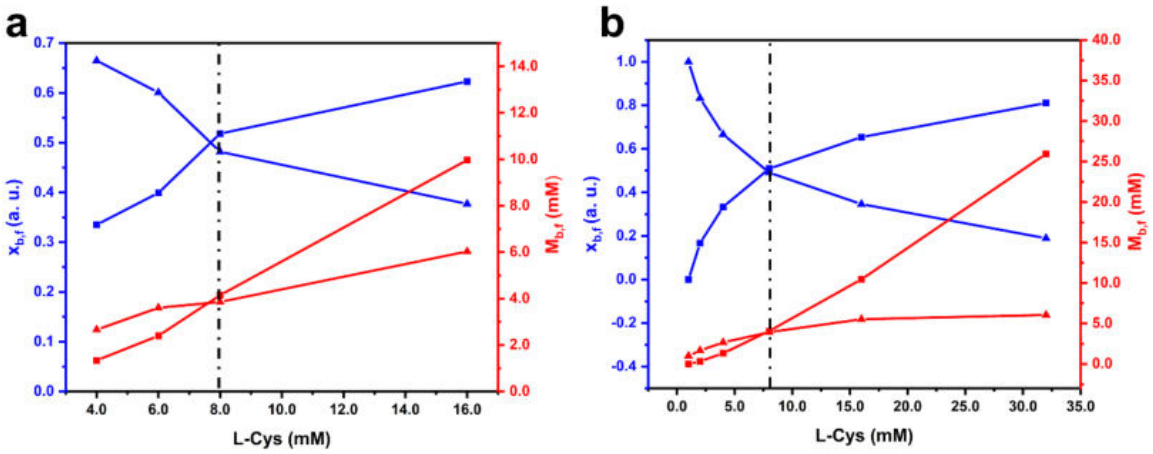

Figure 17: Calculated molar fractions ($x_{b,f}$) and molarity ($M_{b,f}$) for the bonded (triangle) and free (square) forms of the ligand, using DOSY NMR data (A) and fitting of the CD band at 222 nm (b).

different contribution of the two forms obtained from the fitting are used to estimate the molar fractions. This method shows a trend very similar to the one obtained by the NMR analysis and the same saturation point at about 8.0 mM. This finding agrees with the effect observed on the exciton transition by CD.

A similar behaviour can be observed also for the disulfide dimer L-cystine, as this specie is present as an impurity in commercial cysteine (**Fig. A7**) and it is in equilibrium with its monomeric form.[120] The negative NOESY cross peaks show that even this specie is involved in the coordination equilibria with the particle surface (**Fig. 14b,c**). Furthermore, as observed with L-Cys, the diffusion coefficient for both the H_α and H_β in L-cystine are shifted towards higher values with increasing of the ligand concentration (**Fig. A12**). However, due to the low content of dimers in solution, the analysis shows a huge broadening in the diffusion dimension and for this reason our considerations are mainly focused only on L-Cys as the principal chiral ligand present in solution.

Based on our observations, chiral ternary AIS QDs produced via coprecipitation reaction in the presence of a chiral ligand present similar chiroptical properties compared to the more investigated Cd-based QDs. The particle morphology, crystalline structure and entity of the chiral induction suggest that the chirality is originated at the ligand-nanocrystal interface. As successfully employed for Cd-based chiral QDs, chiral AIS QDs can be described as a hybrid core-shell system composed by an achiral inorganic core surrounded by a chiral organic ligand shell (**Fig. 18**).[107,108,121,122] In such nanosystem, the chiroptical activity can be originated by different processes that can mainly described

as electronic or structural. The electronic mechanism arises from the ligand chemisorbed on the particle surface which can affects the electronic states of the inorganic achiral core via dipolar induction.[107,123,124] On the other hand, structural chirality can be introduced at the ligand-nanocrystal interface by distortions of the nanocrystals surface by the chiral ligand.[121,125,126] Further analysis would be needed to clearly address the entity of the different contributions to the QDs chirality.

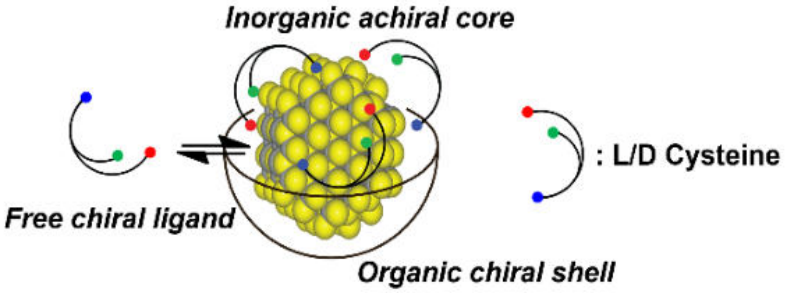

Fig. 18 Schematic representation on the ligand-nanoparticle chiral hybrid structure.

The main difference respects the Cd-based chiral QDs is the fast exchange of the ligand molecules on the particle surface observed by NMR spectroscopy. The analysis reveals that in presence of low ligand concentration (2.0 mM) sub-coordinated particles are present, and in this condition the chiroptical properties can be increased by increasing the concentration of the ligand in solution (**Fig. 16c, d**). In this way it possible to drive the chemisorption equilibrium toward the saturation of the particles surface sites increasing the surface coverage which consequently increases the chiroptical activity. The organic chiral shell can be populated until a certain value corresponding to the surface saturation, which is reached for a ligand concentration above 8.0 mM, evidenced by both CD and DOSY analyses. A further increase of the ligand concentration in solution mainly affects the free ligand population with only minor variation of the bonded population, that does not affect the particle chirality. This behaviour is different from the concentration dependent study reported by Kuznetsova et al.[106] for CdSe/CdS core-shell QDs produced via post-synthetic phase-transfer ligand exchange. In that case, the intensity of the CD signal grew on increasing the ligand concentration until a critical point, and for higher ligand concentration a strong reduction of the CD signal was observed. This behaviour was ascribed to the variation of the cysteine binding mode that is preferentially tridentate in the low ligand concentration condition, while a bidentate coordination is favoured at higher ligand concentrations, causing a

loss of the QDs chirality. It is reasonable to conclude that the stability of the chiroptical properties for the present AIS QDs in high ligand concentrations is related to the lower affinity of the cysteine for the Ag^{+} ad In^{3+} ions exposed on the particle surface. As showed in **Fig. 17**, the excess of ligand produced in the concentration above the saturation conditions (above 8.0 mM) contributes largely to the free ligand population without affecting the ligand-nanocrystal interface and consequently also the chiroptical activity. This conclusion is supported by the evidence of a slow exchange regime observed by Kuznetsova et al.[106] in the NMR study of the interaction between cystine and CdSe/CdS QDs, clearly evidencing a higher ligand affinity for the Cd^{2+} cations exposed on the QDs surface in the investigated conditions. Similar dynamic was reported in the NMR analysis of interface chemistry of water soluble CdTe QDs stabilised with thioglycolic acid which shows close (3.39 and 3.36 ppm) but distinct resonances for the α protons related to free and bonded ligands, which contributions can be resolved by deconvolutions of the peaks.[127] However, it must be considered that the effect on the ligand dynamics can be also affected by the different pH as the stability of thiolate ligand on the surface of Cd-based quantum dots strongly increases in alkaline pH[128] and further studies on the effect of pH and solvent on the dynamics of the chiral ligand shell seems to be fundamental to understand the optimization of the chiroptical activity of chiral QDs.

2.3 AIS/ZnS core shell QDs

In order to improve the optical properties of chiral **AIS14** QDs, a post synthesis treatment for the deposition of a ZnS shell is investigated. The process, depicted in **Fig. 19** is based on the thermal decomposition of thioacetamide at 80 °C in a solution of $Zn(OAc)_2$, cysteine and **AIS14** QDs. In order to avoid heterogeneous nucleation of ZnS, the concentration of the shell pre-

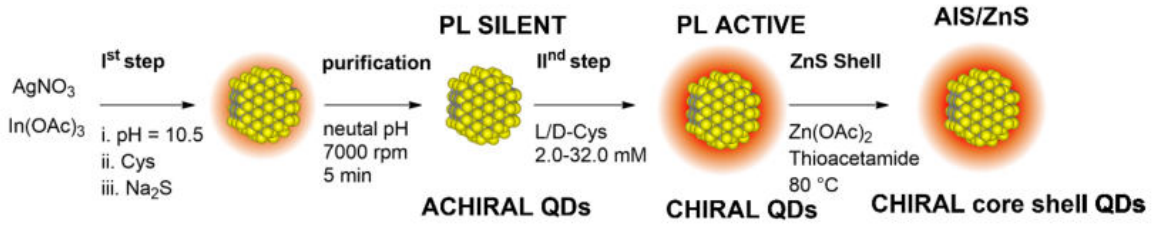

Figure 19: schematic representation of the synthetic steps employed to produce AIS/ZnS core shell QDs

cursors is kept at 0.03 mM and raised step by step with successive injections (100 µl of precursor solution 10mM) at intervals of 0.5 h. The duration of these steps is optimised according to the increment of the photoluminescence activity.

To collect evidence on the shell formation, the PLQY of colloidal solution is analysed after different treatments. **Fig. 20a** shows the variation of the PLQY with the increasing of the total shell precursor solution added in the reaction mixture. The initial PLQY of **AIS14** QDs is around 0.26. After the first injection it raises to 0.38 and, after the second injection, it reaches a plateau at around 0.42. Further addition of ZnS precursors solution causes a decrease of the PLQY, due to the aggregation of the nanocrystal and to the loss of colloidal stability. The value of 0.29 observed after the fourth injection is purely indicative since the measurement is severely affected by the scattering of the solution and the precipitation of the nanocrystals during the measurement. To observe independently the contribution to the PLQY related to the annealing process at 80 °C, the variation of the PLQY of a **AIS14** QDs colloidal solution is monitored without the addition of the shell precursors solution. **Fig. 20b** shows that after 2.0 h the PLQY increases from 0.26 to 0.31. This behaviour can be related to the reduction of surface defects involved in non-radiative recombination process. Furthermore, the experimental value, lower than the PLQY observed in the presence of ZnS, suggests that the passivation of some of the defect on the particle surface is taking place. This observation agrees with the deposition of

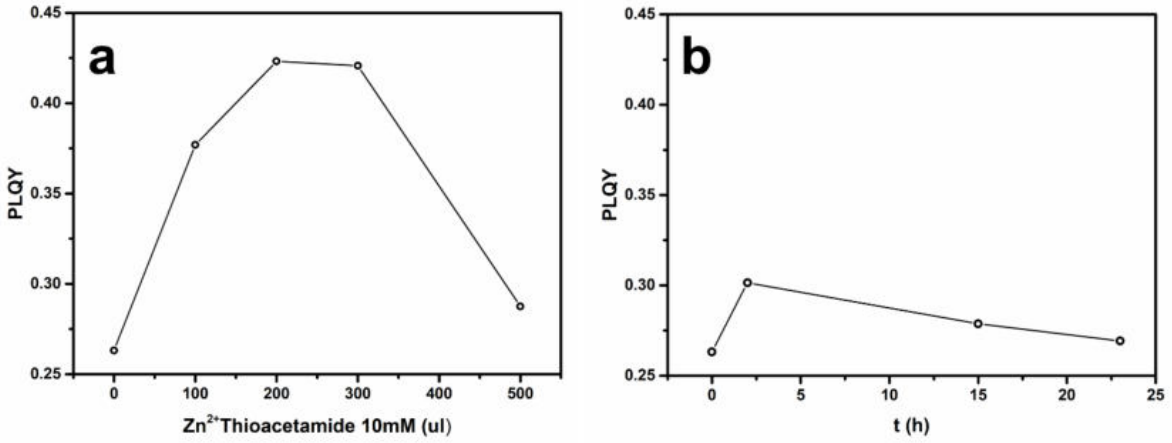

Figure 20: PLQY analyses, a) effect of the ZnS precursor solution, each step is followed by a 0.5 h of heating to allow the precipitation of ZnS. b) effect of the thermal annealing at 80 °C for different times.

an inorganic shell of a large band gap semiconductor such as ZnS. The chemical composition analysis of different batches of **AIS14/ZnS** core shell QDs via EDS reveal that this method produced nanocrystals with a molar ratio of zinc ion (N_{Zn}) to silver ion N_{Ag} (N_{Zn}/N_{Ag}) of 0.16.

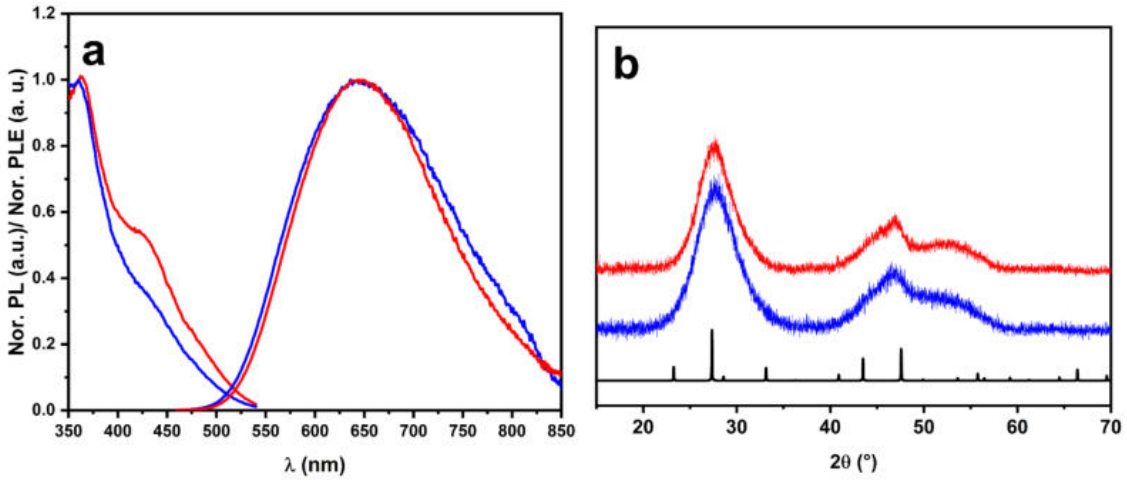

Figure 21: PL and PLE analysis of **AIS14** QDs (blue) and **AIS14/ZnS** core shell QDs (red), b) XRD analysis of **AIS14** QDs (blue) and **AIS14/ZnS** core shell QDs (red), the reference pattern (black) is related to the spinel $AgIn_5S_8$ phase ICSD1619

The PL spectra of **AIS14** QDs and **AIS14/ZnS** core shell (see **Fig. 21a)** show only a minor variation of the emission band that remain centred at 635 nm, in contrast with multiple evidence on the blue-shift of the electronic transition in AIS and CIS QDs after the deposition of the ZnS shell. This effect is usually associated to the Zn diffusion in the QDs core that can cause alloying or can reduce the size of the confinement. Both these effects can cause a blue-shift of the absorption and emission bands.[57,129] Even though in our case it is possible that the low temperature employed can facilitate the deposition of an outer layer of ZnS it is not high enough to induce ion migration in the particle core. Similar observations were collected by Song et al.[130] on a shell deposition method at temperature around 30 °C. The effect of the shell presence on the PLE is more remarked and the shoulder at 420 nm increases suggesting that the ZnS efficiently passivate some surface defects increasing the efficiency of the radiative recombination of the defect mediated emission. The XRD analysis **Fig. 21b** shows only little variation of the crystal structure related to the effect of the annealing process and no peaks associated to the presence of ZnS are observed.

The effect of the ZnS deposition on the nanocrystals chirality is investigated by CD spectroscopy. As can be seen in **Fig. 22** the treatment causes little to no variation to the UV/Vis spectra in the exciton region meaning that the electronic transitions characteristic of the nanocrystal core are mainly unaffected by the deposition of the ZnS layer. Instead, a variation of the CD activity is observed with a reduction of the intensity at 420 nm and the increasing of the intensity at 375 nm. Since the origin of the chirality in QDs is mainly localized at the particle ligand interface, it is possible that CD spectroscopy is particularly sensible to variation of the structure on the particle surface. However, the observation of CD active transition confirms

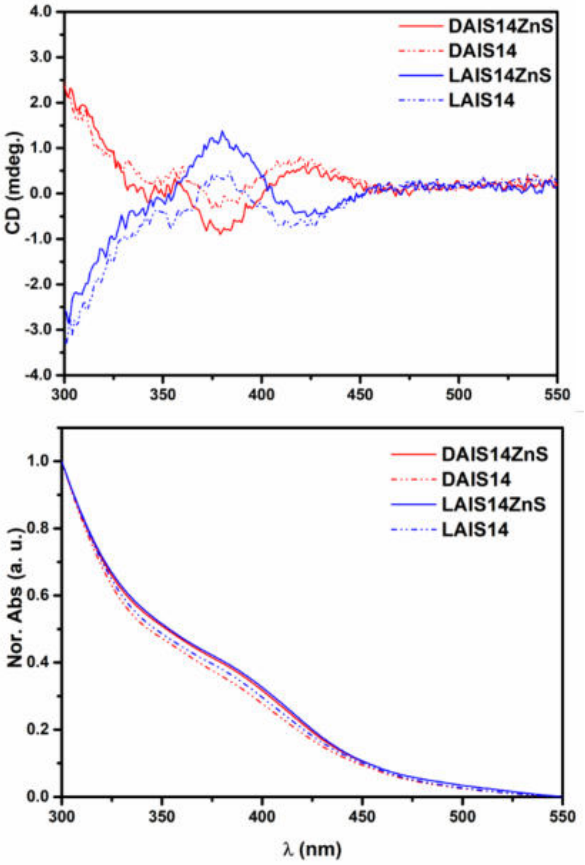

Figure 22: CD (top) and UV/Vis absorption spectra (bottom) of AIS14 QDs and AIS14/ZnS core shell QDs.

the isolation of chiral AIS/ZnS core-shell QDs. Despite our attempts to directly investigate the effect of the deposition of the ZnS shell on the QDs morphology by TEM, at the moment we are still struggling to collect satisfying micrographs on AIS/ZnS QDs. The main issue associated to the morphological characterisation is the above-mentioned aggregation during the preparation of the TEM grids.

2.4 COMPOSITIONAL STUDY

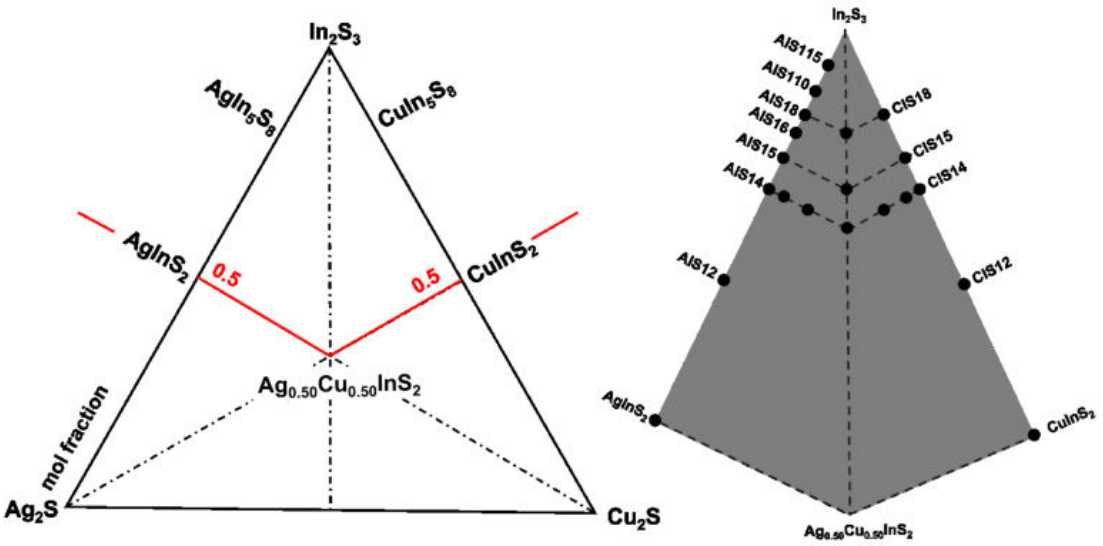

Figure 23: Ternary diagram representing the different sulfide solid solutions in the In_2S_3-Ag_2S-Cu_2S system (left). Detail of the area of the ternary diagram interested in the discussed investigations with marks related the samples considered in the following discussion (right).

Since the electronic properties of I-III-VI QDs are known to be easily tunable by changing the nanoparticles composition, we extended our investigation to probe the effect of different chemical compositions on the QDs structure, on the optical and the chiroptical properties. Through small variations in the synthetic procedure developed for the preparation of **AIS14** QDs, it is possible to produce a wide variety of ternary systems (both AIS and CIS), with a fine control on the particle composition. The properties of quaternary phases produced with different silver, copper and indium content (ACIS) and their core-shell systems produced after the deposition of ZnS in a post synthesis treatment are also explored.

Fig 23 represents the ternary diagram of the chalcogenide phases. The binary sufides (In_2S_3, Ag_2S and Cu_2S) are reported in the corners, the ternary phases, such as $AgInS_2$ and $CuInS_2$, lie on the edge of the diagram, according to their relative compositions, and different quaternary solid solutions lie in the area into the diagram (e.g. $Ag_{0.50}Cu_{0.50}InS_2$). The red lines highlight the conditions of molar fraction 0.5 M_2S (M: Ag or Cu)-0.5 In_2S_3 that give the formation of the stoichiometric $MInS_2$ phases and their quaternary derived systems. Since the optical properties of In-rich phases are particularly promising, this study is mainly focused on the investigation of the portion of the diagram related to In-rich solid solutions, and so beyond the red lines in the direction of In_2S_3. This region is further detailed in **Fig 23** and the qualitative position of the prepared samples is reported as black dots with their relative labels.

Concerning the core shell QDs systems, since the effect of the ZnS shell deposition affects mainly the PLQY, the discussion in the following text is focused on the physico-chemical characterisations collected by the analysis of the QDs core. The core shell systems are considered only for the evaluation of the PLQY increasing after the treatment, and in for the general PL/PLE characterisations in the cases of non-luminescent QDs cores (as observed for the CIS QDs that without the shell treatment do not present photoluminescence activity). These cases are properly labelled in the text.

2.4.1 $AgInS_2$ - In_2S_3

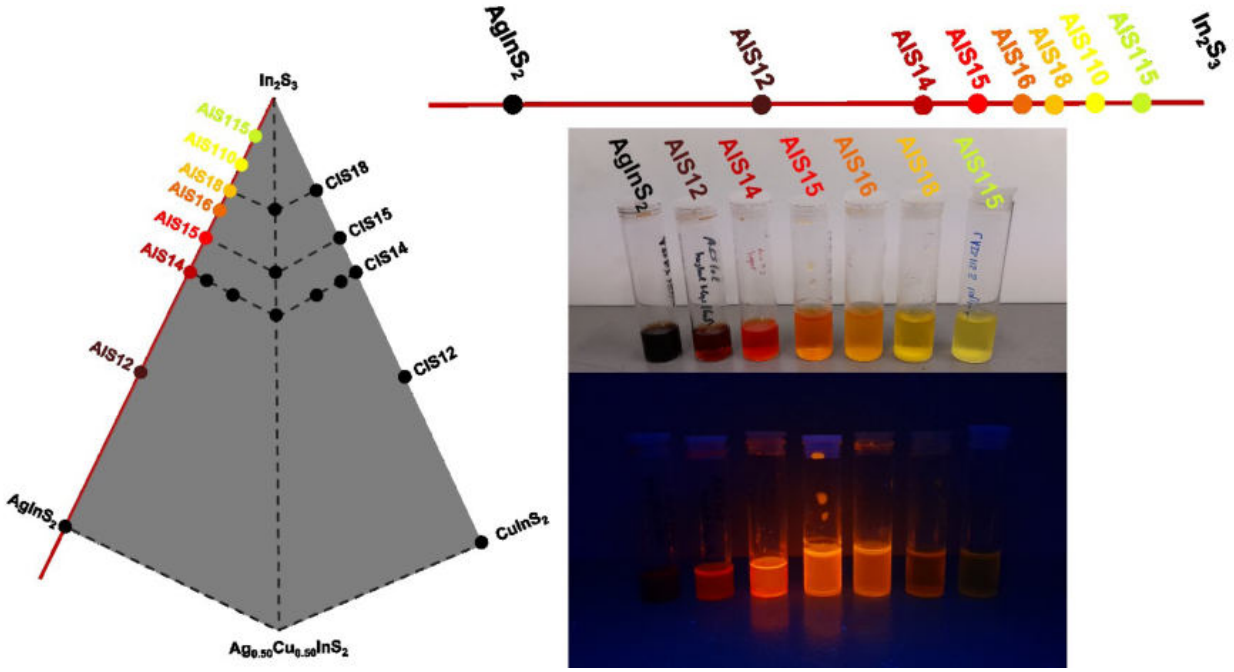

Figure 24: left) detail of the sulfide phases diagram, the position of the sample considered in this study is evidenced. Right) pictures of the QDs colloidal solutions under ambient light (top) and UV light at 365 nm (bottom).

AIS QDs, with different Ag/In contents, are synthetised by adjusting the metal ratio N_{Ag}/N_{metal} (molar ratio) in reaction mixture using different volumes of silver nitrate 0.1 M and indium acetate 0.1 M solution as reported in Materials and Methods section (**Table 5**). The composition and pictures of the QDs colloidal solution are shown in **Fig. 24.** The labels of the samples and some characteristic properties of the sample are reported in **Table 1** (and plotted in **Fig. A13**).

The second and the third columns of **Table 1**, show a change of composition between the molar ratio used for the preparation of the reaction mixture (N_{Ag}/N_{metal} RM) and the value (N_{Ag}/N_{metal} QDs) determined by EDS and ICP analysis In particular, an excess in the Ag^+ content is observed for all systems (**AIS11** – **AIS115**). This effect is accentuated with the reduction of the N_{Ag}/N_{metal} ratio (as shown also in **Fig. A14**). However, the variation in the composition of the reaction mixture is reflected in the nanoparticles composition and a linear trend can be appreciated in **Fig. A14.** Similar observations are already reported using other methods.[55]

Table 1

Sample name	N_{Ag}/N_{metal} RM	N_{Ag}/N_{metal} QDs	Eg (eV)	λem (nm)	FWHM (nm)
AIS11	0.50	0.51	2.32	780	183
AIS12	0.33	0.36	2.69	693	207
AIS14	0.20	0.24	2.84	635	172
AIS15	0.17	0.20	2.88	613	147
AIS16	0.14	0.18	2.89	608	138
AIS18	0.11	0.14	2.92	597	95
AIS110	0.09	0.12	2.94	585	120
AIS115	0.06	0.09	2.83	587	115

The trends observed reducing the N_{Ag}/N_{metal} ratio clearly show the expected blue shift of the band edge and of the position of the emission band. The optical energy gap (E_g), evaluated according to Tauc Plot (**Fig. A15a,b**), evidences an increasing of the band gap energy from 2.32 eV, sample **AIS11,** to 2.94 eV for **AIS110**. Sample **AIS115** shows a significant variation with respect to the trend for the samples from **AIS11** to **AIS110**, with an E_g to 2.83 eV (**Fig. A15c**). This behaviour can be ascribed to the low silver content. The inorganic matrix is probably close to a transition between $AgIn_5S_8$ and In_2S_3, causing the anomalous variation of the electronical properties. The maximum of PL emissions follows the trend observed for the E_g with a consisted blue shift, from 780 to 585 nm, when N_{Ag}/N_{metal} ratio is reduced. A consistent reduction of the FWHM can be also measures with the narrowest emission (95 nm) observed for the

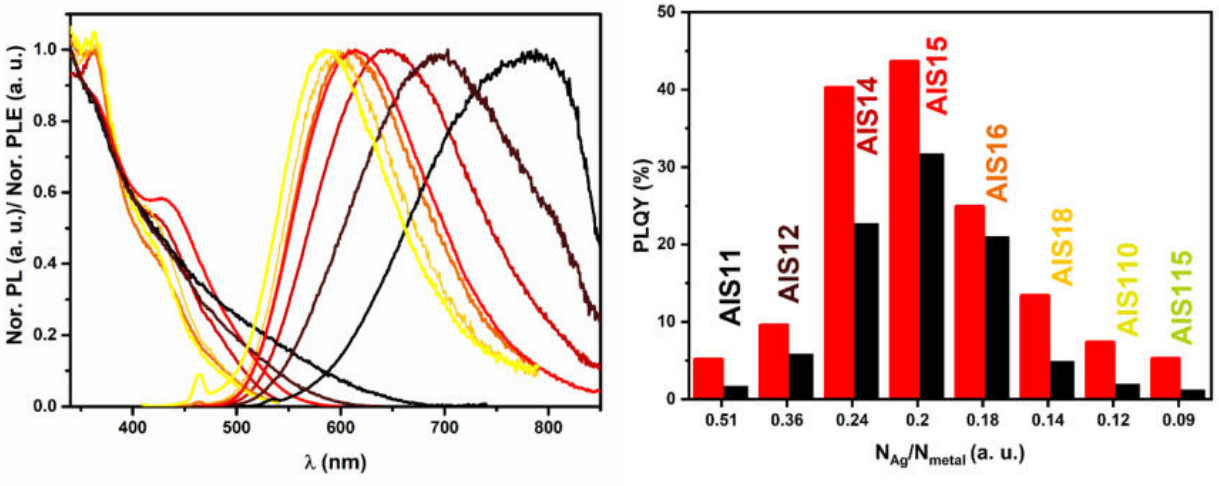

Figure 25: left) PL and PLE spectra of AIS QDs with different chemical composition. Right) PLQY AIS QDs (black) and AIS/ZnS core shell QDs with different chemical composition.

sample **AIS18** (**Fig. 25**). It should be remarked that the FWHM for the sample **AIS11** is clearly underestimated due to the low sensitivity of the detector in the near infrared region. The variations of the band gap energy agree with the results of another paper,[55] and as discussed above, they are associated to the variation of the contribution related to the silver orbital to the maximum of the valence band.

Fig. 25 shows the trend for the PLQY of the AIS QDs core (black) and the AIS/ZnS core-shell QDs (red). For all the sample an increasing of the PLQY is observed after the deposition of the ZnS shell. **AIS14** and **AIS15** show the highest PLQY, more than 0.40 for the core-shell QDs, that correspond to a ratio N_{Ag}/N_{metal} of 0.24 and 0.20 respectively. Instead, a reduction to a value

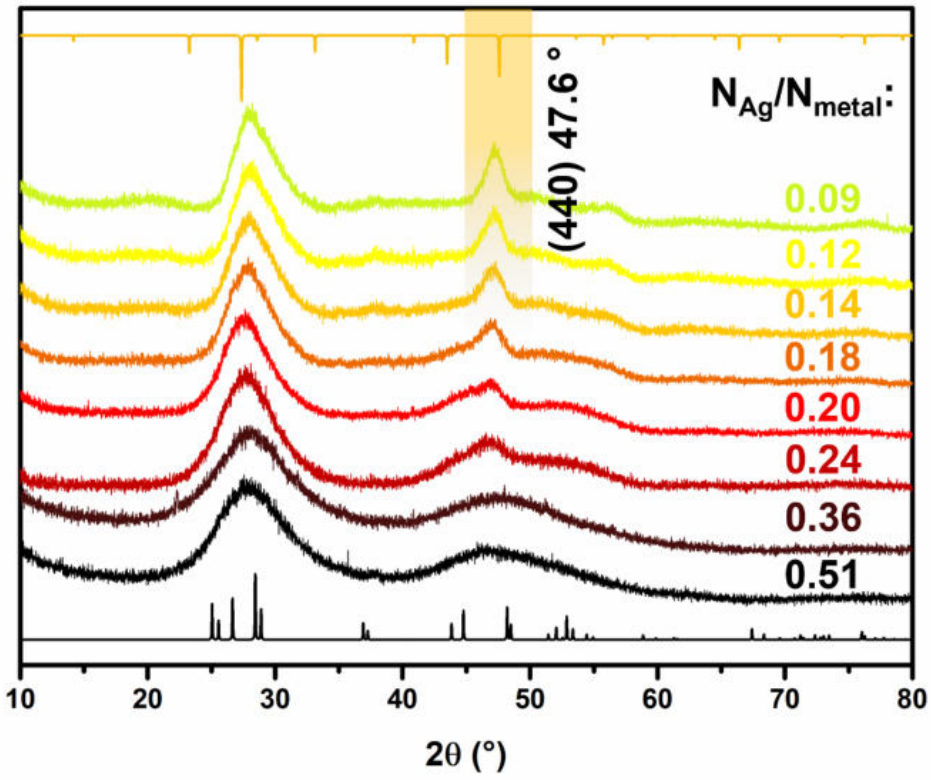

Figure 26: XRD patterns of AIS QDs with different chemical composition, according to their N_{Ag}/N_{metal} ratio in the QDs. The reference patterns are related to the $AgIn_5S_8$ spinel phase (yellow) ICSD51619 and $AgInS_2$ tetragonal phase (black) ICSD51617

around 0.10 is observed for the samples with both highest Ag content (**AIS11** and **AIS12**) or lowest Ag content (**AIS18** and **AIS10**).

The structure of the nanocrystals is investigated by XRD (**Fig. 26**). Even though the profiles are very broadened, the orthorhombic $AgInS_2$ phase can be detected for the samples with highest N_{Ag}/N_{metal} ratio (**AIS11** and **AIS12**). The wide, but defined peak at 47.6 °, ascribed to the (440) planes of the cubic spinel phase, appears for N_{Ag}/N_{metal} ratio equal or lower of 0.24 (**AIS14** – **AIS115**). The large broadening of the peaks of the orthorhombic phase can be related to the

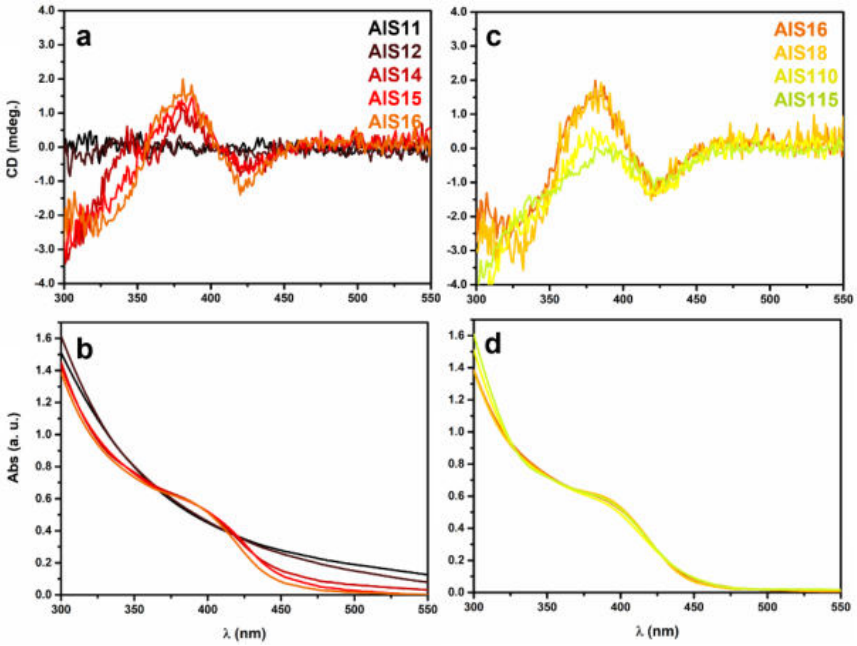

Figure 27: CD and UV/Vis absorption spectra of the sample **AIS11** - **AIS16** (a and b) and **AIS16** – **AIS115** (c,d).

contribution of a higher number of profiles present in this phase with lower symmetry with respect to the spinel phase. However, further analysis on the nanocrystal morphology by TEM are required to exclude effect of the particle size on the diffraction patterns. The position of the profiles of the cubic phase is slightly shifted toward higher angle with the increasing of the indium content, this effect can be appreciated for the (311) peak in **Fig. A16** and it is related to the reduction of the silver content that present a larger ionic radius r_{Ag+} (129 pm) than r_{In3+} (94 pm). A similar trend was reported by Sachanyuk et al.[131] in $AgIn_5S_8$ thin films prepared with different chemical composition.

The effect of the chemical composition on the optical chirality is investigated by CD spectroscopy. **Fig**. **27** Shows the CD spectra in the excitonic region of the L-QDs colloidal solutions at

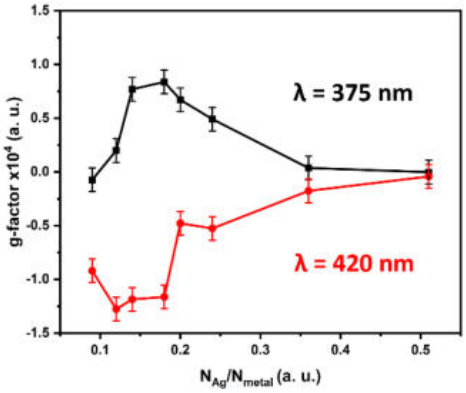

Figure 28: plot of the g-factor value observed for AIS QDs with different composition, the error bars represent the noise of the CD measurements.

the same nanocrystal and L-cysteine concentrations. The spectra of **AIS11** and **AIS12** does not show any CD active transition and the UV/Vis absorption shows the typical diffuse spectra of the $AgInS_2$ QDs without any characteristic transition.[55] When the N_{Ag}/N_{metal} ratio drops below 0.24 (**AIS14** – **AIS110)** a band centred around 400 nm is observed. This is a typical feature observed in non-stoichiometric indium-rich phases and characterise the absorption spectra of the $AgIn_5S_8$ phase.[50] The samples show the characteristic CD transition as already discussed for **L-AIS14** in the previous section: a negative band is centred at 420 nm and positive one at 375 nm.

The intensity of the CD transitions is clearly affected by the nanocrystals composition. To exclude effect of the different absorption, the optical chirality of the different QDs is compared considering the g-factor. **Fig 28** shows the intensity of the transitions at 375 and 420 nm at different N_{Ag}/N_{metal} ratio. The observed trend shows a higher efficiency of the chiral induction for the sample **AIS14**, **AIS15** and **AIS16**. These samples are close to the ideal stoichiometry of the $AgIn_5S_8$ phase, suggesting that this crystallographic phase is particularly sensible at the effect of the chiral ligand. At low silver content (**AIS18** and **AIS115**) a reduction of the efficiency of the chiral transfer is observed. In this condition the contribution of the silver 4d orbitals to the maximum of the valence band decreases with the silver molar concentration affecting the multipolar coupling with the chiral ligand and causing the reduction of the interaction. Moreover, due to the depopulation of exposed silver cations, a variation of the ligand binding mode on the particle surface could affect the chemistry at the particle-ligand interface.

2.4.2 $CuInS_2$ - In_2S_3

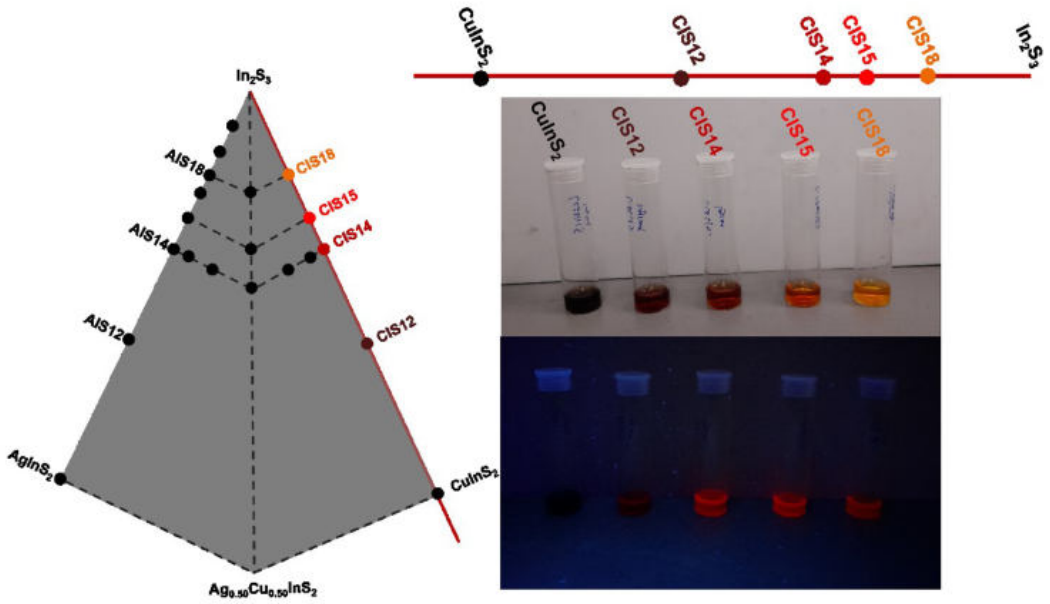

Figure 29: left) detail of the sulfide phases diagram, the position of the sample considered in this study is evidenced. Right) pictures of the QDs colloidal solutions under ambient light (top) and UV light at 365 nm (bottom).

The synthesis conditions optimised for the production of AIS QDs are adapted to produce CIS QDs. The $AgNO_3$ solution is replaced with $Cu(OAc)_2$ solution and the Cu(II) is reduced in situ by the cysteine to Cu(I). To avoid reoxidation of Cu(I) and undesired catalytic process that cause the cysteine decomposition,[132–134] all the synthesis of CIS QDs and of the corresponding core-shell systems are conducted under nitrogen atmosphere and with the use of purging procedures to reduce the oxygen content in the deionized water. **Fig 29** shows the compositions and pictures of the QDs colloidal solutions under ambient and UV light.

The labels of the samples and some characteristic properties of the CIS QDs samples are reported in **Table 2** and **Fig. A17.** Even in this case, the EDS and ICP analyses on the QDs compositions, reveal that the N_{Cu}/N_{metal} molar ratio used in the reaction mixture (based on the ratio of the precursor solutions, Materials and Methods, **Table 6**) is not the same of the final QDs. As observed for silver in AIS QDs, CIS QDs contain an excess of copper with respect to the N_{Cu}/N_{metal} in the RM. However, in the case of CIS QDs the differences are larger for the samples **CIS11** and **CIS12** with high N_{Cu}/N_{metal} ratio, as can be appreciated in **Fig. A18**. Even in this case a good linear trend in the composition is observed in **Fig. A18**.

TABLE 2 (* indicate the data related to the CIS/ZnS core shell QDs)

Sample name	N_{Cu}/N_{metal} RM	N_{Cu}/N_{metal} QDs	Eg (eV)	λem (nm)	FWHM (nm)
CIS11	0.50	0.62	2.00	-	-
CIS12	0.33	0.42	2.12	694*	131*
CIS14	0.20	0.25	2.27	678*	134*
CIS15	0.17	0.18	2.37	660*	135*
CIS18	0.11	0.14	2.45	639*	138*

The reduction of the N_{Cu}/N_{metal} ratio caused the blue shift of the electronic transition (see the Tauc plot reported in **Fig. A19**). The E_g increases from 2.00 eV (**CIS11**) to 2.45 (**CIS18**) with the reduction of the N_{Cu}/N_{metal} ratio from 0.62 to 0.14. The blue shift is also reflected in the photoluminescence. In this case only the core-shell CIS/ZnS QDs systems are considered for the PL and PLE characterisations since CIS QDs show no appreciable photoluminescence. Furthermore, **CIS11** is excluded by this comparison since no PL activity is observed even with the ZnS shell. It should be remarked that the ZnS shell deposition method has been optimised for AIS QDs and then adapted to the CIS preparation with the only variation that all the manipulations are performed in nitrogen atmosphere. Further optimizations are probably necessary to improve the photoluminescence activity of CIS/ZnS core-shell QDs. The PL and PLE analysis of the colloidal solutions are reported in **Fig. 30**. The analyses show an evident blue shift of the emission maximum, from **CIS12/ZnS** λ_{em} = 694 nm to **CIS18/ZnS** λ_{em} = 639 nm. This trend is very close to the trend of AIS QDs. In contrast to AIS QDs, the FWHM of the emission band does not show any variation with the reduction of the N_{Cu}/N_{metal} ratio and a broad PL band

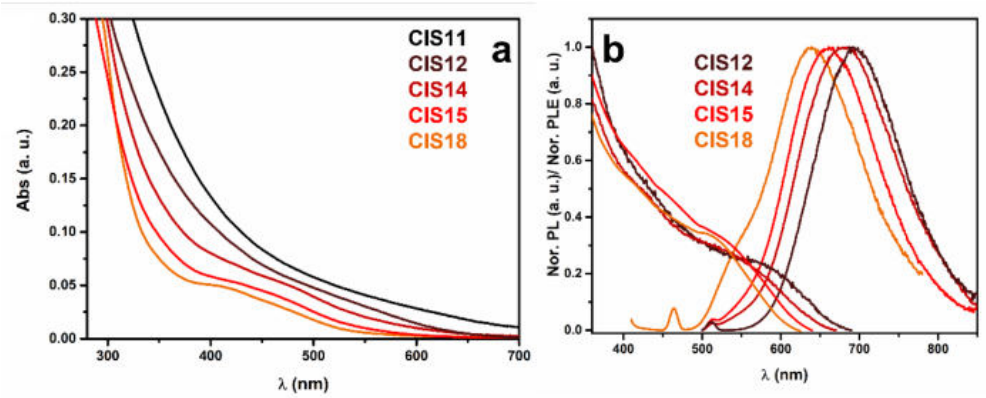

Figure 30: a) UV/Vis absorption spectra of **CIS11** – **CIS18** QDs colloidal solution. b) PL and PLE spectra of **CIS12/ZnS** – **CIS18/ZnS** core-shell QDs colloidal solution.

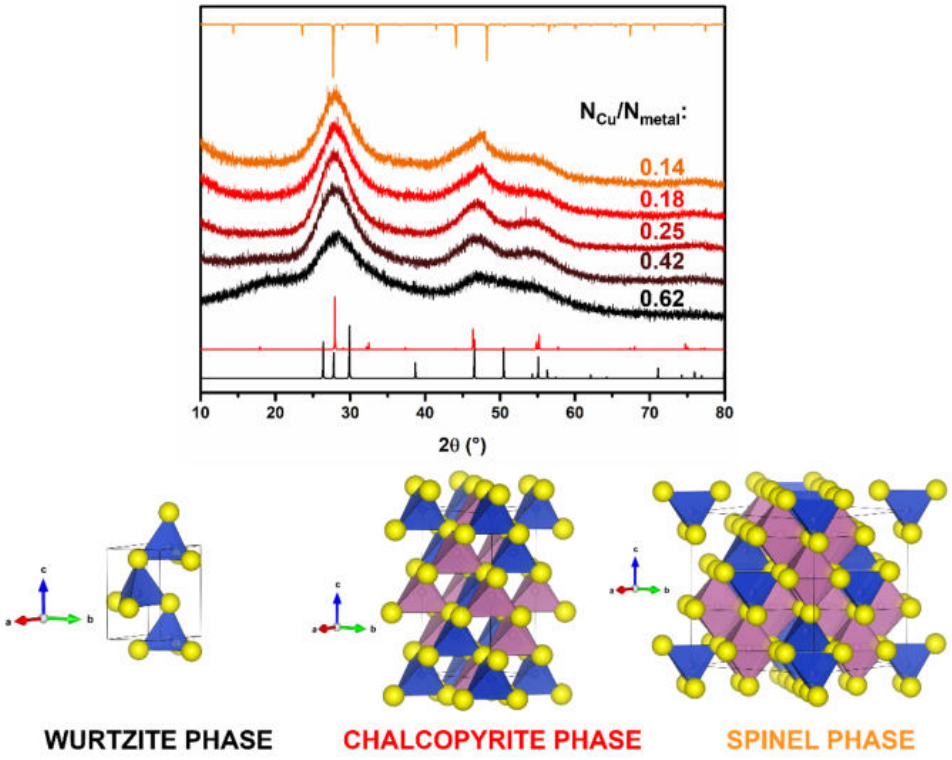

Figure 31: XRD patterns of CIS QDs produced with different chemical composition according to their N_{Cu}/N_{metal} ratio in the QDs (top), the reference patterns correspond to: $CuInS_2$ wurtzite phase ICSD163489 (black), $CuInS_2$ chalcopyrite phase ICSD66865 (red) and $CuIn_5S_8$ spinel phase ICSD16423 (yellow). Representation of the unit cells of the different crystallographic structures (bottom).

with FWHM of about 135 nm is observed for all the samples. The PLQY of core shell CIS/ZnS is estimated to be 1.9, 3.5, 3.9 and 1.4 % for **CIS12/ZnS**, **CIS14/ZnS**, **CIS15/ZnS** and **CIS18/ZnS**. CIS/ZnS QDs show lower PLQY than AIS QDs, even though they evidence a similar trend characterised by a maximum of the PLQY for the specimens with chemical composition close to the idea stoichiometry of the I-III_5-VI_8 spinel phase (N_{Cu}/N_{metal} ratio 0.25 and 0.18).

The structural investigations are performed by XRD analysis (**Fig**. **31**). Even though the line broadening prevents any detailed investigation, the analysis of **CIS11** (N_{Cu}/N_{metal} = 0.62) suggests the presence of the wurtzite phase. With the reduction of the Cu content (samples **CIS12** and **CIS14**) the chalcopyrite phase can be observed. Finally, the spinel phase can be detected for N_{Cu}/N_{metal} = 0.18 and 0.14 (samples **CIS15** and **CIS18**). This finding suggests that a higher $N_{monovalent\ cation}/N_{metal}$ ratio is required to stabilise the spinel $CuIn_5S_8$ with respect to $AgIn_5S_8$. Indeed, the CIS systems at a composition close to $N_{Cu}/N_{metal} \approx 0.25$ shows the preferential formation of the chalcopyrite phase, while for a composition very closed, N_{Ag}/N_{metal} = 0.24, AIS systems evidence the spinel phase.

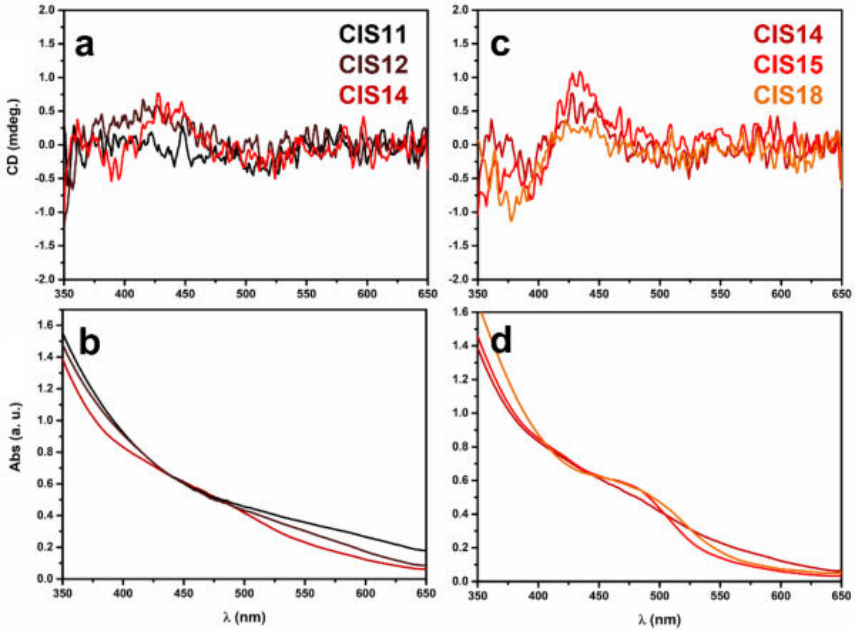

Figure 32: CD and UV/Vis absorption spectra of the sample **CIS11** - **CIS14** (a and b) and **CIS14** – **CIS18** (c,d).

Fig 32 shows the CD and UV/Vis absorption spectra of the different L-QDs colloidal solution at the same nanocrystal and L-cysteine concentrations. The analysis revealed: *i*) the total absence of CD activity for **CIS11**, *ii*) a low CD signal, at around 450 nm for the **CIS12** and **CIS14**, and *iii*) a more defined transition for **CIS15** and **CIS18**. To further analyse the meaning of the CD signal of CIS QDs, **L-CIS15** and **D-CIS15** QDs results are reported in **Fig. 33**. **L-CIS15** QDs shows a weak negative CD band at 525 nm, a positive CD band at 433 and a second negative peak below 410 nm. **D-CIS15** gives the opposite signal.

Our analyses evidence that the transfer of chirality for CIS QDs, using cysteine as chiral ligand, is less effective than for the AIS QDs. However, even in the case of CIS QDs the highest optical chirality is observed in the samples that presents a spinel $CuIn_5S_8$ phase.

Further studies on the transfer of chirality in $CuIn_5S_8$ QDs using other chiral ligands are required. Moreover, the investigation of the effect of copper ions on the coordination chemistry at the particle ligand interface are in progress.

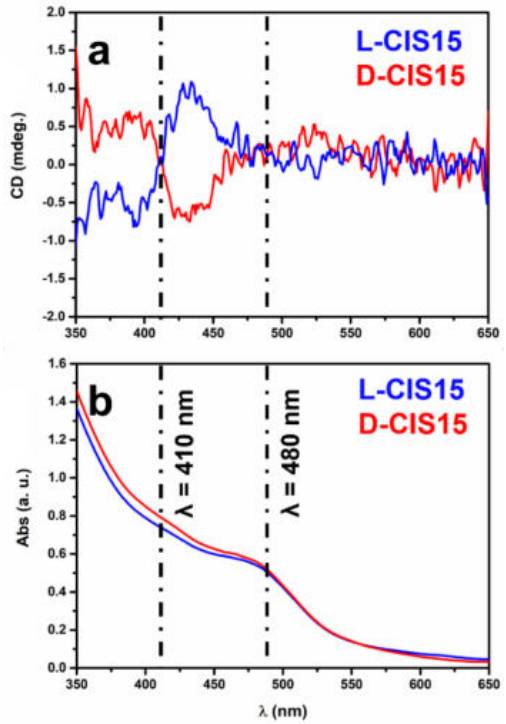

Figure 33: a) CD and b) UV/Vis absorption spectra of **L-CIS15** (blue) and **D-CIS15** (red).

2.4.3 AIS14 - CIS14

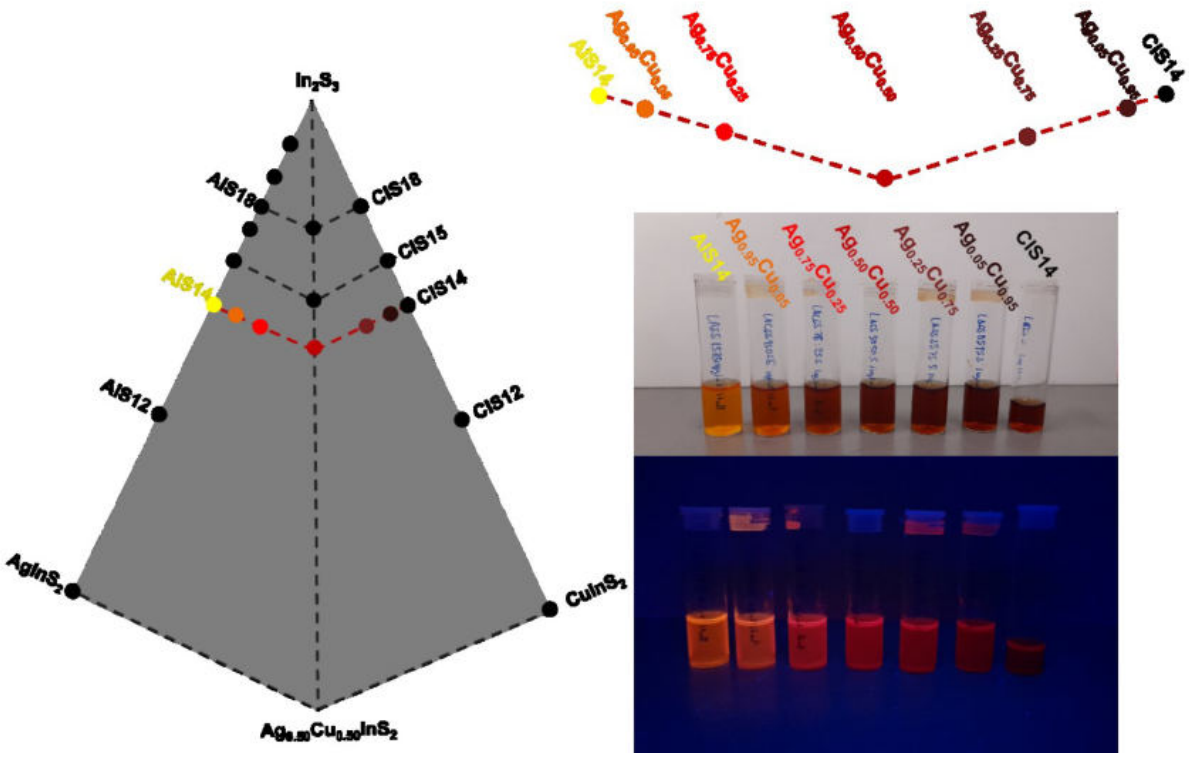

Figure 34: left) detail of the sulfide phases diagram, the position of the sample considered in this study is evidenced. Right) pictures of the QDs colloidal solutions under ambient light (top) and UV light at 365 nm (bottom).

This study covers the investigation on quaternary silver copper indium QDs considering the variation of the silver to copper ratio and keeping constant (around 0.25) the molar ratio of the monovalent cations (silver and copper) to the total metal ions (N_{Ag+Cu}/N_{metal}). The N_{Ag+Cu}/N_{metal} ratio of 0.25 is chosen due to the promising optical properties (PLQY) observed for the QDs with this composition. **Fig. 34** shows the compositions and pictures of the QDs colloidal solutions under room and UV light.

QDs with the different compositions are produced by adjusting the ratio between silver and copper in the reaction mixture. The labels of the samples and some of their properties are reported in **Table 3**. The EDS and ICP analyses reveal a QDs composition very close to the ones used for the preparation of the reaction mixture (Material and Methods, **Table 7**). The main variation is observed for **ACIS5050** that presents a 0.45:0.55 ratio. The constant N_{Ag+Cu}/N_{metal} ratio is confirmed to be 0.25 (**Fig. A20a**). The analysis of the Zn content in the ACIS/ZnS core shell QDs (**Fig. A20b**) shows a molar ratio $N_{Zn}/N_{(Ag+Cu)}$ around 0.16 for all the samples, confirming that the method used for the shell deposition produces samples with comparable amount of zinc.

Table 3

Sample name	N_{Ag}:N_{Cu} RM	N_{Ag}:N_{Cu} QDs	Eg (eV)	λem (nm)	FWHM (nm)
AIS14	1.0:0	1.0:0	2.84	635	174
ACIS9505	0.95:0.05	0.93:0.07	2.59	663	175
ACIS7525	0.75:0.25	0.74:0.26	2.48	676	178
ACIS5050	0.50:0.50	0.45:0.55	2.42	691	177
ACIS2575	0.25:0.75	0.26:0.74	2.41	694	182
ACIS9505	0.05:0.95	0.08:0.92	2.39	695	195
CIS14	0:1.0	0:1.0	2.37	698	134

The increasing of the copper content reduces the energy gap as clearly appreciable by the UV/Vis spectra (**Fig. 35a**). The same figure shows the red shift of the shoulder located at 400 nm for **AIS14** and 435 nm for **CIS14**. We determined the optical energy gap E_g by the analysis of the Tauc plot. The red-shift is observed moving from **AIS14** (E_g = 2.84 eV) to **ACIS5050** (E_g 2.42 eV), and further increasing of the copper content affect only slightly the position of the E_g. Sample **CIS14** (2.37 eV) shows the smallest value. This behaviour was described by Huges et al.[63] for $Ag_{1-x}Cu_xInS_2$ QDs produced by Cu(I) ion exchange in $AgInS_2$ QDs. The observed dramatic effect of Cu(I), even at low concentration, was related to the formation of copper-related defect with energy in the energy gap region. The increase of the copper concentration to 0.2 causes the formation of a copper related bands and only minor variations are observed for higher copper concentration.

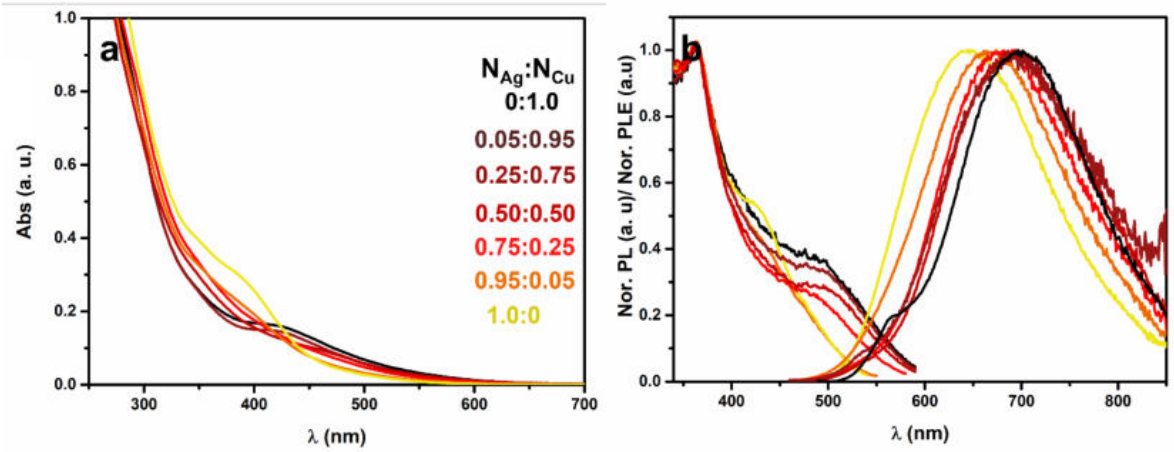

Figure 35: Optical characterisation of ACIS QDs colloidal solutions with different compositions, according to their silver to copper ratio in the reaction mixture. a) UV/Vis absorption spectra of **AIS14** – **CIS14** QDs colloidal solution. b) PL and PLE spectra of **AIS14** – **CIS14** QDs colloidal solution.

The PL analysis (**Fig. 35b**) reveals a red shift of the emission maximum at increased copper content. The effect on the PL is more homogeneous than the variation reported by other authors.[63] The PLE (**Fig. 35b**) analysis shows a decrease of the contribute at 440 nm observed in **AIS14** at higher copper content. A new band, located at around 500 nm, raises when the cop-

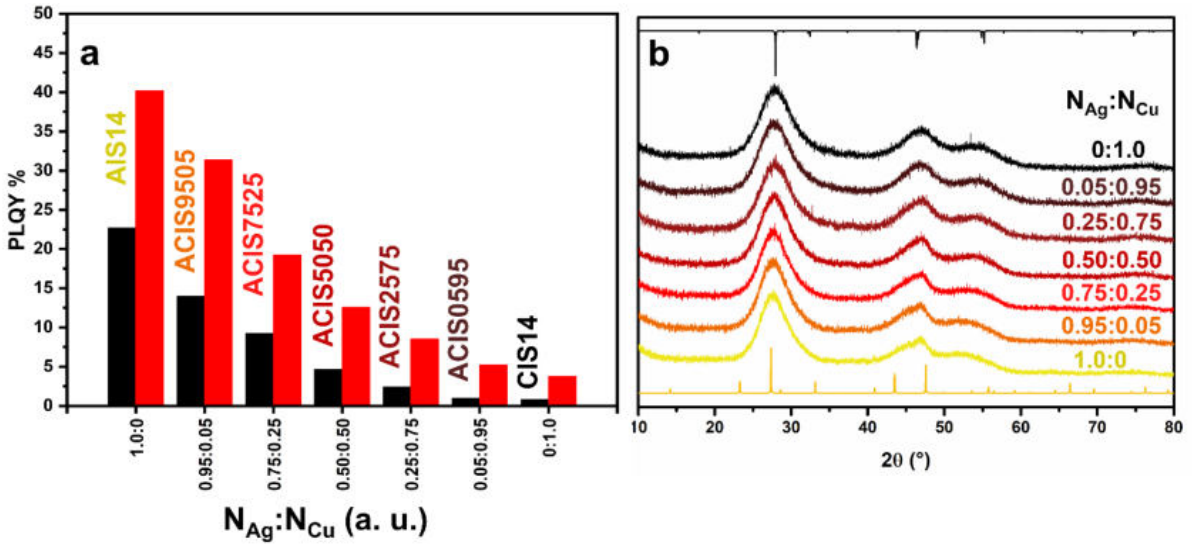

Figure 36: a) PLQY for ACIS QDs (black) and ACIS/ZnS core shell QDs /red). b) XRD patterns of QDs with different chemical compositions, according to their silver to copper ratio in the reaction mixture. The reference patterns represent $AgIn_5S_8$ spinel phase ICSD51619 (yellow) and $CuInS_2$ chalcopyrite phase ICSD66865 (black).

per content is higher than 0.5 (**ACIS5050** to **CIS14**). This transition can be associated to copper related defects and to the copper related band. The effect of the copper content on the PLQY is represented in **Fig. 36a**, a monotonic reduction follows the red-shift observed in the PL with the increase of the copper concentration. This behaviour is observed in both ACIS core QDs and ACIS/ZnS core shell QDs.

The structural investigation is performed by XRD (**Fig. 36b**). The diffraction patterns show similar broadening of the peak at 28.1 °. The variation of the shape and intensity of the peaks, between 40 and 60 °, suggests a crystallographic transition. In particular, the increase of the copper content reduces the intensity of the profiles associated to the (440) planes of the spinel phase and the peaks of the chalcopyrite phase can be observed. The line broadening related to the small crystal size complicates the exact evaluation of the conditions that cause the phase transition. However, the trend suggests that the samples **AIS14**, **ACIS9505** and **ACIS7525** present a spinel phase and the sample with higher copper content (**ACIS5050** - **CIS14**) seem to adopt a chalcopyrite structure.

The chiroptical properties of the L-QDs colloidal solution are investigated by CD spectroscopy. **Fig. 37** show the CD spectra in the excitonic region of solution containing the same QDs and

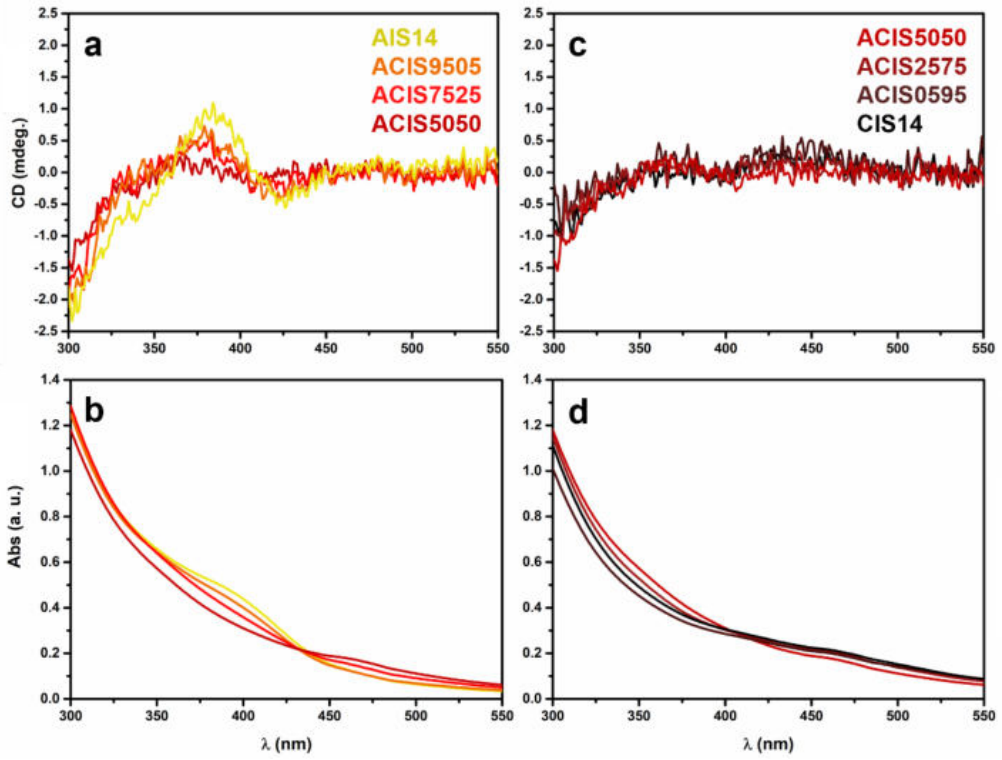

Figure 37: CD and UV/Vis absorption spectra of the sample **AIS14**- **ACIS5050** (a and b) and **ACIS5050** – **CIS14** (c,d).

L-Cysteine concentrations. The CD transition of **AIS14** rapidly decreases by increasing the copper content and all the CD signals, in the visible region, are lost for the sample **ACIS5050**. Small positive bands can be observed for the samples with higher copper content **ACIS2575** – **CIS14**. As already discussed for CIS QDs, the chiral transfer from cysteine has a low efficiency for chalcopyrite CIS QDs. This finding supports the hypothesis that the structural transition from spinel to chalcopyrite occurs around the QDs composition close to a N_{Ag}:N_{Cu} ratio of 0.50:0.50 as the case of the **ACIS5050** sample.

To further prove that the efficiency of the chiral induction in cysteine stabilised quaternary copper indium sulfide QDs is strongly affected by the crystallographic phase, samples with a silver to copper ratio 0.5:0.5 and with increasing indium content are prepared. The condition used for this investigation and pictures of the QDs solutions are reported in **Fig. 38** The labels of the samples and some characteristic properties are reported in **Table 4.** The chemical composition investigated by EDS and ICP analysis, reveals a lower indium content with respect to the reaction mixture. This trend is accentuated reducing the $N_{(Ag+Cu)}/N_{metal}$ ratio, as observed for AIS QDs.

Table 4

Sample name	$N_{(Ag+Cu)}/N_{metal}$ RM	$N_{(Ag+Cu)}/N_{metal}$ QDs	Eg (eV)	λem (nm)	FWHM (nm)
ACIS14	**0.20**	**0.26**	**2.41**	**709**	**195**
ACIS15	**0.17**	**0.21**	**2.47**	**691**	**161**
ACIS18	**0.11**	**0.15**	**2.56**	**591**	**155**

The UV/Vis absorption spectra, **Fig. 39a,** show a broad absorption with minor features for all the colloidal solutions. The effect of the increase of the indium content can be recognised by the higher absorption at 400 nm observed for **ACIS18** and by the progressive reduction of the

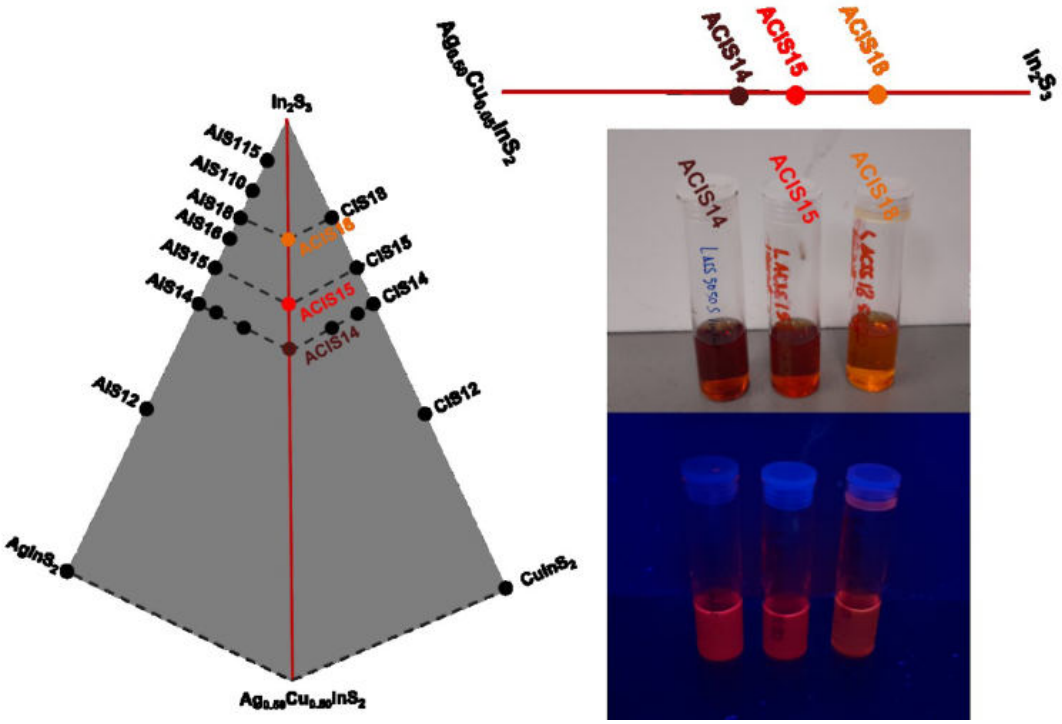

Figure 38: left) detail of the sulfide phases diagram, the position of the sample considered in this study is evidenced. Right) pictures of the QDs colloidal solutions under ambient light (top) and UV light at 365 nm (bottom).

absorption at longer wavelengths. The E_g is estimated by the analysis of the Tauc plot (**Fig A21**). By increasing of the indium content, a characteristic blue-shift from 2.56 to 2.41 eV is observed. This effect has been related to the reduction of the contribution of copper orbitals to the valence band maximum that causes the widening of the band gap.

The PL and PLE analysis are reported in **Fig. 39b**. Increasing of the indium content the photo-luminescence spectra are blue-shifted from 709 to 658 nm and by a reduction of the FWHM

from 195 to 155. The PLE spectra show a variation of the contribution of the band locate at around 500 nm that is slightly blue shifted in the case on **ACIS18**.

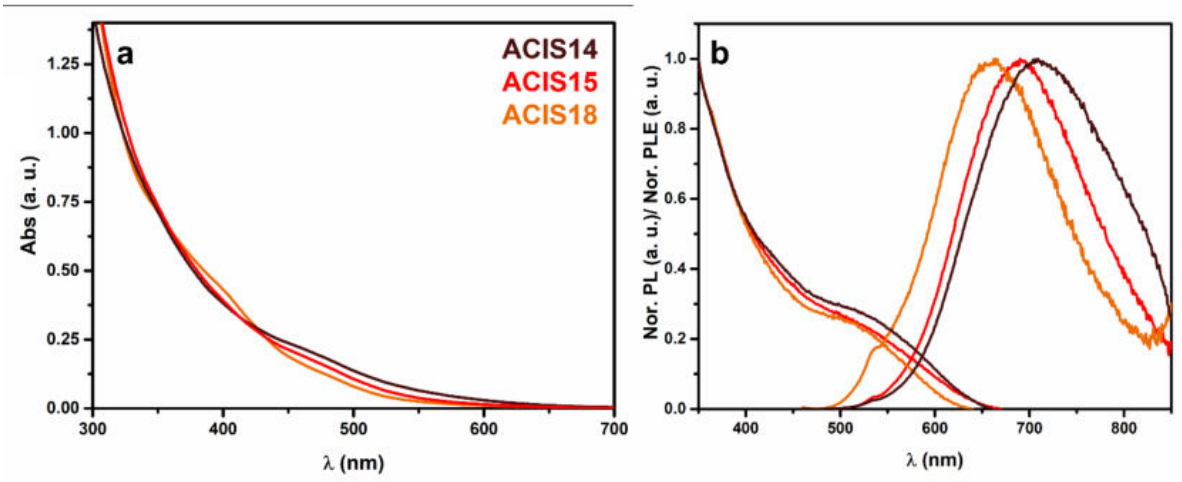

Figure 39: a) UV/Vis absorption spectra of **ACIS14**, **ACIS15** and **ACIS18** QDs colloidal solution. b) PL and PLE spectra of **ACIS14/ZnS**, **ACIS15/ZnS** and **ACIS18/ZnS** core-shell QDs colloidal solution.

The structural investigations are reported in **Fig. 40.** The line broadening prevents any detailed investigation. However, for the samples **ACIS15** and **ACIS18** the formation of the cubic spinel phase could be suggested by the intensity of the (440) peak at 46.7°. The patterns of $AgIn_5S_8$ and $CuIn_5S_8$ are reported for comparison.

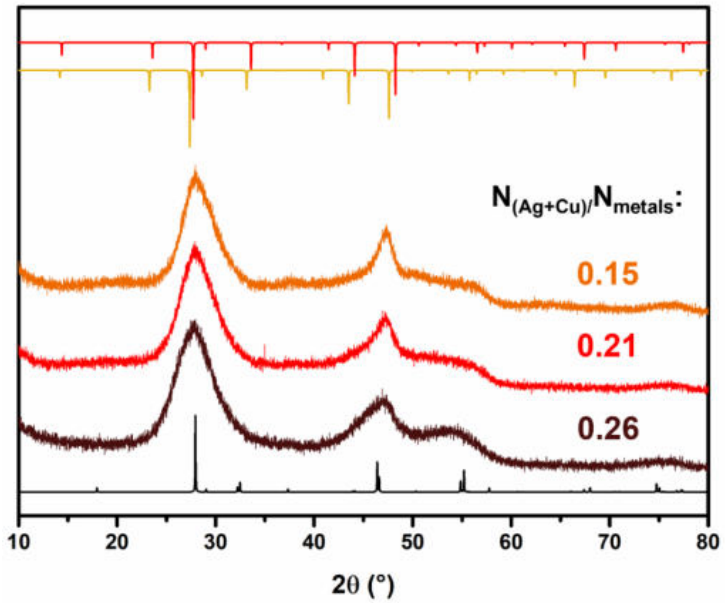

Figure 40: XRD patterns of QDs with different chemical composition, according to their $N_{(Ag+Cu)}/N_{metal}$ ratio in the QDs. The reference patterns represent $AgIn_5S_8$ spinel phase ICSD1619 (yellow), $CuIn_5S_8$ spinel phase (red) ICSD16423 and $CuInS_2$ chalcopyrite phase ICSD66865 (black).

The CD analysis of L and D QDs colloidal solution (**Fig. 41**) reveals that all the samples show a diffuse dichroic band in the UV region. This contribution can be related to the transition located at 222 nm and associated to the M-S-Cys bond. However, although **ACIS14** does not show any CD active transition in the excitonic region, **L-ACIS15** and **L-ACIS18** show a negative broad band centred at 425 nm. **D-ACIS15** and **D-ACIS18** show the opposite CD signal with a positive broad band centred at 425 nm. This evidence further supports our hypothesis that the crystallographic phase plays a fundamental role on the transfer of chirality in I-III-VI QDs. In particular, the spinel phase present higher chiroptical properties with respect to other crystallographic phases that can be observed for this chalcogenide system.

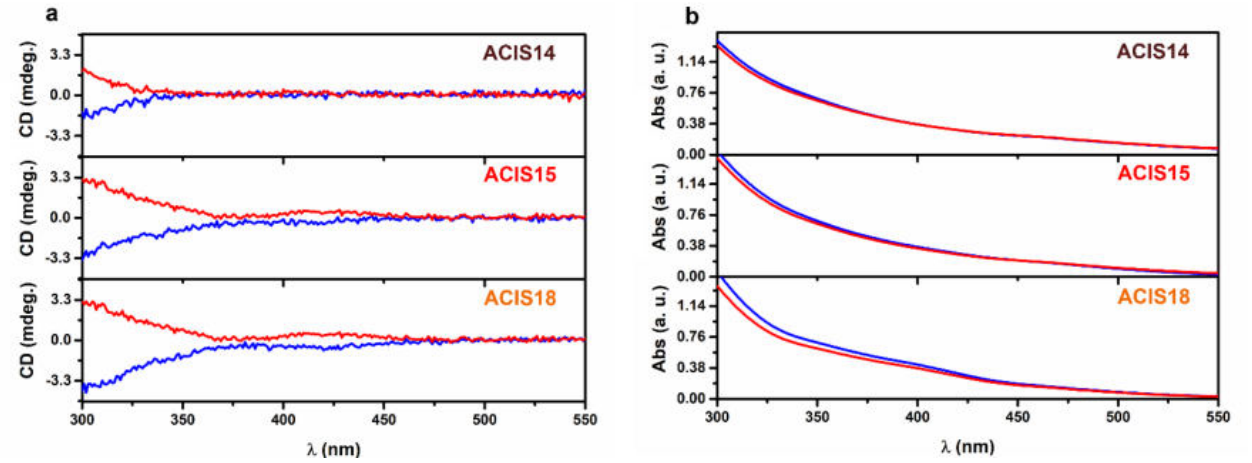

Figure 41: CD (left) and UV/Vis absorption (right) spectra of the samples **ACIS14**, **ACIS15** and **ACIS16**. The L and D QDs are reported in blue and red respectively.

2.5 INVESTIGATION ON THE FORMATION MECHANISM

The analysis of the crystallographic structure of the nanocrystals isolated after the first and after the second reaction step (**Fig. 12**), shows a dramatic variation of their structure during the ageing process. In particular, the narrowing of the XRD peaks suggests an increase of the particle size. This hypothesis is further confirmed by the XRD analysis of **AIS14** QDs samples collected at different ageing times (**Fig. 42**). The presence of $In(OH)_3$ impurity are clearly detectable in the patterns. However, since the presence of $In(OH)_3$ is detected only in the kinetic investigation, probably, its presence is related to the specific treatment adopted for the preparation of the samples rather than to some characteristic feature of the phenomenon that is taking place. For this reason the $In(OH)_3$ contribution is not considered in the interpretation of the data, even though further study will be necessary to elucidate this point. During the second reaction step, the narrowing of the diffraction starts to be appreciable after 4.0 h. At the same time the (440) peaks at 47.6 ° starts to appear, suggesting the formation of the spinel $AgIn_5S_8$ phase. Longer ageing time causes a further narrowing of the peaks and the end of the process is observed after 24 - 48 h. **Fig.42b** reports the comparison of the diffraction at 28.1 ° collected at t = 0 and t = 72h: the FWHM narrowing of the peak, from 7.7 ° to 4.3 °, can be related to the increase of the nanocrystal size. By the Scherrer equation a crystallite size of 1.8

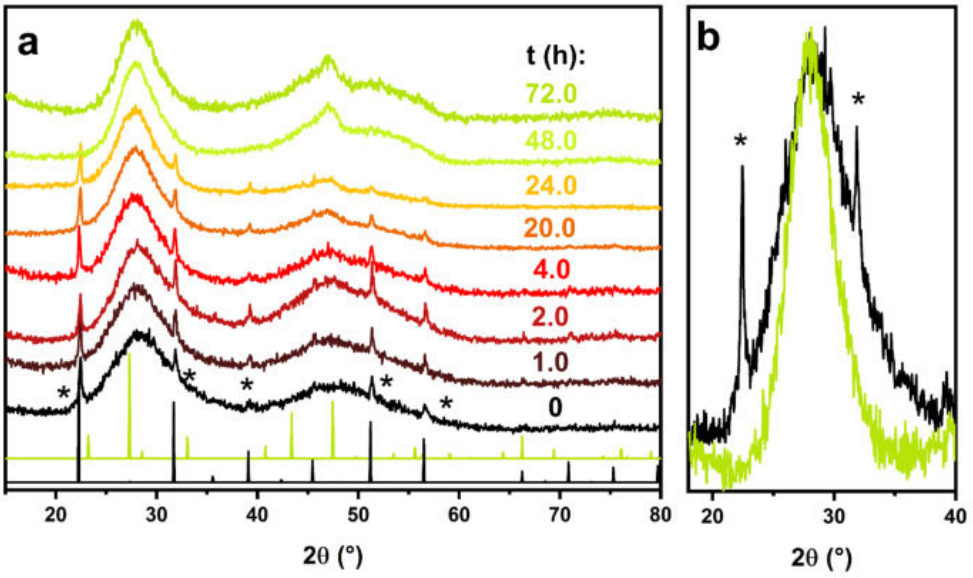

Figure 42: a) XRD patterns of samples of **AIS14** isolated at different time intervals during the 2nd reaction step, the reference patterns are related to $AgIn_5S_8$ spinel phase (light green) ICSD1619 and $In(OH)_3$ (black) ICSD35637. b) detail of the diffraction at 28.10 ° for the sample collected at t = 0 (black) and t = 72 h (light green). The $In(OH)_3$ diffractions are marked with an *.

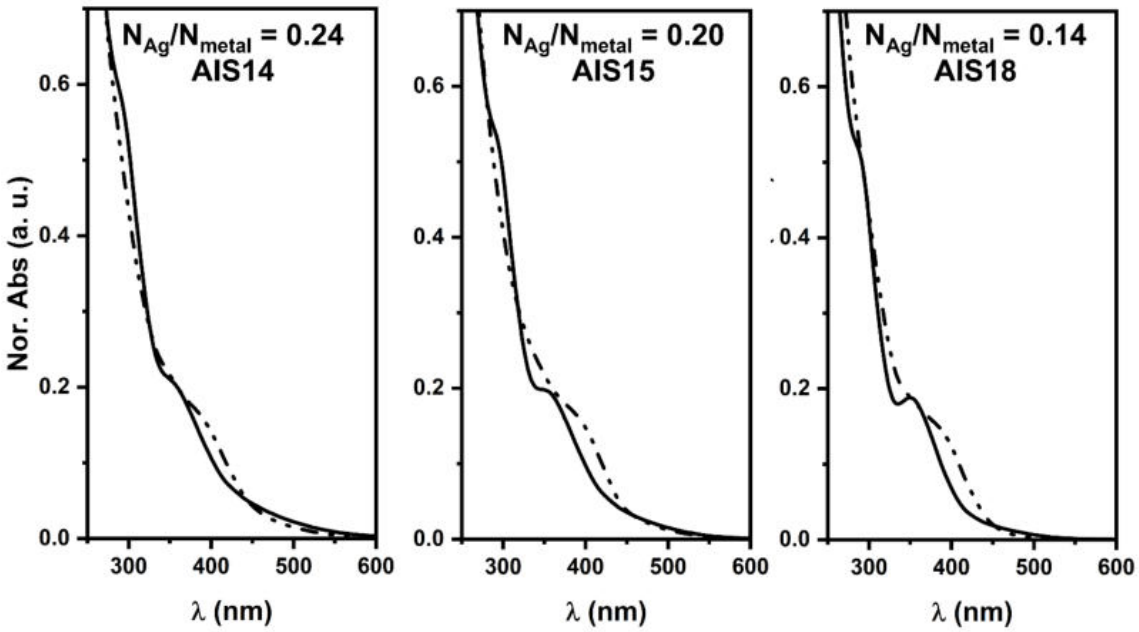

Figure 43: UV/Vis Absorption spectra of colloidal solutions with different chemical compositions before (solid line) and after (dashed line) the 2nd step.

nm and 2.2 nm of the samples at t = 0 and t = 72 h (k = 0.8 is used for the analysis of the line profile) is determined. For the sample at t = 72h, the analysis gives an average size very close to the value determined by TEM and the value obtained for the sample at t = 0 gives a good approximation of the expected size of this sample.

The analysis of the UV/Vis absorption of **AIS14**, **AIS15** and **AIS18** QDs colloidal solutions, before and after the 2nd step, is shown in **Fig**. **43.** Two absorption bands, at 350 and at 290 nm, are characteristic of the absorption of the system before the 2nd step. The position of these transitions, in the UV range, is independent from the chemical composition, that instead affects the shape of the peaks and the tail observed at longer wavelengths (similar behaviour has been found for CIS QDs **Fig A22**). In particular, decreasing the N_{Ag}/N_{metal} ratio the peaks are narrower and the contribution at longer wavelength is reduced. The QDs after the 2nd step show the characteristic absorption of the $AgIn_5S_8$ located at around 400 nm with some variations related to the chemical composition as already discussed in the previous section. Similar variations are observed in the photoluminescence. During the 2nd step the PL position is red-shifted at around 50 nm (**Fig. A6**) and an increasing of the PLQY is usually observed.

According to our findings, we proposed the possible involvement of semiconductor nanocluster (NCs) as intermediate in the formation of I-III-VI QDs via the cysteine assisted coprecipitation. These inorganic species are produced by the 1st step of the synthesis and are probably characterised by an average size smaller than the QDs average size isolated after the second

step (2.1 nm for **AIS14** according to the TEM investigation). The structure of NCs is usually highly distorted and cannot be related to the structure of the bulk material, these NCs are characterised by molecular-like electronic transitions, that can explain the unusual narrow UV/Vis bands observed for **AIS14**, **AIS15** and **AIS18**. Similar evidence was reported by Soares et al.[135] on AIS and AIS/ZnS QDs produced by aqueous microwave assisted synthesis and stabilised by 3-mercaptopropionic acid. They observed a narrow peak at 290 nm that disappeared after 1 h of microwave treatment, forming the characteristic band expected for AIS QDs. The authors explained this evidence with the hypothesis of the formation of ternary alloyed nanocluster intermediate. The stabilisation of NCs as metastable intermediate in the formation of semiconductor nanocrystals, is related to the presence of a relative minimum in the plot ΔG vs reaction coordinate of the nucleation process which brings molecular precursor to form the final nanocrystal **Fig. 44a**. The stabilisation of the NCs depends on the energy barrier that prevent their further growth into nanocrystals. In our study, the energy barrier is likely related to the electrostatic repulsion associated to the cysteine ligand and the stabilisation of the cluster surface by the ligand binding. Since the binding mode of cysteine is strongly affected by pH, it has been investigated the effect of this parameter on the energy barrier and consequently, on the stability of the NCs. It has been already established that at pH close to 7.0 used in the 2nd step (see Materials and Methods section) the NCs decompose with the relative formation of QDs in 24 - 48 h. The NCs solutions prepared in the same conditions used for the 2nd step (inorganic 3.0 mg/ml, cysteine 48 mM) but at pH ≥ 11 are characterised by a

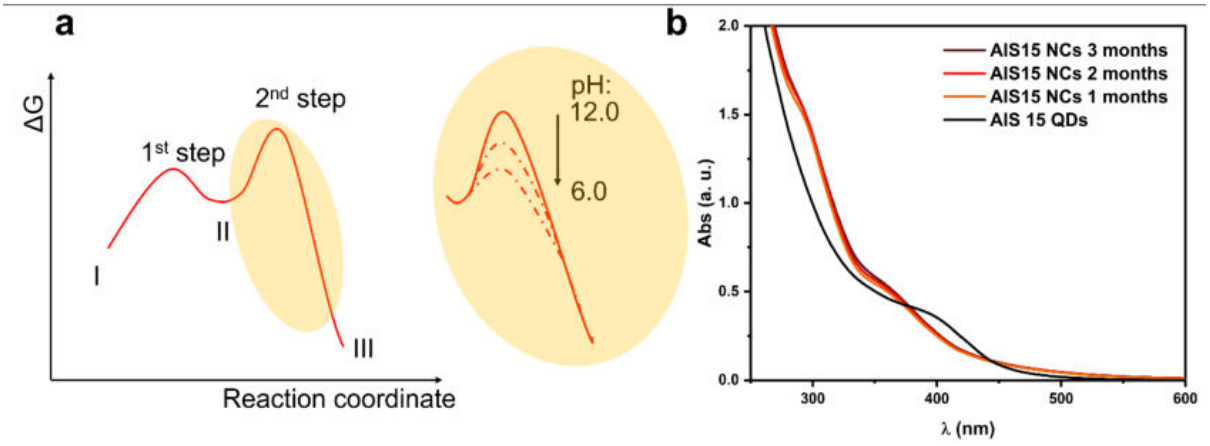

Figure 44: a) Gibbs free energy profile for the QDs formation (left), state I represents the molecular precursors, state II the metastable NCs that exist as intermediate specie and state III the QDs isolated after the 2nd step. The variation of the energy barrier related to the second step according to the pH (right). b) UV/Vis spectroscopy investigation on the stability of **AIS15** NCs at pH 12, the effect on the absorption after ageing for 48 h at pH 7 is reported as a comparison (black) labelled **AIS15** QDs.

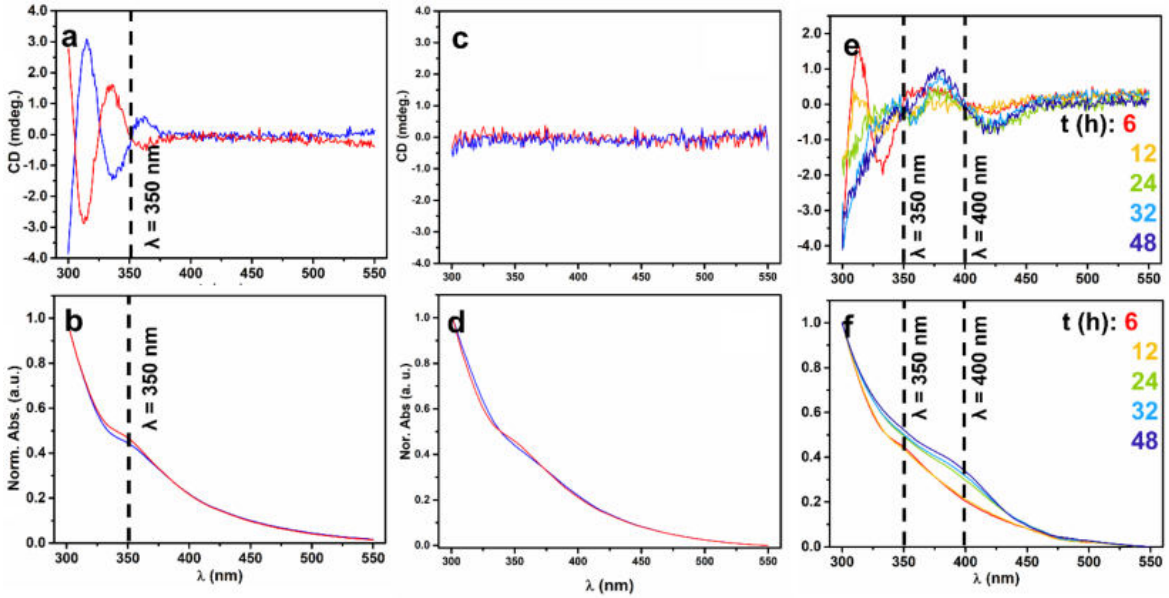

Figure45: CD and UV/Vis absorption spectra of: **L, D AIS14** NCs in 8.0 mM L, D -Cyst (a,b) and **L, D AIS14 NCs** in 8.0 mM in deionized water pH 12 (c,d). Evolution of the CD and UV/Vis spectra during the 2nd reaction step of **AIS14** QDs synthesis.

higher stability and the UV/Vis absorption spectrum characteristic of the NCs remains unaltered for months (**Fig. 44b**). This finding can be mainly associated to the effect of the thiolate binding. The pKa of the thiol group in cysteine is 10.5, at lower pH the thiol form that has lower ability to bind the nanocluster surface is favoured, instead at higher pH the dissociated thiolate form is prevalent, and a stronger interaction is expected. Lowering the pH, the affinity of the ligand for the NCs surface is reduced. This effect is reflected in the height of the energy barrier between the states II and III **Fig. 44**. The reduction of the interaction with the ligand promotes the QDs formation via coarsening or ripening processes.

The analysis of the UV/Vis absorptions evidence NCs with very distinctive optical properties. In particular, the CD activity of **L-AIS14** NCs is characterised by two positive bands at 355 and 310 nm and a negative band at 335 nm. The opposite signal can be observed for **D-AIS14** NCs **Fig. 45a, b**. The CD activity of the NCs is extremely sensitive to the environment, and it is completely lost after few hours if the NCs are redispersed in the absence of chiral ligand **Fig. 45c, d**, instead it can be preserved using an adequate Cys concentration (higher that 8.0 mM for 1 mg/ml samples). This behaviour suggests that at low ligand concentrations a fast desorption of the ligand from the NCs surface is promoted causing the loss of chirality.

The evolution of the chiroptical properties is investigated monitoring the CD spectra of a colloidal solution of **L-AIS14** NCs (**Fig. 45e, f**). The CD transition, associated to the NCs is still evident after 6 h, and it completely disappears after 24 h, while the intensity of the transition

located around 400 nm, associated to the QDs, increases. This behaviour is also reflected in the UV/Vis absorption spectra.

The analysis of the kinetic of the process by CD spectroscopy reveals the dependence of the reaction rate from the ligand concentration **Fig. A23**. When the ligand concentration increases the time required for the appearance of the QDs related transitions is reduced. At L-cysteine concentration of 8.0 – 25.0 mM, the CD band at 310 nm is still present after 48 h. Instead, at high ligand concentrations (50.0 – 100.0 mM) the band disappears completely after 6 h. This finding supports the involvement of the ligand in the transformation of NCs in QDs. It possible that the QDs formation is driven by Oswald ripening.

The NCs are in equilibrium with the metal complexes formed with cysteine at the specific pH. At pH lower than the -SH pKa, the equilibria are more oriented toward the NCs dissolution into molecular complexes. This equilibrium causes the partial dissolution of the smaller NCs and drives the growth of the larger ones into the QDs regime where the growth stops according to the interaction with the ligand and the availability of molecular precursors. It is not yet clear if this process is based on a continuous range of sizes or only some discrete sizes are allowed due to their particular stability as already observed for other semiconductor QDs and for magic number NCs.

3 CONCLUSIONS AND FUTURE PERSPECTIVES

A novel aqueous method for the production of cysteine stabilised I-III-VI QDs with a wide variety of chemical composition is developed. The observation of chiroptical activity in the exciton region confirms the successful chiral induction in ternary AIS, CIS QDs and quaternary ACIS QDs. The investigation on the origin of chirality for **AIS14** QDs, a reference sample with a molar ratio N_{Ag}/N_{metal} of 0.24, revealed the role of the chemisorption equilibrium of the ligand and a characteristic fast chemical exchange dynamics observed by NMR analysis. These findings are fundamental to understand the origin of the QDs chirality and to optimise the chiroptical properties in I-III-VI QDs.

A process to produce core-shell QDs by the deposition of ZnS is also optimised for **AIS14** QDs. The effect of the inorganic shell on both optical (absorption and photoluminescence) and chiroptical properties are analysed.

The effect of the chemical composition is investigated to optimise the optical and chiroptical properties in these systems:

- The structural investigation shows that a broad range of chemical compositions can promote the formation of the cubic spinel phases in AIS, CIS and AICS systems.
- In the ternary system, the effect of the chemical composition on the photoluminescence activity revealed that the highest performances of PLQY are observed in the samples with the spinel phase (**AIS14-AIS16** and **CIS15/ZnS**). In the quaternary system, when the copper content is increased the PLQY decrease.
- The study of the effect of chemical composition on chiroptical activity reveals little or no efficiency in chirality transfer for systems without the spinel phase. (e.g. **AIS11**, **AIS12**, **CIS11**, **CIS12** and **ACIS5050**). The investigation on the variation of the intensity of the CD bands in AIS QDs shows that the optimal conditions is close to the ideal $AgIn_5S_8$ stoichiometry (**AIS14**-**AIS16**), while a reduction of the chirality is observed for the systems with lower silver content (**AIS18**-**AIS115**). This behaviour can be related to effect the electronic structure of the QDs or to the variation of the chemistry at the particles-ligand interface.

The analysis of the formation mechanism supports the role of semiconductor NCs as intermediate in the QDs formation. These elusive structures possess their distinct optical properties

and chirality and they can be stabilised by controlling the interaction with the ligand by adjusting the pH. Moreover, our kinetic analysis supports the involvement of the ligand in the process that converts the NCs into QDs suggesting an Oswald ripening mechanism.

Future activities will be focused on the investigation on the ternary and quaternary semiconductor nanoclusters, to collet further evidence on their structure and composition. Unfortunately, collecting direct evidence on these structures is quite challenging and several attempts in this direction have not been successful so far.

4 MATERIALS AND METHODS

4.1 Chemicals

L-cysteine (97 %), $AgNO_3$ (99 %), $Cu(OAc)_2$ (99 %), $Zn(OAc)_2$ (99 %), $In(OAc)_3$ (99 %), Na_2S anhydrous (99 %), Thioacetamide (>99.0 %), Rhodamine 6G, deuterium oxide (99.9 %), sodium hydroxide and hydrochloric acid (37 %) are purchased by Sigma-Aldrich (Merck). D-cysteine (95 %) is purchased by Fluorochem. All the chemicals are employed without further purifications.

4.2 Synthesis

Synthesis of Cysteine stabilised AIS14 QDs Synthesis, 1st step: In 90.0 ml of deionized water, $In(AcO)_3$ 0.01 M (24.0 ml, 0.24 mmol) and $AgNO_3$ 0.01 M (6.0 ml, 0.06 mmol) are added under constant stirring. The pH of the colourless solution was adjusted to 8.5 with the addition of NaOH 1.0 M, and the solution turns opaque with a dark-yellow colour. Optical pure solution of L- or D- cysteine 0.16 M is added (6.0 ml, 0.96 mmol), and the solution turned colourless. An aqueous solution of Na_2S 1.0 M is added (0.480 ml, 0.48 mmol) and the colour of the resulting solution turns rapidly to orange. This solution is kept under constant stirring at room temperature for 1 h. The QDs are precipitated by addition of HCl 0.1 M, adjusting the pH to approximately 6. The QDs are collected by centrifugation at 7000 rpm for 5 min and washed three times with deionized water.

Synthesis of Cysteine stabilised AIS14 QDs Synthesis, 2nd step: The fresh prepared QD pellet is dispersed in 10.0 ml of enantiomerically pure L- or D-cysteine (48.0 mM) solution and a solution of NaOH 0.1 M is used to adjust the pH to 6.3. The QDs dispersion is stored in air, monitoring the UV/Vis and CD properties for at least 24 h to ensure the complete growth of the nanocrystals. Then, the QDs dispersions are diluted to a final QDs concentration of 1.0 mg/ml and ligand concentration of 16.0 mM.

Synthesis of Cysteine stabilised AIS14/ZnS core shell QDs: 30.0 ml of AIS14 QDs solution (QDs concentration 1.0 mg/ml and cysteine concentration 16.0 mM) are heated to 80 °C under nitrogen atmosphere. A solution of $Zn(OAc)_2$ 10mM and Thioacetamide 10 mM is injected dropwise (0.1 ml) and the reaction mixture is stirred at 80 °C for 0.5 h. Other two injections are performed following the same procedure, then, the reaction mixture is cooled in an ice bath. Core shell QDs are precipitated by the addition of 10 µl of HCl 0.1 M and isolated by centrifugation 7000 rpm for 5 min. The pellet is washed

three times with 10 ml of deionized water and collected by centrifugation. After cleaning, the nanocrystals are redispersed in 30.0 ml of deionized water in the presence of 16.0 mM of cysteine, the pH is adjusted around 7 with the addition of NaOH 0.1 M.

Synthesis of QDs with different chemical compositions: the general process used for the preparation of AIS14 and AIS14/ZnS is used for the preparation of all the other QDs and core shell QDs. The only variation to the protocol is related to the use of nitrogen atmosphere for the preparation of all the systems that contain copper to prevent the oxidation to Cu(II). The different amounts of the starting materials are reported in **Table 5**-**7**.

Synthesis of Cysteine stabilised CIS14 QDs Synthesis, 1st step: All the manipulations required for the preparation of CIS QDs are performed rigorously under nitrogen atmosphere. 90.0 ml of deionized water are placed under vacuum for 15 min and then refilled with nitrogen, this step is repeated 3 times. Then, $In(AcO)_3$ 0.01 M (24.0 ml, 0.24 mmol) and $Cu(OAc)_2$ 0.01 M (6.0 ml, 0.06 mmol) are added under constant stirring, forming a light blue solution. The pH of the solution is adjusted to 8.5 with the addition of NaOH 1.0 M, and the solution turns opaque. Optical pure solution of L- or D- cysteine 0.16 M is added (6.0 ml, 0.96 mmol). An aqueous solution of Na_2S 1.0 M is rapidly added (0.480 ml, 0.48 mmol) and the colour of the resulting solution turns rapidly to bright yellow. This solution is kept under constant stirring at room temperature for 1 h, during this step the colour of the solution changed gradually from yellow to orange. The QDs are precipitated by addition of HCl 0.1 M, adjusting the pH to approximately 6. The QDs are collected by centrifugation at 7000 rpm for 5 min and washed three times with deionized water.

Synthesis of Cysteine stabilised CIS14 QDs Synthesis, 2nd step: The fresh prepared QD pellet is dispersed in 10.0 ml of enantiomerically pure L- or D-cysteine (48.0 mM) solution and a solution of NaOH 0.1 M is used to adjust the pH to 6.3. The QDs dispersion is stored under nitrogen atmosphere, monitoring the UV/Vis and CD properties for at least 24 h to ensure the complete growth of the nanocrystals. Then, the QDs dispersions are diluted to a final QDs concentration of 1.0 mg/ml and ligand concentration of 16.0 mM with deionized water.

Synthesis of Cysteine stabilised ACIS5050 QDs Synthesis, 1st step: All the manipulations required for the preparation of ACIS QDs are performed rigorously under nitrogen

atmosphere. 90.0 ml of deionized water are placed under vacuum for 15 min and then refilled with nitrogen, this step is repeated 3 times. Then, $In(AcO)_3$ 0.01 M (24.0 ml, 0.24 mmol), $AgNO_3$ 0.01 M (3.0 ml, 0.03 mmol) and $Cu(OAc)_2$ 0.01 M (3.0 ml, 0.03 mmol) are added under constant stirring. The pH of the colourless solution is adjusted to 8.5 with the addition of NaOH 1.0 M, and the solution turns opaque with a dark-yellow colour. Optical pure solution of L- or D- cysteine 0.16 M is added (6.0 ml, 0.96 mmol), and the solution turns colourless. An aqueous solution of Na_2S 1.0 M is added (0.480 ml, 0.48 mmol) and the colour of the resulting solution turns rapidly to orange. This solution is kept under constant stirring at room temperature for 1 h. The QDs are precipitated by addition of HCl 0.1 M, adjusting the pH to approximately 6. The QDs are collected by centrifugation at 7000 rpm for 5 min and washed three times with deionized water.

Synthesis of Cysteine stabilised ACIS5050 QDs Synthesis, 2nd step: The fresh prepared QD pellet is dispersed in 10.0 ml of enantiomerically pure L- or D-cysteine (48.0 mM) solution and a solution of NaOH 0.1 M is used to adjust the pH to 6.3. The QDs dispersion is stored under nitrogen atmosphere, monitoring the UV/Vis and CD properties for at least 24 h to ensure the complete growth of the nanocrystals. Then, the QDs dispersions are diluted to a final QDs concentration of 1.0 mg/ml and ligand concentration of 16.0 mM with deionized water.

Table 5: conditions used for the synthesis of AIS QDs

sample	V $AgNO_3$ 0.01M (ml)	V $Cu(OAc)_2$ 0.01M (ml)	V $In(OAc)_3$ 0.01M (ml)	V Na_2S 1.0 M (ml)	N_{Ag}/N_{metal} RM
AIS11	12.0	-	12.0	0.260	0.50
AIS12	6.0	-	18.0	0.330	0.33
AIS14	6.0	-	24.0	0.430	0.20
AIS15	4.8	-	24.0	0.422	0.17
AIS16	4.0	-	24.0	0.420	0.14
AIS18	3.0	-	24.0	0.410	0.11
AIS110	2.4	-	24.0	0.410	0.09
AIS115	1.6	-	24.0	0.400	0.06

Table 6: conditions used for the synthesis of CIS QDs

sample	V $AgNO_3$ 0.01M (ml)	V $Cu(OAc)_2$ 0.01M (ml)	V $In(OAc)_3$ 0.01M (ml)	V Na_2S 1.0 M (ml)	N_{Cu}/N_{metal} RM
CIS11	-	12.0	12.0	0.260	0.50
CSI12	-	6.0	18.0	0.330	0.33
CIS14		6.0	24.0	0.430	0.20
CIS15	-	4.8	24.0	0.422	0.17
CIS18	-	3.0	24.0	0.420	0.11

Table 7: conditions used for the synthesis of ACIS QDs

sample	V $AgNO_3$ 0.01M (ml)	V $Cu(OAc)_2$ 0.01M (ml)	V $In(OAc)_3$ 0.01M (ml)	V Na_2S 1.0 M (ml)	$N_{(Ag+Cu)}/N_{metal}$ RM
ACIS9505	5.7	0.30	24.0	0.430	0.20
ACIS2575	4.5	1.5	24.0	0.430	0.20
ACIS5050	3.0	3.0	24.0	0.430	0.20
ACIS2575	1.5	4.5	24.0	0.430	0.20
ACIS0595	0.30	5.7	24.0	0.430	0.20
ACIS15	2.4	2.4	24.0	0.422	0.17
ACIS182	1.5	1.5	24.0	0.410	0.11

4.3 Characterisations:

Photoluminescence life-time determination: The luminescence decay measurements are collected with a Nanolog/Fluorolog-3-2iHR320 (Horiba) spectrofluorimeter. The luminescence decay curve is acquired on the QDs aqueous dispersion at 1.0 mg/ml concentration and at cysteine concentration of 16.0 mM. The QDs dispersion is excited with a 453 nm Nanoled with pulse width of 1.2 ns. The emission decay curve is collected at 615 nm, centred on the maximum emission of QDs.

Photoluminescence Quantum Yield determination: the PLQY is estimated by comparison with a known fluorescence standard according to **Eqs. A1** and **A2** (Appendix section: Photoluminescence Quantum Yield Determination). Rhodamine 6 G is chosen as standard considering

a PLQY 0.90 ± 0.02 in a water solution.[136] The QDs and standard solution in deionized water are prepared adjusting the dilution in order to obtain absorbance of 0.05 at the excitation wavelength (485 nm). The emission spectra are collected exciting with radiation at 485 nm and measuring the emission in the 500 – 850 nm range. A spectral resolution of 2.0 nm is employed in both excitation and emission.

NMR Titrations: 30.0 mg of L-AIS QD are dispersed in 30.0 ml of D_2O, in the presence of 1.5 mM of acetonitrile as a reference for the diffusion order spectroscopy experiments. Samples of 0.700 ml with different L-cysteine concentrations (2.0, 4.0, 6.0, 8.0, 16.0 mM) were collected.), the pH of the solutions are adjusted to 8.0 ± 0.1 with the addition of few microliters of NaOH 0.1 M in D_2O. The solutions are stored in the dark for 24 h to ensure equilibration, then, the QD dispersions are centrifuged at 9000 rpm for 5 min to remove possible aggregates and the supernatants are transferred in 0.5 mm NMR tubes for the analysis.

Absorption spectra: The UV/Vis analysis are carried out with a Cary 60 (Agilent) UV/Vis spectrophotometer.

Morphological characterisation: The high resolution transmission electron microscopy (HRTEM) and scanning transmission electron microscopy (STEM) high-angle annular dark-field imaging (HAADF) is carried out using a FEI Titan operating at a beam voltage of 300 kV, situated at the advanced microscopy laboratory in Trinity College Dublin.

Structural characterisation: the powder diffraction measurement is recorded with a Panalytical Advanced Powder Diffractometer.

Steady state luminescence spectra: luminescence excitation and emission spectra are collected using a FluoroMax-4 (Horiba).

FTIR spectra: FTIR spectra are recorded using a NEXUS-FTIR instrument implementing a Nicolet Diffuse Reflectance accessory (DRIFT).

XPS spectra: XPS spectra are acquired with nonmonochromatic Al Kα radiation (1486.6 eV) by using a Perkin Elmer Φ 5600ci spectrometer, at a working pressure in the 10−7 Pa range. The BE values are referred to the Fermi level. Uncertainties in the BE values are around 0.2 eV. Fits of raw spectra are done adopting a Shirley-type background and Gaussian–Lorentzian peak shapes by using a non-linear least-square fitting program

(XPSPEAK41 software). Atomic fractions are evaluated using sensitivity factors as provided by Θ V5.4A software. The relative uncertainty of the calculated atomic fraction of the different elements is around 5−10%.

CD spectroscopy: The Circular Dichroism spectra are recorded with Jasco spectropolarimeters J1500 and J815 using a scan speed of 50 nm/min and five acquisition for each spectrum. The g-factor is calculated according to **Eq. 13**:[137]

Eq. 13

$$g = \frac{2(A_L - A_R)}{A_L + A_R} = \frac{\Delta A}{A}$$

Where A_L and A_R are the absorption of the left and right circular polarized lights, and A is the absorbance of unpolarized light. The conversion of the circular dichroism express as ellipticity in millidegree units to the differential absorption is reported in **Eq. 14**. Finally, **Eq. 15** combine **Eq. 14** and **Eq. 13** to give a direct relationship between the g-factor and the circular dichroism.

Eq. 14

$$CD\ (mdeg.) = \frac{180 \ln(10)}{4\pi} 10^3\ \Delta A = 32982\ \Delta A$$

Eq. 15

$$g = \frac{CD\ (mdeg.)}{A * 32982}$$

Chemical composition analysis: Energy Dispersive X-ray Spectroscopy (EDS) is used for the evaluation of the chemical compositions of the different systems. The samples for the analysis are prepared by deposition of a thick layer of powder on a carbon tape and analysed by Zeiss sigma VP field emission Scanning Electron Microscope using a Bruker Quantarax 200 detector for the EDS analysis working with an ETH voltage of 10 kV. The signal is collected from a large area 200 x 200 µm and five different areas of each sample are analysed to ensure reproducibility. The uncertainties on the relative composition values estimated by EDS are around 2 – 5 %. The chemical composition data collected by EDS are further supported by Inductively Coupled Plasma Optical Emission Spectrometry (ICP-EOS). In this case, the fresh pellet isolated after centrifugation is solubilised in 1.0 ml of aqua regia (3:1 HCl:HNO_3 v/v, using ultrapure grade acids) under

sonication for 20 min. Then, the solutions are diluted 1 to 500 with HNO_3 2 % and used for the analysis. The samples are analysed with an ICP-EOS Perkin Elmer Optima 5300V

NMR: A Bruker Avance III 400 MHz (proton frequency of 400.23 MHz) equipped with a 5.0 mm BBOF probe is employed for the ^1H titration experiment and the NOESY spectra (mixing time 500 ms). The DOSY investigation are carried out on a Bruker Avance II 600 MHz (proton frequency 600.13 MHz) equipped 5.0mm TLC cryo probe. The DOSY data are processed with TopSpin Dynamics Center software.

Spectrophotometric determination of the Energy gap: the energy gap (Eg) is estimated from the UV/Vis absorption spectra according to the Tauc method. The variation of the absorption coefficient α according to the energy of the incident photon is expressed by **Eq. 16**.

Eq. 16

$$(\alpha h\nu)^{1/\gamma} = B(h\nu - E_g)$$

Where h is the Planck constant, ν is the photon frequency and B is a constant. The parameter γ depend on the nature of the electronic transition (γ = ½ for direct and γ = 2 for indirect band gap). The E_g values were extrapolated by the α^2 versus E plot from the intersection of the linear fit at α = 0, using γ = ½ (direct band gap) according to other study on $AgIn_5S_8$ nanocrystals.[50,138]

5 REFERENCES

1 L. E. Brus, *J. Chem. Phys.*, 1983, **79**, 5566–5571.
2 L. E. Brus, *J. Chem. Phys.*, 1984, **80**, 4403–4409.
3 A. L. Efros and L. E. Brus, *ACS Nano*, 2021, **15**, 6192–6210.
4 A. I. Ekimov, A. L. Efros and A. A. Onushchenko, *Solid State Commun.*, 1993, **88**, 947–950.
5 R. Rossetti, R. Hull, J. M. Gibson and L. E. Brus, *J. Chem. Phys.*, 1985, **83**, 1406–1410.
6 R. Rossetti, R. Hull, J. M. Gibson and L. E. Brus, *J. Chem. Phys.*, 1985, **82**, 552–559.
7 N. Chestnoy, R. Hull and L. E. Brus, *J. Chem. Phys.*, 1986, **85**, 2237–2242.
8 M. L. Steigenwald, A. P. Alivisator, J. M. Gibson, T. D. Harris, R. Kortan, A. J. Muller, A. M. Thayer, T. M. Duncan, D. C. Douglass and L. E. Brus, *J. Am. Chem. Soc.*, 1988, **110**, 3046–3050.
9 A. Henglein, M. Meyer, C. Walberg, K. Kurihara, J. H. Fendler, P. Lianos, J. K. Thomas, T. ; Dannhauser, M. O'neil, K. Johansson, D. Witten, G. Mclendon, C. Petit, M. P. Pileni, L. E. Brus, K. Ploog, H. C. Youn, S. Baral, J. K. Leland and A. F. ; Bard, *J. Am. Chem. Soc.*, 1990, **112**, 1327–1332.
10 M. G. Bawendi, A. R. Kortan, M. L. Steigerwald and L. E. Brus, *J. Chem. Phys.*, 1989, **91**, 7282–7290.
11 C. B. Murray, D. J. Norris and M. G. Bawendi, *J. Am. Chem. Soc.*, 1993, **115**, 8706–8715.
12 A. Chemseddine and H. Weller, *Ber. Bunsenges. Phys. Chem.*, 1993, **97**, 636–637.
13 T. Kippeny, L. A. Swafford and S. Rosenthal, *J. Chem. Edu.*, 2002, **79**, 1094–1100.
14 Z. A. Peng and X. Peng, *J. Am. Chem. Soc.*, 2001, **123**, 183–184.
15 L. Qu, Z. A. Peng and X. Peng, *Nano Lett.*, 2001, **1**, 333–337.
16 J. van Embden, A. S. R. Chesman and J. J. Jasieniak, *Chem. Mater.*, 2015, **27**, 2246–2285.
17 O. Chen, X. Chen, Y. Yang, J. Lynch, H. Wu, J. Zhuang and Y. C. Cao, *Angew. Chem. Int. Ed.*, 2008, **47**, 8638–8641.
18 L. Li, A. Pandey, D. J. Werder, B. P. Khanal, J. M. Pietryga and V. I. Klimov, *J. Am. Chem. Soc.*, 2011, **133**, 1176–1179.
19 W. S. Song and H. Yang, *Chem. Mater.*, 2012, **24**, 1961–1967.
20 B. Chen, H. Zhong, W. Zhang, Z. Tan, Y. Li, C. Yu, T. Zhai, Y. Bando, S. Yang and B. Zou, *Adv. Funct. Mater.*, 2012, **22**, 2081–2088.
21 L. Li, T. J. Daou, I. Texier, T. T. K. Chi, N. Q. Liem and P. Reiss, *Chem. Mater.*, 2009, **21**, 2422–2429.
22 L. Jing, S. v. Kershaw, Y. Li, X. Huang, Y. Li, A. L. Rogach and M. Gao, *Chem. Rev.*, 2016, **116**, 10623–10730.
23 A. Fojtik, H. Weller, U. Koch and A. Henglein, *Ber. Bunsenges. Phys. Chem.*, 1984, **88**, 969–977.
24 H. Weller, U. Koch, M. Gutikrrez and A. Henglein, *Ber. Bunsenges. Phys. Chem*, 1984, **88**, 649–656.
25 A. Fojtik, H. Weller and A. Henglein, *Ber. Bunsenges. Phys. Chem.*, 1985, **120**, 552–554.
26 U. Resch, H. Weller and A. Henglein, *Langmuir*, 1989, **5**, 1015–1020.
27 T. Rajh, O. I. Micic' and A. J. Nozik', *J. Phys. Chem.*, 1993, **97**, 11999–12003.
28 A. L. Rogach, L. Katsikas, A. Kornowskiv, D. Su, A. Eychmüller and H. Weller, *Ber. Bunsenges. Phys. Chem.*, 1997, **101**, 1668–1670.
29 A. L. Rogach, A. Kornowski, M. Gao, A. Eychmüller and H. Weller, *Journal of Physical Chemistry B*, 1999, 103, 3065–3069.
30 M. Gao, S. Kirstein, H. Möhwald, A. L. Rogach, A. Kornowski, A. Eychmüller and H. Weller, *J. Phys. Chem. B*, 1998, **102**, 8360–8363.
31 H. Zhang, Z. Zhou, B. Yang and M. Gao, *J. Phys. Chem. B*, 2003, **107**, 8–13.
32 Y. Yu, K. Zhang and S. Sun, *Appl. Surf. Sci.*, 2012, **258**, 7181–7187.
33 O. M. Primera-Pedrozo, Z. Arslan, B. Rasulev and J. Leszczynski, *Nanoscale*, 2012, **4**, 1312–1320.
34 M. v. Kovalenko, E. Kaufmann, D. Pachinger, J. Roither, M. Huber, J. Stangl, G. Hesser, F. Schäffler and W. Heiss, *J. Am. Chem. Soc.*, 2006, **128**, 3516–3517.
35 C. Wang, Y. Wang, L. Xu, D. Zhang, M. Liu, X. Li, H. Sun, Q. Lin and B. Yang, *Small*, 2012, **8**, 3137–3142.
36 W. W. Xiong, G. H. Yang, X. C. Wu and J. J. Zhu, *ACS Appl. Mater. Interfaces*, 2013, **5**, 8210–8216.
37 Y. Chen, S. Li, L. Huang and D. Pan, *Inorg. Chem.*, 2013, **52**, 7819–7821.
38 S. Liu, H. Zhang, Y. Qiao and X. Su, *RSC Adv.*, 2012, **2**, 819–825.
39 W. W. Xiong, G. H. Yang, X. C. Wu and J. J. Zhu, *J. Mat. Chem. B*, 2013, **1**, 4160–4165.
40 M. D. Regulacio, K. Y. Win, S. L. Lo, S. Y. Zhang, X. Zhang, S. Wang, M. Y. Han and Y. Zheng, *Nanoscale*, 2013, **5**, 2322–2327.
41 X. Kang, L. Huang, Y. Yang and D. Pan, *J. Phys. Chem. C*, 2015, **119**, 7933–7940.

42 S. Jain, S. Bharti, G. K. Bhullar and S. K. Tripathi, *J. Lumin.*, 2020, **219**, 226912.
43 X. Bai, F. Purcell-Milton and Y. K. Gun'ko, *Nanomaterials*, 2019, 9.
44 H. Lu, Z. Hu, W. Zhou, J. Wei, W. Zhang, F. Xie and R. Guo, *Mater. Chem. Front.*, 2022, **6**, 418–429.
45 S. Liu and X. Su, *RSC Adv.*, 2014, **4**, 43415–43428.
46 O. Stroyuk, F. Weigert, A. Raevskaya, F. Spranger, C. Würth, U. Resch-Genger, N. Gaponik and D. R. T. Zahn, *J. Phys. Chem. C*, 2019, **123**, 2632–2641.
47 P. J. Whitham, A. Marchioro, K. E. Knowles, T. B. Kilburn, P. J. Reid and D. R. Gamelin, *J. Phys. Chem. C*, 2016, **120**, 17136–17142.
48 Y. Hamanaka, T. Ogawa, M. Tsuzuki and T. Kuzuya, *J. Phys. Chem. C*, 2011, **115**, 1786–1792.
49 N. M. Gasanly, *Infrared Phys. Technol.*, 2016, **75**, 168–172.
50 N. S. Han, H. C. Yoon, S. Jeong, J. H. Oh, S. M. Park, Y. R. Do and J. K. Song, *Nanoscale*, 2017, **9**, 10285–10291.
51 A. Hirase, Y. Hamanaka and T. Kuzuya, *J. Phys. Chem. Lett.*, 2020, **11**, 3969–3974.
52 T. Uematsu, K. Wajima, D. K. Sharma, S. Hirata, T. Yamamoto, T. Kameyama, M. Vacha, T. Torimoto and S. Kuwabata, *NPG Asia Mater.*, 2018, **10**, 713–726.
53 A. Raevskaya, V. Lesnyak, D. Haubold, V. Dzhagan, O. Stroyuk, N. Gaponik, D. R. T. Zahn and A. Eychmüller, *J. Phys. Chem. C*, 2017, **121**, 9032–9042.
54 R. Xie, M. Rutherford and X. Peng, *J. Am. Chem. Soc.*, 2009, **131**, 5691–5697.
55 M. Dai, S. Ogawa, T. Kameyama, K. I. Okazaki, A. Kudo, S. Kuwabata, Y. Tsuboi and T. Torimoto, *J. Mater. Chem*, 2012, **22**, 12851–12858.
56 I. Tsuji, H. Kato, H. Kobayashi and A. Kudo, *J. Am. Chem. Soc.*, 2004, **126**, 13406–13413.
57 S. P. Hong, H. K. Park, J. H. Oh, H. Yang and Y. R. Do, *J. Mater. Chem.*, 2012, **22**, 18939–18949.
58 W. Xiang, C. Xie, J. Wang, J. Zhong, X. Liang, H. Yang, L. Luo and Z. Chen, *J. Alloys Compd.*, 2014, **588**, 114–121.
59 X. Hu, T. Chen, Y. Xu, M. Wang, W. Jiang and W. Jiang, *J. Lumin.*, 2018, **200**, 189–195.
60 S. H. You, K. J. Hong, C. J. Youn, T. S. Jeong, J. D. Moon, H. S. Kim and J. S. Park, *J. Appl. Phys.*, 2001, **90**, 3894–3898.
61 J. Krustok, J. Raudoja, M. Krunks, H. Mändar and H. Collan, *J. Appl. Phys.*, 2000, **88**, 205–209.
62 M. Uehara, K. Watanabe, Y. Tajiri, H. Nakamura and H. Maeda, *J. Chem. Pys.*, 2008, **129**, 134709.
63 K. E. Hughes, S. R. Ostheller, H. D. Nelson and D. R. Gamelin, *Nano Lett.*, 2019, **19**, 1318–1325.
64 M. P. Moloney, Y. K. Gun'ko and J. M. Kelly, *Chem. Commun.*, 2007, 3900–3902.
65 J. K. Choi, B. E. Haynie, U. Tohgha, L. Pap, K. W. Elliott, B. M. Leonard, S. v. Dzyuba, K. Varga, J. Kubelka and M. Balaz, *ACS Nano*, 2016, **10**, 3809–3815.
66 U. Tohgha, K. K. Deol, A. G. Porter, S. G. Bartko, J. K. Choi, B. M. Leonard, K. Varga, J. Kubelka, G. Muller and M. Balaz, *ACS Nano*, 2013, **7**, 11094–11102.
67 S. A. Gallagher, M. P. Moloney, M. Wojdyla, S. J. Quinn, J. M. Kelly and Y. K. Gun'Ko, *J. Mater. Chem.*, 2010, **20**, 8350–8355.
68 K. Varga, S. Tannir, B. E. Haynie, B. M. Leonard, S. v. Dzyuba, J. Kubelka and M. Balaz, *ACS Nano*, 2017, **11**, 9846–9853.
69 G. Li, X. Fei, H. Liu, J. Gao, J. Nie, Y. Wang, Z. Tian, C. He, J. L. Wang, C. Ji, D. Oron and G. Yang, *ACS Nano*, 2020, **14**, 4196–4205.
70 T. Nakashima, Y. Kobayashi and T. Kawai, *J. Am. Chem. Soc.*, 2009, **131**, 10342–10343.
71 Y. Zhou, M. Yang, K. Sun, Z. Tang and N. A. Kotov, *J. Am. Chem. Soc.*, 2010, **132**, 6006–6013.
72 J. E. Govan, E. Jan, A. Querejeta, N. A. Kotov and Y. K. Gun'ko, *Chem. Commun.*, 2010, **46**, 6072–6074.
73 A. Ben-Moshe, A. Teitelboim, D. Oron and G. Markovich, *Nano Lett.*, 2016, **16**, 7467–7473.
74 A. K. Visheratina, A. O. Orlova, F. Purcell-Milton, V. A. Kuznetsova, A. A. Visheratin, E. v. Kundelev, V. G. Maslov, A. v. Baranov, A. v. Fedorov and Y. K. Gun'Ko, *J. Mater. Chem. C*, 2018, **6**, 1759–1766.
75 V. A. Kuznetsova, E. Mates-Torres, N. Prochukhan, M. Marcastel, F. Purcell-Milton, J. O'Brien, A. K. Visheratina, M. Martinez-Carmona, Y. Gromova, M. Garcia-Melchor and Y. K. Gun'Ko, *ACS Nano*, 2019, **13**, 13560–13572.
76 V. Kuznetsova, Y. Gromova, M. Martinez-Carmona, F. Purcell-Milton, E. Ushakova, S. Cherevkov, V. Maslov and Y. K. Gun'Ko, *Nanophotonics*, 2020, **10**, 797–824.
77 X. Gao, X. Zhang, K. Deng, B. Han, L. Zhao, M. Wu, L. Shi, J. Lv and Z. Tang, *J. Am. Chem. Soc.*, 2017, **139**, 8734–8739.

78 S. D. Elliott, M. P. Moloney and Y. K. Gun'ko, *Nano Lett.*, 2008, **8**, 2452–2457.
79 J. Kumar, K. G. Thomas and L. M. Liz-Marzán, *Chem. Commun.*, 2016, **52**, 12555–12569.
80 A. O. Govorov, Y. K. Gun'Ko, J. M. Slocik, V. A. Gérard, Z. Fan and R. R. Naik, *J. Mater. Chem.*, 2011, **21**, 16806–16818.
81 M. Naito, K. Iwahori, A. Miura, M. Yamane and I. Yamashita, *Angew. Chem. Int. Ed.*, 2010, **49**, 7006–7009.
82 R. Zhou, K. Y. Wei, J. S. Zhao and Y. B. Jiang, *Chem. Commun.*, 2011, **47**, 6362–6364.
83 U. Tohgha, K. Varga and M. Balaz, *Chem. Commun.*, 2013, **49**, 1844–1846.
84 F. Purcell-Milton, A. K. Visheratina, V. A. Kuznetsova, A. Ryan, A. O. Orlova and Y. K. Gun'Ko, *ACS Nano*, 2017, **11**, 9207–9214.
85 X. Gao, X. Zhang, L. Zhao, P. Huang, B. Han, J. Lv, X. Qiu, S. H. Wei and Z. Tang, *Nano Lett.*, 2018, **18**, 6665–6671.
86 W. Xiang, C. Xie, J. Wang, J. Zhong, X. Liang, H. Yang, L. Luo and Z. Chen, *J Alloys Compd*, 2014, **588**, 114–121.
87 S. P. Hong, H. K. Park, H. J. Oh, H. Yang and R. Y. Do, *J. Mat. Chem.*, 2012, **22**, 18939–18949.
88 X. Hu, T. Chen, Y. Xu, M. Wang, W. Jiang and W. Jiang, *J Lumin*, 2018, **200**, 189–195.
89 M. D. Regulacio, K. Y. Win, S. L. Lo, S.-Y. Zhang, X. Zhang, M.-Y. Han and Y. Zheng, *Nanoscale*, 2013, **5**, 2322–2327.
90 G. Greczynski and L. Hultman, *Sci. Rep.*, 2021, **11**, 11195.
91 R. C. M. Salles, L. H. Coutinho, A. G. Veiga and M. M. Sant'Anna, *J. Chem. Phys.*, 2018, **148**, 045107.
92 G. Gonella, S. Terreni, D. Cvetko, A. Cossaro, L. Mattera, O. Cavalleri, R. Rolandi, A. Morgante, L. Floreano and M. Canepa, *J. Phys. Chem. B*, 2005, **109**, 18003–18009.
93 C. N. Carvalho, A. M. B. Rego, A. Amaral, P. Brogueira and G. Lavareda, *Surf. Coat. Technol.*, 2000, **124**, 70–75.
94 L. B. Hoch, T. E. Wood, P. G. O'Brien, K. Liao, L. M. Reyes, C. A. Mims and G. A. Ozin, *Adv. Sci.*, 2014, **1**, 1400013.
95 NIST X-ray Photoelectron Spectroscopy Database, NIST Standard Reference Database Number 20, National Institute of Standards and Technology, Gaithersburg MD, 20899 (2000), doi:10.18434/T4T88K.
96 M. Dai, S. Orawa, T. Kameyama, K.-I. Okazaki, A. Kudo, S. Kuwabata, Y. Tsuboi and T. Torimoto, *J. Mater. Chem.*, 2012, **22**, 12851–12858.
97 H. Guo, J. Liu, B. Luo, X. Huang, J. Yang, H. Chen, L. Shi, X. Liu, D. Benetti, Y. Zhou, G. S. Selopal, F. Rosei, Z. Wang and X. Niu, *J. Mat. Chem. C*, 2021, **9**, 9610–9618.
98 L. Lin, C. Wu, C. Lai and T. Lee, *Chem. Mater.*, 2008, **20**, 4475–4483.
99 L.-H. Lin, C.-C. Wu and T.-C. Lee, *Cryst. Growth Des.*, 2007, **12**, 4–11.
100 J. X. Soares, K. D. Wegner, D. S. M. Ribeiro, A. Melo, I. Häusler and J. L. M. Santos, *Nano Res.*, 2020, **13**, 2438–2450.
101 O. Stroyuk, F. Weigert, A. Raevskaya, F. Spranger, C. Würth, U. Resch-Genger, N. Gaponik and D. R. T. Zahn, *J. Phys. Chem. C*, 2019, **123**, 2632–2641.
102 G. Socrates, *Infrared and Raman Characteristic Group Frequencies Contents*, John Wiley & Sons Ltd., Baffis Lane, 3rd editio., 2001.
103 N. Kazuo, *Infrared and Raman Spectra of Inorganic and Coordination Ccompounds. Part B: Applications in Coordination, Organometallic and Bioinorganic Chemistry*, 6th edn., 2009.
104 A. Pawlukojć, J. Leciejewicz, A. J. Ramirez-Cuesta and J. Nowicka-Scheibe, *Spectrochim. Acta A*, 2005, **61**, 2474–2481.
105 N. Kojima, Y. Sogiura and H. Tanaka, *Bull. Chem. Soc. Jpn.*, 1976, **49**, 3023–3028.
106 V. A. Kuznetsova, E. Mates-torres, N. Prochukhan, M. Marcastel, F. Purcell-milton, J. O. Brien, A. K. Visheratina, M. Martinez-carmona, Y. Gromova, M. Garcia-melchor and Y. K. Gun, *ACS Nano*, 2019, **13**, 13560–13572.
107 A. Ben-Moshe, A. Teitelboim, D. Oron and G. Markovich, *Nano Lett.*, 2016, **16**, 7467–7473.
108 U. Tohgha, K. K. Deol, A. G. Porter, S. G. Bartko, J. K. Choi, B. M. Leonard, K. Varga, J. Kubelka, G. Muller and M. Balaz, *ACS Nano*, 2013, **7**, 11094–11102.
109 X. Gao, X. Zhang, K. Deng, B. Han, L. Zhao, M. Wu, L. Shi, J. Lv and Z. Tang, *J. Am. Chem. Soc.*, 2017, **139**, 8734–8739.
110 M. Puri and V. E. Ferry, *ACS Nano*, 2017, **11**, 12240–12246.
111 X. Ji, D. Copenhaver, C. Sichmeller and X. Peng, *J. Am. Chem. Soc.*, 2008, **130**, 7012–7021.

112 M. Malicki, J. M. Hales, M. Rumi, S. Barlow, L. McClary, S. R. Marder and J. W. Perry, *Phys. Chem. Chem. Phys.*, 2010, **12**, 6267–6277.
113 R. Grisorio, D. Quarta, A. Fiore, L. Carbone, G. P. Suranna and C. Giansante, *Nanoscale Adv.*, 2019, **1**, 3639–3646.
114 M. J. Hostetler, J. E. Wingate, C.-J. Zhong, J. E. Harris, R. W. Vachet, M. R. Clark, J. D. Londono, S. J. Green, J. J. Stokes, G. D. Wignall, G. L. Glish, M. D. Porter, N. D. Evans and R. W. Murray, *Langmuir*, 1998, **14**, 17–30.
115 D. A. Brain, *Prog. Nucl. Magn. Resons. Spectrosc.*, 2003, **43**, 63–103.
116 Z. Hens and J. C. Martins, *Chem. Mater.*, 2013, **25**, 1211–1221.
117 C. S. Johnson, *J. Magn. Reson. A*, 1993, **102**, 214–218.
118 B. Fritzinger, I. Moreels, P. Lommens, R. Koole, Z. Hens and J. C. Martins, *J. Am. Chem. Soc.*, 2009, **131**, 3024–3032.
119 B. Fritzinger, I. Moreels, P. Lommens, R. Koole, Z. Hens and J. C. Martins, *J Am Chem Soc*, 2009, **131**, 3024–3032.
120 A. Rigo, A. Corazza, M. Luisa, M. Rossetto, R. Ugolini and M. Scarpa, *J. Inorg. Biochem.*, 2004, **98**, 1495–1501.
121 S. D. Elliott, M. P. Moloney and Y. K. Gun'ko, *Nano Lett.*, 2008, **8**, 2452–2457.
122 G. Li, X. Fei, H. Liu, J. Gao, J. Nie, Y. Wang, Z. Tian, C. He, J.-L. Wang, C. Ji, D. Oron and G. Yang, *ACS Nano*, 2020, **14**, 4196–4205.
123 A. O. Govorov, Z. Fan, P. Hernandez, J. M. Slocik and R. R. Naik, *Nano Lett.*, 2010, **10**, 1374–1382.
124 Y. Zhou, Z. Zhu, W. Huang, W. Liu, S. Wu, X. Liu, Y. Gao, W. Zhang and Z. Tang, *Angew. Chem. Int. Ed.*, 2011, **50**, 11456–11459.
125 T. Nakashima, Y. Kobayashi and T. Kawai, *J. Am. Chem. Soc.*, 2009, **131**, 10342–10343.
126 R. Zhou, K. Wei, J. Zhao and Y. Jiang, *Chem. Commun.*, 2011, **47**, 6362–6364.
127 C. A. Martínez Bonilla, M.-H. Torres Flórez, D. R. Molina Velasco and V. V. Kouznetsov, *New, J. Chem.*, 2019, **43**, 8452–8458.
128 J. Aldana, N. Lavelle, Y. Wang and X. Peng, *J. Am. Chem. Soc.*, 2018, **127**, 3901–3909.
129 M. Mrad, T. ben Chaabane, H. Rinnert, B. Lavinia, J. Jasniewski, G. Medjahdi and R. Schneider, *Inorg. Chem.*, 2020, **59**, 6220–6231.
130 J. Song, C. Ma, W. Zhang, X. Li, W. Zhang, R. Wu, X. Cheng, A. Ali, M. Yang, L. Zhu, R. Xia and X. Xu, *ACS Appl. Mater. Interfaces*, 2016, **8**, 24826–24836.
131 V. P. Sachanyuk, G. P. Gorgut, V. v. Atuchin, I. D. Olekseyuk and O. v. Parasyuk, *J. Alloys Compd.*, 2008, **452**, 348–358.
132 D. Cavallini, C. de Marco, S. Duprb and G. Rotilio, *Arch. Biochem.*, 1969, **130**, 354361.
133 L. Pecci, G. Montefoschi, G. Musci and D. Cavallini, *Amino Acids*, 1997, **13**, 355–367.
134 A. Hanaki and H. Kamide, *Chem. Pharm. Bull.*, 1975, **23**, 1671–1676.
135 J. X. Soares, K. D. Wegner, D. S. M. Ribeiro, A. Melo, I. Häusler, J. L. M. Santos and U. Resch-Genger, *Nano Res.*, 2020, **13**, 2438–2450.
136 D. Magde, R. Wong and P. G. Seybold, *Photochem. Photobiol.*, 2002, **75**, 327–334.
137 W. Kuhn, *Z. Physik. Chem.*, 1930, **14**, 293–308.
138 S. Jeong, H. C. Yoon, N. S. Han, J. H. Oh, S. M. Park, B. K. Min, Y. R. Do and J. K. Song, *J. Phys. Chem. C*, 2017, **121**, 3149–3155.
139 U. Resch-Genger and K. Rurack, *Pure Appl. Chem.*, 2013, **85**, 2005–2026.
140 A. M. Brouwer, *Pure Appl. Chem.*, 2011, 83, 2213–2228.

6 APPENDIX

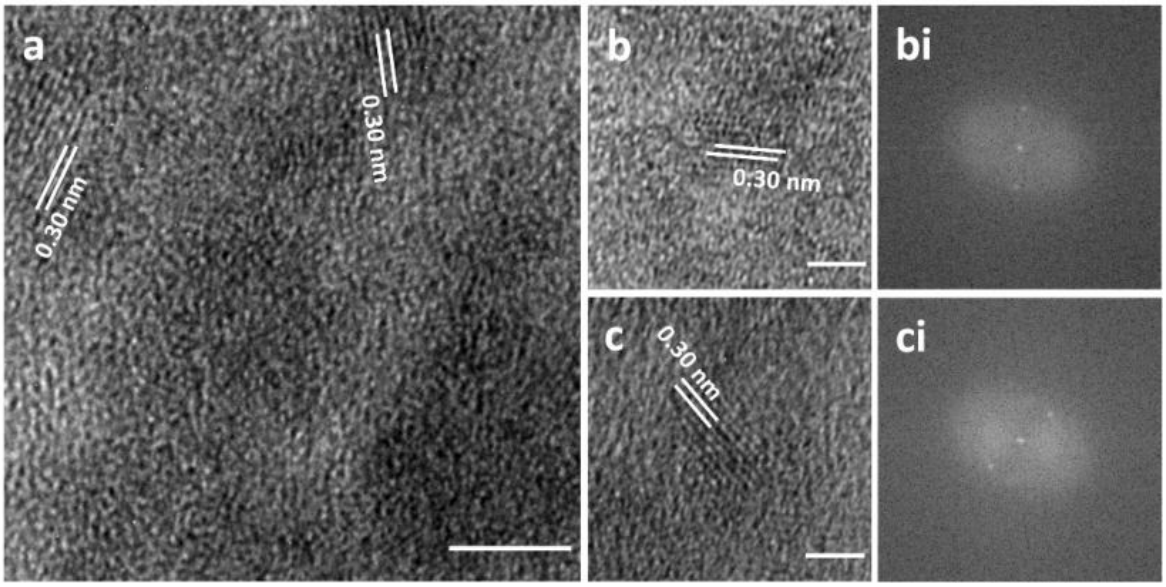

Fig. A1 (a-c): phase contrast TEM images of non-stoichiometric AIS QDs, scale bars: a = 4.0 nm; b and c = 2.0 nm; (bi), (ci): Fourier Transform images of b and c, respectively.

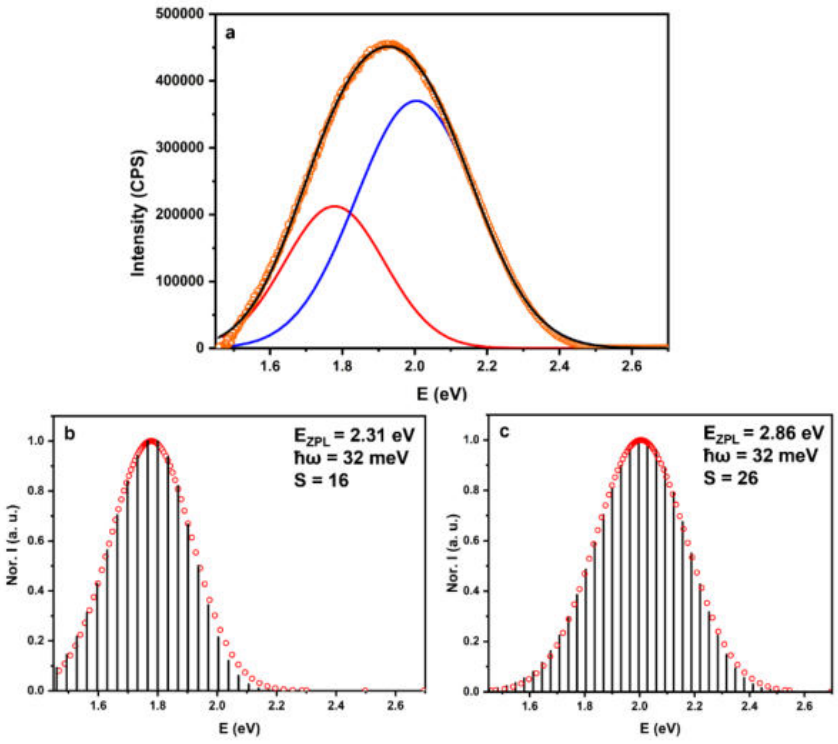

Figure A2: analysis of the electron-phonon coupling for **AIS14** QDs: a) bigaussian fitting of the emission band, b and c) simulation of the broadening of the emission from intrinsic and surface defects respectively.

Photoluminescence Quantum Yield Determination:

Equation A1[139,140]

$$\Phi_{QDs} = \Phi_{st} \frac{I_{QDs} f_{st} n_{QDs}^2}{I_{st} f_{QDs} n_{st}^2}$$

The subscripts *QDs* and *st* refer to the quantum dots or the fluorescence standard respectively. The PLQY is represented by *Φ*, *I* represent the integrated intensity corrected by the fluorimeter sensitivity and the source intensity, *n* represents the diffraction index of the solvent and *f* the absorption factor

Equation A2[139,140]

$$f_{QDs,st} = 1 - 10\text{^}(-A_{QDs,st})$$

Where *f* and *A* represent the absorption factor and the absorbance for quantum dots (*QDs*) and fluorescence standard (*st)*.

Photoluminescence Lifetime Analysis

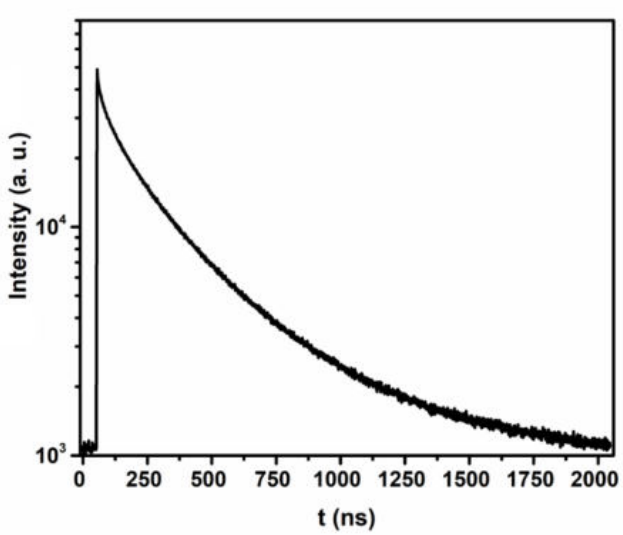

Fig. A3 PL decay curve of **L-AIS14** QDs solution

Equation A3

$$I(t) = A_1 e^{-\frac{t}{\tau_1}} + A_2 e^{-\frac{t}{\tau_2}} + A_3 e^{-\frac{t}{\tau_3}}$$

I(t) represents the linear combination of three single-exponential functions, where A_i are the amplitudes and τ_i are the time constants of the separate single-exponential terms.

Table A1 Lifetimes and amplitudes obtained from the fit of the PL decay curve.

τ_1 (ns)	169.6
A1	0.33
τ_2 (ns)	606.3
A2	0.41
τ_3 (ns)	21.0
A3	0.19

Equation A4

$$\tau_{Av} = \frac{\sum A_i \tau_i^2}{\Sigma A_i \tau_i}$$

Where τ_{Av} is the average photoluminescence lifetime calculated by weighting the different components of the fitting functions.

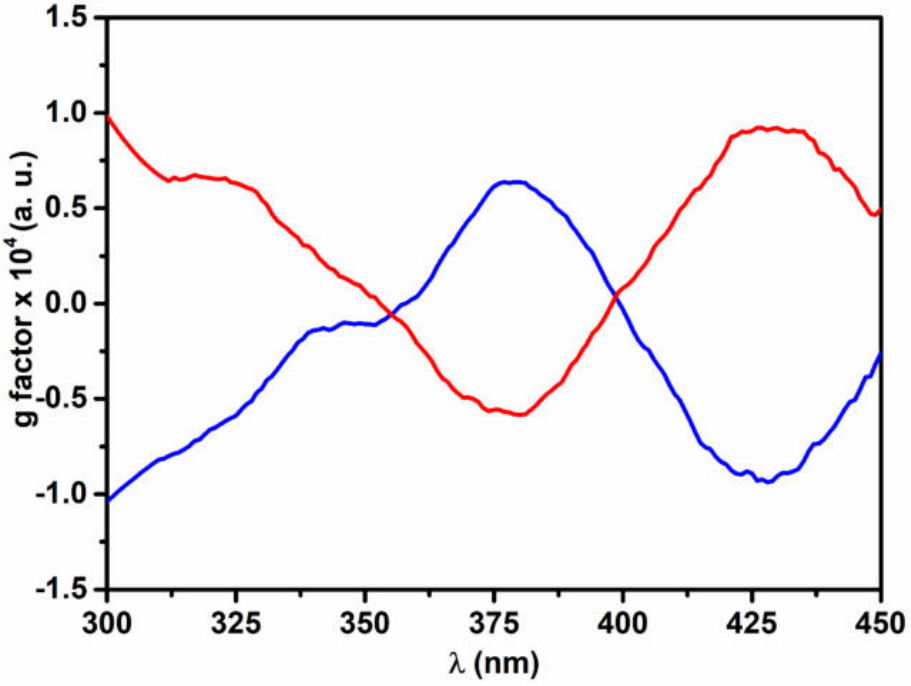

Fig. A4 Anisotropic g-factor of **L-AIS14** (blue line) and **D-AIS14** (red line) QDs stabilised in a 16.0 mM solution of L- or D-cysteine, respectively.

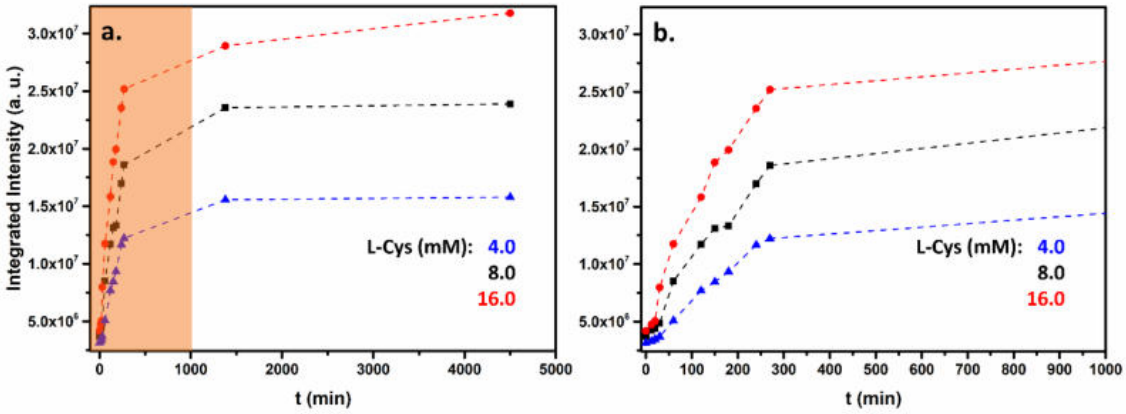

Fig. A5 a) PL integrated intensity vs time of QDs dispersions for different L-Cys concentrations. b) Magnification of the 0-1000 min region (highlighted in orange in fig a).

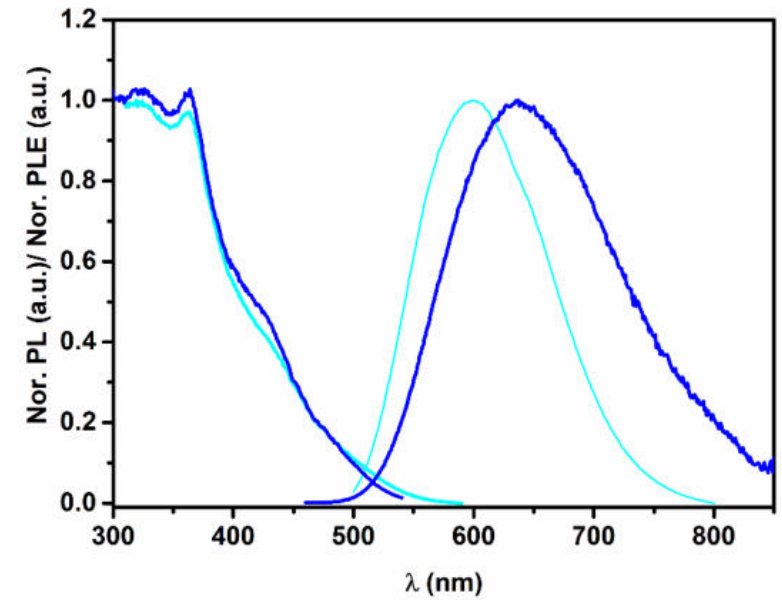

Figure A6: PL and PLE spectra of the nanocrystals isolated after the 1st (light blue) and 2nd (blue) step respectively.

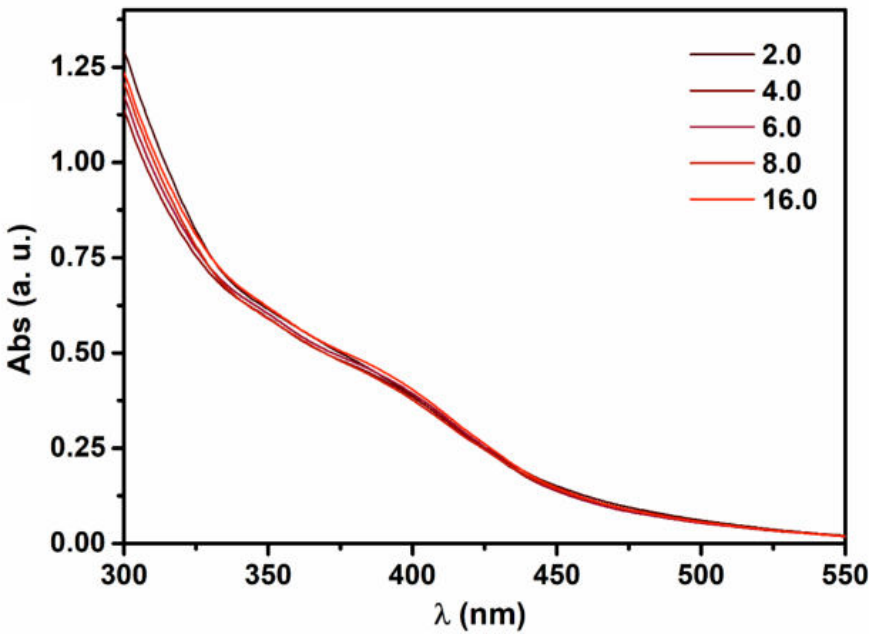

Fig. A7: UV/Vis spectra of the **AIS14** QDs colloidal solutions with different ligand concentrations.

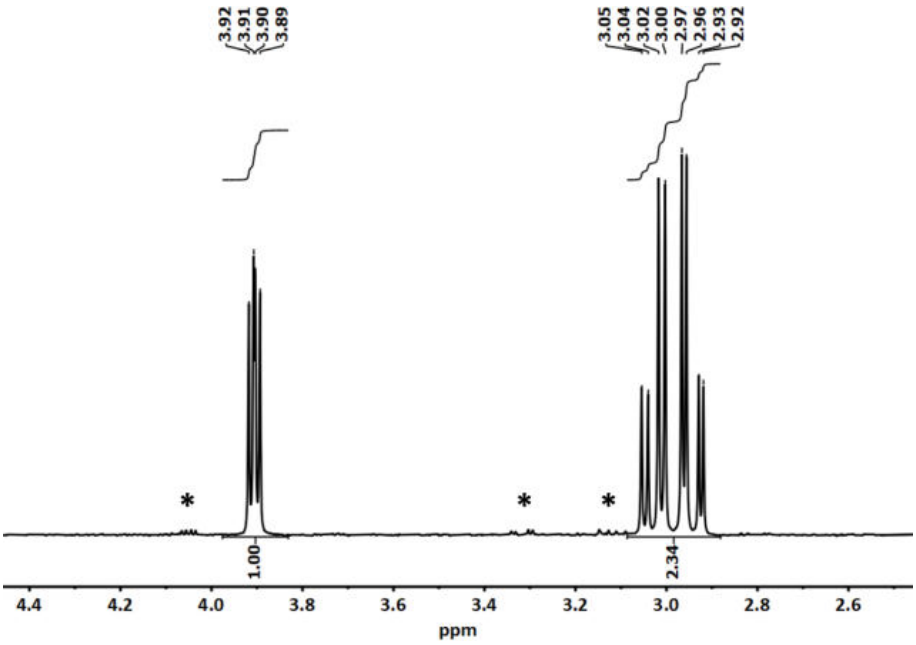

Figure A8 : ^{1}H-NMR spectra of a solution of L-Cys 16.0 mM in D_2O, the signals from L-cystine are marked with an asterisk.

Investigation on the particle-ligand interaction via CD

We related the electronic transition observed at 222 nm to a characteristic chromophore formed by the interaction of cysteine with the nanocrystal surface, probably by the coordination of the thiol group. As can be seen in **Fig. A9**, this electronic transition is observed for the **AIS14** QDs solution in the presence of different ligand concentrations. The analysis of the CD transition located at 222 nm is performed by the fitting of the spectra collected in the presence of different ligand concentration adjusting the magnitude of two contributions (free and bonded cysteine) in order to replicate the experimental data. The shapes of the signals related to free and bonded cysteine are extrapolated using: the CD spectra of the ligand in the case of the free cysteine (**Fig. A10**), instead the signal of the bonded form is approximated to the signal observed for QDs stabilised in the lowest ligand concentration. As can be seen in **Fig. A11**. The relative population of the free and bonded forms are estimated from the factors used to scale the contributions to the total CD signal after normalisation.

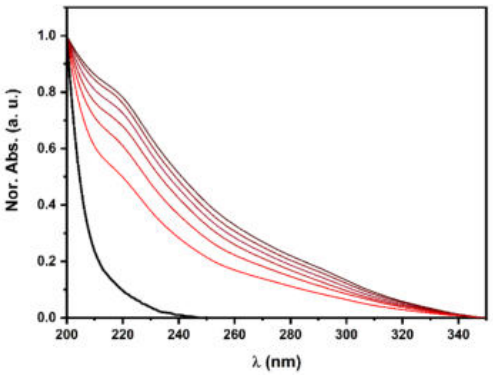

Figure A9: UV/Vis absorption spectra of **L-AIS14** QDs colloidal solutions in the presence of different concentration of L-Cysteine.

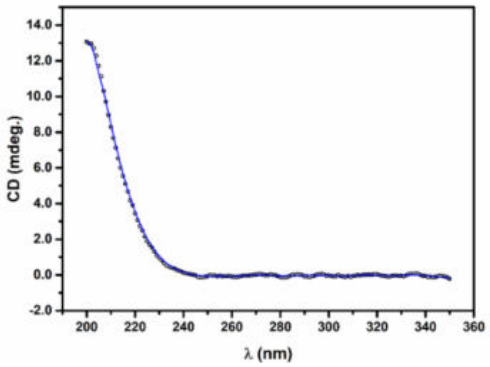

Figure A10: CD spectra of a L-cysteine solution in deionized water pH around 7.

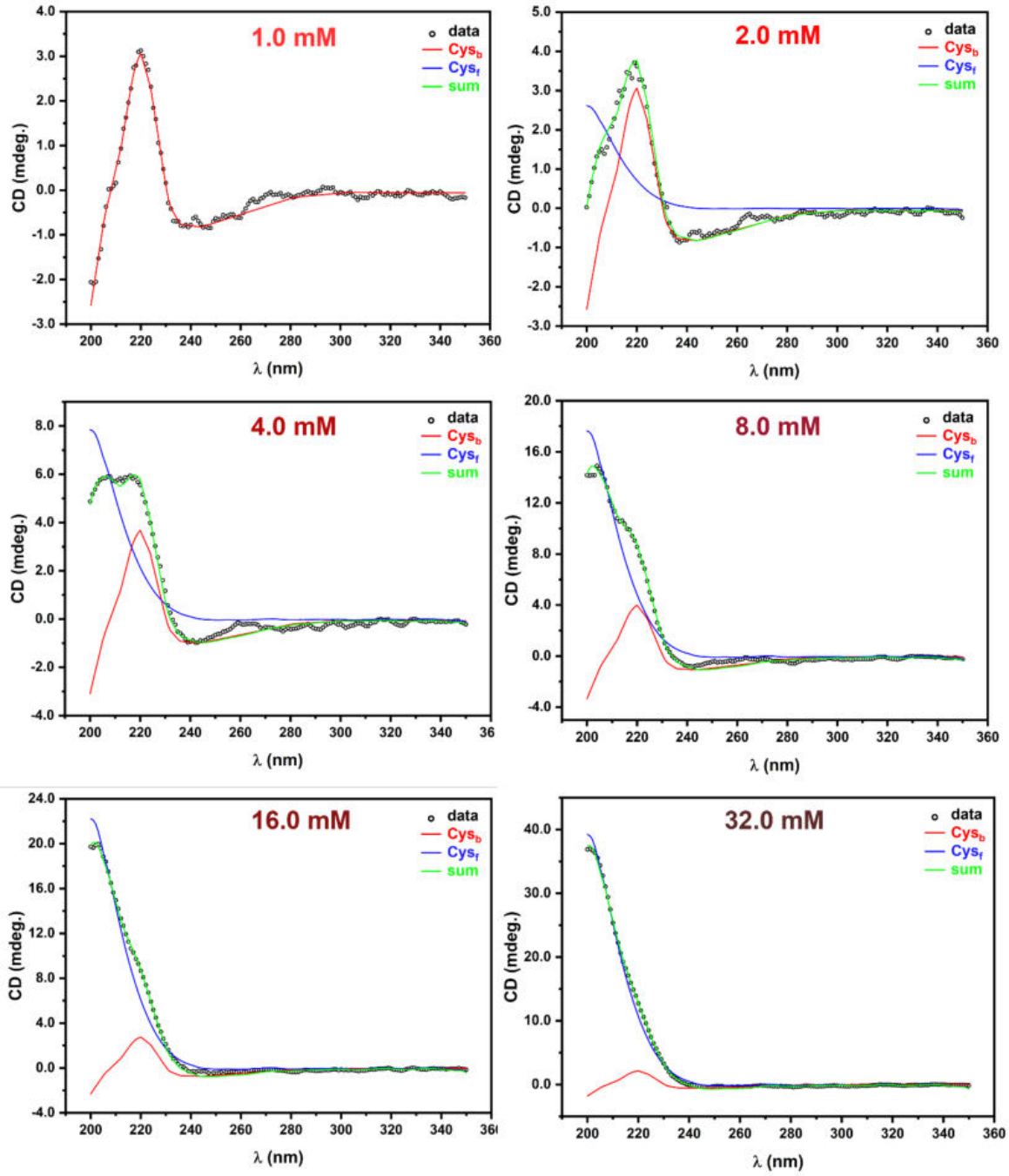

Figure A11: CD spectra of **L-AIS14** QDs in the presence of different concentrations of L-Cysteine and the fitting considering the contribution of the bonded (red) and free (blue) ligand.

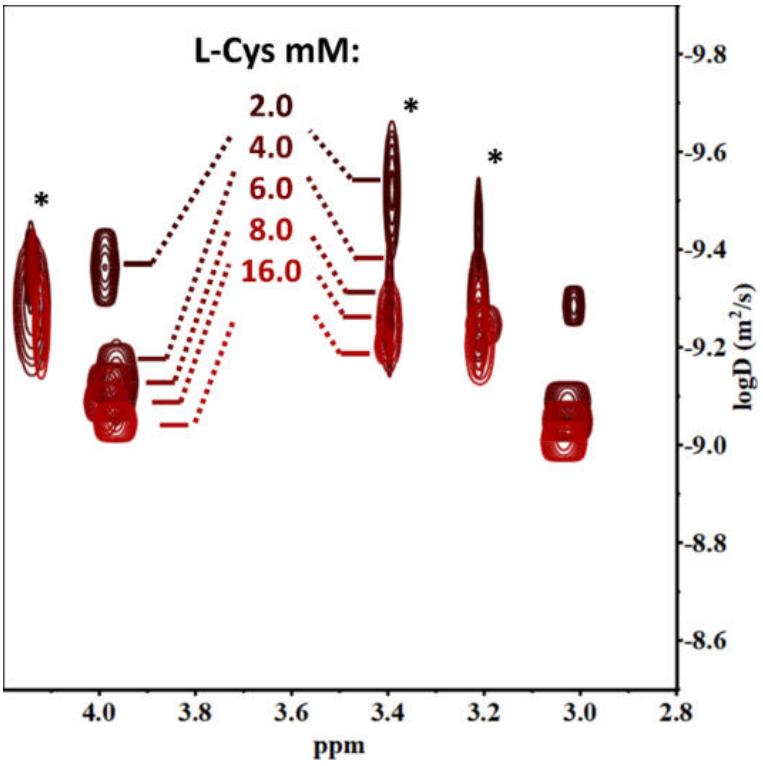

Figure A12: DOSY analysis of **L-AIS14** QDs solution in the presence of different concentration of L-Cys. The signals from L-cystine are marked with an asterisk.

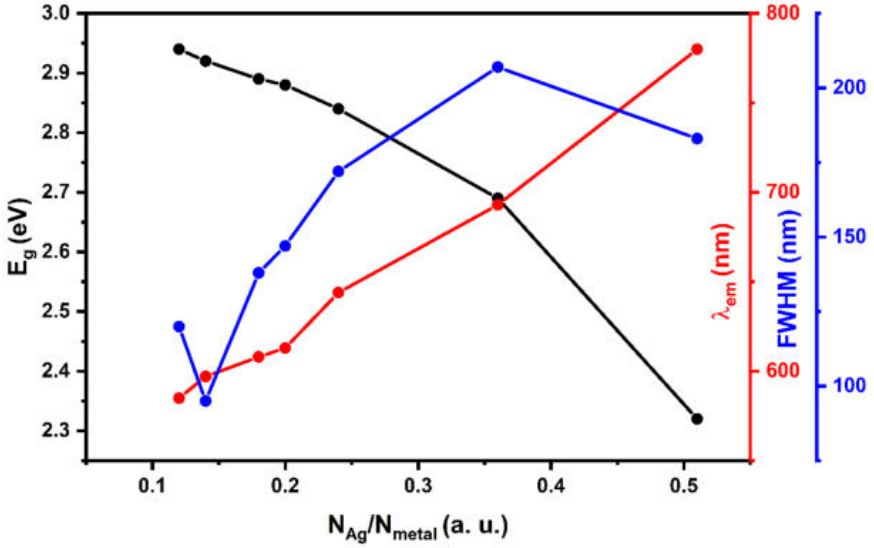

Figure A13: variation of the optical properties of AIS QDs in function of their chemical composition.

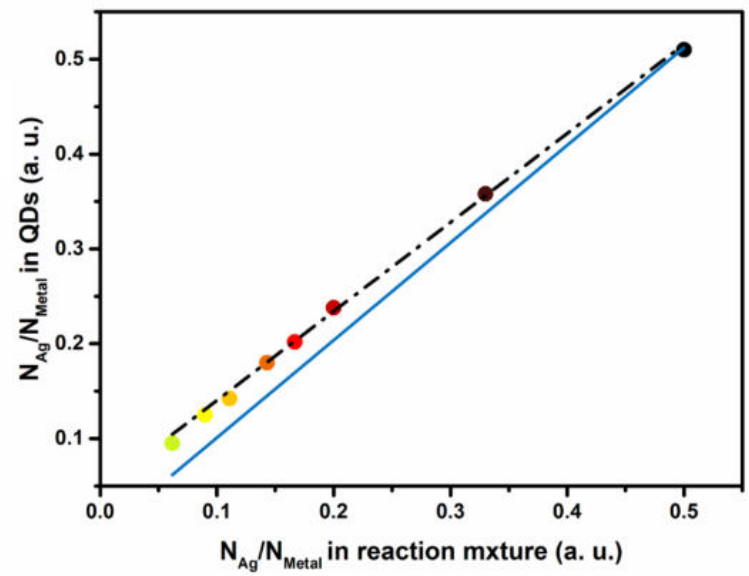

Figure A14: plot of the chemical composition observed in AIS QDs against the precursors ratio used in the reaction mixture, the linear fitting (**Eq. A5**) is indicated by the dashed line. The blue line is an indicative reference for y = x.

Eq. A5

$$N_{Ag}/N_{Metal}{}^{QDs} = 0.046 + 0.94\ N_{Ag}/N_{Metal}{}^{RM}$$

$$r^2 = 0.9942$$

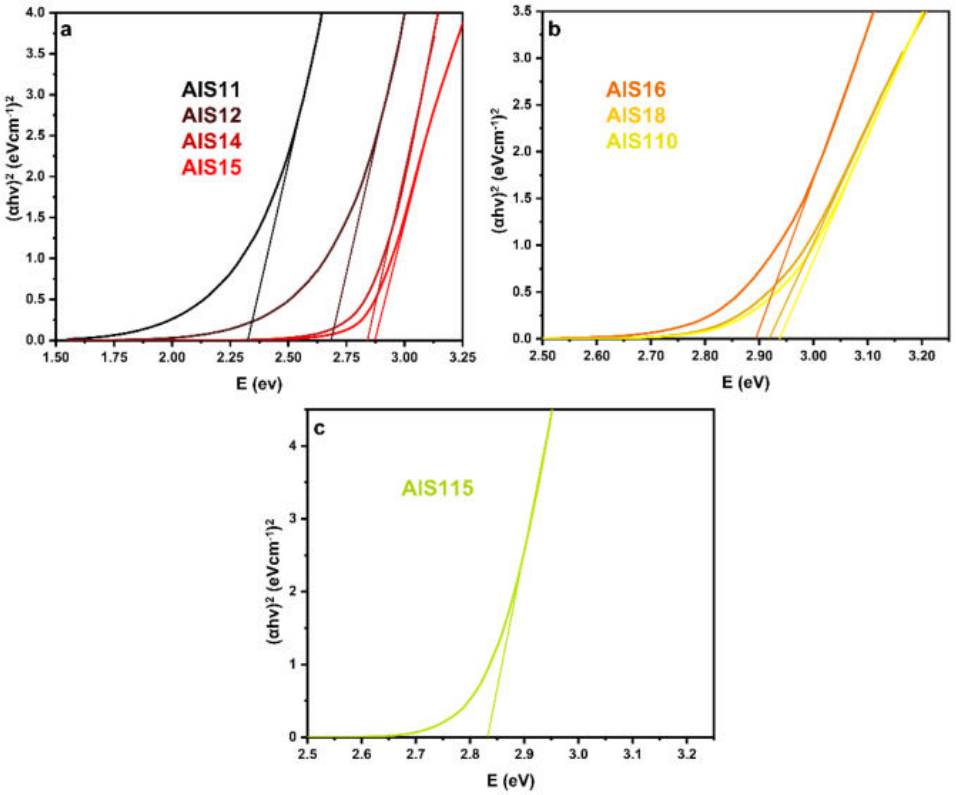

Figure A15: Tauc plot analysis of AIS QDs. a) **AIS11** -**AIS15** QDs, b) **AIS16** – **AIS110** QDs and c) **AIS115** QDs

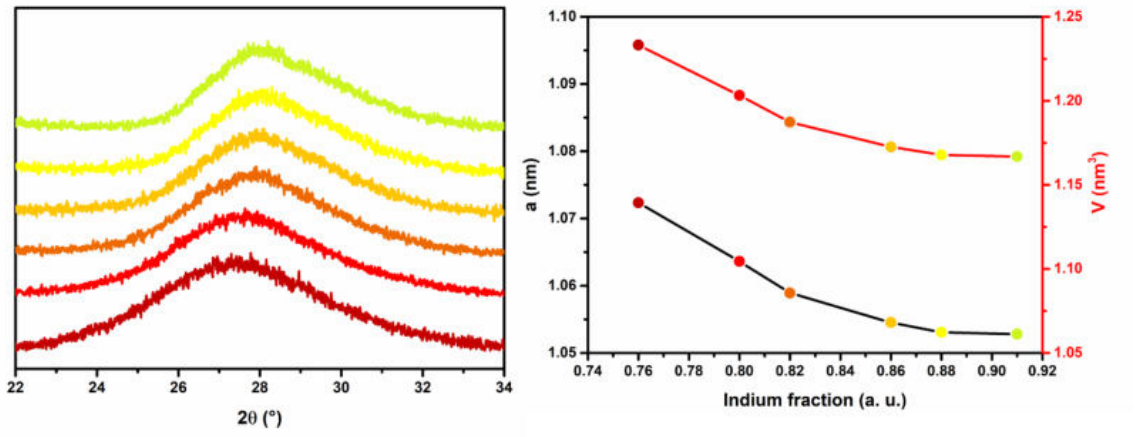

Figure A16: detail of the XRD pattern of AIS QDs (left), plot of the cell parameter and cell volume against the nanocrystals composition calculated from **Eq. A6**.

Eq. A6

$$d_{hkl} = \frac{a}{\sqrt{h^2 + k^2 + l^2}}$$

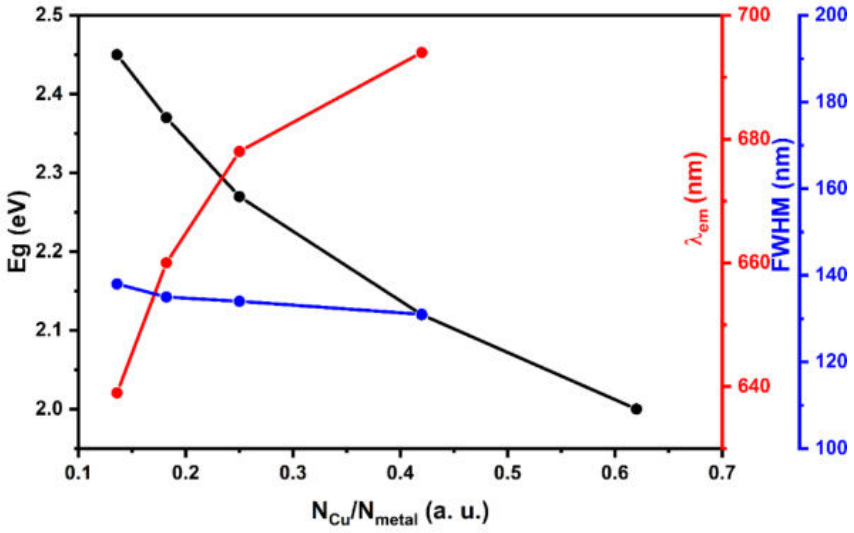

Figure A17: variation of the optical properties of CIS QDs in function of their chemical composition.

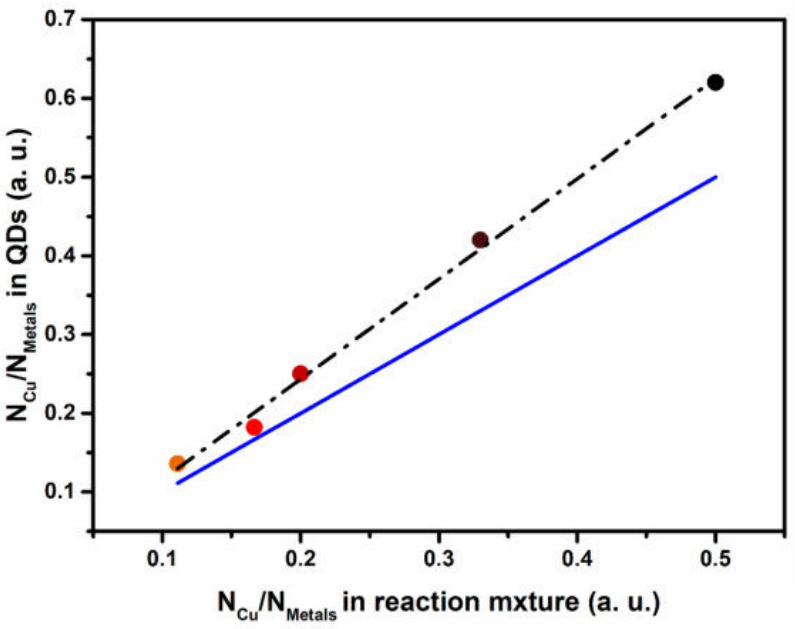

Figure A18: plot of the chemical composition observed in CIS QDs against the precursors ratio used in the reaction mixture, the linear fitting is indicated by the dashed line **Eq. A7**. The blue line is an indicative reference for y = x.

Eq. A7

$$N_{Cu}/N_{Metals}{}^{QDs} = -0.011 + 1.273\ N_{Cu}/N_{Metals}{}^{RM}$$

$r^2 = 0.995$

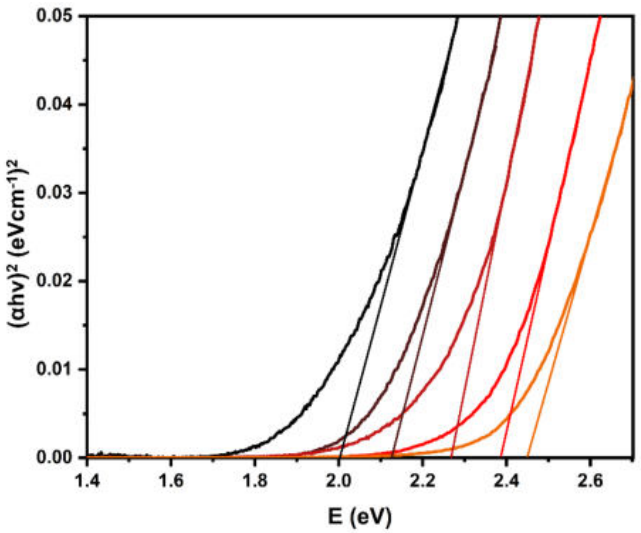

Figure A19: Tauc plot of CIS QDs with different chemical compositions

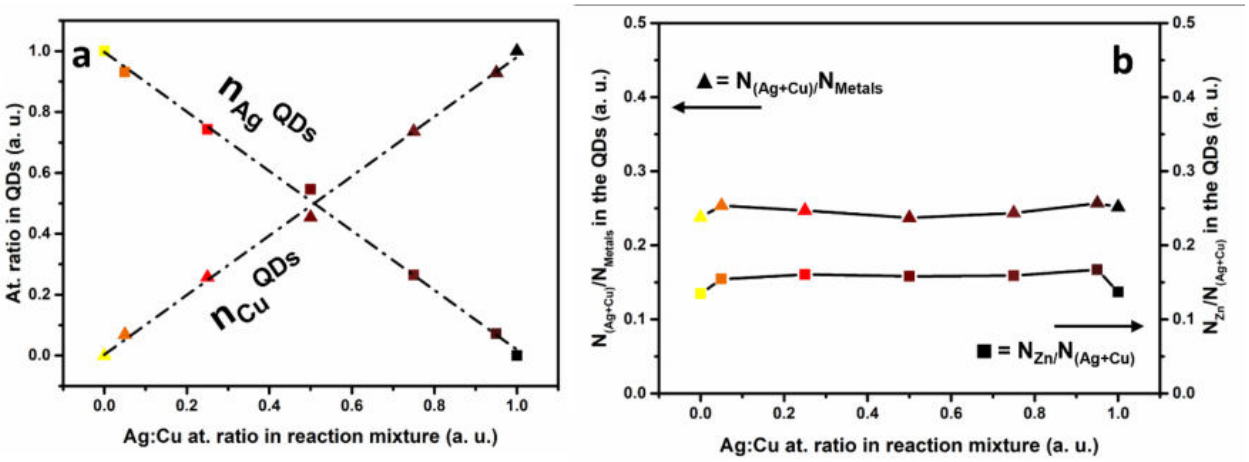

Figure A20: plot of the chemical composition of ACIS QDs: (left) silver and copper molar ratio observed in the QDs. (right) Indium and zinc content* (* = in the ACIS/ZnS core shell QDs).

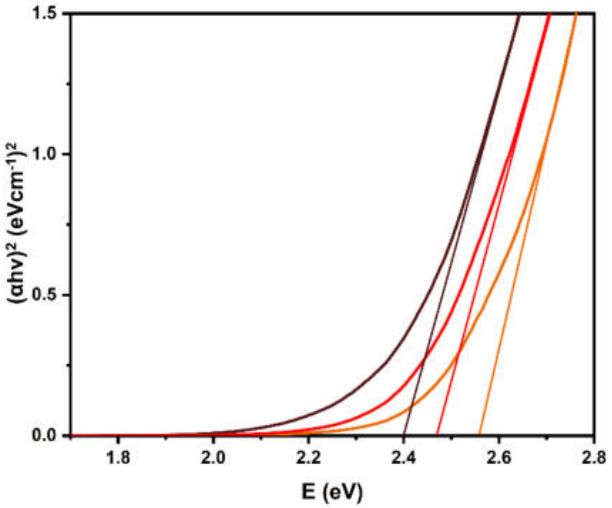

Figure A21: Tauc plot of ACIS QDs sample with different chemical compositions.

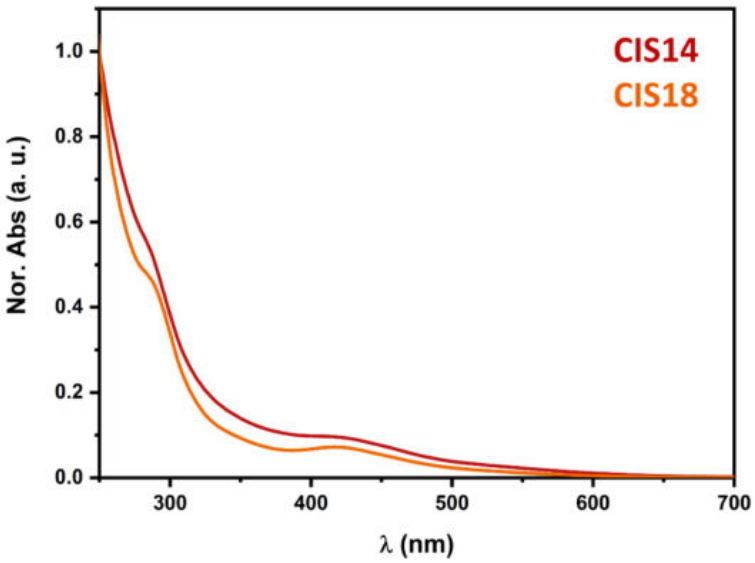

Figure A22: UV/Vis absorption spectra of **CIS14** and **CIS18** NCs colloidal solutions

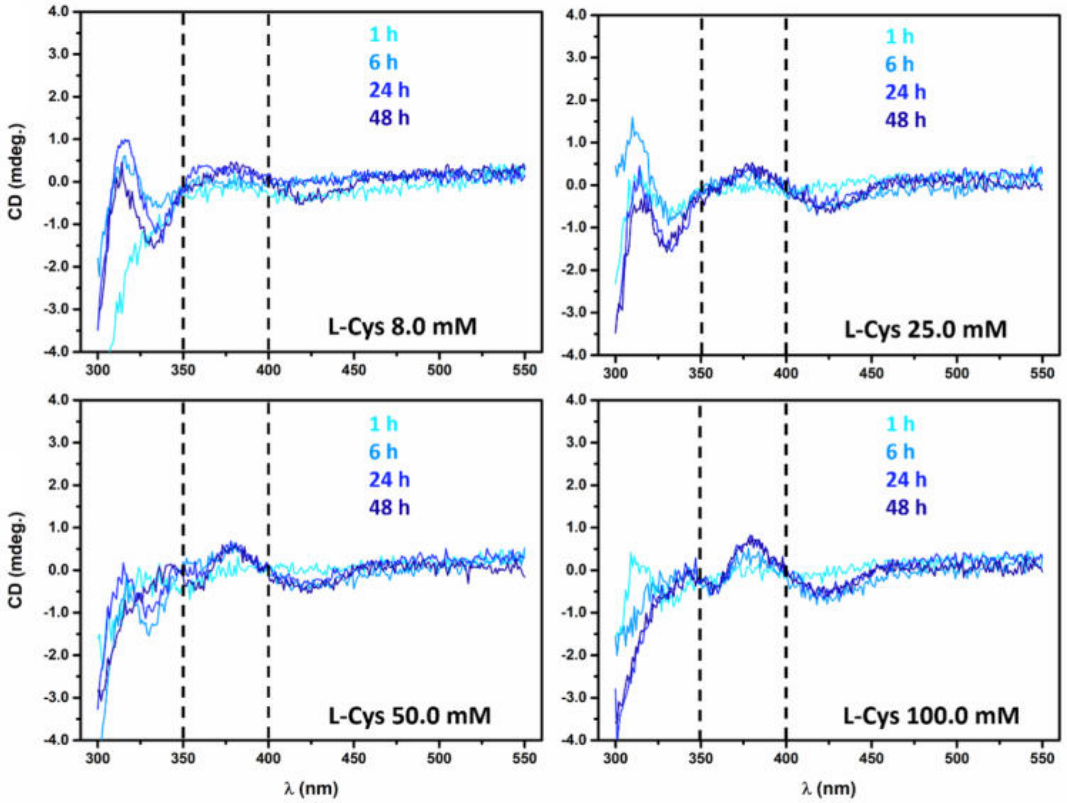

Figure A23: Evolution of the CD signal in the exciton region of during the 2nd step to produce **L-AIS14** QDs in the presence of different L-cysteine concentration, spectra collected at different time intervals after the addition of the ligand.

CHAPTER IV

ARGININE STABILISED CHIRAL COPPER HALIDES

This chapter deals with a preliminary investigation of the synthesis of novel lead-free chiral metal halides focusing on cesium copper halides. This class of inorganic and organic-inorganic hybrid materials have recently become extremely popular due to the large interest of the scientific community on lead halide perovskites and their outstanding optical properties. However, due to the toxicity of lead-based material, several other perovskites and non-perovskites metal halides characterised by promising optical properties, have attracted the attention of several researchers. Among these materials, copper halides are characterised by high photoluminescence quantum yield, high stability and high exciton recombination energy, very attractive properties for their application in photonics. For this reason, several reports on the application of these materials for the production of light emitting diodes (LEDs) can be found in literature.

This chapter starts with a brief introduction that describes the wide family of halide perovskites and related non-perovskites halides, considering in a more general way the metal halides that present promising optical properties. The description covers the following general aspects: i) different type of metal halides, ii) the most studied synthetic approaches for their production, iii) the introduction of chirality in metal halides according to the different strategies that proved to be successful.

In the Results and Discussion section are reported:

- the development of a synthetic method based on the ligand assisted reprecipitation process for the production of chiral $Cs_3Cu_2Br_5$,
- the characterisation of the material produced by this novel approach, as well as the study of the chiroptical activity which represents the main goal of the project,
- the effect of the chiral ligand on chiroptical activity and on the particles morphology,
- a preliminary investigation covering other lead-free metal halides that can be produced by variations of the presented method.

ACRONYMS LIST:

LED: light emitting diode

MA: methylammonium

FA: formamidinium

HOIP: hybrid organic-inorganic perovskite

PLQY: photoluminescence quantum yield

DMSO: dimethyl sulfoxide

DMF: N,N-dimethylformamide

HI: hot injection

LARP: ligand assisted reprecipitation

MBA: methylbenzylamine

CD: circular dichroism

CPL: circular polarized luminescence

PEA: 1-phenylethylamine

GAm: N,N'-bis(octadecyl)-L/D-glutamic diamide

APTES: (3-aminopropyl)triethoxysilane

CCB: $Cs_3Cu_2Br_5$

EDS: energy dispersive spectroscopy

FFT: fast Fourier transform

XRD: X-ray diffraction

FTIR: Fourier transform infrared

CONTENTS

1 INTRODUCTION

1.1 LEAD-BASED METAL HALIDES

Even though, the first observations on the formation of a ternary compound by the reaction of CsX and PbX_2 in aqueous solutions are dated back to the end of the 19th,[1] the perovskite structure of these materials was confirmed only in the 50s. The study of their polymorphism showed the low temperature tetragonal or orthorhombic phases and the high temperature cubic aristotype *Pm*-3*m* phase, characteristic of materials with a perovskite structure.[2] The architype of the perovskite group $CaTiO_3$ was discovered by Gustav Rose 1839 and named after the Russian mineralogist Lev Alekseyevich von Perovski.[3] This type of structure is commonly observed for a large variety of ternary oxides ($CaTiO_3$, $BaTiO_3$, $SrTiO_3$, $NaNbO_3$, $ZnSnO_3$), associated with a generic formula ABX_3, where *B* is a small multivalent cation, A is a large monovalent cation and X an anion.[4] The perovskite structure is characterised by a 3D network of corner sharing [BX_6] octahedra which forms cubo-octahedral voids inside of which the A cation is hosted. The aristotype high temperature phase undergoes to a series of phase transition at lower temperature, producing phases with lower symmetry, such as the tetragonal (*P*4*/nmn* n° 127) or the orthorhombic (*Pnma* n° 62) phases reported for $CsPbI_3$ at room temperature. As shown in **Fig. 1**, the formation of the distorted structures is related to multiple distortion processes (octahedral Glazer tilting and B atom off centering according to Jahn Teller octahedral distortion) of the cubic phase. The [BX_6] tilting in the *ab* plane gives a bending angle $\theta_{ab} < 180$ ° and $\theta_c = 0$ °, and produces the tetragonal phase (glazer tilting system $a^0a^0c^+$). Instead, when the tilting of the [BX_6] units affects both equatorial and apical direction, the bending angles satisfy the condition $\theta_{ab} = \theta_c < 180$ ° giving the formation of the orthorhombic phases (glazer tilting system $a^+a^+b^-$).[5]

In the last decade, the scientific interest in lead-halide system is rapidly increased due to their outstanding optical properties such as: highly tunable emission according to the halide composition and morphology, long diffusion length, high carriers' mobility, bright and narrow emission that are promising for the applications in light-emitting diodes,[6–8] lasers[9–12] and field-effect transistor.[13,14] Moreover, they proved to be efficient light absorber materials for the production of photovoltaic cells,[15–18] and combined to a simple processability (low crystallisation temperature and film processing in liquid phase),[19] stimulated a large interest in the production of photovoltaic cells. Recent investigations established a power conversion efficiency

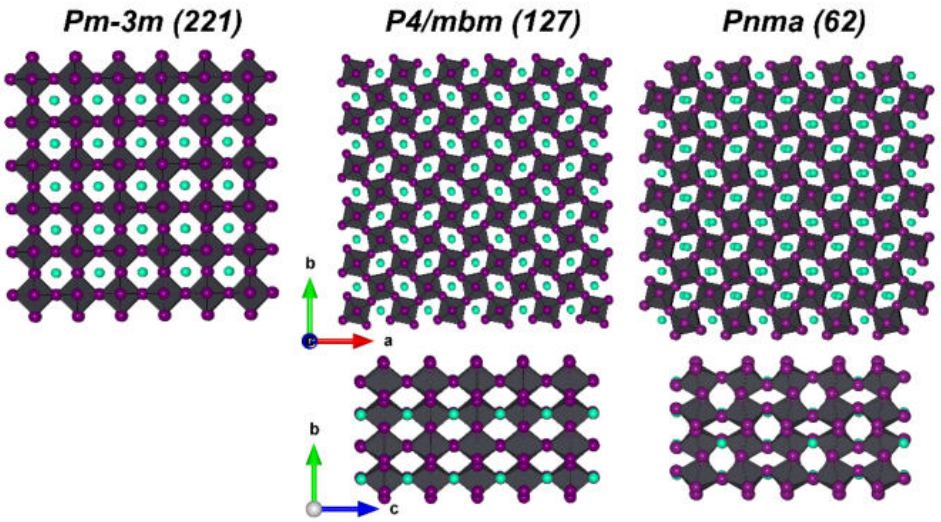

Figure 1: representation of $CsPbI_3$ structures according to its different polymorphs, simulated according to reported data: ICSD161481, ICSD231018 and ICSD264725 for the cubic *Pm*-3*m*, tetragonal *P4/mbm* and orthorhombic *Pnma* phases respectively

for perovskite based photovoltaic single junction cells comparable with other more established technologies like quantum dots and polycrystalline silicon.[20,21]

Following the guidelines on the stability of the perovskite phase dictated by the Goldsmith tolerance parameter and the octahedra factor, several halide-based compounds with a stable perovskite structure have been predicted.[22] Along with theoretical predictions, a large amount of new perovskite phases were discovered expanding the series of inorganic $CsPbX_3$ (X = Cl, Br, I) perovskites. Furthermore, different combination of A cation, both inorganic (e.g. Cs and Rb) and organic (e.g. methylammonium MA, formamidinium FA), and anions (e. g. Cl, Br and I) were reported. In addition, several non-perovskite metal halides have been reported with different stoichiometry (e.g. Cs_4PbX_6 and $CsPb_2X_5$ shown in **Fig. 2a**) which do not present a structure characterised by the 3D network of corner sharing [BX_6] octahedra, and they cannot form the aristotype cubic phase without drastic variation of their structure.[23] The post-perovskites structures such as $CsPb_2X_5$ and Cs_4PbX_6, where the inorganic network is structurally confined in 2D, 1D or 0D, represent some interesting examples. Finally, the hybrid organic-inorganic perovskites (HOIPs) are formed when a large organic cation which cannot fit inside the *A* site is introduced into the structure producing a layered structure composed by alternating inorganic and organic layers. The number of inorganic units staked in the single layer *n* (which can span from the single monolayer n = 1 to the bulk 3D phase n > 5), can be controlled by

adjusting the molar ratio between the large and the small cations, and it defines the final electronic and optical properties. This strategy has become incredibly useful to finely tune the exciton confinement with atomic precision.[24]

The major drawbacks related to the lead halide perovskites are associated to the high lead toxicity along with the low stability of the lead metal halide against moisture, heat and photodegradation. For these reasons, several other lead-free metal halides systems have been investigated in order to evaluate potential candidates in a wide range of applications spanning from photovoltaic to LEDs.

1.2 LEAD-FREE METAL HALIDES:

As reported above, several efforts have been made studying lead-free metal halides systems in order to find a less toxic alternative to these promising materials. Due to the high solubility of lead halides in water, related to the high ionic character of the structures, the devices based on lead-halide perovskites have risen a serious concern on the environmental pollution.[25] Thanks to the similar ionic radius of Sn (1.18 Å) and Pb (1.19 Å) divalent cations, Sn(II) can be considered as an optimal candidate to replace Pb(II). For this reason, several $ASnX_3$ systems

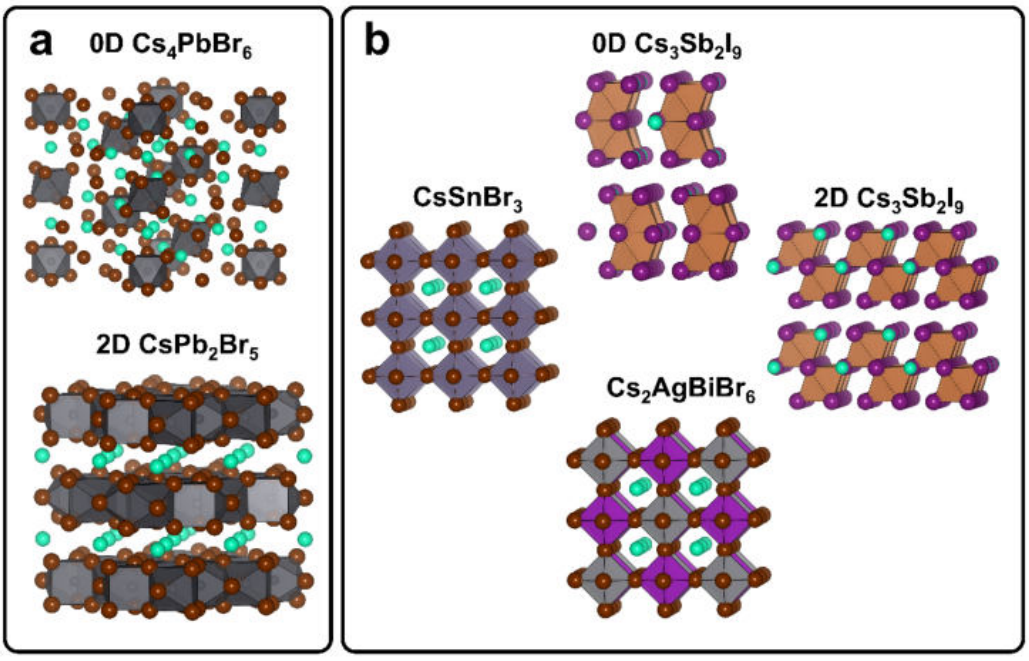

Figure 2: a) representation of the crystal structure of different types of all-inorganics lead bromide halide perovskites with the characteristic 0D and 2D confinements. b) representation of the crystal structure of some remarkable examples of lead-free metal halides. The structures are produced according to the deposited data: ICSD162158 (Cs_4PbBr_6), ICSD254290 ($CsPb_2Br_5$), ICSD241646 ($CsSnI_3$), ICSD84989 (0D $Cs_3Sb_2I_9$), ICSD84990 (2D $Cs_3Sb_2I_9$), ICSD18989 ($Cs_2AgBiBr_6$).

presenting the expected perovskite structure (e.g. $CsSnBr_3$ represented in **Fig. 2b**) have been reported.[26]

However, although these systems exhibit promising optical properties such as high absorption, high photoluminescence quantum yield (*PLQY)*, narrow emission and direct band gap, they show low chemical stability under environmental condition. This behaviour is mainly due to the spontaneous oxidation of Sn(II) to more stable Sn(IV),[27] and it represents an obstacle to consider Sn(II) based systems as potential candidate for replacing led halide perovskites in industrial applications. Other elements such as Ge, Sb and Bi have been investigated.[28] Germanium all-inorganic perovskites present similar characteristics to Sn analogues, along with the typical instability when exposed to ambient atmosphere that significantly hampered the investigation on these systems.[27] Instead, trivalent cations such as antimonium and bismuth form stable $A_3B_2X_9$ (B = Sb, Bi) phases in 0D or 2D layered polymorphs (**Fig. 2b**) depending on the different combination of *A*, *X* and synthetic conditions. A 1D polymorph has been also reported for $(MA)_2BiI_9$.[29] However, despite the superior stability associated to the oxidation state of the B cations, these systems show less interesting optical properties especially concerning photoluminescence (PL) related to the nature of their optical band-gap. Indeed, an indirect band gap of 2.40 eV was reported for 0D $Cs_3Sb_2I_9$ dimer structure and a nearly direct band-gap of 2.05 eV was measured for the 2D $Cs_3Sb_2I_9$ layered structure **Fig 2b**.[30–32]

Another strategy to preserve the perovskite structure involves the replacement of the divalent Pb with two different cations: a monovalent (Ag) and a trivalent (In, Bi).[33] These systems, characterised by the formula $A_2BB'X_6$, are named double perovskites (**Fig 2b**),[34] and are usually characterised by low PLQY associated to their indirect optical band gap.[33] For this reason, ions doping has become a largely investigated strategy to improve the optical performances in double perovskites.[35]

1.3 COPPER-BASED HALIDES

Copper based halides are a class of luminescent materials with structure, physical-chemical and chemical properties closely related to other metal halide perovskites. The scientific interest on the copper systems arises from their low toxicity, high abundance of copper ores in the earth crust, high chemical stability, low cost and high PLQY. Copper ternary halides are stable in a wide variety of structures which do not show the typical perovskite structure characterised by the 3D corner-sharing octahedra network.

The monovalent Cu(I) produce stable ternary halides with two main stoichiometries, $CsCu_2X_3$ (that is mainly observed for the iodide) and $Cs_3Cu_2X_5$ (X = Cl, Br and I). The $CsCu_2I_3$ crystallise in the orthorhombic *Cmcm* space group with a structure composed by 1D chains of $[CuI_4]^{3-}$ tetrahedra sharing corners and edges (**Fig. 3a**). The $Cs_3Cu_2Br_5$ and $Cs_3Cu_2I_5$ phases crystallise in the orthorhombic *Pnma* space group and their structure does not contain the typical octahedra coordination polyhedral (**Fig. 3b**). Cu(I) is found in two different coordination environments, tetrahedra $[CuX_4]^{3-}$ and trigonal planar $[CuX_3]^{2-}$ (**Fig. 3b**), these two structures form isolated $[Cu_2X_5]^{3-}$ dimers by edge sharing.

The $Cs_3Cu_2Cl_5$ phase crystallises in the *Cmcm* space group (**Fig. 3c**). Even in this case the transition metal cation forms $[Cu_2X_5]^{3-}$ dimers by edge sharing, but the chloride phase presents 1D chains where the $[Cu_2X_5]^{3-}$ units are connected via corner sharing, while in the bromide and iodide phases the $[Cu_2X_5]^{3-}$ units are separated by Cs^+ in a 0D structure (**Fig. 3b**).[36] These all-inorganic Cu(I) ternary halides are characterised by intense photoluminescence in the green-blue visible region with excitation in the UV range. In particular, $Cs_3Cu_2I_5$ nanocrystals, produced by hot injection show a strong emission around 440-445 nm (*PLQY* of 67.8[37], 29.2[38] and

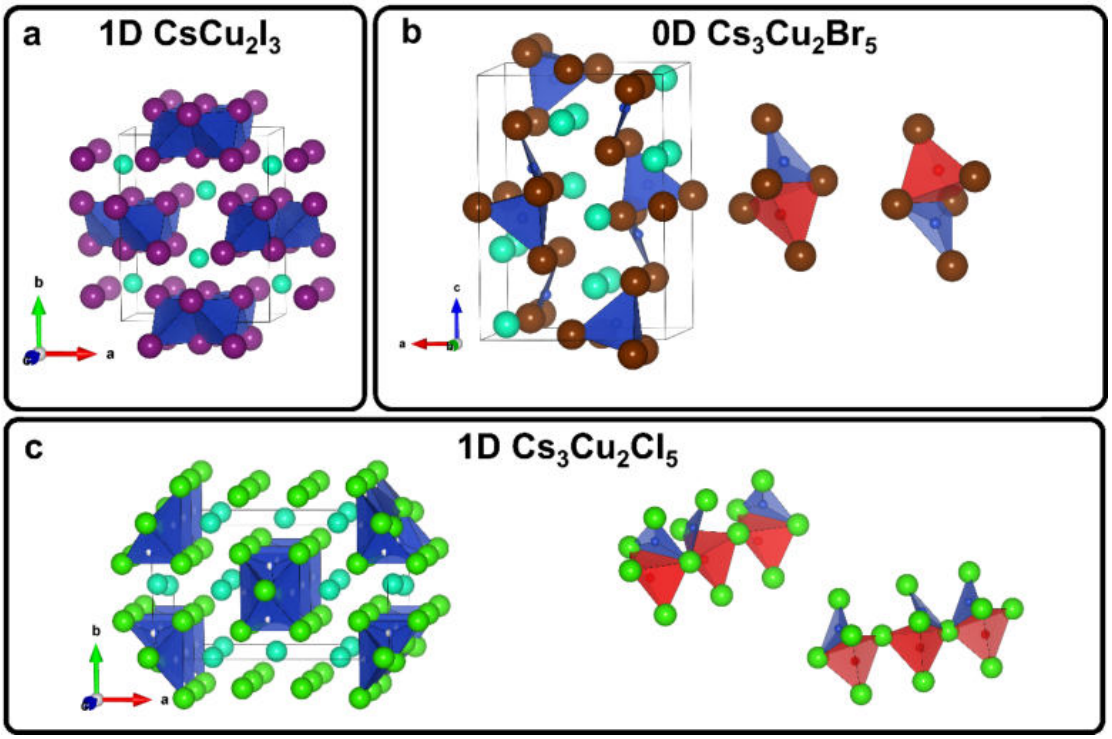

Figure3: representation of the crystal structure of a) $CsCu_2I_3$, b) $Cs_3Cu_2Br_5$ and detail on the $[Cu_2Br_5]^{3-}$ dimeric units (the tetrahedral site is represented in red and the trigonal planar is represented in blue), c) $Cs_3Cu_2Cl_5$ and detail on the 1D chain composed by $[Cu_2Br_5]^{3-}$ dimeric units connected by corner sharing (the tetrahedral site is represented in red and the trigonal planar is represented in blue). The structures are produced according to the deposited data: ICSD12631 ($CsCu_2I_3$), ICSD22950 ($Cs_3Cu_2Br_5$) and ICSD22951 ($Cs_3Cu_2Cl_5$).

73.7[39]). The $Cs_3Cu_2Br_5$ phase presents a red-shift of the emission wavelength at 450 - 460 nm

and a lower PLQY (16.9[38], 3.9[39] and 17.3[40]), while, the $Cs_3Cu_2Cl_5$ phase is characterised by a green emission at around 510 – 520 nm and in some case an almost unit PLQY associated to the 1D structure.[41,42] Finally, the 1D $CsCu_2I_3$ phase is characterised by a yellow emission centred around 560 -570 nm (PLQY of 11[41], 6[36] and 12.1[43])

All the $Cs_3Cu_2X_5$ halides show a characteristic emission with large Stokes shift and a relatively broad FWHM. These characteristics are associated to the specific recombination process that is dominated by a self-trapped exciton mechanism (STE). Moreover, the characteristic trend that shows a red shift of the *PL,* starting from iodide to chloride is in contrast with the observations on other metal halides and has been largely investigated.[44]

Along with the metal halide of the Cu(I) series, a variety of organic inorganic layered halide perovskite structure based on Cu(II) is also known. Cortecchia et al.[45] reported the first evidence on the isolation of metal halides of the $(MA)_2CuCl_xBr_{4-x}$ series. Highly stable $(MA)CuBrI_2$ films with a high environmental stability were isolated by Saparov and coworkers.[46] These systems show promising applications in solar cells and thermoelectric devices rather than photonics due to their high electrical conductivity and absorption coefficient. [46,47]

1.4 METAL HALIDES SYNTHESIS

Several synthetic approaches have been developed during the past years to produce metal halides in different forms: single crystals, thin films, powders and colloidal nanocrystals. Due to the similar chemical behaviour of metal halides the synthetic approaches are usually very similar. The minor adaptations are related to the choice of the specific precursors employed for the preparation of the different matrixes.

Due to the aim of the thesis, the following discussion will be focused on the copper halides. In the next sections the different approaches used to produce metal halides are briefly described along with some relevant examples with a particular focus on the colloidal synthesis.

Single crystals: single crystals with sizes of few millimeters are produced *via* antisolvent infiltration methods (or antisolvent vapor assisted crystallisation). According to this method a saturated metal halide solution is produced by solubilisation of the reagents in coordinating solvent such as dimethyl sulfoxide (DSMO) or N,N-dimethylformamide (DMF). Then, a solvent with lower polarity which acts as antisolvent is added in order to induce the perovskite precipitation. At the saturation condition, the supernatant is collected by filtration and exposed

to an atmosphere saturated of vapours of an antisolvent to induce the formation of large single crystals. The process is relatively slow (e.g. 48 h or longer), and the control of the temperature with a hotplate can accelerate the antisolvent diffusion in the metal halide solution. Jun et al. [48] reported the production of $Cs_3Cu_2I_5$ single crystals with a PLQY of 91.2 % by precipitation in the presence of methanol from a 1 M metal halide solution with an ageing of 48 h at 60 °C. Lin et al. [49] isolated centimeter scale high-quality $CsCuI_3$ single crystals after an ageing of several days of the metal halide mixture in a DMSO:DMF (1:4) solution under methanol atmosphere at room temperature.

Thin films: thin film preparation techniques are mainly divided in solution processing (such as spin coating that requires organic solvents like *DMSO* and *DMF*) and dry processing (e.g. single source vapor deposition or dual source thermal deposition). During the spin coating processes, the metal halide solution, in DMSO-DMF mixture solvent, is deposited on a desired substrate. Then, crystalline films are produced by thermal annealing at temperature between 70 and 100 °C under inert atmosphere. Jun et al. [48] prepared a $Cs_3Cu_2I_5$ thin film on indium tin oxide/zinc silicate substrate for the fabrication of a LED device by spin coating a CuI, CsI solution, at 3000 rpm for 60 s in an argon filled glovebox, followed by annealing at 100 °C. Similar approaches are also reported by other authors.[50,51]

Single source vapor-deposition is an important solvent-free approach for the preparation of thin films. In this case a crucible with a pre-synthetised polycrystalline powder is loaded in a vacuum chamber (working pressure 8 x 10^{-6} mbar). The powder is rapidly heated (target temperature of 600 °C and a heating ramp of 50 °C/min) to induce the sublimation of the powders which is deposited on a desired substrate.[50] Another example of solvent-free process was reported by Liu and coworkers.[52] They reported on the production of $Cs_3Cu_2I_5$ thin film with a *PLQY* of 58 % via dual-source thermal-deposition. According to this process, CsI and CuI were separately heated inside the deposition chamber to form the desired product on top of a substrate, with high degree of crystallinity and phase purity.

Polycrystalline powders: Grandhi G. K. et al. [36] reported a rapid and solvent-free mechanochemical process for the production of $Cs_3Cu_2X_5$ (X = Cl, Br and I) and $CsCu_2I_3$ microcrystalline powders by hand-grinding of a proper ratio of the halide precursors. Despite the low temperature approach, the products showed a high degree of crystallinity and phase purity, characteristics that were related to the high ionic character of the copper halide perovskite which

facilitated ion mobility in solid state reactions. They also evidenced the reversible transformation of $Cs_3Cu_2I_5$ to $CsCu_2I_3$ according to different addition of CuI or CsI, followed by 5 min of grinding at room temperature to guarantee the completion of the reaction. The authors reported PLQYs of 62, 10, 60 and 6 % for $Cs_3Cu_2I_5$, $Cs_3Cu_2Br_5$, $Cs_3Cu_2Cl_5$ and $CsCu_2I_3$ respectively. Moreover, high quality polycrystalline samples could be produced by the slow thermal quenching of a melted salt mixture in quartz ampoules sealed under vacuum condition. Using this procedure, Roccanova R. et al.[53] reported the isolation of different copper halides of the $CsCu_2X_3$ series (X = I and the Cl and Br phases that are not accessible via colloidal synthesis) and Li et al.[54] investigated different structures and the novel 1D $Cs_5Cu_3Cl_6I_2$ mixed halide, that shows high *PLQY* (95 %) and stability. In particular, no sign of decomposition was observed after three months under ambient atmosphere.[54] Finally, Sebastia-Luna et al. reported a wide variety of $CsCu_2X_3$ and $Cs_3Cu_2X_5$ with a fine modulation of the halide composition, using the ball milling approach.[50]

Colloids: Colloidal solutions of nanoparticles and microcrystals are conventionally prepared via wet chemical route. Several different synthetic techniques have been adapted from other colloidal syntheses of inorganic, organic or polymeric nanoparticles. The wet syntheses use solvents as reaction media and the particle formation occurs in the presence of ligands which play multiple critical roles during the particles formation. In particular, the ligand affects both the kinetics of the crystal growth and the particles stabilisation in the colloidal solution. These aspects are fundamental from the synthetic point of view: the former is essential to control morphology and size of the nanoparticles, the latter ensures stability against aggregation and precipitation. For the specific case of metal halides the most explored colloidal approaches are the hot-injection (*HI*) and the ligand assisted reprecipitation method (*LARP*).

- **Hot injection techniques (*HI*):** this approach is generally based on the rapid injection of a Cs^+ precursor (such as cesium oleate) at high temperature in a solution containing copper and the halide precursors. A fast cooling of the reaction mixture usually follows the injection step to avoid the excessive growth of the nanoparticles. The rapid injection step is followed by a fast heterogeneous nucleation step that is characterised by a size focusing phenomenon, typical of a diffusion-controlled growth. Thanks to these features, *HI* methods have become especially common in colloidal chemistry to produce small nanoparticles with a narrow size distribution. For longer reaction times,

Oswald ripening process causes an increasing in the particles size and size distribution.[55] Moreover, at the temperatures, accessible using high boiling point solvents (e.g. 1-octadecene), the production of highly crystalline nanoparticles is usually observed. This approach has been largely exploited to produce monodisperse semiconductors nanoparticle colloids[56] and it has been efficiently adapted for several metal halides. Cheng et al.[37] reported the production of 1D $CsCu_2I_3$ nanorod and 0D $Cs_3Cu_2I_5$ nanocrystals via *HI*. They observed that the temperature plays a crucial role in the phase stabilisation: the $CsCu_2I_3$ phase can be isolated when the injection is performed at higher temperature (110 °C), instead at lower temperature (70 °C) it is possible to isolate the $Cs_3Cu_2I_5$ phase. However, working with a similar approach, Lian et al.[40] isolated different $Cs_3Cu_2X_5$ (X = Cl, Br, I) phases by hot injection of the cesium oleate precursor at 120 °C followed by a rapid quenching of the reaction after 20 s. Unfortunately, the characterisation of the particle morphology is not available. A similar approach was also reported by Vashishtha and coworkers.[57] Instead, Luo et al. [38] reported an adaptation of the HI method. In their approach the halide source is injected (a solution contains oleyilamonium salts solubilised in oleylamine) in the reaction mixture containing both cesium and copper. Moreover, with this approach Cu(I) is produced in situ exploiting the reducing activity of oleylamine at high temperature to reduce the Cu(II) ions.

- **Ligand Assisted Reprecipitation (*LARP*)**: This approach was originally developed to produce organic or polymeric nanoparticles[58–60] and it was adapted for the first time for the synthesis of $(MA)PbX_3$ (X = Cl, Br and I) by Zheng et al.[61] This technique is based on the solubilisation of the metal halides precursors in a solution of a strong coordinating polar solvent such as DMF, DMSO or their mixtures. Then, the metal halide solution is added drop by drop to a solvent with lower polarity which acts as antisolvent triggering the precipitation of metal halide particles. Toluene and ethyl acetate are typically used as antisolvents. Zhang et al.[61] highlighted the fundamental role played by the addition of ligands to control the crystal growth and the stability of the colloid. They employed a mixture of oleic acid and n-octylamine to produce nanocrystals with an average size of about 3.3 nm that present high PLQY and stability. Moreover, in absence of the ligand, the formation of micrometrical size crystal with low PLQY (< 0.1

%) was observed.[61] After this fist report, The LARP method has been successfully employed to produce several other metal halides such as: the all-inorganic $CsPbX_3$ series,[62,63] $Cs_3Bi_2X_9$,[64,65] $Cs_3Sb_2Br_9$[66] and Cs_2AgBiX_6[67] double perovskites. Despite the large success in the synthesis of several different metal halide phases, the application of LARP approach for the synthesis of cesium copper halides is still quite unexplored. At the best of our knowledge, the only report available in the literature on the synthesis of copper-based halides via *LARP* is from Vashishtha and collaborators.[68] They reported the synthesis of Rb_2CuBr_3 and Rb_2CuCl_3 by the initial solubilisation of the halides in *DMSO* in the presence of oleic acid as ligand and toluene is used as antisolvent.[68]

1.5 CHIRALITY IN METAL HALIDES

Chiral luminescent metal halides present promising properties like spin-filtering activity, circular polarize luminescence, circular polarization detection and non-liner optical activity which have stimulated several investigations on synthesis and characterisation of these novel chiral systems.[69–71] Most of the reports available in the scientific literature are mainly focused on lead-based halide perovskite. In this context, there is a clear distinction between three main strategies exploited to introduce chirality in metal halides:

1) chiral structure: introducing an organic large chiral A cation in the 3D network to promote structural distortions which causes a loss of symmetry. This approach is a natural implementation of a chiral cation for the production of layered hybrid organic inorganic perovskites which crystallise in chiral space groups,

2) chiral interface: chiral ligands are employed to stabilise the particles surface of achiral inorganic metal halides. This approach is also suitable for all-inorganic metal halides, and it is characterised by the transfer of chirality at the particle-ligand interface.

3) chiral assembly: the assembly of achiral nanocrystal is directed by a chiral template producing heterostructure which in proper conditions can show an efficient transfer of chirality. The chiral template can be either a soft template (gels and liquid crystals) or a hard template (silica or cellulose microcrystals).

These different strategies and some remarkable examples are discussed in this section.

1.5.1 Chiral structure

The first observations of chiral HOIPs structures are dated back to D. G. Billing and A. Lemmerer.[72,73] In 2003 they reported the structure of (S-MBA)$PbBr_3$ which crystalizes in the chiral orthorhombic $P2_12_12_1$ space group.[72] The structure of chiral HOIPs is composed by 1D chain of distorted face sharing $[PbBr_6]^{4-}$ octahedra that extend parallel to the a-axis and separated by layers of *S-MBA* cations. Later in 2006 they further investigated other organic inorganic chiral hybrid systems including the 2D layered (S-MBA)$_2PbI_4$ and (R-MBA)$_2PbI_4$ composed by inorganic layers of corner sharing $[PbI_6]^{4-}$ octahedra isolated by layers of methylbenzylamine (MBA) (**Fig. 4a**).[73] However, despite the production of these chiral HIOPs, the characterisation of the chiroptical properties was reported only in 2017 by Ahn et al.[74] who characterised the circular dichroism (*CD*) activity of 2D layered (R-MBA)$_2PbI_4$ (S-MBA)$_2PbI_4$ and (rac-MBA)PbI_4 thin films. The presence of a bisignated CD signal in the band edge region (497 nm) highlighted the successful induction of chirality in the material. They established by powder XRD analysis, that homochiral halides which showed chiroptical activity crystallise in the chiral space group $P2_12_12_1$, instead the *CD* silent racemic one crystallises in the achiral $P2_1/a$ space group. Their detailed investigation on the modulation of the chiroptical activity in (R-MBA)$_2PbI_{1-x}Br_{4x}$ and (S-MBA)$_2PbI_{1-x}Br_{4x}$ according to the different halide composition highlighted, along with the expected variation of the band-gap energy, the loss of optical chirality in the band edge region (**Fig. 4b** top) for the samples that presented higher bromide content. The authors ascribed this feature to a structural transition modulated by the halide composition. A preferential crystallisation in the chiral $P2_12_12_1$ space group (defined as iodide-determinant phase) was observed for iodide-rich samples, while the stability of an achiral phase (define as the bromide-determinant phase) was promoted with the increasing the bromide content (**Fig. 4b** bottom), causing the loss of chirality.[75]

As reported above, the origin of the chiroptical properties in HOIPs is usually related to the crystal structure and associated to the structural flexibility of the *HOIPs*.[76] A chiral large organic cation is used as insulator layer between the inorganic layers and can introduce structural distortions that produce the symmetry breaking causing the material to crystallise in a chiral space group. Other requirements, such as the halides composition and the size of the

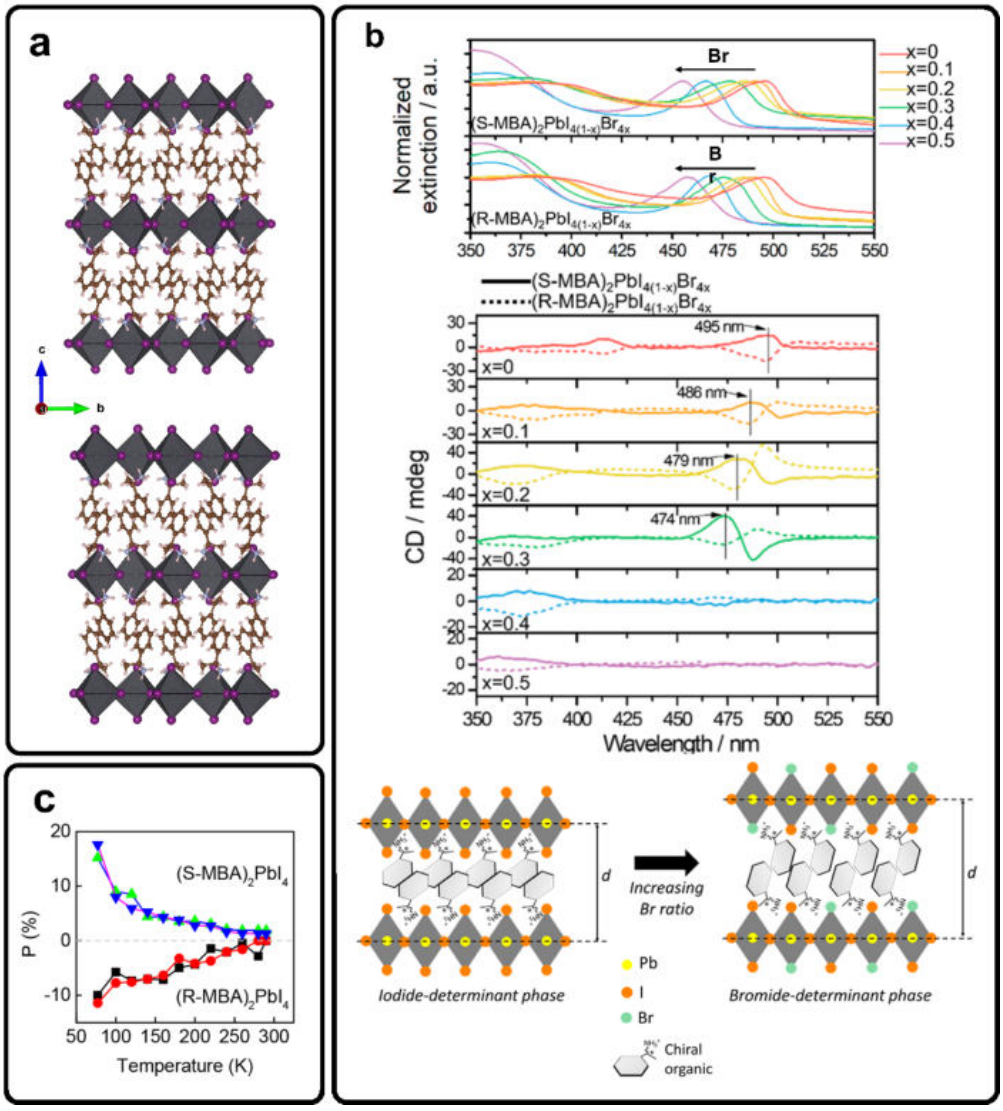

Figure 4: a) representation of the crystal structure of $(R\text{-}MBA)_2PbI_4$ $(S\text{-}MBA)_2PbI_4$. b) effect of the bromide content on the absorption and CD spectra (top) and schematic representation of the proposed structural transition from the chiral iodide-determinant phase to the achiral bromide-determinant phase (bottom) Ref. 72. c) The effect of the temperature on the degree of polarization of the CPL light investigated by Fang. Et al. Ref. 74.

chiral cation, dramatically affect the crystal structure and the efficiency of the transfer of chirality.[75] However, *HOIPs* are usually produced as thin films and in order to compare the CD activity with other type of samples, such as colloids, it is fundamental to remove artifacts such as scattering contribution.[74]

Several efforts have been made to maximize the chiroptical properties of these systems and to preserve appreciable photoluminescence activity. The pure 2D halide with number of inorganic layer (*n*) equal to one, is expected to present the highest chiroptical properties due to the largest organic to inorganic ratio. However, the photoluminescence of these structures is severely affected by non-radiative recombination processes that cause low or no photoluminescence activity.[76] Increasing *n* allows to isolate a wide range of *quasi*-2D phases ($n \geq 2$). If

the increase of the content of the staked inorganic layers raises the PLQY, this is also associated to an extensive reduction of the efficiency of the transfer of chirality. Pseudo bulk perovskites with *n* = 5 show a complete loss of chiroptical activity.[77] Long et al.[77] reported that the optimal condition for an appreciable photoluminescence and chiral transfer was achieved at *n* = 2.

Finally, due to the structural softness of HOIPs*,* a temperature dependence on the transfer of chirality is observed. The effect on the degree of polarization of the Circular Polarized Luminescence (CPL) light for R/S$(MBA)_2PbI_4$ was reported by Fang and coworkers.[78] They evaluated the degree of polarization at 0 tesla *P* $(I_{left}-I_{right})/(I_{left}+I_{right})$ at different temperature from 77 to 290 K. Their measures showed a monotonously decreasing of the degree of polarization from around 10 % observed at 77 K to nearly none as the temperate approaches 290 K. This finding agrees with the structural origin of the chiroptical activity in *HOIPs*. Furthermore, the authors suggest that the origin of this phenomena is related to the electron-phonon interactions and thermal expansion that, increasing the temperature reduces the effect of the lattice distortions.

1.5.2 Chiral interface

In 3D metal halides, chiroptical properties can be induced by exploiting the interaction of a chiral ligand on the metal halide particles surface. By this approach it is possible to introduce chirality even in all-inorganic metal halides and 3D structures, incompatible with the chiral structure approach.

He et al.[79] reported the first example of a chiral $CsPb(I/Br)_3$ nanocrystal produced via a two steps route. In the first step, achiral metal halide nanoparticles covered with oleylamine were produced. The chirality was introduced during a second post-synthetic ligand exchange with (R,R) or (S,S) diaminocyclohexane under microwave treatment at 100 °C for 30 min. They observed at high chiral ligand concentrations, a CD signal characterised by strong peaks in the UV region (below 300 nm), which they related to the formation of ligand aggregates. Instead, at low ligand concentration, they observed the presence of CD active electronic transition even at longer wavelength (below 550 nm). This result can be related to the successful transfer of chirality to the inorganic phase.[79] However, this first paper does not show presence of CD active bands in the position of the band edge and the chiral induction seems to affect mainly charge transfer transitions.[80] The variation of the particles morphology, observed during the

microwave treatment, highlights the possibility that these harsh reaction conditions can affect not only the particle-ligand interface, but also structure and composition of the inorganic core.

Cheng et al.[81] reported the first investigation on the two-photons up-converted circularly polarized luminescence (TP-UCPL) in chiral $CsPbBr_3$. Cubical $CsPbBr_3$ nanocrystals with average size of 20 nm were produced via tip-sonication in the presence of a ligand mixture composed by oleic acid, oleylamine and R/S α-octylamine. The nanoparticles chirality was confirmed by the observation of a CD signal in the bend-edge region at 504 nm and with a g_{CD} factor of 6.5 x 10^{-4} and -1.0 x 10^{-3} for R and S α-octylamine stabilised nanocrystals respectively. Moreover, the nanoparticles embedded in a PMMA matrix show high CPL activity with a characteristic g_{lum} of 4.5 x10^{-3} and - 2.8 x10^{-3} for R and S nanocrystals respectively. Similar values were also observed for the TP-UCPL, 3.5 x10^{-3} and - 2.3 x10^{-3}. The authors explained the origin of chirality in term of ligand induced chirality, according to the magnitude of the chiral induction and to the observation of the centrosymmetric structure for the inorganic core via high resolution transmission electron microscopy.[81]

Debnath et al.[80] reported a systematic study on the chiral induction via chiral ligand passivation. In their work, several chiral ligands were investigated to induce chirality in $CsPbBr_3$ nanoparticles produced via hot-injection. They investigated in detail the post-synthetic ligand exchange with R/S 1-phenylethylamine (PEA which is also called MBA*)*, to partially replace oleylamine via a room temperature ligand exchange in the presence of different concentration of *PEA*. The successful ligand exchange was confirmed *via* ^{1}H-NMR spectroscopy by solubilisation of the nanocrystal in DMSO-d_6 to observe the ligand without the broadening effects related to the interaction with the nanoparticle surface. The transfer of chirality was confirmed by the *CD* active electronic transition in the band edge region (400 – 460 nm). The variation of the intensity of the *CD* transitions with the increasing ligand concentration, showed a plateau at concentrations of about 20 mM that they related to the saturation of the nanoparticles surface. The effect of a thermal treatment evidenced a significant reduction of the chiral induction at 80 °C. This effect was explained by the authors in terms of ligand desorption promoted by the increasing temperature. The chiral induction with other chiral ligand such as R/S 1-naphthylethylamine and R/S 2-amminoctane were successfully achieved and confirm the generality of the post-synthetic ligand exchange approach.

The extensive work reported in these papers which deal on the successful attempts to introduce chirality in the electronic transition of the metal halide inorganic structure via surface passivation with organic chiral ligand, stimulated the interest on theoretical investigations. The effect of the coordination of diaminocyclohexane chiral ligand on cesium lead halide clusters was investigated by Forde et al.[82] using atomistic time dependent-density functional theory. The analysis on single ligand molecule revealed strong effect of the binding mode (mono or bidentate) on the shape of the CD signal. Furthermore, they related the chiral transfer mainly to electronic coupling between a static dipole of the chiral ligand and the transition dipole moment of the metal halide cluster rather than other mechanisms such as structural distortions of charge-transfer excitation.

1.5.3 Chiral assembly

Nanoparticles assembly assisted by a chiral template is an efficient method to introduce chiroptical properties into achiral nanoparticles. Different approaches have been successfully employed to induce chirality in achiral lead halide perovskites *via* assembly assisted by chiral templates. These approaches can be divided according to the nature of the chiral template between soft templates such as liquid crystals and cogels, formed by chiral molecular building blocks held together by supramolecolar interactions, and hard templates such as inorganic chiral structures or chiral organic crystals.

Shi et al.[83] reported on a simple method to introduce chirality in $CsPbX_3$ (X = Cl, Br, I and mixed halide compositions) nanocrystal produced by tip sonication via the formation of a chiral cogel with N,N'-bis(octadecyl)-L/D-glutamic diamide (L/D-GAm*).* The addition of L/D-Gam to a perovskite colloidal solution in hexane caused the formation of the cogel. This result was related to the partial substitution of the nanocrystals original ligands (oleylamine and oleic acid) by the gelating agent. The characterisation of the chiroptical activity of the cogels by CD spectrometry was complicated by a strong scattering. However, a strong CPL signal, up to 7.3×10^{-3}, was observed for the assembly. The CPL signal disappear completely when the cogel was dissociated with the addition of chlorobenzene, confirming the origin of chirality. In another example, Yang et al. [84] employed chiral nematic liquid crystals to introduce chirality in a system composed by upconverting nanoparticles and $CsPbBr_3$ perovskite nanocrystal. They successfully characterised the CPL activity. Moreover, they observed the amplification of degree of polarization of the CPL emission under excitation with a 980 nm laser.

Chiral silica helixes were employed by Liu et al.[85] as hard template for the formation of a $CsPbBr_3$ perovskite-silica chiral heterostructure. For this purpose, the surface of the chiral silica helixes was functionalized, by cross-linking, with (3-aminopropyl)triethoxysilane (APTES) to produce surfaces covered with terminal amines. The dynamic interaction between the $CsPbBr_3$ nanocrystal surface and its original amine ligands, such as oleylamine (used during the nanocrystals synthesis), guarantees an easy substitution with the amine groups of the APTES molecules cross-linked on the silica chiral helixes surface. The authors observed the chiral transfer after drying the reaction mixture, the product showed strong CD and CPL signals $g_{CD} \approx 6.2$ and -6.4×10^{-3} and g_{lum} of ≈ 6.9 and -5.7×10^{-3}. Instead, the heterostructure produced by the assembly in solution did not show appreciable chiroptical activity. The Cryo-electron microscopy observation revealed the formation of a less regular heterostructures when the self-assembly was conducted in solution. Another example of hard templating was reported by Li and coworkers.[86] They presented the encapsulation of $CsPbBr_3$ perovskite crystals inside the porous structure of chiral mesoporous silica. The mesoporous structure of the silica particles presented well-resolved hexagonal pore arrangement with a chiral helical shape. Perovskite nanocrystals were produced inside the pores volume by a first impregnation of the mesopores with a perovskite precursor solution, and a subsequent thermal annealing step. This product showed high CPL activity combined with the beneficial effect on the stability related to the encapsulation in the silica mesostructured.

2 RESULTS AND DISCUSSION

2.1 ARGININE STABILISED $Cs_3Cu_2Br_5$ SYNTHESIS AND CHARACTERISATIONS

A modified version of the LAPR process is developed to produce $Cs_3Cu_2Br_5$ colloids using L/D-arginine (Arg) as chiral ligand. The procedure summarized in **scheme 1** is based on the solubilisation of the metal precursors in *DMF* in the presence of the chiral ligand. An appropriate amount of HBr is employed to facilitate the solubilisation of metal salts. The formation of Cu(I) is triggered in situ by the addition of thioglycolic acid that quickly reduces Cu(II) forming the corresponding disulfide dimer. The crystallisation of the metal halide phase is induced by the dropwise addition of the precursor solution in isopropyl alcohol which acts as antisolvent. The reaction mixture is stirred at room temperature for 5 min, then the product is collected by centrifugation (7000 rpm for 5 min) and washed three times with 10.0 ml of isopropyl alcohol. The particles can be redispersed in isopropyl alcohol and they preserve a colloidal stability for days. Further details on the procedure are available in the Material and Methods section.

Scheme 1 L/D-Arg $\xrightarrow{\text{DMF, HBr 2.0 M, TGA}}$ $\xrightarrow{CuBr_2, CsBr}$ $\xrightarrow{\text{i-PrOH}}$ L/D-Arg $Cu_3Cu_2Br_5$

The crystal structure of the products synthetised in the presence of L and D Arginine, named **L** and **D-CCB**, is investigated by PXRD. The diffraction patterns reported in **Fig. 5** prove the successful synthesis of $Cs_3Cu_2Br_5$ with an orthorhombic *Pnma* (n° 62) phase, well in agreement

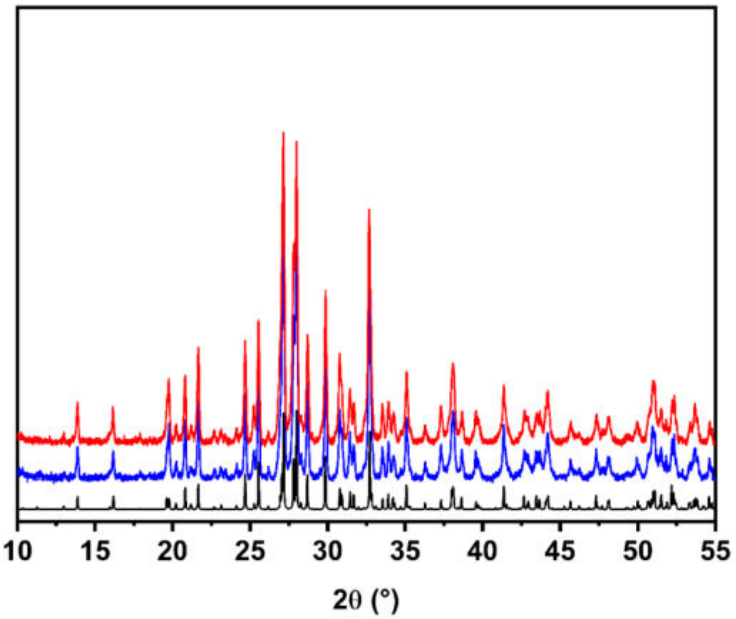

Figure 5: XRD pattern of **L-CCB** (blue), **D-CCB** (red) and the reference pattern of orthorhombic $Cs_3Cu_2Br_5$ (black) according to the reported data ICSD22950.

with the reference pattern (black line). The absence of diffraction peaks related to CsBr further confirm the purity of the product. Moreover, no peaks related to the presence of arginine crystals can be detected, and consequently, the presence of chiral ligand impurity related to the Arg coprecipitation in isopropanol can be excluded. The morphology of the product is investigated by scanning electron microscopy (SEM) and transmission electron microscopy (TEM). SEM micrographs reported in **Fig. 6a** shows the presence of micrometrical wires with a broad size distribution. Moreover, several larger crystals made by bunches of merged

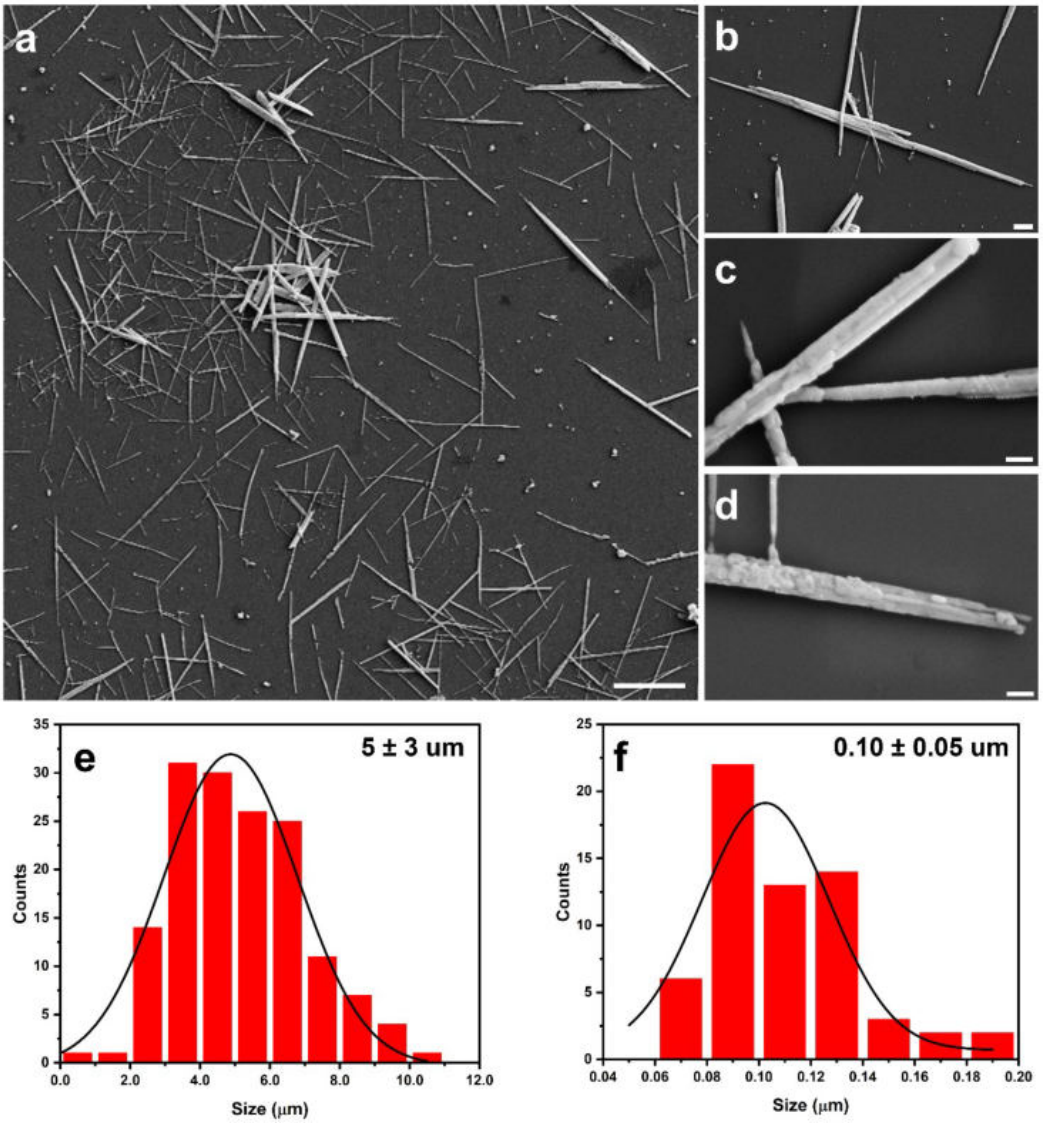

Figure 6: a-d) SEM analysis of L-CCB, the scale bars: corresponds to: a = 2.0 µm, b = 1.0 µm c and d = 200 nm e and f) size distributions of length e and width f of **L-CCB** microwires, the average values are evaluated according to the normal distribution.

smaller wires can be observed at higher magnification in **Fig. 6b-d**. The average length and width of the microcrowires are about 5 micrometers and 100 nm respectively. The

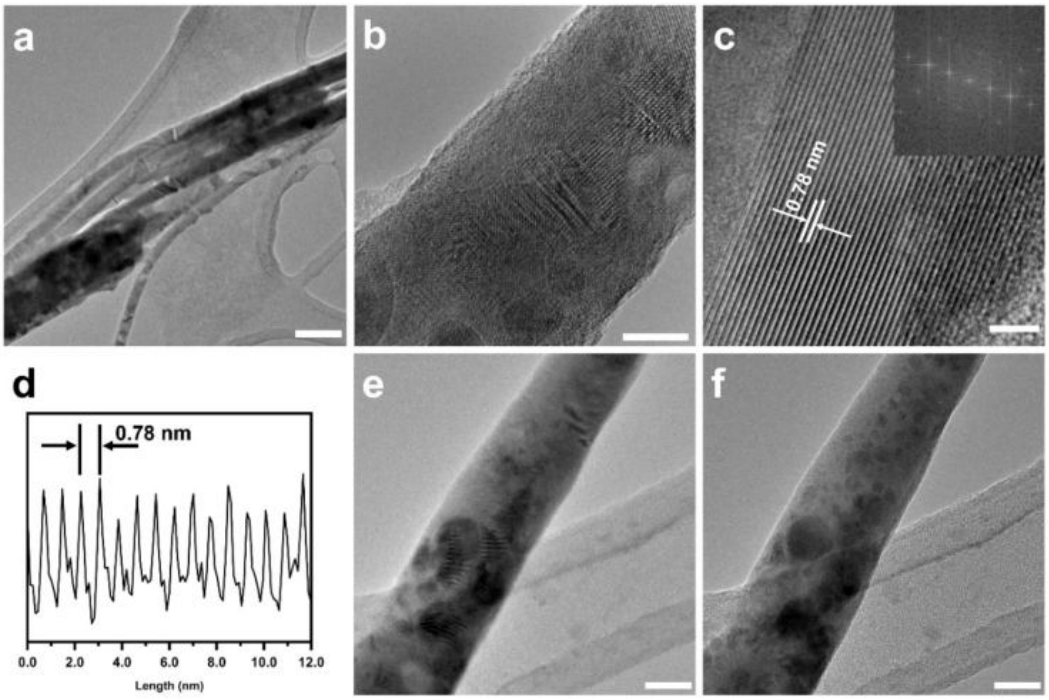

Figure 7: TEM investigation of **L-CCB**, a) morphological detail of a crystal composed by multiple microwires, b and c) phase contrast analysis of a single microwire. c inset) FFT analysis of the diffraction pattern. d) line profile analysis of the fringes reported in figure c. e and f) observation of the decomposition under constant irradiation with an electron beam at 300 kV. Scale bars: a = 100 nm, b = 10 nm, c = 5 nm, e and f = 25 nm.

microcrystals present an average aspect ratio of 50 that highlights the high degree of anysotropy of this crystal morphology. A similar morphology was reported by Li and coworkers.[87] The authors observed the formation of $Cs_3Cu_2Br_5$ micro-rods produced via a one-pot antisolvent precipitation using dichlorometane as antisolvent, DMSO as main solvent and oleic acid as surface ligand. They observed the formation of anysotropic crystals with a length around 10 µm and a broad distribution of widths spanning from hundreds of nanometers to micrometers.[87]

For **L-CCB** microwires, composition values of 3.1, 2.0, 5.7 for Cs, Cu and Br respectively are estimated by Energy Dispersive X-ray Spectroscopy (EDS). The observed values are close to the stoichiometric composition with an excess of bromide related to the synthetic conditions. Despite the high level of noise, due to the sample thickness, the elemental mapping (see **Fig. A1**) shows a homogeneous distribution across the crystal.

Further detail on the structure of the **L-CCB** microwires are collected by TEM analysis (**Fig. 7**). The structure of a microwire, composed by a bunch of smaller wires, is clearly evidenced in **Fig. 7a.** The detail of the structure of a single microwire is reported in **Fig. 7b, c**. The phase

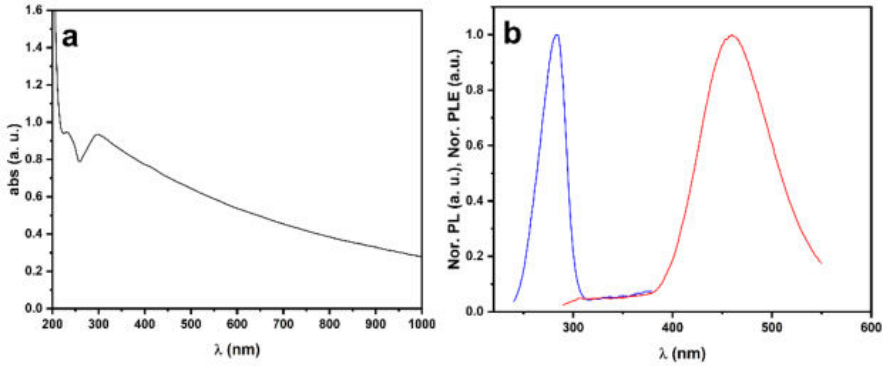

Figure 8: a) UV/Vis absorption spectra and b) PL (red) and PLE (blue) spectra of **L-CCB** colloidal dispersion in isopropanol.

contrast analysis of a single wire shows the high crystallinity of the particles and the Fast Fourier transform (FFT) analysis of the fringes reveals a *d*-spacing of 0.78 nm related to the (101) diffraction of orthorhombic $Cs_3Cu_2Br_5$ phase. This analysis suggests that the preferential growth direction of the microwires, during the antisolvent assisted recrystallisation, occurs along a crystallographic direction perpendicular to (101). This finding is further confirmed by the analysis of the line profile **Fig. 7d**. As already observed for other metal halides, the specimen is very sensible to the irradiation of the electron beam. In addition to a significant burning of the crystals, after a short exposition under the electron beam, the formation of nanometrical spherical particles on the surface and inside the nanocrystal itself can be observed (**Fig. 7e,f**). Similar behaviour is commonly observed for lead halides.[35] However, in the case of copper halide is still not clear if the impurity formed by the system decomposition can be related to metallic copper or CsBr nanoparticles.

The UV/Vis absorption analysis (**Fig. 8**) of **L-CCB** colloidal solution in isopropyl alcohol shows the presence of a maximum around 310 nm (4.0 eV) that can be related to the band-edge absorption of $Cs_3Cu_2Br_5$, Luo et al.[88] observed a slightly blue shifted energy gap (4.4 eV) for colloids prepared via *HI*, suggesting that the variation could be related to the quantum confinement of the nanocrystals. The strong contribution of the tail, observed at longer wavelength, is probably related to a scattering process associated with the micrometrical size of the microwires. The photoluminescence activity of $Cs_2Cu_3Br_5$, prepared via the modified *LARP* version, is investigated in isopropyl alcohol. The PL profile shows an emission band centred at 460 nm (2.69 eV) with a full width half maximum of 87 nm (505 meV). The photoluminescence excitation (*PLE*) analysis reveals a narrow excitation window centred around 283 nm (4.38 eV) and a large Stokes shift of 177 nm (1.69 eV). These observations are in well agreement with the value presented by other papers on $Cs_3Cu_2Br_5$ phase prepared via different approaches

such as mechanochemical synthesis.[89,90] A PLQY of 12.5 % is estimated by the comparison with a tryptophan solution in MilliQ water (absorbance 0.01 a. u). This value agrees with other papers on $Cs_3Cu_2Br_5$.[90,91]

The large Stokes shift is indicative of the relaxation process via self-trapped excitation mechanism. *STE* emission is the principal process observed in structures like 0D metal halides where, in addition to strong electron-phonon coupling, the exciton is localized in the metal halide clusters which, due to the lack of an interconnected coordination network, are easily distorted.[92] The energy of the emitted radiation by *STE* mechanism is described by **Eq. 1**, where E_g is the energy of the band to band transition and the negative terms represent the exciton binding energy E_e, the self-tapping energy E_S and the lattice deformation energy E_l respectively. These different contributions are represented in the schematic energy diagram (**Fig. 9a**), after excitation to the Free Charges (*FC*) state, the charges couple undergoes to a series of non-radiative relaxations. First producing an exciton that is affected by coulombic interaction in the Free Exciton (*FE*) state and then a more stable Self Trapped Exciton (*STE*) state is formed thanks to consistent contribution of the lattice distortions. Finally, the radiative recombination occurs between the *STE* and Ground State (*GS*) with the emission of a photon.

Eq. 1

$$E_{PL} = E_b - E_e - E_S - E_l$$

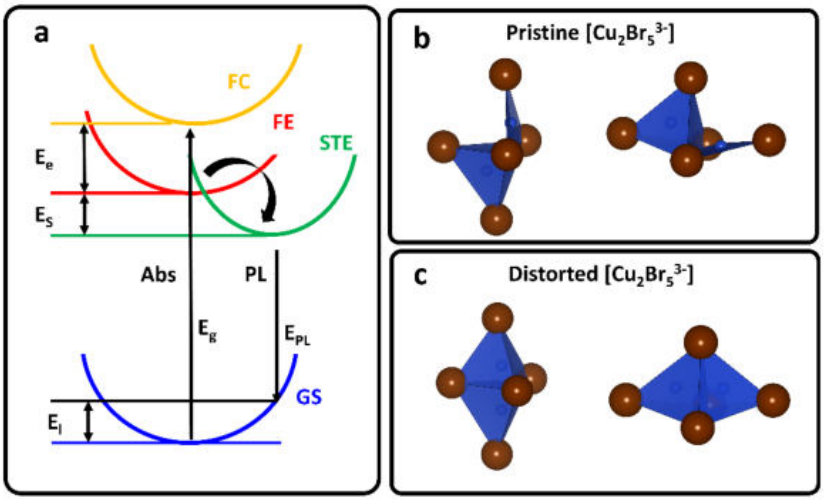

Figure 9: a) schematic representation of the energy states involved in the photoluminescence mechanism, labelled as: Free Charges (FC), Free Exciton (FE), Self-Trapped Exciton (STE) and Ground State (GS). Representation of the $[Cu_2X_5]^{3-}$ dimer structure in the pristine ground state (b) and photoexcited distorted state (c).

Interestingly, in contrast to the 2D layered lead halides perovskites, characterised by a narrow emission peak (related to a free-exciton recombination mechanism combined with a red-shifted and broader emission peak associated to *STE* emission), the *FE* emission has never been reported for copper halides, suggesting the absence of energy barrier between *FE* and *STE* energy levels.[92] Concerning the photoluminescence mechanism in cesium copper halides Lian et al.[44] investigated the origin of *STE* emission in $Cs_3Cu_2X_5$ by experimental and theoretical studies. They reported on the formation of unusual lattice distortions in the photoexcited state that affect the $[Cu_2X_5]^{3-}$ clusters causing an increasing in local symmetry. According to *DFT* calculations, the authors observed that the cluster in the pristine state, composed by tetrahedral and trigonal planar units (**Fig. 9b**) was rearranged during the photoexcitation. This process caused the conversion of the trigonal planar unit into a tetrahedral one, forming a

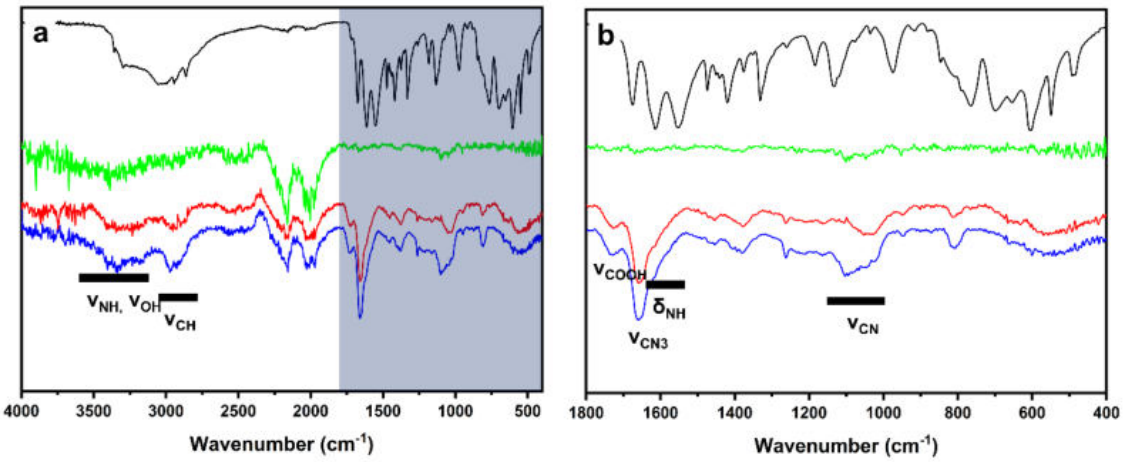

Figure 10: a) FTIR spectra of L-Arg (black), bulk-CCB (green), **D-CCB** (red) and **L-CCB** (blue). b) expanded plot of the area highlighted in blue in panel a) between 1800 and 400 cm^{-1}.

photoexcited distorted structure which presents a more symmetrical clusters characterised by C_{2v} symmetry (**Fig 9c**).

The presence of chiral ligand molecules in $Cs_3Cu_2Br_5$, produced by *LARP* method is investigated via FTIR analysis (**Fig. 10a,b**) comparing **L/D-CCB** with L-arginine and a bulk $Cs_3Cu_2Br_5$ sample prepared without the addition of ligands (named bulk-CCB). Despite the low intensity of all the *FTIR* signals observed for both L and D-CCB samples (as can be observed in comparison to the CO_2 signal that covers the whole 2350 to 1770 cm^{-1} region), the presence of a broad peak centred at around 3340 cm^{-1} can be related to ν_{NH} and ν_{OH} of the ammonium cations and the carboxylic groups. The peaks at 2970 and 2915 cm^{-1} can be attributed to ν_{CH} sp^3 in the side chain. The distinctive signals at 1730 and 1656 cm^{-1} are related to the ν_{COOH} of the protonated carboxylate group and symmetric ν_{CN3} of the guanidinium hydrobromide followed by a broad

band of the δ_{NH}. [93,94] The broad band between 1000 and 1130 cm^{-1} can be related to the ν_{CN} of the primary ammonium group. The observed signals proves that the ligand is still bonded on the copper halide particles surface after the purification step in its cationic form.

2.2 CHIROPTICAL ACTIVITY IN ARGININE STABILISED $Cs_3Cu_2Br_5$

The transfer of chirality is investigated by electronic CD (**Fig. 11**). The successful induction of chirality is confirmed by a CD active transition in the band-edge region around 310 nm (**Fig. 11a-d**). The observation of opposite signal, according to the chirality of the chiral ligand, highlights the enantioselectivity of the synthesis. The transition in the band-gap region has a positive CD signal, + 4.04 mdeg for **L-CCB** and a negative one, -4.07 mdeg for **D-CCB**. Other CD active transitions are observed at shorter wavelengths: CD values of – 2.87 mdeg at 280 nm and + 2.88 mdeg at 250 nm for **L-CCD** and + 3.58 mdeg at 280 nm and -2.96 mdeg at 250 nm for **D-CCB**. In contrast, L-Arg ligand CD spectrum is characterised by a single positive band at 210 - 212 nm.[95] The anisotropic g-factors are used to evaluate the intrinsic chirality of the structures (**Fig. 11e**). The maximum of the g-factor of + 1.60 and -1.42 x 10^{-4} are determined

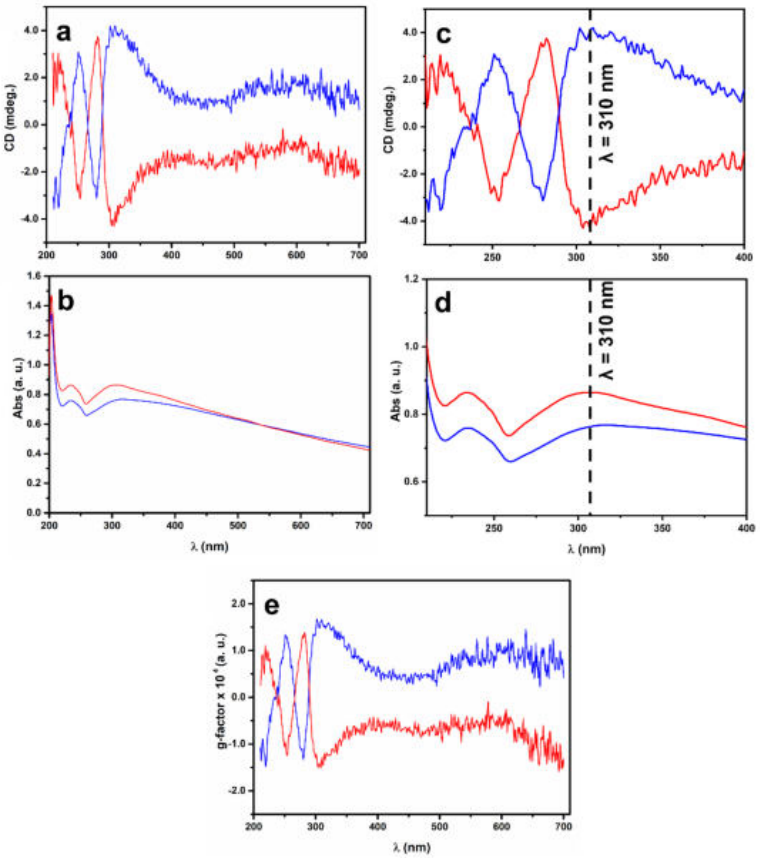

Figure 11: chiroptical characterisation of **L** (blue) and **D** (red)-**CCB** colloidal dispersions. a,b) CD (top) and UV/Vis spectra in the 210 to 700 nm region, c,d) detail of the 210 to 400 nm region. e) analysis of the anisotropic g-factor.

for the peak at the band edge region (310 nm) for **L** and **D-CCB**. The unstructured signal observed at longer wavelength is probably related to a significant scattering contribution due to the micrometrical size of the crystals.

According to the particle morphology analysed by SEM and TEM, a structural origin of the particles chirality can be excluded. Moreover, the XRD analysis confirms the orthorhombic centrosymmetric structure. Consequently, the origin of the particle chirality can be related to the effect of the chiral ligand adsorbed on the particles surface. As reported above, ligand induced chirality has been already observed in some examples of metal halides.[79,81,96] Moreover, the magnitude of the g-factor further suggests the origin of the particle chirality at the particle-ligand interface.

Scheme 2

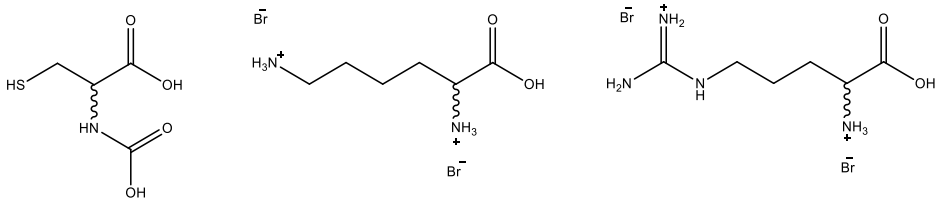

[1]pKa_{SH} = 9.52
[2]pKa_{COOH} = 3.24

[3]pKa_{NH3r} = 10.53
[3]pKa_{NH3} = 8.95
[3]pKa_{COOH} = 2.18

[4]pKa_{CN3} = 13.2
[4]pKa_{NH3} = 9.09
[4]pKa_{COOH} = 2.18

1 Serjeant, E.P., Dempsey B.; Ionisation Constants of Organic Acids in Aqueous Solution. International Union of Pure and Applied Chemistry (IUPAC). IUPAC Chemical Data Series No. 23, 1979. New York, New York: Pergamon Press, Inc., p. 154.
2 Osol, A. (ed.). Remington's Pharmaceutical Sciences. 16th ed. Easton, Pennsylvania: Mack Publishing Co., 1980., p. 805.
3 O'Neil, M.J. (ed.). The Merck Index - An Encyclopedia of Chemicals, Drugs, and Biologicals. Whitehouse Station, NJ: Merck and Co., Inc., 2006., p. 977.
4 Budavari, S. (ed.). The Merck Index - An Encyclopedia of Chemicals, Drugs, and Biologicals. Whitehouse Station, NJ: Merck and Co., Inc., 1996., p. 817.

To highlight the role of the chiral ligand in the particles formation and in the optical activity, the morphology and chiroptical activity are evaluated by preparing $Cs_3Cu_2Br_5$ samples changing the chiral ligand. Using this approach, three $Cs_3Cu_2Br_5$ samples are prepared: the first one without ligand (**bulk-CCB**), the second one stabilised with N-acetyl-L-cysteine (**NAC-CCB**) and the last one with L-Lysine (**LYS-CCB**). The structure and dissociation constants of the ligands are reported in **Scheme 2**. The ligands are represented in their form with highest protonation as it is the most relevant according to the acidic reaction environment. The SEM micrographs in **Fig. 12** show the effect of the ligand. Concerning the sample bulk-CCB (**Fig. 12a i – iii**), the process forms large crystals with a wire shape with a longitudinal length of hundreds of micrometers and a lateral length of about 2 – 8 µm. This morphological insight highlights the dramatic effect of Arg on the crystal growth process. Despite the weak interaction with the particles surface, the ligand addition causes a significant reduction on the particles size with a critical effect on the colloidal stability. The observation of wire-shaped crystals detected in the

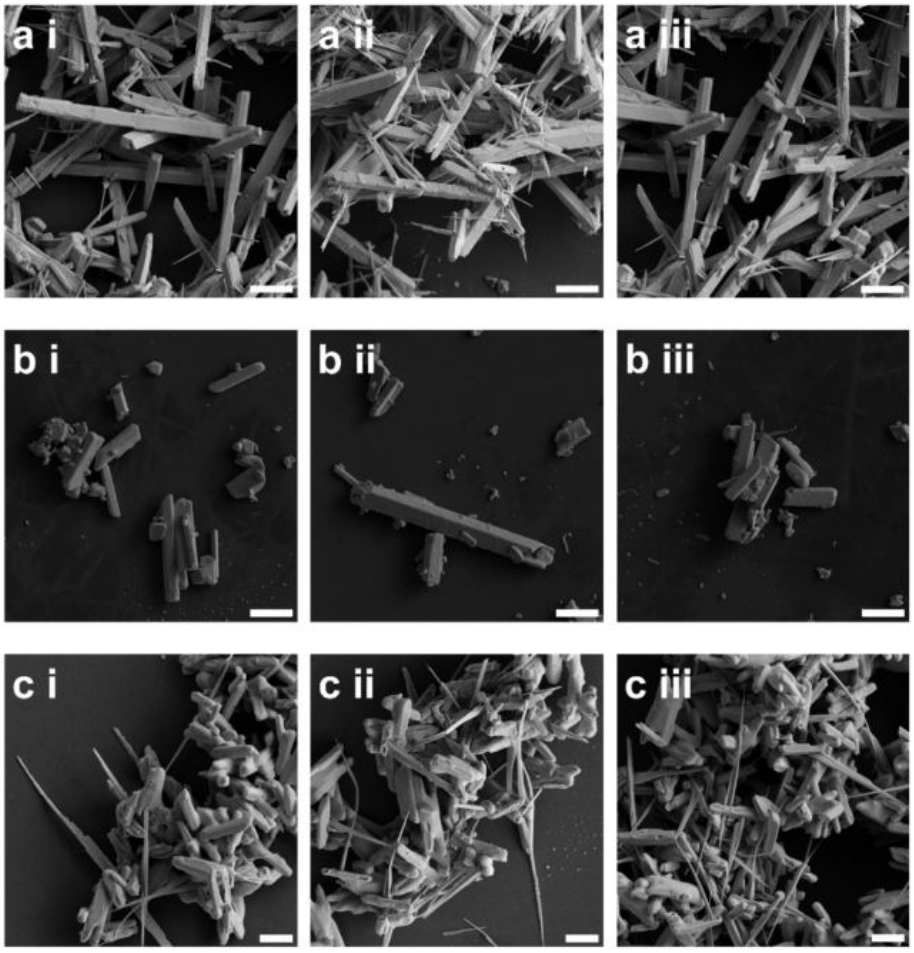

Figure 12: SEM micrographs of $Cs_3Cu_2Br_5$ prepared in the presence of different ligands. a i-iii) bulk-CCB, no ligand is employed during the synthesis, b i-iii) NAC-CCB is prepared in the presence of N-acetyl-L-cysteine and c i-iii) LYS-CCB is prepared in the presence of L-lysine. Scale bars: a i - iii, b i - iii = 10 µm and c i - iii = 3 µm.

sample prepared without ligands highlights the formation of anisotropic crystals favourited by the intrinsic energy of the crystal facets. Instead, plays a fundamental role on the particles size. *EDS* analysis gives elemental composition vales of 3.0, 2.0, 6.1 for Cs, Cu and Br respectively. These findings confirm that this LARP approach produces halide-rich $Cs_3Cu_2Br_5$ crystals even without the support of the halide ammonium ligands. Also, in the case of **bulk-CCB**, the *EDS* elemental mapping shows a homogeneous distribution of the elements across the whole crystal surface (**Fig. A3**).

The effect of N-acetyl-L-cysteine (NAC) and L/D-Lysine (LYS) as chiral ligands is also investigated. The morphological characterisation of the sample **NAC-CCB** (**Fig. 12b i – iii)** shows only little variations on the overall morphology with a small reduction of the longitudinal size from hundreds of microns (observed for bulk-CCB) to around 10 µm**. LYS-CCB** sample (**Fig. 12c i – iii**) is characterised by a mixed morphology: the largest portion of the sample presents a rod

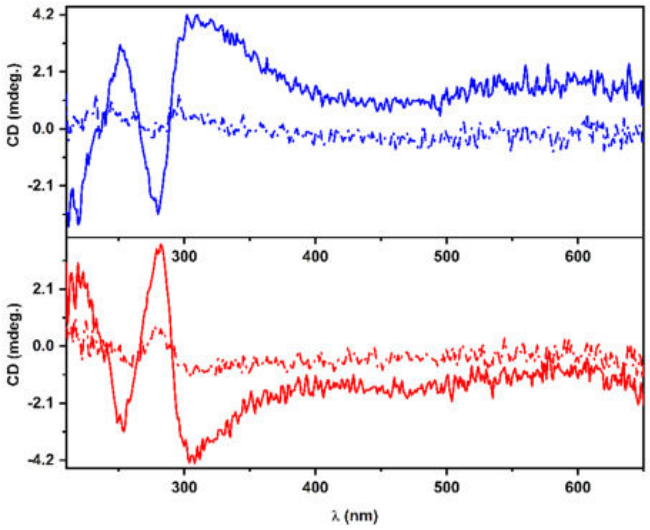

Figure 13: CD spectra of $Cs_3Cu_2Br_5$ microcrystals produced in the presence of L amino acids (top panel) L-Arg (solid line), L-Lys (dashed line) and D amino acids (bottom panel) D-Arg (solid line) and D-Lys (dashed line)

like shape with average length of about 5 µm and width of 1 µm (see **Fig. A2**), and smaller portion present a similar morphology to **L/D-CCB** samples with a length of about 10 µm and width of 0.15 µm. This evidence supports the hypothesis that lysine has similar effect of Arginine on the crystal growth. Further investigations are required to achieve a fine control on the product morphology by means of LARP synthesis in the presence of lysine.

The CD analysis of the particles, produced in the presence of L or D-Lys, reveals the successful chiral transfer (**Fig. 13**). The analysis of a colloidal solutions in isopropanol shows similar signal characteristic of arginine stabilised samples. A similar pattern of the electronic transitions centred at 310, 280 and 250 nm is observed. However, the intensity relative to **L/D LYS-CCB** is about five times lower than the intensity of the arginine stabilised counterpart ($g^{L\text{-}ArgCCB}$ 1.6 x 10^{-4}, $g^{D\text{-}ArgCCB}$ -1.4 x 10^{-4} $g^{L\text{-}LysCCB}$ 0.27 x 10^{-4} and $g^{D\text{-}LysCCB}$ -0.29 x 10^{-4}). This effect can be appreciated in **Fig. 13** comparing the CD spectra of **L/D-CCB** (solid line) and **L/D LYS-CCB** (dashed line) colloidal solutions. For both samples an absorbance of 0.8 at 310 nm is used.

Thanks to this preliminary study of the effect of the chiral ligand on morphology and optical properties of $Cs_3Cu_2Br_5$ crystals, we can summarize some major considerations:

- Despite the use of a chiral ligand to stabilise the particles, the sample prepared by LARP approach in the presence of NAC, do not present a sufficient colloidal stability to be analysed via CD spectroscopy in liquid phase. The use of diffusive CD meas-

urements may help to investigate the chiral transfer. However, the particles morphology suggests the absence of significant interaction between the ligand and the particle surface. **NAC-CCB** shows a similar morphology to **bulk-CCB** produced without the addition of any ligand. This evidence suggests that basic amino acids (such as lysine and arginine) are characterised by stronger interactions with the particle surface. Indeed, the use of amines (and the respective ammonium salts) as ligands for the stabilisation of metal halide particles has been widely investigated for a broad variety of structures.[35,97] According to previous studies on $CsPbBr_3$ nanocrystals,[98,99] the ligand interaction on the particle surface is mediated by the formation of hydrogen bonds between the N-H hydrogen donor group and X-M (X = halide) hydrogen acceptor group via a substitution mechanism. A similar behaviour could be hypothesized for $Cs_3Cu_2Br_5$ prepared via our adapted LARP approach. In the reaction mixture, the particles are produced in the presence of a large excess of HBr that guarantee both the protonation of the ligand, with the formation of the ammonium salts, and the availability of bromide anions for the passivation of surface defects (such as halide vacancies). If basic amino acid like lysine and arginine can interact with the particle surface in a chelate fashion, only a weak interaction mediated by the amide group is possible for N-acetyl-L-cysteine.

- Comparing the effect of the two basic amino acids, arginine clearly shows a higher efficiency in the transfer of chirality. This behaviour could be related to the multiple potential interactions mediated by hydrogen bonds established between the guanidium cation present in the Arg lateral chain and the bromide-rich surface of $Cs_3Cu_2Br_5$ microwires. It is important to consider that the effect of the ligand affinity for the particle surface is not only affecting the transfer of chirality, but also the particle morphology. At the same ligand concentration, lysine is not able to drive the formation of microwires and a material with a mixed morphology is observed.

2.3 LARP SYNTHESIS FOR THE PREPARATION OF OTHER LEAD-FREE METAL HALIDES

A preliminary investigation, to assess the formation of the desired crystallographic phases has been conducted without the addition of organic ligands. In this context, the preparation of 1D $Cs_3Cu_2Cl_5$, 0D and 2D bismuth-based halides $Cs_3Bi_3X_9$ (X = Br and I) and $Cs_2AgInCl_6$ double perovskite are considered.

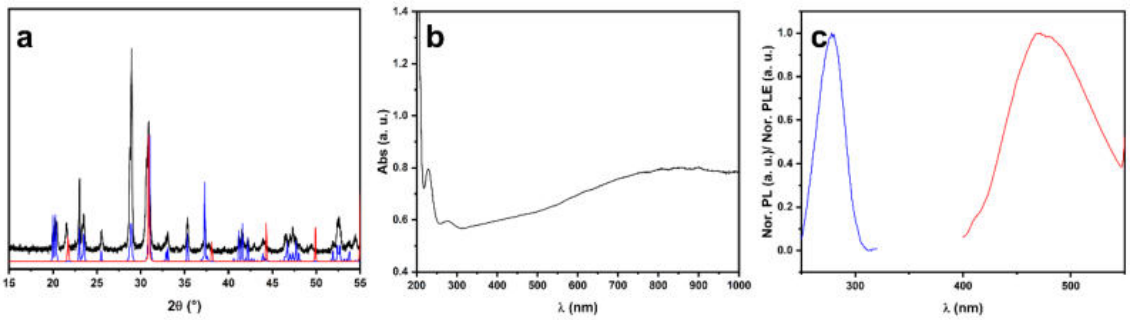

Figure 14: a) XRD, b) UV/Vis absorption, c) PL (red) and PLE (blue) analyses of $Cs_3Cu_2Cl_5$ produced by reprecipitation DMF to isopropanol. Simulated XRD pattern according to ICSD 22951.

We replaced CsBr, $CuBr_2$ and HBr, employed to prepare $Cs_3Cu_2Br_5$ with the corresponding chloride precursors (see Material and Methods section), to synthetise the $Cs_3Cu_2Cl_5$ phase. The XRD analysis reported in **Fig. 14a** confirms the synthesis of 1D $Cs_3Cu_2Cl_5$ orthorhombic *Cmcm* phase by the reprecipitation process. The presence of CsCl impurity is observed, suggesting that the optimization of composition of the metal halide precursor solution must be improved to isolate the pure phase. However, the presence of CsCl could also be related to the instability of the pure chloride phase under ambient condition considering the formation of Cu(II) and CsCl observed after ageing for few days with a significant colour change from white to green.[100] The UV/Vis Absorption spectra (**Fig. 14b**) shows two narrow bands at 227 and 277 nm. The latter band can be related to the band-to-band electronic transition.[88] At longer wavelength, a diffuse absorption band probably associated to a large scattering contribution, is observed. The *PL* and *PLE* spectra (**Fig. 14c** red) show an emission peak at 480 nm, and a narrow excitation window centred at about 280 nm. A PLQY of 20.3 % is estimated using tryptophan as PLQY standard.

The characteristic red-shift of the PL, observed for $Cs_3Cu_2X_5$ metal halides from bromide (460 nm) to chloride (480 nm), is in complete contrast with the observation reported for lead halide

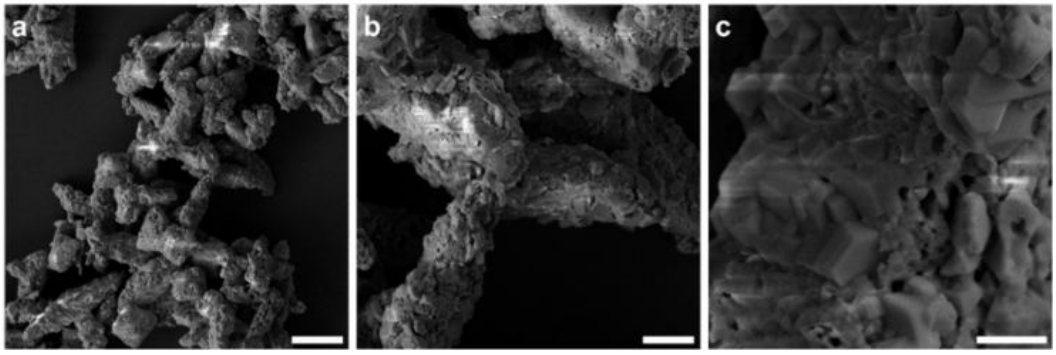

Figure 15: SEM micrographs of $Cs_3Cu_2Cl_5$, scale bars: a = 10 µm, b = 3 µm and c = 1 µm.

perovskite.[35] Lian et al.[44] explained this effect considering both the band gap energy and the exciton binding energy of the photoexcited distorted structure. Under photoexcitation, band-gap energies of 3.30 and 3.20 eV and the exciton binding energies of 0.72 and 0.84 eV can be estimated for the chloride and bromide respectively. These two quantities show opposite trends, and their combination causes the increase of the PL energy from 2.46 to 2.48 eV with the halide substitution from chloride to bromide.

SEM micrographs show the particle morphology (**Fig. 15**). The formation of crystals with size of tents of microns with a complex morphology is observed. As can be seen in **Fig. 15c**, the crystals surface presents a complex microstructure.

Regarding the other systems ($Cs_3Bi_3Br_9$, $Cs_3Bi_3I_9$ and $Cs_2AgInCl_6$), the XRD analyses (**Fig. 16i)** confirmed the synthesis of pure single phases. All the samples show a good agreement between the experimental and reference patterns (details of the crystal structures are reported in **Fig. 16ii**).

As can be evidenced by *SEM* analysis in **Fig. 16a iii**, $Cs_3Bi_3Br_9$ is made by micrometrical aggregated of spherical particles with diameter around 200 nm, meanwhile, $Cs_3Bi_3I_9$ (**Fig. 16b iii**) is characterised by crystals with a plate like morphology. $Cs_2AgInCl_6$ evidences the presence of octahedral microparticles with a broad size distribution. The particles morphology suggests that the crystal formation is dominated by a preferential growth along the (101) facets of the cubic lattice, giving the formation of microcrystal enclosed in (111) facets. However, phase contrast *TEM* micrographs and selected area electron diffraction analysis should be collected to support this hypothesis.

Further morphological characterisation of these systems can be found in the appendix section. **Fig. A4**, **Fig. A5** and **Fig. A6** show the SEM characterisations of $Cs_3Bi_3Br_9$, $Cs_3Bi_3I_9$ and $Cs_2AgInCl_6$.

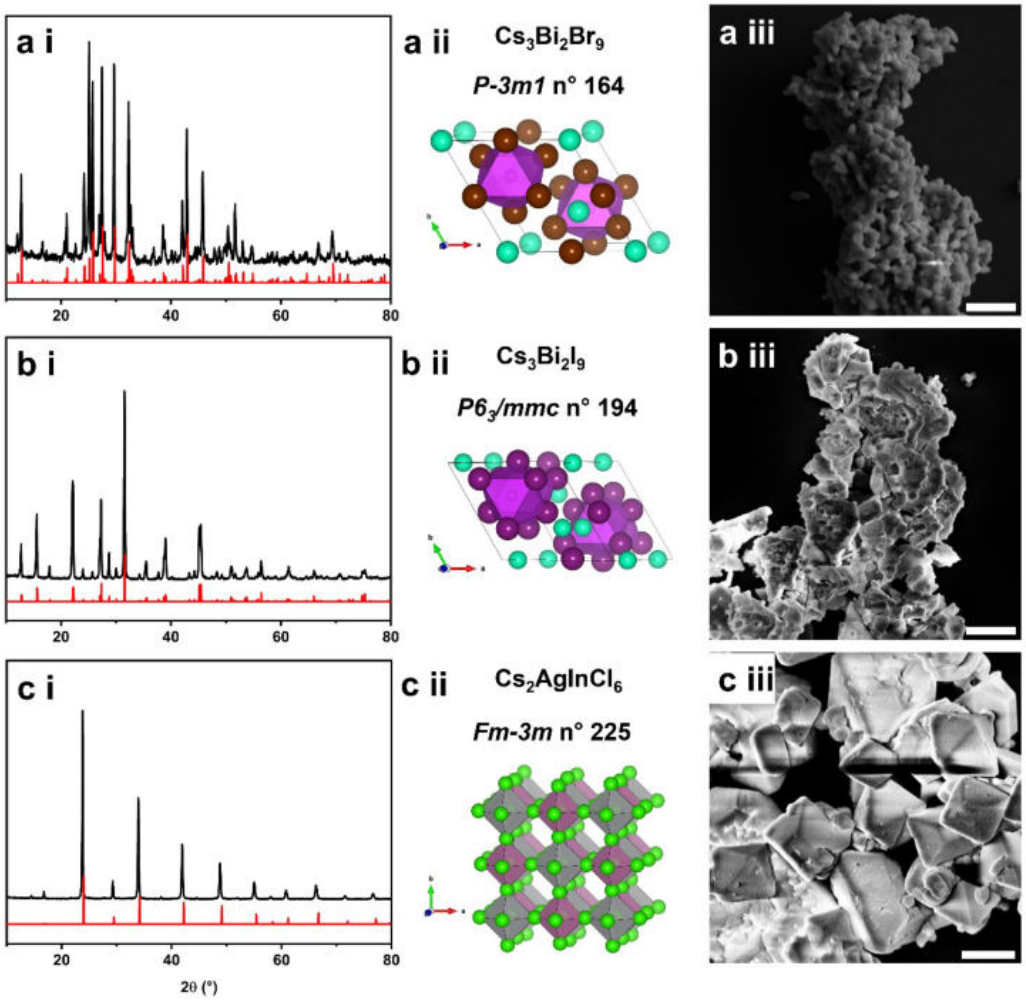

Figure 16: XRD analysis (i), representative details related to the crystallographic structure (ii) and SEM characterisation (iii) of: $Cs_3Bi_3Br_9$ (a), $Cs_3Bi_2I_9$ (b) and $Cs_2AgInCl_6$ (c). The experimental and reference XRD patterns are reported in black and red respectively. The following CIF data are employed as reference structures: $Cs_3Bi_3Br_9$ ICSD1142, $Cs_3Bi_2I_9$ ICSD 1448 and $Cs_2AgInCl_6$ ICSD 11524. The scale bars in the SEM micrographs correspond to 1 μm

3 CONCLUSIONS AND FUTURE PERSPECTIVES

A novel LARP approach to produce chiral $Cs_3Cu_2Br_5$ stabilised by L/D-arginine has been developed. The method allows the synthesis of chiral metal-halide particles via a simple single-step coprecipitation method in the presence of the chiral ligand. As evidenced by XRD and TEM, $Cs_3Cu_2Br_5$ particles show high phase purity and crystallinity. The morphology of the particles is characterised by the presence of microwires with a length of 10 µm and a lateral size of 0.1 µm. The effect of arginine on the crystal growth leads to a reduction of the particles size, fundamental to achieve colloidal stability. The optical properties show an emission centred at around 460 nm with a *PLQY* of 12.5 %. These values are in well agreement with the activity of $Cs_3Cu_2Br_5$ produced by other synthetic methos.[88,90,91]

The chiroptical investigation evidences the successful transfer of chirality by the presence of CD active bands in the region corresponding to the band gap transition. An anisotropic *g*-factor of 1.60 and -1.42 x 10^{-4}, determined for the particle in colloidal dispersion, is in-line with the hypothesis of a ligand induced chirality mechanism. The lower chiroptical activity of $Cs_3Cu_2Br_5$ produced in the presence of lysine, suggests a superior efficiency of arginine in the transfer of chirality. This finding could be associated to the multiple interaction via hydrogen bond that can be established by the guanidinium group in the Arginine lateral chain.

To prove the general application of the reprecipitation using DMF and HBr as main solvents and isopropanol as antisolvent, this approach has been used to prepare other metal halides. The synthesis of 1D $Cs_3Cu_2Cl_5$, 0D $Cs_3Bi_2I_9$, 2D Cs_3Bi_2Br9 and $Cs_2AgInCl_6$ double perovskite has been investigated in a preliminary study without the addition of organic ligand. The XRD analyses showed a high degree of crystallinity as well as phase purity, with the only exception of $Cs_3Cu_2Cl_5$ that presents CsCl contamination.

Future prospective of this project are mainly focused on increasing the control of size and morphology. With the aim to optimise the synthetic procedure to reduce the particle size down to the nanocrystal regime. Future investigation will also cover other chiral ligand to further understand the origin of the chiral transfer at the particle-ligand interface. Moreover, the two-step method, has proved to be successful to isolate chiral $CsPbBr_3$[80] nanocrystals. This approach is also promising for the synthesis of lead-free metal halides as well, and it will be covered in future investigation. Finally, the preliminary observation on the synthesis of several metal halide phases proved the feasibility of the reprecipitation step suggesting the possible

implementation of the chiral ligand to study its effect on morphology and chiroptical activity for these systems.

4 MATERIALS AND METHODS

4.1 Chemicals:

CsBr 99.9 % Alfa Aesar, CsCl 99.9 % Sigma Aldrich, CsI > 99.9 % Sigma Aldrich, $CuBr_2$, $CuCl_2*2H_2O$, Ag(OAc), $In(OAc)_3$, $Bi(OAc)_3$ ≥ 99.99 % Sigma Aldrich, N,N-dimethylformamide (DMF) ACS reagent ≥ 99.8 %, HCl 37 % Sigma Aldrich, HBr 48 % Merck, L-Arginine ≥ 98 % Sigma Aldrich, D-Arginine 98 % Sigma Aldrich, N-Acetyl-L-cysteine 99 % Sigma Aldrich , L-Lysine ≥ 98 %, D-Lysine 98 % Alfa Aesar, Thioglycolic acid 98 % Sigma Aldrich. All the chemicals have been used without further purifications.

4.2 SYNTHESIS:

L/D- Arginine $Cs_3Cu_2Br_5$ synthesis: in a typical synthesis, L/D- Arginine (62 mg, 0.36 mmol) are solubilised in DMF (0.5 ml) and HBr 2.0 M (375 µl), then thioglycolic acid (22.5 µl, 0.32 mmol) is added. CsBr (48 mg, 0.22 mmol) and $CuBr_2$ (33 mg, 0.15 mmol) are added to the ligand solution. The copper (II) addition is followed by a rapid colour transition, the solution turns rapidly from colourless to green due to the formation of Cu (II) complexes, this fist transition is immediately followed by a second colour change to yellow that is associated to the reduction to Cu (I) due to the thioglycolic acid. The final mixture is sonicated for 30 min in a sonication bath to ensure the complete solubilisation of the precursors. Then, the metal halide precursor solution (270 µl) is added dropwise to 90.0 ml of isopropyl alcohol under constant stirring at room temperature, during the additions the antisolvent solution turns cloudy due to the precipitation of the metal-halide crystals. The reaction mixture is stirred for 5.0 min, then, the product is precipitated by centrifugation (7000 rpm, 3.0 min). The supernatant is discharged, the pellet is washed three times with 10.0 ml of isopropyl alcohol and collected by centrifugation (7000 rpm, 3.0 min). After cleaning, the product is redispersed in 10.0 ml of isopropyl alcohol under sonication, the colloidal solutions are stored in a fridge.

$Cs_3Cu_2Br_5$ Ligand effect study: for the study of the ligand effect, the same procedure reported above (L/D- Arginine $Cs_3Cu_2Br_5$ synthesis) is employed with the only variation of the organic ligand. Instead of L/D-Arg (62 mg, 0.36 mmol), L/D- Lysine (62 mg, 0.36 mmol), N-Acetylcysteine or no ligand are employed for the synthesis of L/D-Lys CCB, L-NAC CCB and CCB bulk. All the other synthetic steps are reproduced using the same method.

Cs_3Cu2Cl_5 synthesis: thioglycolic acid (22.5 µl, 0.32 mmol) is added to a mixture of DMF (1.0 ml) and HCl 2.0 M (0.375 ml, 0.75 mmol). CsCl (48 mg, 0.22 mmol) and $CuCl_2*2H_2O$ (33 mg, 0.15 mmol) are added to the solution. The copper (II) addition is followed by a rapid colour transition, the solution turns rapidly from colourless to green due to the formation of Cu (II) complexes, this fist transition is immediately followed by a second color change to yellow that is associated to the reduction to Cu (I) due to the thioglycolic acid. The final mixture is sonicated for 30 min in a sonication bath to ensure the complete solubilisation of the precursors. Then, the metal halide precursor solution (270 µl) is added dropwise to 90.0 ml of isopropyl alcohol under constant stirring at room temperature. The reaction mixture is stirred for 5.0 min, then, the product is precipitated by centrifugation (7000 rpm, 3.0 min). The supernatant is discharged, the pellet is washed three times with 10.0 ml of isopropyl alcohol and collected by centrifugation (7000 rpm, 3.0 min). After cleaning, the product is dried under vacuum at room temperature for the XRD and SEM characterisations.

$Cs_3Bi_2Br_9$ synthesis: CsBr (48 mg, 0.22 mmol) and $Bi(OAc)_3$ (58 mg, 0.15 mmol) are added to a mixture of DMF (1.5 ml) and HBR 2.0 M (0.750 ml, 1.5 mmol). The final mixture is sonicated for 30 min in a sonication bath to ensure the complete solubilisation of the precursors forming a yellow-green solution. Then, the metal halide precursor solution (270 µl) is added dropwise to 90.0 ml of isopropyl alcohol under constant stirring at room temperature, the solution turns rapidly to a cloudy green mixture. The reaction mixture is stirred for 5.0 min, then, the product is precipitated by centrifugation (7000 rpm, 3.0 min). The supernatant is discharged, the pellet is washed three times with 10.0 ml of isopropyl alcohol and collected by centrifugation (7000 rpm, 3.0 min). After cleaning, the product is dried under vacuum at room temperature for the XRD and SEM characterisations.

$Cs_3Bi_2I_9$ synthesis: CsI (57 mg, 0.22 mmol) and $Bi(OAc)_3$ (58 mg, 0.15 mmol) are added to a mixture of DMF (1.5 ml) and HBR 2.0 M (0.750 ml, 1.5 mmol). The final mixture is sonicated for 30 min in a sonication bath to ensure the complete solubilisation of the precursors forming a deep red solution. Then, the metal halide precursor solution (270 µl) is added dropwise to 90.0 ml of isopropyl alcohol under constant stirring at room temperature, the solution turns rapidly to a cloudy red mixture. The reaction mixture is stirred for 5.0 min, then, the product is precipitated by centrifugation (7000 rpm, 3.0 min). The supernatant is discharged, the pellet is washed three times with 10.0 ml of isopropyl alcohol and collected by centrifugation (7000

rpm, 3.0 min). After cleaning, the product is dried under vacuum at room temperature for the XRD and SEM characterisations.

$Cs_2AgInCl_6$ synthesis: CsCl (54 mg, 0.32 mmol), $In(OAc)_3$ (43 mg, 0.15 mmol) and $Ag(NO_3)$ (25 mg, 0.15 mmol) are added to a mixture of DMF (10.0 ml) and HCl 2.0 M (3.0 ml, 6.0 mmol). The final mixture is sonicated for 30 min in a sonication bath to ensure the complete solubilisation of the precursors forming a colourless solution. Then, the metal halide precursor solution (3.0 ml) is added dropwise to 90.0 ml of isopropyl alcohol under constant stirring at room temperature, the solution turns rapidly to a cloudy mixture. The reaction mixture is stirred for 5.0 min, then, the product is precipitated by centrifugation (7000 rpm, 3.0 min). The supernatant is discharged, the pellet is washed three times with 10.0 ml of isopropyl alcohol and collected by centrifugation (7000 rpm, 3.0 min). After cleaning, the product is dried under vacuum at room temperature for the XRD and SEM characterisations.

4.3 CHARACTERISATIONS:

Structural characterisation: the powder diffraction measurements are recorded with a Panalytical Advanced Powder Diffractometer.

Morphological characterisation: The high resolution transmission electron microscopy (HRTEM) and scanning transmission electron microscopy (STEM) high-angle annular dark-field imaging (HAADF) is carried out using a FEI Titan operating at a beam voltage of 300 kV, situated at the advanced microscopy laboratory in Trinity College Dublin. SEM analyses are performed using a Zeiss sigma VP field emission Scanning Electron Microscope and a Bruker Quantarax 200 detector is employed for the EDS analysis working with a ETH voltage of 10 kV.

Absorption spectra: The UV/Vis analysis is carried out with a Cary 60 (Agilent) UV/Vis spectrophotometer.

Photoluminescence Quantum Yield determination: the quantum yield was estimated by comparison with a known fluorescence standard according to **Eqs. A1** and **A2**. Tryptophan was chosen as standard considering a quantum yield 0.15 ± 0.01 in a water solution.[101] The metal halide colloidal dispersion is prepared in isopropanol ($\eta = 1.377$) and standard solution in deionized water ($\eta = 1.333$) are prepared adjusting the dilution in order to obtain absorbance of 0.05 at the excitation wavelength (280 nm). The emission spectra are collected exciting with radiation at 280 nm and measuring the emission

in the 300 – 550 nm range. A spectral resolution of 2.0 nm is employed in both excitation and emission.

Steady state luminescence spectra: luminescence excitation and emission spectra are collected using a Horiba Jobin Yvon FluoroMax-4.

FTIR spectra: FTIR spectra were recorded using a NEXUS-FTIR instrument implementing a Nicolet Diffuse Reflectance accessory (DRIFT).

CD measurements: the CD spectra are collected with a Jasco J815 using colloidal dispersion in isopropanol and adjusting the particles concentration to keep the absorbance at 310 nm around 0.8. For the spectra acquisitions, the scan speed is set to 50 nm/min using 5 accumulations for each spectrum. The g-factor is calculated according to **Eq. 2**:[102]

Eq. 2

$$g = \frac{2(A_L - A_R)}{A_L + A_R} = \frac{\Delta A}{A}$$

Where A_L and A_R are the absorption of the left and right circular polarized lights, and A is the absorbance of unpolarized light. The conversion of the circular dichroism express as ellipticity in millidegree units to the differential absorption is reported in **Eq. 3**. Finally, **Eq. 4** combine **Eq. 2** and **Eq. 1** to give a direct relationship between the g-factor and the circular dichroism.

Eq. 3

$$CD\ (mdeg.) = \frac{180 \ln(10)}{4\pi} 10^3\ \Delta A = 32982\ \Delta A$$

Eq. 4

$$g = \frac{CD\ (mdeg.)}{A * 32982}$$

5 REFERENCES

1 H. L. Wells and W. R. Johnston, *Allg. Chem.*, 1893, **3**, 195–210.
2 C. K. Moller, *Nature*, 1958, **182**, 1436.
3 G. Rose, *De novis quibusdam fossilibus quae in montibus Uralis inveniuntur*, AG Shade, Berlin, 1839.
4 R. J. D. Tilley, *Perovskites, Structure-Property Relationship*, 2016.
5 J. Chen, Q. Zhao, N. Shirahata, J. Yin, O. M. Bakr and O. F. Mohammed, *ACS Materials Lett.*, 2021, **3**, 845–861.
6 T. Chiba, Y. Hayashi, H. Ebe, K. Hoshi, J. Sato, S. Sato, Y. Pu, S. Ohisa and J. Kido, *Nat Photonics*, 2018, **12**, 681–688.
7 K. Lin, J. Xing, L. N. Quan, F. P. G. De Arquer, X. Gong, J. Lu, L. Xie, W. Zhao, D. Zhang, C. Yan, W. Li, X. Liu, Y. Lu, J. Kirman, E. H. Sargent, Q. Xiong and Z. Wei, *Nature*, 2018, **562**, 245–248.
8 B. Zhao, S. Bai, V. Kim, R. Lamboll, R. Shivanna, F. Auras, J. M. Richter, L. Yang, L. Dai, M. Alsari, X. She, L. Liang, J. Zhang, S. Lilliu, P. Gao, H. J. Snaith, J. Wang, N. C. Greenham, R. H. Friend and D. Di, *Nat Photonics*, 2018, **12**, 783–789.
9 Z. Shi and X. Li, *J. Mat. Chem. C*, 2016, **4**, 8373–8379.
10 S. Yuan, D. Chen, X. Li, J. Zhong and X. Xu, *ACS Appl. Mater. interfaces*, 2018, **10**, 18918–18926.
11 Y. Jia, R. A. Kerner, A. J. Grede, A. N. Brigeman, B. P. Rand and N. C. Giebink, *Nano Lett.*, 2016, **16**, 6–11.
12 Y. Xu, Q. Chen, C. Zhang, R. Wang, H. Wu, X. Zhang and G. Xing, *J. Am. Chem. Soc.*, 2016, **138**, 3761–3768.
13 C. Huo, X. Liu, X. Song, Z. Wang and H. Zeng, *J. Phys. Chem. Lett.*, 2017, **8**, 4785–4792.
14 W. Yu, F. Li, L. Yu, M. R. Niazi, Y. Zou, D. Corzo, A. Basu, C. Ma, S. Dey, M. L. Tietze, U. Buttner, X. Wang, Z. Wang, M. N. Hedhili, C. Guo, T. Wu and A. Amassian, *Nat. Commun.*, 2018, **9**, 5354.
15 A. Swarnkar, A. R. Marshall, E. M. Sanehira, B. D. Chernomordik, D. T. Moore, J. A. Christians, T. Chakrabarti and J. M. Luther, *Science (1979)*, 2016, **354**, 92–95.
16 M. Que, L. Zhu, Y. Guo, W. Que and S. Yun, *J. Mat. Chem. C*, 2020, **8**, 5321–5334.
17 J. Yuan, A. Hazarika, Q. Zhao, X. Ling, T. Moot, W. Ma and J. M. Luther, *Joule*, 2020, **4**, 1160–1185.
18 L. Liu, A. Najar, K. Wang, M. Du and S. F. Liu, *Adv. Sci.*, 2022, **9**, 21104577.
19 B. V Lotsch, *Angew. Chem. Int. Ed.*, 2014, **53**, 635–637.
20 A. Dey, J. Ye, A. De, E. Debroye, S. K. Ha, E. Bladt, A. S. Kshirsagar, Z. Wang, J. Yin, Y. Wang, L. N. Quan, F. Yan, M. Gao, X. Li, J. Shamsi, T. Debnath, M. Cao, M. A. Scheel, S. Kumar, J. A. Steele, M. Gerhard, L. Chouhan, K. Xu, X. Wu, Y. Li, Y. Zhang, A. Dutta, C. Han, I. Vincon, A. L. Rogach, A. Nag, A. Samanta, B. A. Korgel, C. Shih, D. R. Gamelin, D. H. Son, H. Zeng, H. Zhong, H. Sun, H. V. Demir, I. G. Scheblykin, J. K. Stolarczyk, J. Z. Zhang, J. Feldmann, J. Hofkens, J. M. Luther, P. Julia, L. Li, L. Manna, M. I. Bodnarchuk, M. V Kovalenko, M. B. J. Roe, N. Pradhan, O. F. Mohammed, O. M. Bakr, P. Yang, P. Mu, P. V Kamat, Q. Bao, Q. Zhang, R. Krahne, R. E. Galian, S. D. Stranks, S. Bals, V. Biju, W. A. Tisdale, Y. Yan, R. L. Z. Hoye and L. Polavarapu, *ACS Nano*, 2021, **15**, 10775–10961.
21 J. S. Manser, A. Christians and P. V Kamat, *Chem. Rev.*, 2016, **116**, 12956–13008.
22 V. V. M. Goldschid, *Naturwissenschaften*, 1926, **17**, 477–485.
23 Q. A. Akkerman and L. Manna, *ACS Energy Lett.*, 2020, **5**, 604–610.
24 M. D. Smith, B. A. Connor and H. I. Karunadasa, *Chem. Rev.*, 2019, **119**, 3104–3139.
25 G. Schileo and G. Grancini, *J. Mater. Chem. C*, 2021, **9**, 67–76.
26 C. H. Lu, G. v. Biesold-Mcgee, Y. Liu, Z. Kang and Z. Lin, *Chem. Soc. Rev.*, 2020, **49**, 4953–5007.
27 A. Swarnkar, V. K. Ravi and A. Nag, *ACS Energy Lett.*, 2017, **2**, 1089–1098.
28 X. Li, X. Gao, X. Zhang, X. Shen, M. Lu, J. Wu, Z. Shi, V. L. Colvin, J. Hu, X. Bai, W. W. Yu and Y. Zhang, *Adv. Sci.*, 2021, **8**, 2003334.
29 Q. Fan, G. V Biesold-mcgee, J. Ma, Q. Xu, S. Pan, J. Peng and Z. Lin, *Angew. Chem. Int. Ed.*, 2020, **59**, 1030–1046.
30 B. Saparov, F. Hong, J. Sun, H. Duan, W. Meng, S. Cameron, I. G. Hill, Y. Yan and D. B. Mitzi, *Chem. Mater.*, 2015, **27**, 5622–5632.
31 F. Jiang, D. Yang, Y. Jiang, T. Liu, X. Zhao, Y. Ming, B. Luo, F. Qin, J. Fan, H. Han, L. Zhang and Y. Zhou, *J. Am. Chem. Soc.*, 2018, **140**, 1019–1027.
32 J. Pal, S. Manna, A. Mondal, S. Das and K. V Adarsh, *Angew. Chem. Int. Ed.*, 2017, **56**, 14187–14191.
33 A. H. Slavney, T. Hu, A. M. Lindenberg and H. I. Karunadasa, *J. Am. Chem. Soc.*, 2016, **3**, 3–6.
34 F. Igbari, Z. Wang and L. Liao, *Adv. Energy Mater.*, 2019, **1803150**, 1–32.
35 A. Dey, J. Ye, A. De, E. Debroye, S. K. Ha, E. Bladt, A. S. Kshirsagar, Z. Wang, J. Yin, Y. Wang, L. N. Quan, F. Yan, M. Gao, X. Li, J. Shamsi, T. Debnath, M. Cao, M. A. Scheel, S. Kumar, J. A. Steele, M. Gerhard, L. Chouhan, K. Xu, X. G. Wu, Y. Li, Y. Zhang, A. Dutta, C. Han, I. Vincon, A. L. Rogach, A. Nag, A. Samanta, B.

A. Korgel, C. J. Shih, D. R. Gamelin, D. H. Son, H. Zeng, H. Zhong, H. Sun, H. V. Demir, I. G. Scheblykin, I. Mora-Seró, J. K. Stolarczyk, J. Z. Zhang, J. Feldmann, J. Hofkens, J. M. Luther, J. Pérez-Prieto, L. Li, L. Manna, M. I. Bodnarchuk, M. v. Kovalenko, M. B. J. Roeffaers, N. Pradhan, O. F. Mohammed, O. M. Bakr, P. Yang, P. Müller-Buschbaum, P. v. Kamat, Q. Bao, Q. Zhang, R. Krahne, R. E. Galian, S. D. Stranks, S. Bals, V. Biju, W. A. Tisdale, Y. Yan, R. L. Z. Hoye and L. Polavarapu, *ACS Nano*, 2021, **15**, 10775–10981.

36 G. K. Grandhi, N. S. M. Viswanath, H. Bin Cho, J. H. Han, S. M. Kim, S. Choi and W. Bin Im, *J. Phys. Chem. Lett.*, 2020, **11**, 7723–7723.

37 P. Cheng, L. Sun, L. Feng, S. Yang, Y. Yang, D. Zheng, Y. Zhao, Y. Sang, R. Zhang, D. Wei, W. Deng and K. Han, *Angew. Chem. Int. Ed.*, 2019, **58**, 16087–16091.

38 Z. Luo, Q. Li, L. Zhang, X. Wu, L. Tan, C. Zou and Y. Liu, *Small*, 2020, **5**, 1–5.

39 L. Lian, M. Zheng, W. Zhang, L. Yin, X. Du, P. Zhang, X. Zhang, J. Gao, D. Zhang, L. Gao, G. Niu, H. Song, R. Chen, X. Lan, J. Tang and J. Zhang, *Adv. Sci*, 2020, **7**, 2000195.

40 L. Lian, M. Zheng, P. Zhang, Z. Zheng, K. Du, W. Lei, J. Gao, G. Niu, D. Zhang, T. Zhai, S. Jin, J. Tang, X. Zhang and J. Zhang, *Chem. Mater.*, 2020, **5**, 3462–3468.

41 Y. Li, P. Vashishtha, Z. Zhou, Z. Li, S. B. Shivarudraiah, C. Ma, J. Liu, K. S. Wong, H. Su and J. E. Halpert, *Chem. Mater.*, 2020, **5**, 5515–5524.

42 R. Zhang, X. Mao, D. Zheng, Y. Yang, S. Yang and K. Han, *Laser Photonics rev.*, 2020, **14**, 2000027.

43 S. Fang, Y. Wang, H. Li, F. Fang, K. Jiang, Z. Liu, H. Li and Y. Shi, *J. Mater. Chem. C*, 2020, **4**, 4895–4901.

44 L. Lian, M. Zheng, P. Zhang, Z. Zheng, K. Du, W. Lei, J. Gao, G. Niu, D. Zhang, T. Zhai, S. Jin, J. Tang, X. Zhang and J. Zhang, *Chem. Mater.*, 2020, **32**, 3462–3468.

45 D. Cortecchia, H. A. Dewi, J. Yin, A. Bruno, S. Chen, T. Baikie, P. P. Boix, M. Grätzel, S. Mhaisalkar, C. Soci and N. Mathews, *Inorg. Chem.*, 2016, **55**, 1044–1052.

46 B. Saparov and D. B. Mitzi, *Chem. Rev.*, 2016, **116**, 4558–4596.

47 Y. Liu, X. Li, J. Wang, L. Xu and B. Hu, *J. Mater. Chem. A*, 2017, **5**, 13834–13841.

48 T. Jun, K. Sim, S. Iimura, M. Sasase and H. Kamioka, *Adv. Mater.*, 2018, **30**, 1804547.

49 R. Lin, Q. Guo, Q. Zhu, Y. Zhu, W. Zheng and F. Huang, *Adv. Mater.*, 2019, **31**, 1905079.

50 P. Sebastia-Luna, J. Navarro-alapont, M. Sessolo, F. Palazon and H. J. Bolink, *Chem. Mater.*, 2019, **31**, 10205–10210.

51 Z. Zhang, C. Li, Y. Lu, X. Tong, F. Liang, X. Zhao, D. Wu, C. Xie and L. Luo, *J. Phys. Chem. Lett.*, 2019, **10**, 5343–5350.

52 X. Liu, Y. Yu, F. Yuan, C. Zhao, H. Dong, B. Jiao and Z. Wu, *ACS Appl. Mater. Interfaces*, 2020, **12**, 52967–52975.

53 R. Roccanova, A. Yangui, G. Seo, T. D. Creason, Y. Wu, D. Y. Kim, M. Du and B. Saparov, *ACS Matterials Lett.*, 2019, **3**, 3–9.

54 J. Li, T. Inoshita, T. Ying, A. Ooishi, J. Kim and H. Hosono, *Adv. Mater.*, 2020, **32**, 2002945.

55 S. G. Kwon and T. Hyeon, *Small*, 2011, 2685–2702.

56 C. B. Murray, D. J. Norris and M. G. Bawendi, *J. Am. Chem. Soc.*, 1993, **115**, 8706–8715.

57 P. Vashishtha, G. V. Nutan, B. E. Griffith, Y. Fang, D. Giovanni, M. Jagadeeswararao, T. C. Sum, N. Mathews and S. G. Mhaisalkar, *Chem. Mater.*, 2019, **31**, 9003–9011.

58 F. Debuigne, L. Jeunieau and M. Wiame, *Langmuir*, 2000, 7605–7611.

59 H. Fu and J. Yao, *J. Am. Chem. Soc*, 2001, 1434–1439.

60 D. Horn and J. Rieger, *Angew. Chem. Int. Ed.*, 2001, **40**, 4330–4361.

61 F. Zhang, H. Zhong, C. Chen, X. Wu, X. Hu and H. Huang, *ACS Nano*, 2015, **3**, 4533–4542.

62 X. Li, Y. Wu, S. Zhang, B. Cai, Y. Gu, J. Song and H. Zeng, *Adv. Funct. Mater.*, 2016, **26**, 2435–2445.

63 Q. Zhong, M. Cao, Y. Xu, P. Li, Y. Zhang, H. Hu, D. Yang and Y. Xu, *Nano Lett.*, 2019, **19**, 4151–4157.

64 B. Yang, J. Chen, F. Hong, X. Mao, K. Zheng, S. Yang, Y. Li, T. Pullerits, W. Deng and K. Han, *Angew. Chem. Int. Ed.*, 2017, **56**, 12471–12475.

65 M. Leng, Y. Yang, K. Zeng, Z. Chen, Z. Tan, S. Li, J. Li, B. Xu, D. Li, M. P. Hautzinger, Y. Fu, T. Zhai and L. Xu, *Adv. Funct. Mater.*, 2018, **28**, 1704446.

66 J. Zhang, Y. Yang, H. Deng, U. Farooq, X. Yang, J. Khan, J. Tang and H. Song, *ACS Nano*, 2017, **11**, 9294–9302.

67 B. Yang, J. Chen, S. Yang, F. Hong, L. Sun, P. Han, T. Pullerits, W. Deng and K. Han, *Angerw. Chem. Int. Ed.*, 2018, **57**, 5359–5363.

68 P. Vashishtha, T. J. N. Hooper, Y. Fang, D. Kathleen, D. Giovanni, M. Klein, T. C. Sum, S. G. Mhaisalkar, N. Mathews and T. White, *Nanoscale*, 2021, **13**, 59–65.

69 S. Ma, J. Ahn and J. Moon, *Adv. Mater.*, 2021, **33**, 2005760.

70 Y. Dang, X. Liu, B. Cao and X. Tao, *Matter*, 2021, **4**, 794–820.

71 Y. Dong, Y. Zhang, X. Li, Y. Feng, H. Zhang and J. Xu, *Small*, 2019, **15**, 1902237.

72 D. G. Billing and A. Lemmerer, *Acta Cryst.*, 2003, **E59**, 381–383.
73 D. G. Billing and A. Lemmerer, *CrystEngComm*, 2006, **8**, 686–695.
74 J. Ahn, E. Lee, J. Tan, W. Yang, B. Kim and J. Moon, *Mater. Horiz.*, 2017, **4**, 851–856.
75 J. Ahn, S. Ma, J. Kim, J. Kyhm, W. Yang, J. A. Lim, N. A. Kotov and J. Moon, *J. Am. Chem. Soc.*, 2020, **142**, 4206–4212.
76 S. Ma, J. Ahn and J. Moon, *Adv. Mater.*, 2021, **33**, 2005760.
77 G. Long, C. Jiang, R. Sabatini, Z. Yang, M. Wei, L. N. Quan, Q. Liang, A. Rasmita, M. Askerka, G. Walters, X. Gong, J. Xing, X. Wen, R. Quintero-bermudez, H. Yuan, G. Xing, X. R. Wang, D. Song, O. Voznyy, M. Zhang, S. Hoogland, W. Gao, Q. Xiong and E. H. Sargent, *Nat Photonics*, 2018, **12**, 528–533.
78 C. Fang, C. Chen, L. Jin, J. Wang, S. Wang, J. Tang and D. Li, *ACS Nano*, 2019, **13**, 3659–3665.
79 T. He, J. Li, X. Li, C. Ren, Y. Luo, F. Zhao, R. Chen, X. Lin and J. Zhang, *Appl. Phys. Lett.*, 2017, **111**, 151102.
80 G. H. Debnath, Z. N. Georgieva, B. P. Bloom, S. Tan and D. H. Waldeck, *Nanoscale*, 2021, **13**, 15248–15256.
81 W. Chen, S. Zhang, M. Zhou, T. Zhao, X. Qin, X. Liu, M. Liu and P. Duan, *J. Phys. Chem. Lett.*, 2019, **10**, 3290–3295.
82 A. Forde, D. Ghosh, D. Kilin, A. C. Evans, S. Tretiak and A. J. Neukirch, *J. Phys. Chem. Lett.*, 2022, **13**, 686–693.
83 Y. Shi, P. Duan, S. Huo, Y. Li and M. Liu, *Adv. Mater.*, , DOI:10.1002/adma.201705011.
84 X. Yang, M. Zhou, Y. Wang and P. Duan, *Adv. Mater.*, , DOI:10.1002/adma.202000820.
85 P. Liu, W. Chen, Y. Okazaki, Y. Battie, L. Brocard, M. Decossas, E. Pouget, P. Müller-Buschbaum, B. Kauffmann, S. Pathan, T. Sagawa and R. Oda, *Nano Lett.*, 2020, **20**, 8453–8460.
86 Z. Li, Y. Yan, W. Ma, J. Zhao, Y. Fan and Y. Wang, *CCS Chem.*, 2022, **4**, 3447–3454.
87 T. Li, X. Mo, C. Peng, Q. Lu, C. Qi, X. Tao, Y. Ouyang and Y. Zhou, *Chem. Commun.*, 2019, **55**, 4554–4557.
88 Z. Luo, Q. Li, L. Zhang, X. Wu, L. Tan, C. Zou, Y. Liu and Z. Quan, *Small*, 2020, **16**, 1905226.
89 P. Sebastia-Luna, J. Navarro-Alapont, M. Sessolo, F. Palazon and H. J. Bolink, *Chem. Mater.*, 2019, **31**, 10205–10210.
90 G. K. Grandhi, N. S. M. Viswanath, H. bin Cho, J. H. Han, S. M. Kim, S. Choi and W. bin Im, *J. Phys. Chem. Lett.*, 2020, **11**, 7723–7729.
91 S. Fang, Y. Wang, H. Li, F. Fang, K. Jiang, Z. Liu, H. Li and Y. Shi, *J. Mater. Chem. C*, 2020, **8**, 4895–4901.
92 S. Li, J. Luo, J. Liu and J. Tang, *J. Phys. Chem. Lett.*, 2019, **10**, 1999–2007.
93 R. M. Webster, F. X. Kiemle, D. J. Bryce and J. Wiley, *Spettrometric Identification of Organic Compounds*, John Wiley & Sons, Chichester, 8th edition., 2005.
94 G. Socrates, *Infrared and Raman Characteristic Group Frequencies*, John Wiley & Sons, Chichester, third edition., 2001.
95 N. Amdursky and M. M. Stevens, *ChemPhysChem*, 2015, **16**, 2768–2774.
96 G. H. Debnath, Z. N. Georgieva, B. P. Bloom, S. Tan and D. H. Waldeck, *Electronic Supplementary Information Using Post-synthetic Ligand Modification to Imprint Chirality onto the Electronic States of Cesium Lead Bromide (CsPbBr 3) Perovskite Nanoparticles*, 2021.
97 F. Igbari, Z. K. Wang and L. S. Liao, *Adv. Energy Mater.*, 2019, **9**, 1803150.
98 V. K. Ravi, P. K. Santra, N. Joshi, J. Chugh, S. K. Singh, H. Rensmo, P. Ghosh and A. Nag, *J. Pys. Chem. Lett.*, 2017, **8**, 4988–4994.
99 J. de Roo, M. Ibáñez, P. Geiregat, G. Nedelcu, W. Walravens, J. Maes, J. C. Martins, I. van Driessche, M. v. Kovalenko and Z. Hens, *ACS Nano*, 2016, **10**, 2071–2081.
100 J. Li, T. Inoshita, T. Ying, A. Ooishi, J. Kim and H. Hosono, *Adv. Mater.*, 2020, **32**, 2002945.
101 K. Suzuki, A. Kobayashi, S. Kaneko, K. Takehira, T. Yoshihara, H. Ishida, Y. Shiina, S. Oishi and S. Tobita, *Phys. Chem. Chem. Phys.*, 2009, **11**, 9850–9860.
102 W. Kuhn, *Z. Physick. Chem.*, 1930, **14**, 293–308.
103 U. Resch-Genger and K. Rurack, *Pure Appl. Chem.*, 2013, **85**, 2005–2026.
104 A. M. Brouwer, *Pure Appl. Chem.*, 2011, 83, 2213–2228.

6 APPENDIX

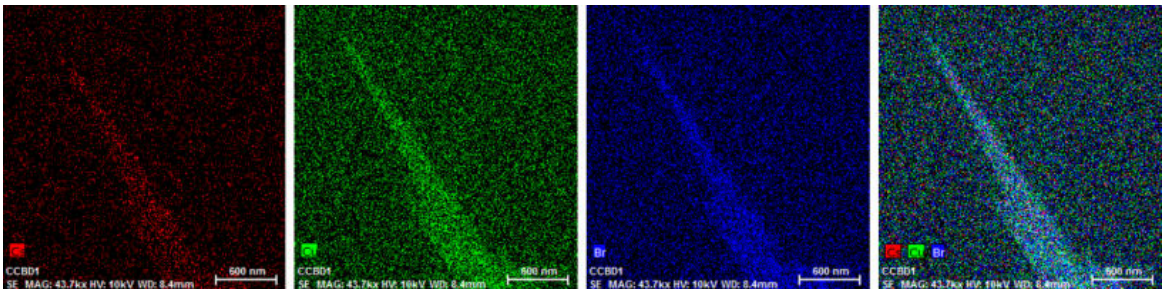

Figure A1: SEM-EDS elemental mapping of L-CCB microwires.

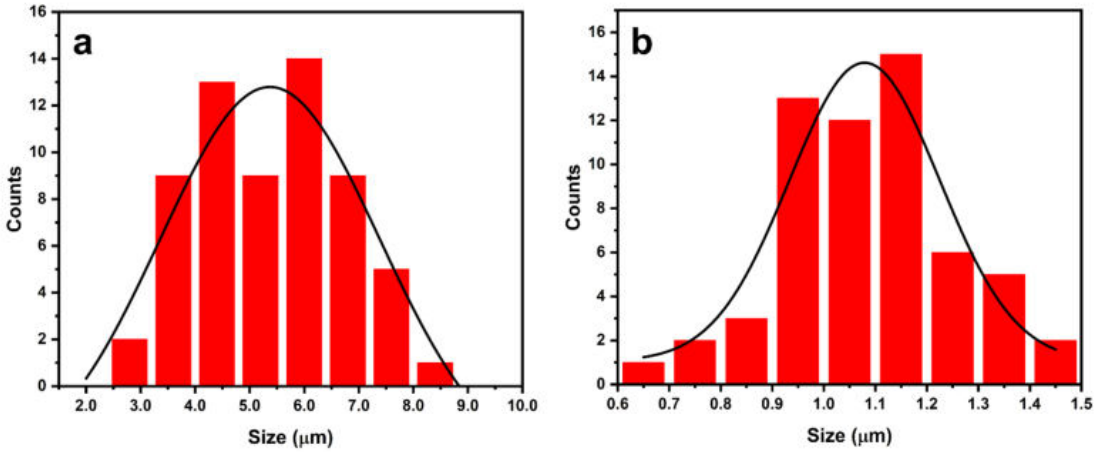

Figure A2: size distributions of a) length and b) width of $Cs_3Cu_2Br_5$ micro-rods stabilised with N-acetyl cysteine. According to a normal distribution the average size of 5 ± 4 μm and 1.0 ± 0.3 μm can be estimated for rod length and width respectively.

Photoluminescence Quantum Yield Determination:

Equation A1[103,104]

$$\Phi_{QDs} = \Phi_{st} \frac{I_{QDs} f_{st} n_{QDs}^2}{I_{st} f_{QDs} n_{st}^2}$$

The subscripts *QDs* and *st* refer to the quantum dots or the fluorescence standard respectively. The PLQY is represented by *Φ*, *I* represent the integrated intensity corrected by the fluorimeter sensitivity and the source intensity, *n* represents the diffraction index of the solvent and *f* the absorption factor

Equation A2[103,104]

$$f_{QDs,st} = 1 - 10\text{^}(-A_{QDs,st})$$

Where *f* and *A* represent the absorption factor and the absorbance for quantum dots (*QDs*) and fluorescence standard (*st)*.

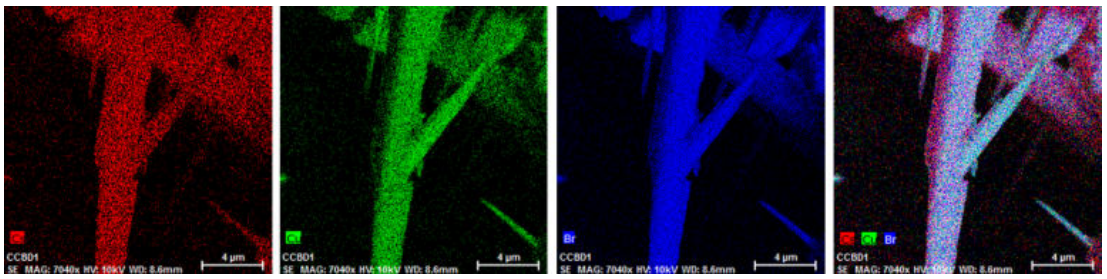

Figur3 A3: SEM-EDS elemental mapping of bulk-CCB microwires.

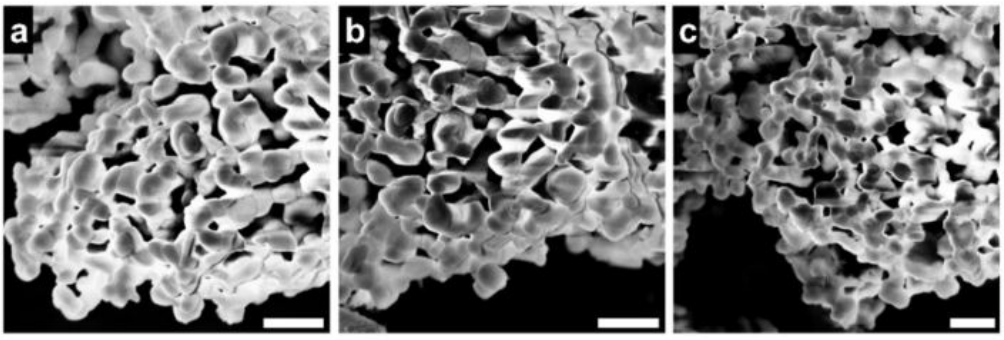

Figure A4: SEM micrographs of $Cs_3Bi_2Br_9$, scale bars = 500 nm

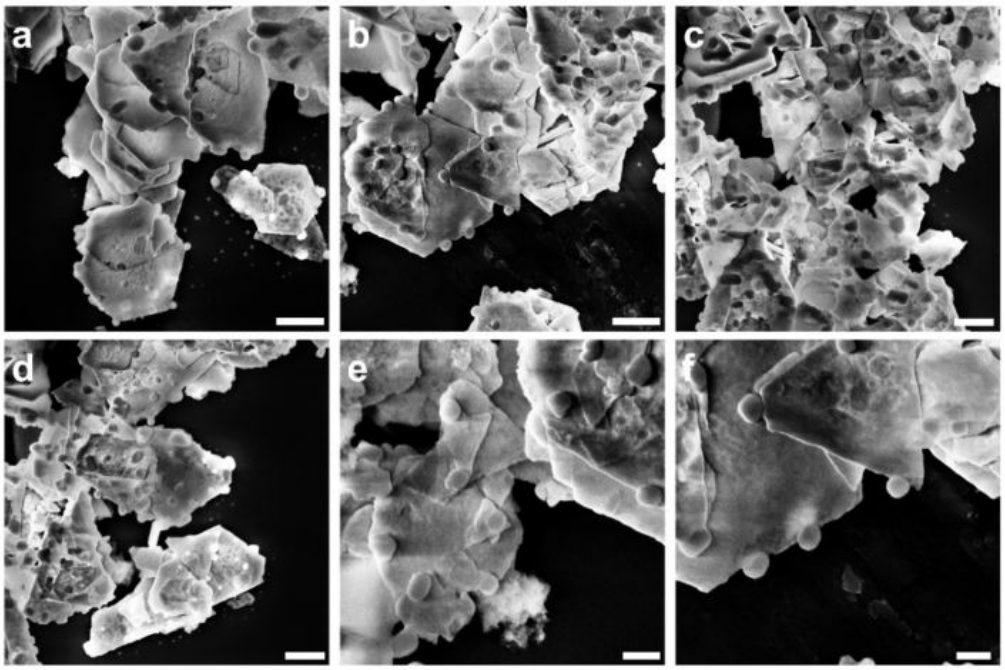

Figure A5: SEM micrographs of $Cs_3Bi_2I_9$, scale bars: a-d = 500 nm, e and f = 200 nm.

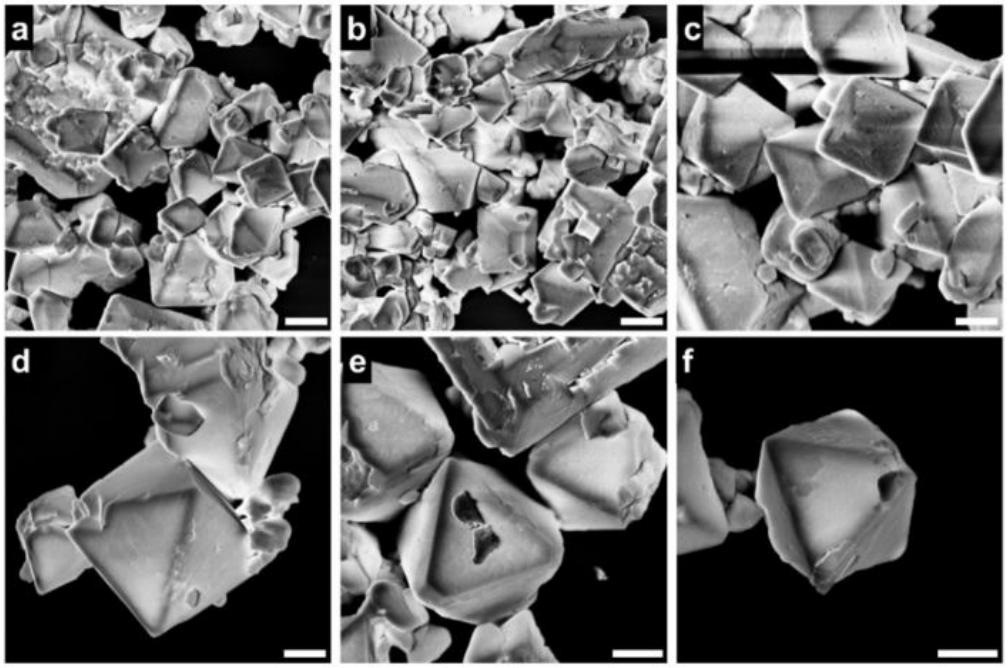

Figure A6: SEM micrographs of $Cs_2AgInCl_6$, scale bars: a – c = 1 µm, d – f = 500 nm

CHAPTER V

ENANTIOSELECTIVE LUMINESCENCE CHEMOSENSING

1 INTRODUCTION

The quantification of the enantiomeric excess is fundamental to characterise any chiral molecules. Several chiral drugs present distinctive activities depending to their stereochemistry. If one enantiomer is associated to the desired pharmaceutical activity the other one is usually not active or even harmful. The different pharmacological activity related to the two dopamine enantiomers is a well-known example of this type of behaviour. L-dopamine is a common drug used to treat parkinsonism, instead D-dopamine causes agranulocytosis and decreases body weight. In severe cases of high dosage of the racemic drug, the effect of the toxic stereoisomer may lead to death.[1] Penicillamine is another example. If D-penicillamine is widely used in the treatment of rheumatoid arthritis, the L form and the racemate show high toxicity related to the interaction with the vitamin B6. Such interaction is prevented in D-penicillamine due to its stereochemistry.[2] Moreover, the analysis of the enantiomeric composition of amino acids and carbohydrates in foodstuffs can reflect microbial and bacterial contamination or food adulteration.[3]

The analysis of the enantiomeric excess relies on circular dichroism spectroscopy, HPLC with chiral stationary phases, nuclear magnetic resonance using chiral shift reagents and electrochemical methods.[4] However, despite their high performances, these techniques are affected by several disadvantages such as: high costs, time-consuming procedures and they require well-trained operators. For these reasons there is a wide interest in the developing of reliable chiral sensors, for rapid in situ quality controls, that allow a fast and a low-cost determination of the concentration of chiral analytes with enantiomer discrimination.[5]

Several examples of enantiomeric discriminations using chiral nanoparticles are reported in literature.[1,5] The main distinction between the different approaches is related to the physicochemical mechanism used for the quantification of the analyte. In this prospective, it is possible to distinguish between: colorimetric sensor based on the variation of the absorption spectra of chiral plasmonic nanoparticles (Ag or Au NPs) and fluorometric sensors based on the

quenching or enhancement of the photoluminescence (PL) activity of chiral quantum dots (QDs) or chiral carbon dots (CDs).

- **Colorimetric sensors:** the selective aggregation of plasmonic nanoparticles was proved to be a potential approach for the enantiomeric discrimination of chiral analytes thanks to the variation of their optical properties with the aggregation state. This approach was used by Su et al.[6] to design a system based on gold nanoparticles, stabilised with N-acetyl-L-cysteine, for the enantioselective discrimination of L and D-tyrosine. The nanoparticles presented an absorption band at 522 nm related to their characteristic surface plasmon absorption; the addition of L-tyrosine shows a new electronic transition at 630 nm that was associated to the formation of aggregates. Instead, no appreciable variations of the optical properties of the colloidal solution were observed by the addition of D-tyrosine. The authors ascribed the enantiomeric discrimination to the preferential interaction between N-acetyl-L-cysteine, present on the particle surface, and L- tyrosine in solution through electrostatic interactions and hydrogen bonds. This approach was investigated by several authors using both gold and silver nanoparticles to design enantioselective colorimetric sensors for a broad range of chiral analytes.[7–10]

- **Fluorometric sensors:** the enantiomeric discrimination properties of different chiral fluorescent nanosystems such as: Quantum Dots (QDs), Carbon Dots (CDs), silicon nanoparticle and fluorescent silver nanoclustes were investigated for their potential application in the enantioselective sensing.[5] Chiral QDs can play a promising role due to their simple design and easy tunability of their optical properties.[11] Han et al.[12] reported the enantiomeric discrimination of cyclodextrin coated CdSe/ZnS QDs for different amino acid. Their system was based on the different stability of the diastereoisomeric complexes between the chiral analyte and the chiral cavity of the cyclodextrin. When the cyclodextrin capped QDs were treated with tyrosine or methionine a luminescence enhancement, sensible to the chirality of the analyte, was observed. After this first report, other different systems based on cyclodextrin coted QDs were investigated.[13,14] Another approach to produce enantioselective luminescent nanoprobes exploits QDs stabilised by small chiral ligands. Interesting results using Cd-based chiral QDs, such as the chemosensing of carnitine enantiomers with CdSe/ZnS QDs stabilised

with cysteine was reported.[15] Another example, presented by Delgado-Pérez et al. [16], used CdSe/ZnS QDs stabilised with N-acetyl-L-cysteine ethyl ester as a sensor for the quantification of chiral drugs (Ketoprofen, Naproxen, flurbiprofen and ibuprofen).

2 RESULTS AND DISCUSSION

The luminescence quenching or the enhancement effect related to the addition of enantiomerically pure analytes are investigated in order to verify the possible application of Chiral AIS QDs and Chiral Cysteine based CDs as luminescent enantioselective chemosensors. To quantify the effect of the analyte on the PL activity we use the Stern-Volmer model described in **Eq. 1** for the luminescence quenching and **Eq. 2** for the enhancement.

Eq. 1

$$\frac{I_0}{I_n} = 1 + K_{sv}\,[Q]_n$$

Eq. 2

$$\frac{I_n}{I_0} = 1 + K_{sv}\,[E]_n$$

I_n and I_0 are the integrated luminescence intensities in the presence of the n^{th} quencher or enhancer concentration and without any quencher or enhancer addition. $[Q]_n$ and $[E]_n$ are the concentrations of the substrate (quencher or enhancer) added to the n^{th} sample and K_{sv} is the Stern Volmer constant.

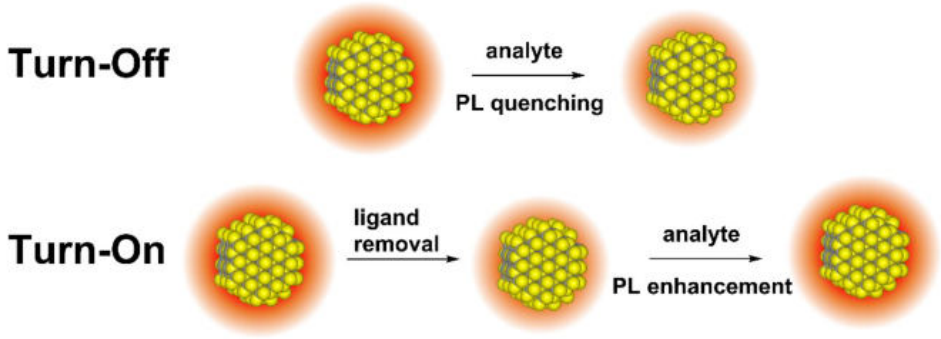

Figure 1: different chemosensor designs used for the chemosensing tests with AIS QDs.

For the design of the QDs-based sensor, we considered two different approaches (schematized in **Fig. 1**): i) Turn-Off chemosensor: it is based on the quenching activity of the chiral analyte, added to the QDs colloidal solution, that causes a reduction of the QDs PL and ii) Turn-

On chemosensor: before the application, QDs are processed by multiple cleaning steps to remove the original ligand (cysteine). In this condition the nanoparticles PL is largely quenched, and alkaline pH (higher than 10) is required to ensure colloidal stability. The addition of the chiral analyte partially restores the PL activity, and the luminescence enhancement is related to the interaction of the QDs with the analyte. Cysteine based chiral CDs are investigated considering only the quenching effect of aromatic amino acids (tryptophan and histidine) according to the Turn-Off chemosensing mode.

2.1 AIS QDs Turn-Off chemosensor

The quenching activity of L and D-tryptophan (Trp) is investigated for **AIS14** QDs in the Turn-Off chemosensing mode. An evident reduction of the luminescence intensity is appreciated for all the solutions with different concentrations of L and D-tryptophan (Trp) (**Fig. 2**), and for the solutions with larger quencher concentrations a small red shift is observed. In absence of tryptophan, the PL maximum of **AIS14** QDs, observed at 660 nm is significantly red-shifted with respect to the emission observed for **AIS14** QDs in cysteine solution (640 nm, data presented in **chapter 3**), this effect is related to the high concentration of phosphate anions present in the buffer solution used for the chemosensing tests. We associated the quenching effect of Trp to the Photoinduced Electron Transfer (PET) mechanism. According to this mechanism, the quencher molecule provides some orbitals with energy between the HOMO-LUMO

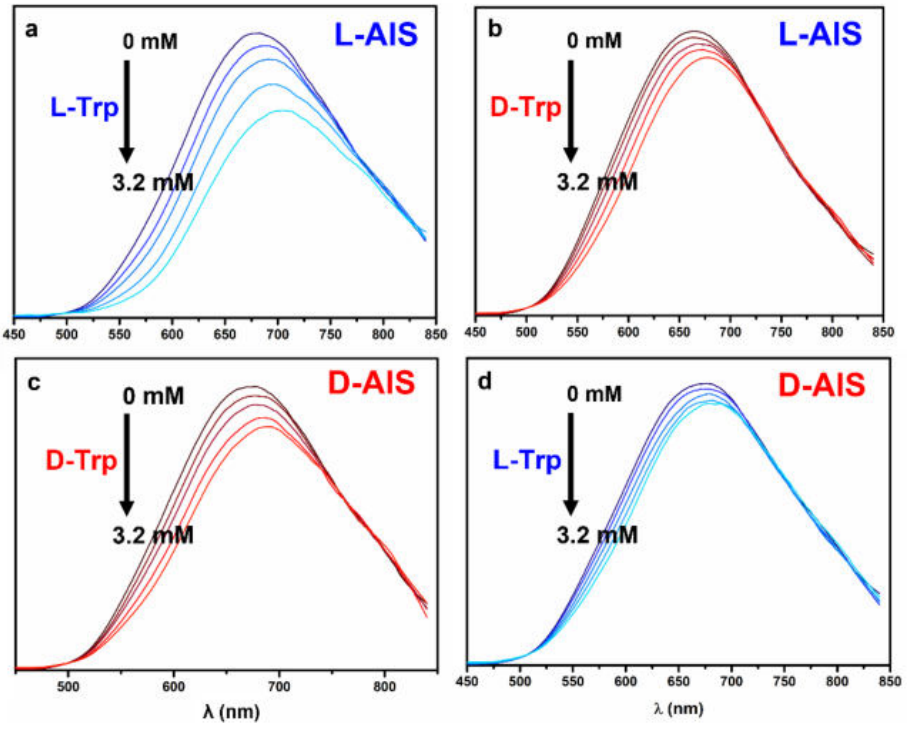

Figure 2: PL spectra of **L-AIS14** (a,b) and **D-AIS14** (c,d) QDs in the presence of different concentrations of L or D-tryptophan.

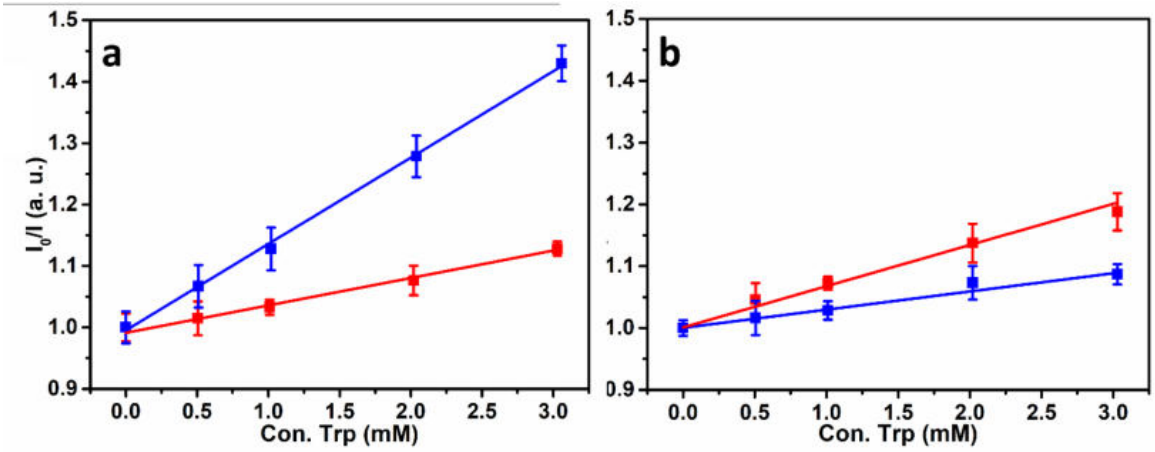

Figure 3: Stern-Volmer plots of the quenching analysis for a) **L-AIS** QDs in the presence of L-Trp (blue) or D-Trp (red) and b) **D-AIS** QDs in the presence of L-Trp (blue) or D-Trp (red). The errors bars refer to the uncertainty considered as three times the standard deviation based on three distinct measurements.

orbitals of the luminophores, introducing new non-radiative recombination pathways for the exciton relaxation.[17]

Moreover, some differences that can be related to the stereochemistry of the quencher and the QDs are observed. The effect of the addition of Trp is evaluated with the Stern-Volmer model. The plot for the quenching analysis of **L-AIS14** (**Fig. 3a**), in the presence of L and D Trp, shows a linear behaviour in the 0.1 - 3.2 mM range from which the Stern-Volmer constants can be calculated. The values of 140.5 and 44.0 M^{-1} for L (K_{SV}^{L}) and D (K_{SV}^{D}) tryptophan, reveal a stronger quenching in the presence of L-Trp. The analysis of the quenching of **D-AIS** (**Fig. 3b**) shows a higher affinity for D-Trp (K_{SV}^{D}= 66.7) than for L-Trp. M^{-1} (K_{SV}^{L} = 29.5 M^{-1}). This finding suggests a preferential interaction between **L-AIS14** QDs and L-Trp and **D-AIS14** QDs and D-Trp. **Table 1** evidences similar results also for other AIS QDs. We implemented a new parameter, Δ_{LD}, to express the difference interaction between the two enantiomers of the analyte for a specific QDs enantiomer, which can represent the sensor enantioselectivity. As reported in **Eq. 3**, Δ_{LD} is the module of the difference between the Stern-Volmer constants of the L-analyte (K_{sv}^{L}) and D-analyte (K_{sv}^{D}), normalised by their sum.

Eq. 3

$$\Delta_{LD} = \frac{| K_{SV}^{L} - K_{SV}^{D} |}{K_{SV}^{L} + K_{SV}^{D}}$$

The maximum of the selectivity for AIS QDs chemosensors, based on the Turn-off chemosensing mode, is observed for **LAIS14** (Δ_{LD} is 0.52). Even though the differences between L and D AIS QDs are quite significant, further investigations are required to understand the origin of this effect. However, the quenching properties show no evident effects related to the QDs

chemical compositions. The limit of detections (LoD) is estimated considering three times the standard deviation (based on 5 consecutive measurements) of the PL intensity values measured for the sample without the quencher addition (I_0) and show values in the 0.1 - 0.5 mM range.

Table 1

Sample	K_{SV}^{L} (mM^{-1})	K_{SV}^{D} (mM^{-1})	Δ_{LD} (mM^{-1})	LoD^{L} mM	LoD^{D} mM
LAIS14	0.141	0.045	0.52	0.091	0.502
DAIS14	0.029	0.067	0.39	0.434	0.076
LAIS16	0.125	0.051	0.42	0.179	0.251
DAIS16	0.045	0.123	0.46	0.156	0.211
LAIS18	0.129	0.050	0.44	0.173	0.257
DAIS18	0.033	0.057	0.27	0.153	0.223

2.2 AIS QDs Turn-On chemosensing

In order to extend the concentration range, we investigate an alternative design based on the Turn-On luminescence chemosensing. In this approach, the QDs PL is quenched and the analyte is quantified by its activity to recover the luminescence. According to this design, quenched **AIS14** QDs are produced by a substantial removal of the surface ligand by several centrifugation steps. After the cleaning process, the QDs solutions show colloidal stability in ammonium hydroxide solution at pH 10 or higher. This result is probably due to an electrostatic stabilisation related to ion adsorbed on the QDs surface. Moreover, little PL activity is observed if compared to the original solution (**Fig. 4**), probably the quenching is related to the effect of unpassivated surface defects whose formation is favourited in the presence of low ligand concentrations. A rapid screening of potential chiral substrates (**Fig. 4**) reveals that penicillamine is particularly active and the addition of 5.0 mM of L-penicillamine (Pen) can increase the photoluminescence of quenched **AIS14** QDs of around 2.7 times. We associated this effect to the passivation of surface defects, such as dangling bonds related to unpassivated metal centres exposed on the QDs surface. This kind of surface defects are probably created by removing the original cysteine ligands. Minor PL recovery is observed for amino acids such as methionine and histidine; however, their activity is not comparable to the penicillamine activity. The effect of penicillamine is in line with the expected preferential interaction mediated by the thiol group as evidenced by other authors that observed similar effects on

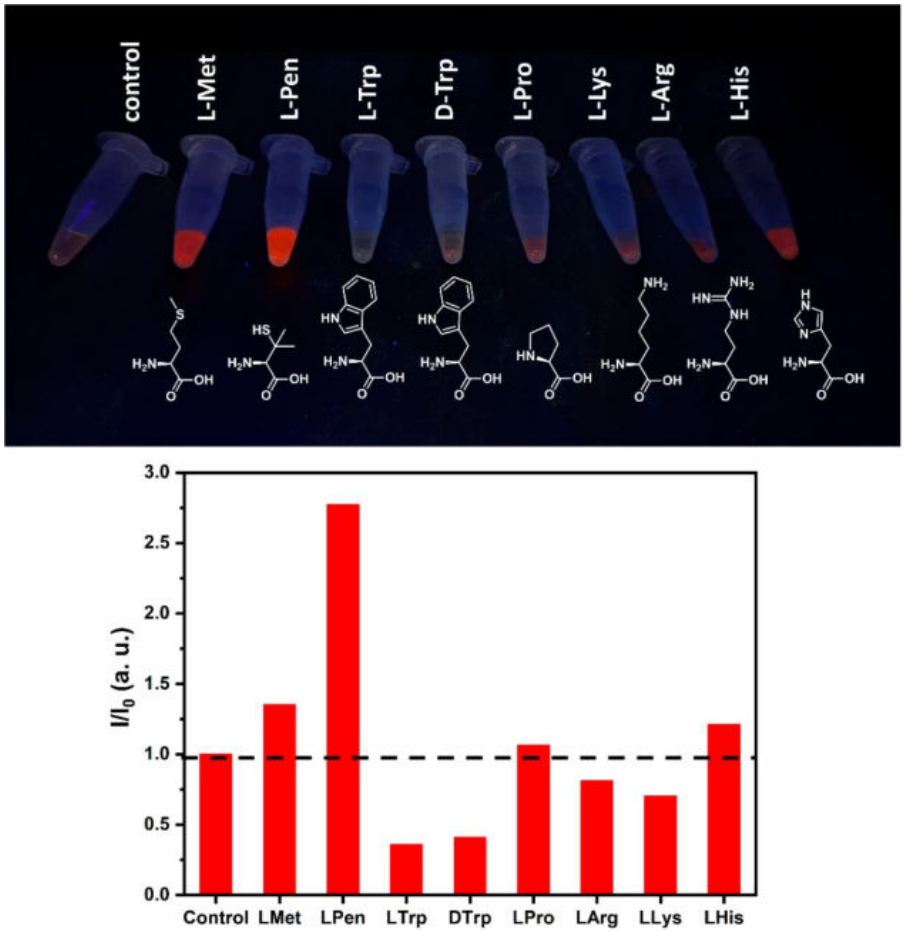

Figure 4: ligands screening for the PL recovery. (top) QDs colloidal solutions after the addition of different ligands under 365 nm lamp and (bottom) the respective integrated intensity value normalised respect the QDs without ligand addition (control). For each test, a ligand concentration of 5.0 mM is used.

the PLQY of chalcogenide QDs.[18,19] The PL enhancement can be obtained even using other thiols such as thioglycolic acid and 2-mercaptopropionic acid. Instead, quenching effects can be observed using tryptophan, lysine and arginine, while proline seems to not affect the PL activity.

Fig. 5a,b show the results of the PL recovery for **L-AIS14** QDs using L and D Pen. As can be seen, both the enantiomers cause the PL enhancement, with a linear behaviour in the 0 – 10.0

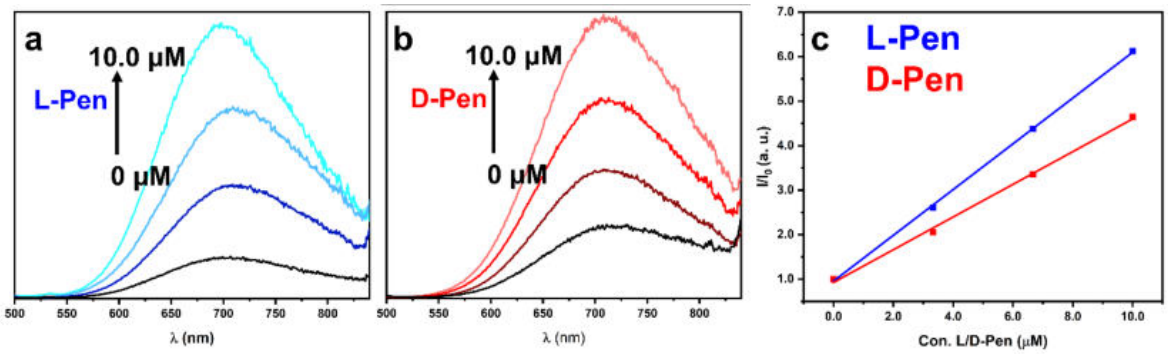

Figure 5: PL enhancement analysis of **L-AIS14** QDs after ligand removal process. Effect of the addition of L-Pen (a) and D-Pen (b) on the PL of **L-AIS14** QDs. Stern-Volmer Plot for the PL enhancement related to the addition of L-Pen (blue) and D-Pen (red).

μM range. The analysis of the Stern-Volmer Plot of **L-AIS14** QDs shows higher sensitivity for L-Pen with a K_{sv}^{L} of 5.14 x 10^5 M^{-1} than for D-Pen with K_{sv}^{D} of 3.80 x 10^5 M^{-1}. This data are only preliminary results and further investigation are required, extending the number of samples, and verifying the reproducibility of the results. However, this finding shows as the analyte concentration can be extended to micromolar ranges. We ascribed this effect to the higher affinity of the QDs surface with new thiol ligands after a proper ligand removal treatment. This type of turn-On chemosensor shows an interesting chemoselectivity toward the detection of thiols, and thanks to the linear response in the micromolar range, it could be suitable for analytical purposes. The lowest stereoselectivity (Δ_{LD} = 0.15), observed using the Turn-Off chemosensing mode, can be related to the reduction of the surface chirality during the ligand removal process. However, the observation of a selective interaction with the penicillamine enantiomers, suggests that the QDs retain some of their chirality even after the ligand removal. This feature is under investigation to assess the possible chiral memory in AIS QDs. Chiral memory is observed when after the removal of the chiral ligand, the QDs retain some of their original chirality. This effect was observed for CdTe[20] QDs and CdS[21] QDs and it was related to the formation of chiral defects on the particle surface that are stable even after the removal of the chiral inductor.

2.1 Cysteine based CDs Turn-Off chemosensor

The analysis of the luminescence quenching of **L-CDs** with D-Trp (**Fig. 6a,b**) shows a linear behaviour up to a quencher concentration of about 1.5 mM. Also, for cysteine-based chiral CDs a different interaction between the enantiomers can be appreciate as shown by the Stern-Volmer plots (**Fig. 6c-f**). **L-CDs** is preferentially quenched by D-Trp (K_{sv}^{D} = 0.431 M^{-1}), instead L-Trp shows a lower efficiency (K_{sv}^{L} = 0.179 M^{-1}). The analysis on **D-CDs** reveals an opposite trend with K_{sv} values of 0.600 and 0.219 M^{-1} for L and D-Trp respectively. We also investigated the effect of histidine as another potential quencher for cysteine based chiral CDs. The analysis show similar results obtained with tryptophan (**Fig. 6e,f**). The results of the luminescence quenching tests for cysteine-based CDs are reported in **Table 2**. Since the number of the tests were less than the AIS QDs ones, further investigations are required to assess the statistical significance of the data. Similar observations were reported by Askari et al.[22] on the chemosensing of L-tryptophan using L and D cysteine functionalized graphene quantum dots.

Table 2

Sample	K_{sv}^{L} (mM^{-1})	K_{sv}^{D} (mM^{-1})	Δ_{LD} (mM^{-1})
L-CDs Trp	0.179	0.431	0.41
D-CDs Trp	0.600	0.219	0.46
L-CDs His	0.128	0.428	0.54
D CDs His	0.331	0.121	0.46

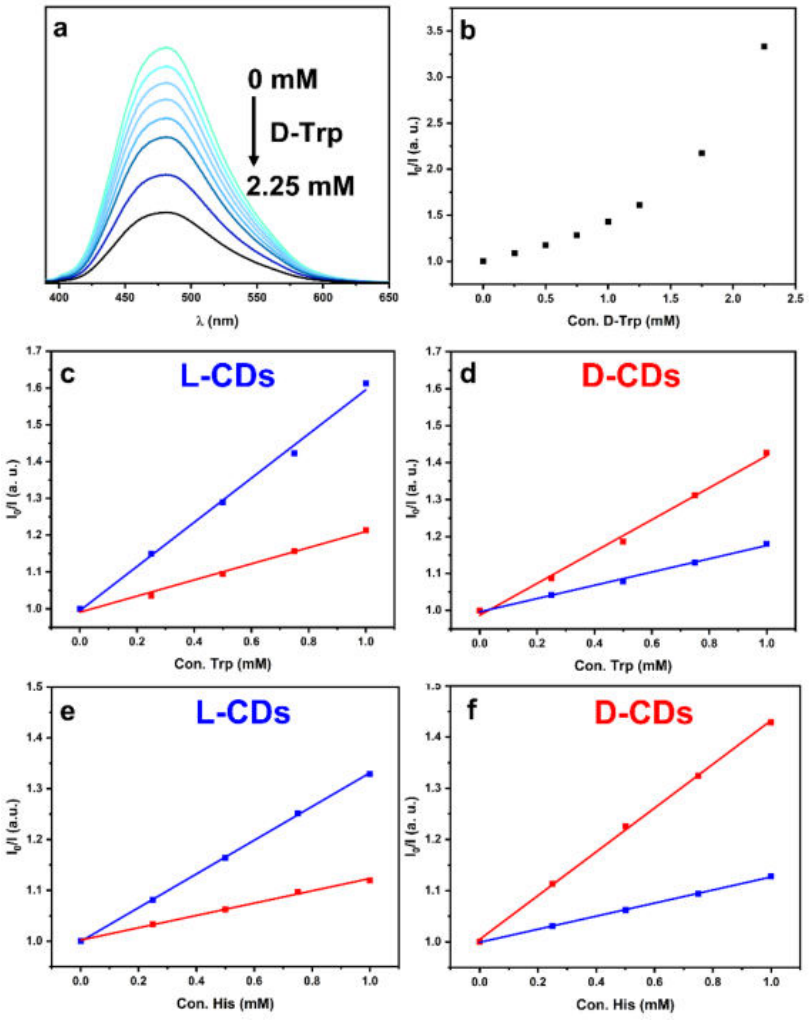

Figure 6: (a) PL spectra of **L-CDs** after the addition of different concentrations of D-Trp. (b) Stern-Volmer plot of the quenching activity of D-Trp for **L-CDs**. (c-f) Stern-Volmer plots for the luminescence quenching of **L-CDs** (c,e) and **D-CDs** (d,f) with the addition of different concentration of L (blue) or D (red) analyte.

3 CONCLUSIONS AND FUTURE PERSPECTIVES

The study on the application of chiral ternary QDs and cysteine-based chiral CDs shows some promising features for possible applications on the enantioselective luminescent chemosensing. In particular:

- The study of the AIS based Turn-Off chemosensors reveals enatioselective quenching for tryptophan in the millimolar concentration range. The analysis of the Stern-Volmer plot of **L-AIS14** QDs (**Table 1**) shows a K_{sv} of 140.5 and 44.0 M^{-1} for L and D-Trp respectively, indicating a higher affinity between **L-ASI14** QDs and L-Trp. The opposite trend is observed for **D-AIS14** QDs that confirms a preferential interaction between **D-AIS14** QDs and D-Trp. Furthermore, similar values are observed for other AIS QDs that are prepared according to different chemical compositions (**Table 1**, **ASI16** and **AIS18**).
- The analysis of the PL enhancement for **AIS14** QDs by penicillamine in the Turn-On chemosensing mode proves the possible application of this different design of the sensor for the enatioselective chemosensing of thiols. Moreover, this mode allows to extend the region down to the micromolar range. This property is probably related to the high reactivity of the QD surface after the ligand removal.
- The analysis of the quenching activity of tryptophane and histidine for cysteine-based CDs reveals enantioselective quenching activity in the millimolar range (**Table 2**) with similar affinity for both the analytes.

The enantioselective chemosensing analyses for AIS QDs and cysteine-based CDs suggest that these nanosystems are potentially suitable for the development of enantioselective chemosensors based on chiral luminescence nanoprobes. However, further investigations are required to optimise the systems:

- The mechanism for the quenching or enhancement must be investigated in detail to assess the type of processes that are involved.
- The Turn-off chemosensors show some degree of enantioselective interaction with the analyte only in the millimolar concentration range. This is probably related to the low affinity of the analyte for the nanoparticle surface, as can be evidenced by the K_{sv} values. To expand the range of concentration toward the micromolar range the design of the particle surface must be improved.

- The Turn-on chemosensing mode allows to reduce the concentration range accessible by the sensor. However, a reduction in the enantioselectivity is also observed. This can be related to the effect of the ligand removal process to the QDs chirality. Further optimization of this step could allow to tune the QDs properties according to the desired affinity and selectivity of the specific chemosensor.
- All the investigated systems require a long equilibration time (between 1 and 2 h) to collect reliable PL data. The use of ions, that can promote the formation of complexes between the ligand on the particle surface and the analyte present in solution, was proved successful for the reduction of the equilibration time and this possibility will be explored in the future.[23]

4 MATERIALS AND METHODS

Chemicals: L-tryptophan (98 %), D-tryptophan (98 %), L-lysine (> 98 %), L-histidine (> 99 %), L-proline (> 99%), L-methionine (> 99%), L-arginine (> 99%), sodium phosphate dibasic dihydrate (> 99%), sodium phosphate monobasic dihydrate (> 99%), ammonium hydroxide (33 %), acetic acid (> 99.7 %) ad HCl (37 %) are purchased by Sigma Aldrich. D-histidine (98 %) is purchased by Fluorochem. All the chemicals are used without further purifications.

AIS QDs Turn-Off chemosensing test: the colloidal dispersions for the chemosensing experiments are prepared by mixing 500 ml of phosphate buffer solution 0.050 M at pH 7.4, different volumes of L- or D-tryptophan 10.0 mM solution are added in order to obtain the desired quencher concentrations and deionized water is added to a reach a final volume of 1.3 ml. Then, 200 µl of L- or D-QDs solution (0.1 mg/ml) is added, and the solution are stirred for a few seconds. The solutions are kept equilibrating at room temperature for 2 h in the dark. The photoluminescence spectra are recorded with an excitation wavelength at 450 nm and emission in the 460 – 850 nm range and slits apertures of 5.0 nm in both excitation and emission.

AIS QDs Turn-On chemosensing test: 1.5 ml of AIS14 QDs solution (1.0 mg/ml QDs concentration) is precipitated with the addition of 10 µl of HCl 0.1 M. The pellet is collected by centrifugation 7000 rpm for 5 min, the pellet is resuspended in 1.5 ml of deionized water after sonication. This step is repeated 5 times to promote the ligand desorption. After the cleaning process, the QDs are redispersed in 1.5 ml of ammonium hydroxide solution 0.1 M. The colloidal dispersions for the chemosensing experiments are prepared by mixing 500 ml of ammonium hydroxide 0.1 M (pH ≈ 11), different volumes of L- or D-penicillamine 0.1 mM solution are added in order to obtain the desired analyte concentrations and deionized water is added to a reach a final volume of 1.3 ml. Then, 200 µl of L- or D-QD solution (1.0 mg/ml) are added, and the solution are stirred for a few seconds. The solutions are kept equilibrating at room temperature for 1 h in the dark. The photoluminescence spectra are recorded with an excitation wavelength at 450 nm and emission in the 460 – 850 nm range and slits apertures of 5.0 nm in both excitation and emission.

Cysteine derived CDs Turn-Off chemosensing test: the colloidal dispersions for the chemosensing experiments are prepared by mixing 500 ml of acetate buffer solution 0.050 M at pH 5.0, different volumes of L- or D-tryptophan (L- or D-histidine) 10.0 mM solution are added in order to obtain the desired quencher concentrations and deionized water is added to a reach a final volume of 1.3 ml. Then, 200 µl of L- or D-CDs solution is added, and the solution are

stirred for a few seconds. The solutions are kept equilibrating at room temperature for 2 h in the dark. The photoluminescence spectra are recorded with an excitation wavelength at 380 nm and emission in the 390 – 650 nm range and slits apertures of 5.0 nm in both excitation and emission.

LIMIT OF DETECTION (LoD): is estimated according to the standard deviation based 5 measurements on the blank sample (QDs without the addition of the quencher). The LOD corresponds to the mean values plus 3 times the standard deviation.[24]

5 REFERENCES

1 X. Zhao, S. Q. Zang and X. Chen, *Chem. Soc. Rev.*, 2020, **49**, 2481–2503.
2 W. F. Kean, P. H. E Howard-Lock and C. C. J L Lock, *Lancet*, 1991, **338**, 1565–1568.
3 G. L. Marcone, E. Rosini, E. Crespi and L. Pollegioni, *Appl. Microbiol. Biotechnol.*, 2020, **104**, 555–574.
4 M. Trojanowicz and M. Kaniewska, *Electroanalysis*, 2009, **21**, 229–238.
5 A. Bigdeli, F. Ghasemi, N. Fahimi-Kashani, S. Abbasi-Moayed, A. Orouji, Z. Jafar-Nezhad Ivrigh, F. Shahdost-Fard and M. R. Hormozi-Nezhad, *Analyst*, 2020, **145**, 6416–6434.
6 H. Su, Q. Zheng and H. Li, *J. Mater. Chem.*, 2012, **22**, 6546–6548.
7 L. Zhang, C. Xu, G. Song and B. Li, *RSC Adv.*, 2015, **5**, 27003–27008.
8 X. Zhou, C. Xu, Y. Jin and B. Li, *Spectrochim. Acta A*, 2019, **223**, 117263.
9 A. Contino, G. Maccarrone, M. Zimbone, P. Musumeci, A. Giuffrida and L. Calcagno, *Anal. Bioanal. Chem.*, 2014, **406**, 481–491.
10 S. H. Seo, S. Kim and M. S. Han, *Anal. Methods*, 2014, **6**, 73–76.
11 A. Bigdeli, F. Ghasemi, N. Fahimi-Kashani, S. Abbasi-Moayed, A. Orouji, Z. J.-N. Ivrigh, F. Shahdost-Fard and M. R. Hormozi-Nezhad, *Analyst*, 2020, **145**, 6416–6434.
12 C. Han and H. Li, *Small*, 2008, **4**, 1344–1350.
13 R. Freeman, T. Finder, L. L. Bahshi and I. Willner, *Nano Lett.*, 2009, **9**, 2073–2076.
14 G. M. Durán, C. Abellán, A. M. Contento and Á. Ríos, *Microchim. Acta*, 2017, **184**, 815–824.
15 C. Carrillo-Carrión, S. Cárdenas, M. B. Simonet and M. Valcárcel, *Anal. Chem.*, 2009, **81**, 4730–4733.
16 T. Delgado-Pérez, L. M. Bouchet, M. de la Guardia, R. E. Galian and J. Pérez-Prieto, *Chem. Eur. J.*, 2013, **19**, 11068–11076.
17 A. C. Vaiana, H. Neuweiler, A. Schulz, J. Wolfrum, M. Sauer and J. C. Smith, *J Am Chem Soc*, 2003, **125**, 14564–14572.
18 A. L. Rogach, A. Kornowski, M. Gao, A. Eychmüller and H. Weller, *Journal of Physical Chemistry B*, 1999, 103, 3065–3069.
19 A. L. Rogach, L. Katsikas, A. Kornowskiv, D. Su, A. Eychmüller and H. Weller, *Ber. Bunsenges. Phys. Chem.*, 1997, **101**, 1668–1670.
20 T. Nakashima, Y. Kobayashi and T. Kawai, *J. Am. Chem. Soc.*, 2009, **131**, 10342–10343.
21 R. Zhou, K. Y. Wei, J. S. Zhao and Y. B. Jiang, *Chem. Commun.*, 2011, **47**, 6362–6364.
22 F. Askari, A. Rahdar and J. F. Trant, *Sens. Bio-Sens. Res.*, 2019, **22**, 100251.
23 L. Zhang, C. Xu, C. Liu and B. Li, *Anal. Chim. Acta*, 2014, **809**, 123–127.
24 D. A. Armbruster and T. Pry, *Clin. Biochem. Rev.*

CHAPTER VI
CONCLUSIONS

The research activities have covered a wide range of luminescent systems, such as: carbon dots (CDs), ternary and quaternary I-III-VI quantum dots (QDs) and copper halides. The most remarkable results presented in this chapter are divided in four paragraphs respectively focused on: 1) synthesis, 2) photoluminescence, 3) chirality and 4) enantioselective chemosensing. Some comparative considerations on the optical and chiroptical properties of the different systems are also reported here.

1 SYNTHESIS

Different synthetic approaches have been investigated to produce chiral luminescent nanosystems. Special attention has been paid to the formation mechanism, revealing critical details for the optimization of the optical and chiroptical properties.

- A novel synthesis to produce chiral CDs, based on the radical assisted decomposition process of cysteine, has been developed. The Transmission Electron Microscopy (TEM) analysis reveals that the process forms CDs with an average size of about 6 nm and a crystalline graphitic core. The physical-chemical characterisation (x-ray photoelectron spectroscopy and Fourier transform infrared spectroscopy) highlights the presence of cysteine-derivates molecules grafted on the particles surface, probably via amide bonds. The formation mechanism analysed by UV/Vis absorption spectroscopy and Nuclear Magnetic Resonance (NMR) reveals the role played by a copper(II)-cysteine complex (*330 compound*) as active species in the catalytic process. Furthermore, the comparison with the reactivity of other substrates with similar structural units of cysteine, evidences: i) the role played by thiol groups in the redox process involving copper ions, ii) the role of the thiol and amino functional groups in the stabilisation of the Cu (II) oxidation state, fundamental to stabilise the catalytically active specie and iii) the role played by the carbon radicals in the carbonization process.
- A two-steps synthesis has been developed to produce chiral silver indium sulfide (AIS) QDs. The method has been optimised considering the molar ratio 1:4 between silver and indium. The TEM analysis shows that the process forms QDs with an average size of 2.1 nm characterised by a spinel $AgIn_5S_8$ phase as evidenced by X-ray Diffraction (XRD). A post-synthetic process to produce AIS/ZnS core shell QDs further enhances

the efficiency of the radiative recombination processes. The synthesis and the ZnS deposition treatment are successfully adapted to produce a wide variety of ternary and quaternary QDs and core shell QDs systems. The method allows to access to a wide variety of silver, copper, indium sulfide systems with different chemical compositions. The investigation of the formation process suggests semiconductors nanoclusters as intermediate specie in the QDs formation. The stability of these nanoclusters is controlled by the interaction with the ligand, and it can be modulated by opportunely adjusting the pH.

- A Ligand Assisted Reprecipitation process (LARP) has been developed to produce chiral $Cs_3Cu_2Br_5$ in the presence of arginine as chiral inductor. The process forms microwires crystals with a lateral size and length of about 100 nm and 5 μm, respectively, as observed by scanning and transmission electron microscopy. The formation of the desired crystallographic phase is verified by XRD. The effect of the ligand on the particle morphology has been investigated considering different ligands and it reveals the preferential interaction for basic amino acids such as arginine and lysine. Finally, a preliminary investigation on the application of the method to produce other metal halides ($Cs_3Cu_2Cl_5$, $Cs_3Bi_2Br_9$, $Cs_3Bi_2I_9$ and $Cs_2AgInCl_6$) proves its potential extension also to other systems. Since, this method does not allow to produce particles with nanometer size, further investigations on different ligands and solvents are required.

2 PHOTOLUMINESCENCE

The different systems investigated are characterised by different photoluminescence activity and distinctive recombination mechanisms are involved in their emissions. **Fig 1** shows the plot of the photoluminescence quantum yield (PLQY) of the different systems versus the wavelength of the maximum of their emission band (λ_{em}). As it can be seen, the photoluminescence spreads over the entire range of the visible light (as also represented qualitatively by the colour used for the symbols) and with very different PLQY values.

- Cysteine based CDs photoluminescence is related to aromatic and heteroaromatic groups with different degree of conjugation which compose the amorphous part of the nanoparticles. The strong dependency of the emission frequency on the excitation frequency is related to the presence of a broad population of different luminophores. The maximum intensity of the emission is observed at 460 nm (considering the excitation

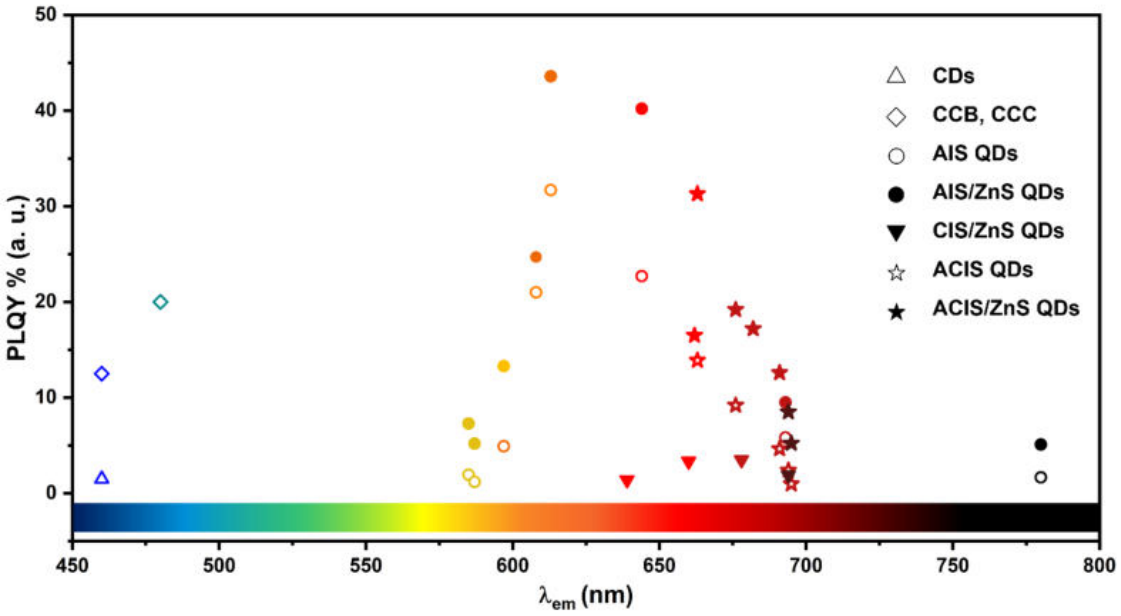

Figure 1: plot of the PLQY % data against λ_{em} maximum observed for the different luminescent investigated in the project, systems, labelled according to the symbol shape. The symbol colour is related to the wavelength of the maximum of the emission band (λ_{em}) and a reference of the visible spectrum is placed as an indicative guide.

at 380 nm) and a PLQY of 1.5 % is estimated. The emission can be modulated from 410 to 580 nm according to the variation of the excitation from 340 to 500 nm.

- The broad PL with large Stoke's shift observed in I-III-VI QDs systems is associated to donor-acceptor recombination mechanism. The emission can be tuned according to the specific chemical composition in the 580 – 700 nm range, with the only exception of the stoichiometric $AgInS_2$ QDs (**AIS11**) that shows an emission at 780 nm. Silver indium sulfide QDs show the highest PLQY (26.1, 31.7 and 21.0 % for **AIS14**, **AIS15** and **AIS16** respectively) for QDs characterised by a N_{Ag}/N_{metal} (molar ratio of silver to all the metal cations) 0.24 - 0.18 (**AIS14** – **AIS16**). Similar trend is observed for CIS/ZnS core-shell QDs, but with lower value of PLQY. This finding suggests a particular efficiency of the $AgIn_5S_8$ and $CuIn_5S_8$ spinel phases to promote radiative recombination processes. The quaternary systems, ACIS QDs, shows the possibility to further modulate the emission properties of the QDs, especially to improve the PLQY in the 670 – 700 nm range. The effect of the deposition of a ZnS shell on the PLQY shows an interesting enhancement (PLQYs of 31.7 and 43.6 % are observed for **AIS15** and **AIS15/ZnS** QDs) of the emission intensity related to the passivation of surface defects.
- $Cs_3Cu_2Br_5$ photoluminescence is dominated by exciton self-trapping recombination mechanism, a process commonly observed in copper-based halides and particularly

favourited by the structural flexibility of 0D halides. The photoluminescence shows an emission catered at 460 nm with a PLQY of 12.5 %. The preliminary investigation on $Cs_3Cu_2Cl_5$ reveals an emission at 480 nm and a PLQY of 20.3 %.

3 CHIRALITY

The chirality of the different nanosystems has been investigated by the characterisation of their chiroptical activity by circular dichroism (CD) spectroscopy. The chirality in all the investigated nanosystems can be mainly associated to surface chirality, originated by the effect of a chiral ligand which forms a chiral organic shell around an achiral inorganic core. However, the different systems exhibit major differences.

- The chirality in cysteine-based CDs can be related to the presence of partially undecomposed cysteine-derivates molecules (**Fig. 2**), probably sulfonic and sulfenic acids, grafted on the outer layer of the carbonaceous particles via covalent bonds (amide bonds). These cysteine-derivates retain some of the substrate chirality associated to the stereogenic centre on the C_α carbon. The observed optical chirality is related to chiral induction on n→π* transitions in the amide groups (CD band at 222 nm) and on π→π* transitions in small aromatic and heteroaromatic groups in close proximity to the stereogenic centre (CD band at 350 nm). The maximum chirality is observed after the first 2 h of the reaction as determined by the study of the effect of the reaction condition on the chiroptical activity. Longer reaction times cause an extensive reduction of the CD signal along with an increase of the population of several chromophores active in the visible range (observed by UV/Vis spectroscopy). This behaviour is related

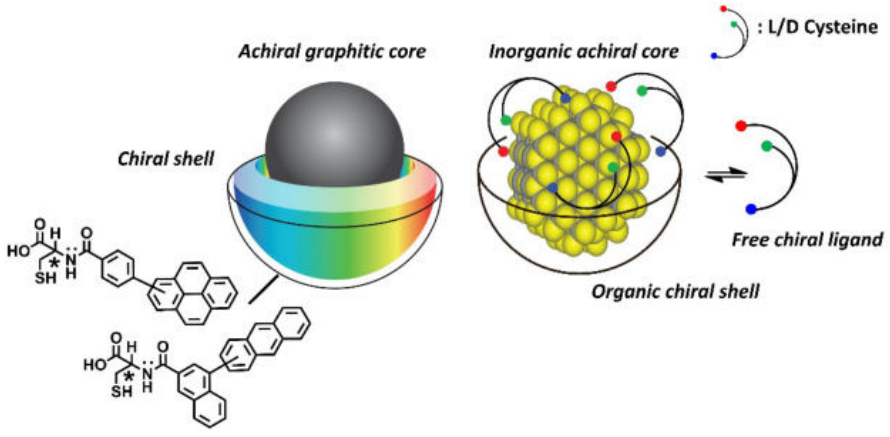

Figure 2: schematic representations of the structure of cysteine-based CDs (left) and chiral I-III-VI QDs stabilised by cysteine (right).

to radical processes involved in the formation of chromophores that affect the stereochemistry of the C_α carbon causing planarization and racemisation.

- The chirality in I-III-VI QDs is originated, at the particle-ligand interface, by electronic coupling or surface distortion introduced by the chiral ligand (**Fig. 2**). The effect of the ligand shell induces chirality in the electronic transition of the core causing the appearance of a CD active transition in the exciton region. A dynamic equilibrium between the ligand bonded on the particle surface and the free ligand in solution is observed and the chiroptical properties show a high sensibility to the ligand concentration. This effect is further enhanced in the nanoclusters, dispersed in low ligand concentration, that show a complete loss of chirality, suggesting a critical role of the ligand adsorption-desorption processes. Finally, the chemosensing investigation suggests that some degree of chirality is preserved for QDs after the ligand removal. Further investigation on the chiral memory to prove the presence of permanent surface chiral surface defects must be performed.

Beside the characterisation of the origin of chirality, the investigation on the chiroptical activity in I-III-VI QDs evidences a strong relation between the transfer of chirality and the QDs chemical composition. The silver indium sulfide systems show the highest chiroptical activity for **AIS14** – **AIS16** with a N_{Ag}/N_{metal} ratio in the range 0.24 - 0.18. Similar observations are also collected for CIS QDs and the quaternary ACIS QDs, suggesting a dramatic role of the QDs core crystallographic structure. In particular the spinel phases seem to be strictly related to the efficiency of the transfer of chirality.

The analysis of the chiroptical activity of $Cs_3Cu_2Br_5$ confirmed the successful transfer of chirality. The comparative study, considering the effect of other chiral ligands, suggests that basic amino acids are fundamental to introduce chirality by the LARP approach. The highest chiroptical activity observed for the particles covered by arginine, evidences a preferential interaction favoured by the guanidium group.

4 ENANTIOSELECTIVE LUMINESCENCE CHEMOSENSING

The analysis of the chemosensing activity of chiral AIS QDs and cysteine-based CDs, shows interesting properties of these systems for potential application. Two different types of chemosensor modes are investigated, i) The turn-Off chemosensor mode, based on the pho-

toluminescence quenching associated to the analyte addition, and ii) the turn-On chemosensor mode, based on the photoluminescence enhancement after the addition of the analyte.

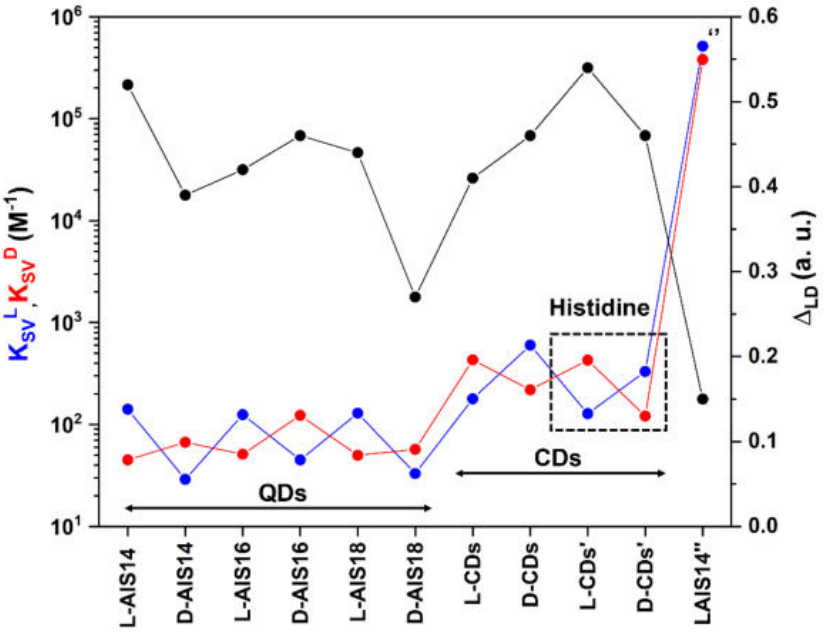

Figure 3: results of the enantioselective luminescence chemosensing investigations of different chiral nanomaterials. The K_{SV}^{L} and K_{SV}^{D} values are reported in blue and red respectively, the Δ_{LD} value are plotted in black. The data relative to the quenching in the presence of Histidine are labelled with (') and marked in the figure. ('') labels the data relative to the chemosensing of penicillamine using the Turn-on chemosensing mode. The uncertainty related to the K_{SV} values is estimated around 5 %.

The photoluminescence quenching or enhancement effect due to the analyte has been evaluated according to the Stern-Volmer model. The effect of the different analyte enantiomers has been followed by the analysis of the K_{sv} (Stern-Volmer constants) used to evaluate the sensitivity of the different systems (Ksv^{L} and Ksv^{D} for the L and D analyte enantiomer respectively). The parameter Δ_{LD} has been employed to express the enantioselectivity of the sensor. **Fig. 3** shows the values observed for all the investigated chemosensors.

- AIS QDs show a linear quenching in the presence of different tryptophan concentration in the millimolar range. This effect is related to non-radiative recombination pathways introduced by tryptophan molecules via photoinduced electron transfer mechanism. Some degree of enantioselectivity in the quenching activity have been evidenced comparing the quenching effect of L and D tryptophan for **L-AIS14** (K_{sv}^{L} 141 M^{-1} and K_{sv}^{D} 45 M^{-1}). Moreover, the opposite trend has been observed using **D-AIS14** (K_{sv}^{L} 29.0 M^{-1} and K_{sv}^{D} 67.0 M^{-1}). Similar values have been found using other AIS QDs with different chemical compositions (**AIS16** and **AIS18**). Among the issues associated with this type of sensor, we have focused our attention on the analyte concentration range. With the

aim to extend this range toward lower analyte concentrations, a Turn-On chemosensor has been prepared by a ligand removal treatment that caused a extensive reduction of the PLQY of **AIS14** QDs. The PLQY could be partially recovered by the surface passivation using thiols. The Turn-On chemosensing of penicillamine has been investigated considering the photoluminescence enhancement. With this approach the sensor applicability could be successfully extended to the micromolar range as evidenced for **AIS14** QDs. This feature is related to the higher affinity of the analyte for the ligand free QDs surface. However, a reduction of the enantioselectivity, related to the effect of the ligand removal process, has been also detected.

- CDs have been employed as Turn-Off chemosensor for tryptophan (Trp) and histidine (His). The analysis of the quenching activity of tryptophan has revealed a linear trend at an analyte concentration lower than 1.5 mM. In this condition, the enantioselective quenching of **L-CDs** in the presence of L- and D-Trp has been observed (K_{sv}^{L} 179 M^{-1} and K_{sv}^{D} 431 M^{-1}). The higher K_{sv} for D-Trp could be related to a preferential interaction between **L-CDs** and D-Trp. The opposite trend has been observed for **D-CDs** (K_{sv}^{L} 600 M^{-1} and K_{sv}^{D} 219 M^{-1}), that are characterised by a preferential interaction for L-Trp. Similar findings have also been reported for the quenching activity of His, in fact **L-CDs** presents a preferential quenching for D-His (K_{sv}^{L} 128 M^{-1} and K_{sv}^{D} 428 M^{-1}), while, **D-CDs** are preferentially quenched by L-His (K_{sv}^{L} 331 M^{-1} and K_{sv}^{D} 121 M^{-1}).

Acknowledgments

I have to thank my supervisor Prof. Alvise Benedetti and my co-supervisors Prof. Adolfo Speghini for all the results obtained during these PhD years. Their constant support, incentives and discussions, along with the possibility to work in their research laboratories have allowed me to realise, in my own way, this PhD project. I need to thank Prof. Yurii K. Gun'ko for hosting me in his laboratory in Trinity College Dublin and for his extensive experience on chiral nanomaterials. Special thanks goes to: Prof. Pietro Riello, Dr. Michele Back, Prof. Nicola Pinna and Prof. Elti Cattaruzza for their priceless technical and scientific supports.
With special consideration, I would like to thank some of the members of the technical staff form the different institutions that were involved in the project: Tiziano Finotto, Martina Marchiori, Davide Cristofori, Francesca Guidi, Dr. Serena Zanzoni, Dr. Marco Giarola, Dr. Manuel Ruether, Dr. John O'Brien and Mark Keegan. Their work has been fundamental to complete this thesis and, every day; it allows students and researchers to achieve incredible results.

Special thanks go to the coworkers from the ETA building for their constant support, friendship and sometimes patience: Dr. Mirena Sakaj, Dr. Vincenzo Lombardi, Davide Redolfi Bristol, Michele Crozzolin and Andrea di Vera. I have also to mention the coworkers from University of Verona and Trinity College Dublin: Dr. Giacomo Lucchini, Dr. Paolo Cortelletti, Lorenzo Rolla, Chiara Cressoni, Emil Milan, Francesco Mazzer, Dr. (Prof.?) Finn Purcell-Milton, Aoife Kavanagh, Aoine Coogan, Dr. Natalia Garcia Domenech, Dr. Sarah McCarthy, Dr. Garret Dee, Dr. Andrew Bethe, Dr. Kevin Behan and Dr. Iftikhar Ahmad.

I would like to thank my family for all the support during these years, in particular I need to thank my parents Marta Nesso and Roberto Branzi which allowed me to undertake this career. A special thank go to my close friends which have always been present (in their peculiar way) and to Liliana Anna Bosso, who endured without efforts, endless discussions fitted between the minimalistic chairs and the post-punk vibes of the Pedrotti Caffe'.

Estratto per riassunto della tesi di dottorato

Studente: Lorenzo Branzi matricola: 956507

Dottorato: Science and Technology of Bio and Nanomaterials

Ciclo: 35°

Titolo della tesi[1] :Novel Chiral Luminescent Nanomaterials: Synthesis, Characterisation and Application in Chemosensing

Abstract:

This thesis is focused on the investigation of novel chiral luminescent nanomaterials. Special attention is dedicated to the development of new synthetic methods, the characterisation of the physico-chemical properties of the chiral nanoparticles and the investigation of the origin of chirality. Finally, the most promising systems are investigated for the application in the enantioselective luminescence chemosensing.

The experimental work covers three classes of nanosystems characterised by a well-known photoluminescent activity: i) Carbon Dots, ii) Quantum Dots, focusing on ternary and quaternary I-III-VI silver, copper and indium sulfide systems and iii) copper halides. The investigation on novel syntheses which allow to introduce chirality in these nanosystems is motivated by their large potential technological applications.

Questa tesi è focalizzata sullo sviluppo di nuovi nanomateriali luminescenti chirali. Particolare attenzione viene dedicata allo sviluppo di nuovi metodi sintetici, alle caratterizzazioni delle proprietà chimico-fisiche delle nanoparticelle chirali e l'indagine sull'origine della chiralità. In fine, i sistemi più promettenti sono stati indagati per la loro potenziale applicazione come chemosensori luminescenti enantioselettivi.

Il lavoro sperimentale copre tre classi di nanosistemi caratterizzati da ben note proprietà di fotoluminescenza: i) Carbon Dots, ii) Quantum Dots, concentrandosi su sistemi ternari e quaternari I-III-VI basati su argento, rame e indio solfuri e iii) alogenuri di rame. L'indagine sui nuovi metodi di sintesi che permettano di introdurre chiralità in questi nanosistemi è motivata dalla loro potenziale applicazione tecnologica.

Firma dello studente

[1] Il titolo deve essere quello definitivo, uguale a quello che risulta stampato sulla copertina dell'elaborato consegnato.